University of Southampton

University of Southampton Research Repository

University of Southampton

Faculty of Engineering and Physical Sciences

<u>School of Engineering</u>

Analysis of Acoustic Cavitation Phenomenon Using Acoustic Emission Technique and Numerical Modelling of the Phenomenon

by

Byoung Guk Kim

Thesis for the degree of <u>Doctor of Philosophy</u>

December 2018

University of Southampton

<u>Abstract</u>

Faculty of Engineering and Physical Sciences

School of Engineering

Thesis for the degree of <u>Doctor of Philosophy</u>

Analysis of Acoustic Cavitation Phenomenon Using Acoustic Emission Technique
and Numerical Modelling of the Phenomenon

by Byoung Guk Kim

As an initial step to develop a new quantitative cavitation erosion model test method using acoustic emission (AE) technique, this thesis aimed to estimate an AE threshold to cause soft paint coat damage by an ultrasonic cavitation apparatus experimentally and to construct a numerical model of acoustic cavitation from such a device to get more insight to the possible physical mechanisms to cause such damage. Especially, in conjunction with the numerical model, a stability problem with a compressible multiphase flow solver using a barotropic relation is addressed. A series of experiments to estimate the AE threshold were carried out using a sonotrode (tip diameter: 16 mm) with the nominal working frequency of 20 kHz and maximum power output of 1 kW mimicking the soft paint tests. AE signals from acoustic cavitation were measured and analysed. To support the experiment and to get more insight to the involved physics, numerical studies were carried out using an open source CFD software package suite, OpenFOAM (v.3.0.1) in three phases. To analyse acoustic cavitation oscillation characteristics by AE, an FFT technique was used. The measured AE signal magnitudes were found to be consistent against various impact loadings. In modelling acoustic cavitation from ASTM G-32 type devices based on a compressible multiphase flow solver using a barotropic cavitation model, it was found to be critical for the stability and the physical soundness of the solution, to ensure boundedness of the mass convection term and to satisfy the CFL number close to one. This research will contribute to future development of a new quantitative model erosion test method based on AE technique.

Contents

Contents

List of Tables

List of Tables

x

List of Figures

Research Thesis: Declaration of Authorship

I, Byoung Guk Kim declare that this thesis entitled as "Analysis of Acoustic Cavitation Phenomenon Using Acoustic Emission Technique and Numerical Modelling of the Phenomenon" and the work presented in it are my own and has been generated by me as the result of my own original research.

I confirm that:

1. This work was done wholly or mainly while in candidature for a research degree at this University;
2. Where any part of this thesis has previously been submitted for a degree or any other qualification at this University or any other institution, this has been clearly stated;
3. Where I have consulted the published work of others, this is always clearly attributed;
4. Where I have quoted from the work of others, the source is always given. With the exception of such quotations, this thesis is entirely my own work;
5. I have acknowledged all main sources of help;
6. Where the thesis is based on work done by myself jointly with others, I have made clear exactly what was done by others and what I have contributed myself;
7. Parts of this work have been published as:

   (1) Kim, B. G., Wilson, P. A. & Turnock, S. R. (2016). *"Numerical Simulation of an Ultrasonic Vibratory Cavitation Device."* In: Wackers, J. (ed.) 19th Numerical Towing Tank Symposium. St. Pierre d'Ole'ron

   (2) Kim, B. G., Wilson, P. A. & Turnock, S. R. (2017). *"Simulation of Acoustic Stream with a Sonotrode"*. In: Lloyd, T. P. & Ploeg, A. V. D. (eds.) 20th Numerical Towing Tank Symposium. Wageningen, the Netherlands: MARIN.

   (3) Kim, B. G., Wilson, P. A. & Turnock, S. R. (2018). "Exploration of a Possibility to Assess Erosive Cavitation by Acoustic Emission Technique". 14-16 May, 10th International Symposium on Cavitation. Baltimore, ML, USA.

Signature: _____

Date: _____

Acknowledgements

Nomenclature

Symbols

A	Signal amplitude	[m]
A_0	Radius of a spherical bubble cluster.	[m]
a	An experimental coefficient for the geometric spreading of the AE signal through a medium.	[-]
a_1	A constant coefficient of turbulent kinetic energy in relation with the shear stress in the boundary layer flows.	[-]
b	An experimental coefficient for the decay of the AE signal through a medium.	[-]
C_{AE}	An experimental AE sensor response coefficient for an external force to generate the AE signal.	[-]
$C_{prod.}$	Vapour production rate coefficient of hydrodynamic cavitation models.	[-]
$C_{dest.}$	Vapour condensation rate coefficient of hydrodynamic cavitation models.	[-]
C_f	Skin friction coefficient.	[-]
C_s	Smagorinky coefficient.	[-]
C_μ	Turbulence model coefficient.	[-]
c	Sound speed in a medium.	[m/s]
d	Distance vector from a cell centre to its neighbour cell centre.	[m]
E	Young's modulus.	[kg/m·s^2]
F	Force exerted by a steel ball dropped from a height.	[N]
f_{AC}	Acoustic pressure impact events frequency from an acoustic cavitation event.	[Hz]
f_{HC}	Acoustic pressure impact events frequency from a hydrodynamic cavitation event.	[Hz]

Nomenclature

f_d	Acoustic driving frequency	[Hz]
f_n	Natural frequency of bubble oscillation.	[Hz]
$\boldsymbol{I}$	Identity tensor.	[-]
k	Turbulent kinetic energy.	[m^2/s^2]
N_b	Total number of bubbles in a fluid domain.	[-]
n_0	number of bubbles within a unit fluid volume.	[1/m^3]
$\boldsymbol{n}$	Surface normal vector.	[-]
p_∞	Reference pressure.	[Pa]
p_b	Pressure inside a vapour bubble.	[Pa]
p_{b0}	Initial pressure inside a vapour bubble.	[Pa]
p_G	Partial pressure of non-resolvable gas inside a cavity bubble.	[Pa]
p_{sat}	Vapour saturation pressure	[Pa]
R_n	Reynolds number	[-]
R	Bubble radius.	[m]
R_0	Initial bubble radius.	[m]
$\dot{R}$	First time derivative of the bubble growth.	[m/s]
$\ddot{R}$	Second time derivative of the bubble growth.	[m/s^2]
r	Radial distance from a bubble centre.	[m]
$\mathbf{S}$	Surface vector.	[m^2]
S	Stress tensor.	[kg/m·s^2]
$S_{prod.}$	Vapour production rate (evaporation rate).	[kg/s]
$S_{dest.}$	Vapour condensation rate.	[kg/s]
S_{net}	Net production rate of vapour.	[kg/s]
S_f	Face flux of a physical quantity.	[1/m^2]
s	A dummy variable for space.	[m]

T	Deviatoric stress tensor.	[kg/m·s^2]
T_B	Natural oscillation period of individual bubbles.	[s]
T_C	Sound propagation time within a bubble cluster.	[s]
t	Relative time elapsed from an event.	[s]
t_{AC}	Test time duration for the soft paint erosion tests with an ultrasonic cavitation apparatus.	[s]
t_{HC}	Test time duration for a soft paint erosion tests with a model ship propeller in a cavitation tunnel.	[s]
U	Fluid velocity vector.	[m/s]
U_f	Face flux of the fluid velocity through a boundary face.	[m/s]
U_i	Fluid velocity component in i-direction.	[m/s]
U_n	Fluid velocity component normal to a face boundary.	[m/s]
U_∞	Reference fluid velocity.	[m/s]
u'	Perturbing part of a fluid velocity vector.	[m/s]
u'_i	Perturbing part of a fluid velocity component in i-direction.	[m/s]
u_τ	The friction velocity.	[m/s]
u^+	Non-dimensional flow velocity with regard to the friction velocity.	[-]
V	Volume of a bubble.	[m^3]
V_s	AE signal voltage output after linear DAQ system.	[V]
V_G	Volume of the vapour phase.	[m^3]
V_L	Volume of the liquid phase.	[m^3]
V_p	AE signal voltage output after logarithmic DAQ system with a 10 kHz peak hold.	[V]
x	Receiver distance from an AE source.	[m]
x_{ref}	A reference receiver distance where the AE signal receiver response characteristic is known.	[m]
y^+	Non-dimensional wall distance with regard to the Kolmogorov length scale.	[-]

Nomenclature

Greek symbols

α	Volume fraction of the vapour phase	[-]
α_0	Volume fraction of the vapour phase before the disturbance propagation.	[-]
α_{nuc}	Nucleation site volume fraction.	[-]
ε	Turbulent kinetic energy dissipation rate.	[m^2/s^3]
Ψ	Compressibility of a fluid ($\equiv d\rho/dp$).	[s^2/m^2]
Δ	Spatial filter size of a spatially discretised calculation domain.	[m]
Δt	Grid size of a temporally discretised time domain.	[s]
γ_G	Mass fraction of the non-condensable gas.	[-]
γ_V	Mass fraction of the vapour.	[-]
$\dot{\varphi}$	First order time derivation of any dummy variable φ.	[m/s]
$\ddot{\varphi}$	Second order time derivation of any dummy variable φ.	[m/s^2]
ρ	Density of a medium	[kg/m^3]
ρ_V	Density of the vapour phase.	[kg/m^3]
ρ_L	Density of the liquid phase.	[kg/m^3]
κ	Specific heat ratio.	[-]
Υ	Poisson ratio.	[-]
μ_t	Turbulent eddy viscosity coefficient.	[kg/m·s]
μ_v	Dynamic viscosity coefficient.	[kg/m·s]
μ_{eff}	Effective dynamic viscosity coefficient including turbulent eddy viscosity effect.	[kg/m·s]
ν_t	Kinematic turbulent eddy viscosity coefficient.	[m^2/s]
ν_v	Kinematic viscosity coefficient.	[m^2/s]
ν_{eff}	Effective kinematic viscosity coefficient including turbulent eddy viscosity effect.	[m^2/s]

Nomenclature

σ	Courant-Friedrichs-Lewy number.	[-]
σ_c	Surface tension.	[J/m]
σ_{ij}	Stress component in j-direction caused by a flow in i-direction.	[kg/m·s^2]
φ	A dummy variable for any physical quantity.	
$(\varphi)_c$	The value at the cell centre of a dummy variable φ for any physical quantity.	
$(\varphi)_f$	The value at the face centre of a dummy variable φ for any physical quantity.	
φ_i^n	A dummy variable for any physical quantity at a discretized spatial node i for n-th time step.	
τ_w	The wall shear stress.	[kg/m·s^2]
ω	Specific dissipation rate.	[1/s]
Ω	Velocity gradient in the normal direction to the flow direction.	[1/s]

Operators

dB$_{AE}$	AE signal level with regard to 1 x 10^{-6} V (volts).
A^T	The transpose of a tensor A.
$\bar{\varphi}$	Temporal averaging of a dummy variable φ (for RANS) or spatial filtering of the dummy variable (for LES).
$\tilde{\varphi}$	Favre density averaging operation for a dummy variable φ.

Abbreviations

AE   Acoustic Emission.

ASTM   ASTM international, formerly known as American Society for Testing and Materials.

CFD   Computational Fluid Dynamics.

CFL number   Courant-Friedrichs-Lewy number.

DAQ   Data Acquisition.

DSME   Daewoo Shipbuilding & Marine Engineering Co. Ltd. in South Korea.

FFT   Fast Fourier Transformation.

FDM   Finite Difference Method.

FEM   Finite Element Method.

FVM   Finite Volume Method.

HEM   Homogeneous Equilibrium Mixture.

ILES   Implicit Large Eddy Simulation

ITTC   International Towing Tank Committee.

LES   Large Eddy Simulation.

LR   Lloyd's Register EMEA in the U.K.

NS   Navier-Stokes (equations).

RANS   Reynolds Averaged Navier-Stokes equations

SSPA   SSPA Sweden AB, the model basin in Gothenburg, Sweden.

STFT   Short Time Fouriter Transformation.

URANS   Unsteady Reynolds Averaged Navier-Stokes equations.

Chapter 1   **Introduction**

1.1   **Motivation**

The current trend in the ship building industry is pushing designers to consider every fraction of efficiency improvement. With regard to ship propeller propulsive efficiency, from the author's personal industry experiences with propeller design, propeller efficiency improvement from design variation usually fell into a window of 1 % gain, which is the same order as the accuracy of ship model tests in the model basins. Even if judging from design competition experiences with a number of well-known third party design companies, it seems to the author that it is hardly expected to see any significant improvement such as beyond 3 % gain between the worst and the best designs under any given design constraints. Since propeller efficiency did not appear so sensitive to propeller design variation, the author as a propeller designer had been in position to choose ample safety margin against cavitation erosion at cost of some efficiency. Now it is hard to take such a "too conservative" position any more to survive market these days. Furthermore, many kinds of energy saving devices are fitted in front of ship propellers to improve the propulsive efficiency of the ships further. Unfortunately, these devices commonly create a more complex inflow to the propellers in return. Hence, the propellers are exposed to new risks of erosion from complex cavitation phenomena that were not experienced before such installation of additional energy saving devices.

Cavitation is a phenomenon of forming a cavity or a bubble in a liquid, which is similar to the phenomenon of boiling. Boiling occurs when a liquid is heated to the boiling point of a liquid. Such a phase change can occur by pressure change also. If a bubble is formed by a pressure change in a liquid without any thermal energy input, it is called 'cavitation'. Forming a bubble out of a liquid is called nucleation. Two ways of nucleation are possible. One is homogeneous nucleation, creation of a vapour from a pure liquid, which requires enormous energy. The other way is heterogeneous nucleation. Heterogeneous nucleation requires pre-existing nuclei in a liquid and a solid surface preferably with defects that can be a place to isolate the vaporised gas from the liquid due to the action of the surface tension. Most of cavitation occurs by heterogeneous nucleation. Cavitation occurs in many places round us; inside the nozzles of the ink-jet printers, in our knuckle joints, ultrasonic humidifiers, air bubble washing machines, fuel injectors of the diesel cars, turbo-machinery, on the ship propellers, etc.

Cavitation has drawn great interest of many researchers because the phenomenon was often accompanied by loud broadband noise, vibrations and damage (erosion) to materials. The first theoretical platform to approach the cavitation had been made by Lord Rayleigh (1917) in conjunction with a ship propeller failure accident on a Royal Navy vessel (Carlton, 2007). Since then the understanding of the mechanism of its destructive potential has been enhanced.

Cavitation erosion is a multi-disciplinary phenomenon involving bubble dynamics, propagation of compressible acoustic pressure waves, nonlinear static/dynamic response of an engineering structure, chemical corrosive action and so forth. Hence, it is still a long way to fully simulate all the involved physics, and ways are still being sought to simulate the phenomenon in a simpler manner whilst preserving the essential of physics.

In the shipbuilding industry, avoiding the risk of cavitation erosion is one of the main tasks for naval architects. Computational Fluid Dynamics (CFD) simulations are being adopted more and more to produce efficient solutions in complex design environment. Currently the assessment of cavitation erosion risk during the design of the ship propellers and the hull appendages may be carried out either by (1) visual observation with and without the aid of the soft paint method, (2) analysis of high speed video images or (3) acoustic impact method (ITTC, 2005). While the first two methods are readily available, the third one has not seen any real adoption that was widely accepted so far in spite of its good potential. The direct motivation to develop a quantitative method of cavitation erosion test comes from the limitations of the existing methods as follows.

Visual observations including the high speed video recordings cannot always be guaranteed to capture the erosive moments. The sight can be easily obscured by increased bubble population in the cavitation tunnel or by obstruction of complex propeller and/or hull geometry, although this handicap might be overcome by repetitive testing. Furthermore, such methods cannot provide the designers with any quantitative index of the cavitation aggressiveness. The visual impression can change even under the same test condition and heavily depends on individual convention of each model basin. If the designers do not have sufficient experiences to build their own correlation between the cavitation at the model scale for each basin and the ship scale, the interpretation of the model test result often becomes an endless argument between ship owner/operator and shipyard. Unfortunately, this kind of practical knowledge cannot be built in a short time.

The soft paint test method is widely recognised as one of the established cavitation erosion test methods for propellers. However, it is difficult to find any efforts to explain the scale effect or any physical correlation between the impact forces or pressures necessary to cause the real cavitation erosion damage and the soft paint coat damage. Furthermore, according to author's

experiment with the soft paint, the test results critically affected by the strength of the applied soft paint coat that largely depends on the humidity in the air and the ambient temperature while it was being prepared. For this reason, it is quite difficult to maintain consistency of the results with the soft paint test method. So it is not used widely.

Therefore, designers seek a new approach to enable them to assess the gain and risk of any new design from CFD and model testing before the real construction. A number of recent studies, e.g. Peters et al. (2015), Hasuike et al. (2009a), Nohmi et al. (2008), Patella et al. (2004), Kato et al. (1996), show such efforts to quantify the risk of erosion and some industrial bodies began to utilise such a tool (Hasuike et al., 2009b, 2011, Ponkratov, 2015).

In a similar line of such efforts, several industrial bodies agreed to a necessity to develop a more repeatable and quantifiable measure for cavitation erosion tests to replace the soft paint test method. The acoustic impact method was thought of as a promising means for the purpose. The acoustic impact method utilises the acoustic emission to determine the severity of cavitation attack. Acoustic emissions (AE) may be either the sound emission propagating through the water or elastic stress waves propagating through the structure subjected to the cavitation. In this study, AE is a term describing propagation of elastic stress waves through a material under cavitation attack. Rus et al. (2007) reported that the AE signal amplitude data showed very similar trends with either underwater noise or vibration measurement data and their amplitude varied according to the cavitation intensity variation.

Lloyd's Register (LR) has been using the AE technique to confirm their full scale observation of the cavitation development that looks erosive on the ship propellers and rudders by investigating the recordings of AE signal levels synchronised with the video images of the cavitation sequences. Once the erosive-looking cavity collapses occur in close-enough proximity to those surfaces, the AE signal level would rise in response to the impact strength. Therefore, by looking at the signal rise, one can confirm if any erosive-looking cavity collapse events really hit the engineering structure at what magnitude with the knowledge of AE response function to the source loadings. According to a business-confidential report of LR (Boorsma, 2009) that was accessible within the joint research programme, the AE signal levels threshold determined from a series of erosion tests with a small steel plate under an ultrasonic cavitation apparatus was similar with the AE levels threshold estimated from the AE measurements for rudder cavitation erosion at full scale.

The key idea of the acoustic impact method is simple. Since it was reported that cavitation impact events always generated a synchronised AE signal which was detectable at a significant level inside a ship's engine room (Boorsma and Fitzsimmons, 2009), it might be useful to determine the severity of impacts by measuring the acoustic emission signal level assuming

consistency of the AE signal response. If the AE signal amplitude would show a 1:1 correlation with the magnitude of the source loadings, and if one can determine a threshold impact loading level to cause the soft paint coat damage, one may use that level in the cavitation tunnel to determine the erosiveness of the cavitation.

1.2   Aims and objectives

The main aim of this work was to estimate experimentally an acoustic emission threshold level that would start to cause damage to a soft paint coated on a test specimen by cavitation collapses using an ultrasonic cavitation apparatus. Since an ultrasonic cavitation apparatus would be used in the experiment, and acoustic cavitation has several different features from the hydrodynamic cavitation, a study on a numerical model of acoustic cavitation was necessary to understand possible physical mechanisms to exert impact loadings that cause damage to the paint coat. Similar works had been carried out to model acoustic cavitation phenomenon numerically (Mottyll and Skoda, 2015, Žnidarčič et al., 2015), but there has not been any study to establish a quantitative threshold at which the soft paint coat starts to be damaged and possible physical mechanisms contributing to the damage.

In order to address these questions, the following objectives were set for the experiment at the start of this project.

(1) To establish an analysis method for the measured AE signals.

(2) To investigate the trend of AE signals by varying test parameters, e.g. the gap distance between the specimen and the ultrasonic horn tip, and power output of the sonotrode.

(3) To develop an empirical transfer function of AE signal level to correlate with the physical impact loadings.

(4) To determine an AE threshold condition that is equivalent to the conventional soft paint erosion tests.

For the numerical model study, the following objectives were set.

(1) To provide a stable and reasonably realistic solution of acoustic cavitation behaviour and the acoustic pressure waves propagation induced from the cavitation.

(2) To provide an insight of the physical mechanisms that contribute to the impact loadings on a test specimen.

In conjunction with the first objective for the numerical model study, addressing the stability problem with a compressible multiphase flow solver using a barotropic cavitation model (Žnidarčič et al., 2015) will be especially valuable for the community of similar research.

1.3   Novel Contribution to knowledge

Through this research work, the following contribution was made to the knowledge:

(1) A numerical model of acoustic cavitation behaviour and the propagation of its pressure waves was constructed based on a pressure-based multiphase flow solver 'cavitatingFOAM' of an open source CFD package suite, OpenFOAM.

(2) The solution stability issue with a compressible multiphase flow solver 'cavitatingFOAM', especially with the Wallis barotropic compressibility model, was addressed.

(3) It was confirmed that AE signal strength can be correlated with acoustic cavitation pressure impact loadings, and the signal can be analysed using the FFT technique based on Welch's method.

1.4   Structure of the thesis

This thesis consists of eight chapters. A fundamental review of cavitation and theories of cavitation erosion mechanism is briefly explained in chapter 2. In relation to this thesis work, acoustic cavitation and its distinctive features are also introduced. Then reviewed relevant works to simulation of acoustic cavitation and prediction models for cavitation erosion.

Chapter 3 describes the experimental work with the sonotrode to establish an analysis methodology of acoustic cavitation phenomenon and the test results to determine a correlation between the AE signal level and the impact loadings. A large portion of the chapter is devoted to describe an investigation on the relations of acoustic cavitation sub-harmonic oscillation frequency with the sonotrode power and the acoustic stream dispersion distance (gap distance between the sonotrode tip and the bottom of test bath) to understand the characteristic feature of acoustic cavitation. This was thought to be also important in terms of the pressure impact loadings to whom the sub-harmonic oscillation acoustic bubble cluster was the most dominant contributor as well with the individual oscillation of the acoustic bubbles. Finally a preliminary AE threshold was determined from the accelerated soft paint tests with the sonotrode.

Chapter 4 covers fundamentals of the numerical method to simulate acoustic cavitation and the details of the numerical methods used to construct a model are described. From chapter 5 to chapter 6, an exploration with a homogeneous equilibrium mixture (HEM) based compressible two-phase solver to set up an appropriate acoustic cavitation model is described.

Chapter 5 describes study results with a compressible multiphase flow solver based on a barotropic cavitation model. Unsteady Reynolds Averaged Navier-Stokes equations (URANS) approach was changed to a Large Eddy Simulation (LES) approach in the middle of the study which was not described in any detail since any distinct difference had not been identified while it was being studied. The effect of domain size on the predicted pressure waves, interference from the reflected pressure waves at the wall boundaries with the pressure waves in the calculation domain were mainly discussed here.

Chapter 6 revisits the convection schemes, turbulent wall functions and the mesh grid quality effect on the solution. The importance of the boundedness of mass convection scheme for the accuracy and stability of the solution was identified. The mesh grid quality was also very critical to the solution quality. Qualitative validation results of the numerical model against the benchmark experimental results reported by Žnidarčič et al. (2014) are presented.

Finally, chapter 7 summarizes the whole thesis work and describes limitation and necessary future work. Acoustic cavitation was analysed using an AE technique. The power spectrum of the AE signals indicated very similar characteristics with acoustic pressure waves reported by other researchers. A rough estimate of an AE threshold was extracted from a series of experiment using the sonotrode to mimic the soft paint erosion tests. It was noted the paint test results might be significantly affected by the drying condition of the paint. Therefore, a more reliable method to estimate an AE threshold at the model scale would be desirable for future development. Acoustic cavitation was modelled using a barotropic cavitation model based on either the linear or the Wallis model with large eddy simulation. A stability issue of a compressible two-phase flow solver was addressed. The numerical model indicated reasonable agreement with the experimental results of Žnidarčič et al. (2014). Since it took so long time until the stability issue was resolved, the error analysis of the model and further refinement had to be left for future work.

Chapter 2   **Cavitation Erosion**

2.1   **Introduction**

Cavitation is a phase change phenomenon driven by the local pressure change. Where the local pressure drops below the vapour pressure in a liquid flow field, bubble cavities will form and grow in the liquid. The cavity will start to shrink and eventually collapse when the local pressure increases. The collapse phase of the bubbles are known to have potential to cause mechanical damages on the solid boundary faces that are subject to the cavitation. Such mechanical damage process is called erosion.

According to Carlton's survey of literature, cavitation was not of any interest for engineers or scientists until ship propellers began to suffer from cavitation erosion damages in the 19th century. The earliest attempt to theoretically analyse such development of vapour in a liquid was by Besant in 1859 (Carlton, 2007).

The term 'cavitation' appeared first in a report (Parsons and Cook, 1919, Schneider, 1949) of research initiated in the United Kingdom in 1915 to investigate troublesome erosion damage on warship propellers. In the report, stating the locally repeated hammerings from collapse of small cavities as the cause of such damage, they termed it 'cavitation', which prevails in society to this day. They performed an experiment to demonstrate such pressure impacts could penetrate a metal plate and suggested the pressure magnitude in the order of 2 GPa based on the tensile strength of the plate. However, no theoretical analysis was given.

A simplified theory to explain such phenomenon was put forward by Lord Rayleigh (1917). He considered an idealized single bubble of spherical form posed in infinite expanse of incompressible inviscid liquid in which the bubble growing/collapsing by the pressure difference between the liquid and inside the bubble. Combining the kinematic condition of a bubble and the momentum equation for the liquid and the bubble, he derived what is now called the Rayleigh equation for the bubble motion. The model could explain the emission of high pressure as a result of shrinking bubble and the eventual outburst of the vapour pressure inside it. This can be credited as the beginning of modern history of the bubble dynamics study and his assumptions are often adopted in modern applications for the cavitation problems.

Though his model provided a great theoretical basis for the cavitation erosion mechanism, it suffered several theoretical/experimental issues. Schneider (1949) argued that the problem of the theory arose from the incompressibility assumption and considered the effect of compressibility of the liquid. Furthermore, he suggested that the effect of pressure impulse

from the bubble implosion could not reach so far away. Another theory was suggested that the water-hammering effect by liquid micro-jets in the final collapse phase of the spherically asymmetric bubbles as an extra damaging mechanism in addition to the bubble implosion model. Kornfeld and Suvorov (1944) are said to have suggested such a possibility first. Naudé and Ellis (1961) investigated the non-spherical cavity collapse on a solid surface theoretically and experimentally observed the impinging liquid jet formation through spherically non-symmetric collapse of an electric spark-generated bubble near a solid boundary, which agreed very well with the theory. Benjamin and Ellis (1966) summarized the theory that when a bubble under non-uniform pressure gradient would get translational momentum and accelerated towards a solid boundary, it could not but be distorted into a toroidal form and finally the liquid jet would penetrate the toroidal form of bubble. As seen from the paper of Plesset and Chapman (1971), there were long arguments for the two models. Nowadays both the models are regarded as feasible mechanisms involved in the cavitation erosion process.

Wang and Brennen (1994) suggested another view to explain the cavitation erosion mechanism. They thought the cloud cavitation or a cluster of bubbles imploding as a chain reaction would occur in a geometrically focused manner towards the centre depending on certain flow characteristics. Therefore, the pressure wave impacts loading became intense enough to cause plastic deformations of the material surface and eventually the loss of material.

Through the 80's and 90's, studies have been also made to enhance the understanding of the cavitation erosion from the metallurgical aspect (Karimi and Avellan (1986), Franc et al. (1994), Momma (1991), Momma and Lichtarowicz (1995b)). These studies were largely focused on predicting a feasible life span of materials under repetitive cavitation impacts, for example, in turbo machinery. Therefore, contribution was made to expand the body of knowledge in views of the material properties related to the resistance against erosion, spectral analysis of cavitation aggressiveness and erosion rate, etc. It is understood the plastic deformation in the early stage of cavitation erosion or the material loss in the developed stages are results of accumulated effects by repetitive cavitation (pressure) impacts beyond a certain threshold magnitude, e.g. the yield stress and strain rate sensitivity of a material. The theories of cavitation erosion mechanism will be further described in section 2.3. The key subjects in the cavitation research field are classified in Table 1.

In the following sections, acoustic cavitation is introduced as the means to study cavitation erosion. Then the mathematical/numerical model to simulate acoustic cavitation will be discussed. Finally, literature is reviewed to overview the works to predict the risk of cavitation erosion so far.

Table 1 Field of cavitation research.

Cavitation research field	Relevant literature
Bubble dynamics	Schneider (1949), Gilmore (1952), Plesset and Mitchell (1956), Naudé and Ellis (1961), Ivany and Hammitt (1965), Benjamin and Ellis (1966), Lauterborn and Bolle (1975), Plesset and Prosperetti (1977), Chahine (1982), Konno et al. (1995), (1999), Konno et al. (2002), Brujan et al. (2002), Navarrete et al. (2015)
Cavitation structure of macroscale	Kohama et al. (1993), Chahine (1982), Chahine (1984), Chahine et al. (1992), Ganesh et al. (2016), Hsiao et al. (2014), Hsiao et al. (2016), Ma et al. (2015a), Ma et al. (2015b), Raju et al. (2011), Ceccio and Brennen (1991), Wang and Brennen (1994), (1999)
Fluid-structure interactions	Hammitt (1962), Karimi and Avellan (1986), Karimi and Leo (1987), Franc et al. (1994), Zhong and Chuong (1993), Momma (1991), (1995b), Okada et al. (1995), Fortes-Patella et al. (2001), (2005), Soyama et al. (2001), Dular and Osterman (2008), Osterman et al. (2009), Hattori et al. (2010), Hattori and Kishimoto (2008), Pöhl et al. (2015), Roy et al. (2015)

2.2   Acoustic cavitation

2.2.1   What is acoustic cavitation?

Acoustic cavitation is the name of cavitation phenomenon that is specifically created by the acoustical means. Three physical processes can create cavity bubbles; hydrodynamic, optic and acoustic. Based on the type of sources, we call it hydrodynamic, optic or acoustic cavitation. Hydrodynamic cavitation occurs by dynamic pressure change round a moving body. Optic cavitation can be generated commonly by a short pulsed laser. An instantly super-heated liquid to its thermodynamic stability limit, for example 300 °C for pure water, tends to transit to its vapour phase, which is more stable in such a condition, to produce a fast-growing vapour bubble in the liquid. Acoustic cavitation occurs by a rapidly changing high intensity.

acoustic pressure field in a liquid. Acoustic cavitation has several different characteristics from that of the hydrodynamic or optic cavitation. The size of the acoustic bubbles are almost uniform and oscillate at a fixed frequency, while the hydrodynamic or optic cavitation may include various sizes of bubbles. Hydrodynamic cavitation includes different forms of cavities like sheet, cloud or vortex cavitation at different frequencies (Chahine et al., 2014). The uniformity of the cavity sizes and the fixed oscillation amplitude and frequency with acoustic cavitation enable the researchers to perform cavitation erosion tests in a reproducible way. The hydrodynamic cavities move along the flow stream. However, acoustic cavitation phenomenon is only limited to relatively stationary cloud cavitation and recirculates with the acoustic stream. It is assumed here that this difference in the participating cavitation phenomena would not affect the experimentally obtained impact pressure threshold to cause the soft paint coat damage, since the material would be blind to the mechanism that creates the cavitation bubble and respond only to the exerted impact pressure forces caused by its collapse.

Acoustic cavitation by ultrasonic cavitation apparatus is commonly used to study cavitation erosion resistance in the laboratory environment together with cavitating jet apparatus (Chahine et al., 2014). The typical range of the acoustic driving frequency is between 20 kHz and up to 15 MHz depending on its application purpose. There is a standard testing method guided by ASTM International (formerly American Society for Testing and Materials, website: https://www.astm.org/ABOUT/overview.html) such as ASTM G-32 for acoustic cavitation apparatus.

2.2.2 Distinctive characteristics of acoustic cavitation

The distinctive characteristic of acoustic cavitation from the other types of cavitation is that, owing to its almost adiabatic compression of the bubbles in phase with the ultrasonic pressure oscillation, acoustic cavitation can result in a momentary local extreme temperature rise as thousands °K, pressure peaks of GPa and local flow acceleration to the 12 orders of gravity (Choi, 2017, Louisnard and González-García, 2011, Okitsu and Cavalieri, 2018). Other interesting phenomena may accompany acoustic cavitation such as sonoluminescence (Ashokkumar, 2011, Choi, 2017, Ohl et al., 1999, Yasui, 2002), acoustic streaming (Catarino et al., 2014, Frampton et al., 2003, Lighthill, 1978, Mekki-Berrada et al., 2016, Moudjed et al., 2014, Mozurkewich, 2002, Nowak et al., 2015, Nyborg, 1953, 1958, Schenker et al., 2013, Setareh, 2016), sonochemical reactions (Okitsu and Cavalieri, 2018) as well as the common features of the cavitation, e.g. acoustic emission (generation and propagation of mechanical disturbances and sound wave propagation in the liquid) and erosion.
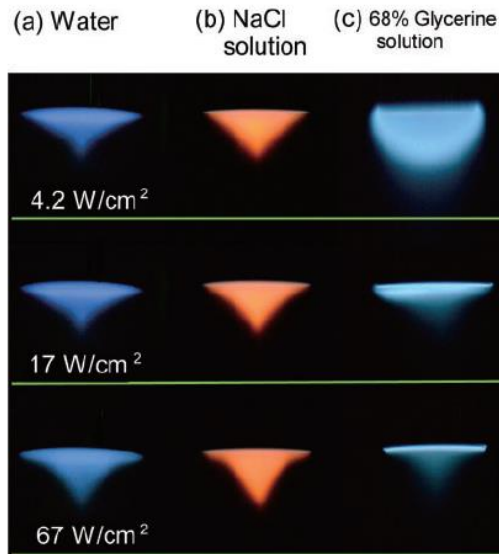
Figure 1 Examples of sonoluminescence using a horn type transducer at 27 kHz (after Choi, 2017).
The adiabatic compression process within the gas bubbles in a very short time scale of
$10^{-4} \sim 10^{-5}$ s can heat the gas within the bubble enough for them to be ionized.
Depending on the ionised gas molecules within the vapour, different colours of light
are emitted.

Sonoluminescence is a light emission phenomenon understood as a result of energy discharge from the ionised gas molecules under the extreme temperature and pressure in the collapsing bubbles that undergo adiabatic compression process within very short time scales as $10^{-5} \sim 10^{-7}$ s. Figure 1 shows such examples showing different colour of light emissions depending on the ionised molecules inside the acoustic bubbles. Sonochemical reactions are a bit more complex. They can be put into three categories; (1) reactions inside the bubble and its interface (formation of radicals and transfer to the liquid through the interface), (2) reactions by the ionised radicals in the liquid and (3) reactions induced by physical effects such as shock impulses from the collapsing bubbles and micro-stirring as a result of acoustic streaming. These peculiar side effects are getting much attention from researchers as a novel technique of advanced chemical treatment and established a field of chemistry, namely sonochemistry. Comprehensive discussion on the mechanism of such effects can be found in Ashokkumar (2011), Leighton (1994), Louisnard and González-García (2011), Mettin (2005) and Choi (2017). The current research will focus on the physical effects of acoustic cavitation in terms of erosion in the following sub-section.

2.2.3   Dynamics of the acoustic bubbles

The physical effects of acoustic cavitation are related to the mechanical energy bursting from the collapsing bubbles and acoustic streaming. Acoustic streaming is the term for the flowing of a liquid in the direction of a given sound field as a result of the sound energy absorption to the medium (Leighton, 1994). The acoustic bubbles are subjected to Bjerknes forces (Bjerknes, 1906, Blake, 1949, Leighton, 1994, Leighton et al., 1990). Bjerknes forces are generalised buoyancy in principle due to the pressure gradient in the liquid subjected to a sound field. There are two kinds of Bjerknes forces. The first one is the force on a single bubble exerted from the acoustic stream. The second Bjerknes force is the same force but between the bubbles. In this case, the affecting sound field is generated from the nearby pulsating bubble(s). The general form of the Bjerknes force can be written as $-V\nabla p$, where V is the volume of a bubble and p is the sound field pressure affecting the bubble. A comprehensive explanation on how the forces work on the acoustic bubbles can be found in Leighton (1994), Leighton et al. (1990). The main consequences from the action of these forces are that (1) the bubbles would gather round the pressure nodes or antinodes depending on their relative sizes against the resonant bubble size, and that (2) only similar sized bubbles would attract each other, whereas different sized ones would repel each other. These forces are the main drivers to form acoustic bubble filaments, which are chains of acoustic bubbles (Mettin, 2005). However, it does not appear to be so important in the mechanism to form a mass of acoustic bubble cloud in a mushroom shape. Žnidarčič et al. (2015) and Mottyll and Skoda (2015) reported successful simulation results of the sub-harmonically oscillating acoustic cavitation behaviour without inclusion of the Bjerknes forces. Therefore, the Bjerknes forces are not regarded as important to explain the sub-harmonic oscillation of the acoustic bubble cluster.

What is the resonant bubble size? Indeed, it is the (spherical) bubble radius that satisfies the continuity and momentum equations for the bubble at a given ambient pressure. Assuming very small sinusoidal perturbation of the ambient pressure field and the adiabatic bubble expansion/contraction in phase with the pressure, this can be found either by considering the kinetic energy of the liquid by the bubble motion (Leighton, 1994, Minnaert, 1933) or solving the Rayleigh equation neglecting the viscosity and surface tension as Eq. (2.1) by substitution of the pressure and bubble radius with Euler representation as $Ae^{-i\omega t}$ (Brennen, 1995). If we assume an initial bubble radius R_0 in a pressure field, we can find an approximate natural frequency f_n of the bubble oscillation corresponding to the ambient pressure or vice versa. This is called Minnaert frequency (Brennen, 1995, Minnaert, 1933) as Eq. (2.2). The symbols p_∞, p_b, ρ_L, κ represent a reference pressure at a far field, pressure inside a vapour bubble, density of a liquid, specific heat ratio of the vapour respectively. Calculating the resonant bubble

radius for the water with the ambient pressure of 101 kPa and driving frequency of 20 kHz and adiabatic process assumption for the vapour, it becomes about 164 µm.

$$R\ddot{R} + \frac{3}{2}(\dot{R})^2 = -\frac{p_\infty - p_b}{\rho_L} \quad [\dot{R} \equiv \frac{dR}{dt}, \ddot{R} \equiv \frac{d^2R}{dt^2}] \tag{2.1}$$

$$f_n = \frac{1}{2\pi R_0}\sqrt{\frac{3\kappa p_\infty}{\rho_L}} \tag{2.2}$$

The inertial cavitation is a term for, simply speaking, all the non-thermal expansion/contraction of the bubbles (Leighton, 1994). Bubbles can grow/shrink either thermally or by other reasons such as pressure change within a liquid. All the cavitation discussed in this work is inertial cavitation.

The Blake threshold (Blake, 1949, Noltingk and Neppiras, 1950) is a theoretical pressure threshold beyond which the bubbles would grow rapidly and eventually collapse maybe with just a few rebounds. This applies only to a very small bubbles with which the surface tension becomes the dominant driver. Below the threshold, the acoustic bubbles will stay stable with small oscillation, which we call 'stable cavitation'. Therefore, mathematically the threshold can be found by finding the critical bubble radius beyond which a bubble becomes unstable. This critical radius can be found by differentiating the equation for the pressure equation at the bubble interface setting the pressure gradient zero.

2.2.4   Sub-harmonic oscillation of the acoustic bubble clusters

Finally, an interesting feature of acoustic cavitation is the presence of a sub-harmonic oscillation of the acoustic bubbles rather than at the acoustic driving frequency. Sub-harmonic oscillation means an oscillation of acoustic bubbles at a frequency of 1/n-th (n: a positive integer) of an acoustic driving frequency. The first report of the sub-harmonic frequency of acoustic cavitation noise was by Esche (1952). Theoretical treatment had been carried out to explain this phenomenon (Crum, 1982, Eller and Flynn, 1969, Hansson and Morch, 1980, Neppiras, 1969, Noltingk and Neppiras, 1950).

It is not so an old story that a reasonable prediction of it became possible (Mottyll and Skoda, 2015, Žnidarčič et al., 2015). Hansson and Morch (1980) suggested an idea to predict the sub-harmonic oscillation frequency. They thought the disturbance propagation speed through a bubble cluster was relevant to the sub-harmonic oscillation frequency and constructed a calculation model of it. Their final form took in essence the same form as Eq. (2.2) assuming the acoustic bubble cluster shape either a hemi-sphere for the unbounded case or a cylindrical
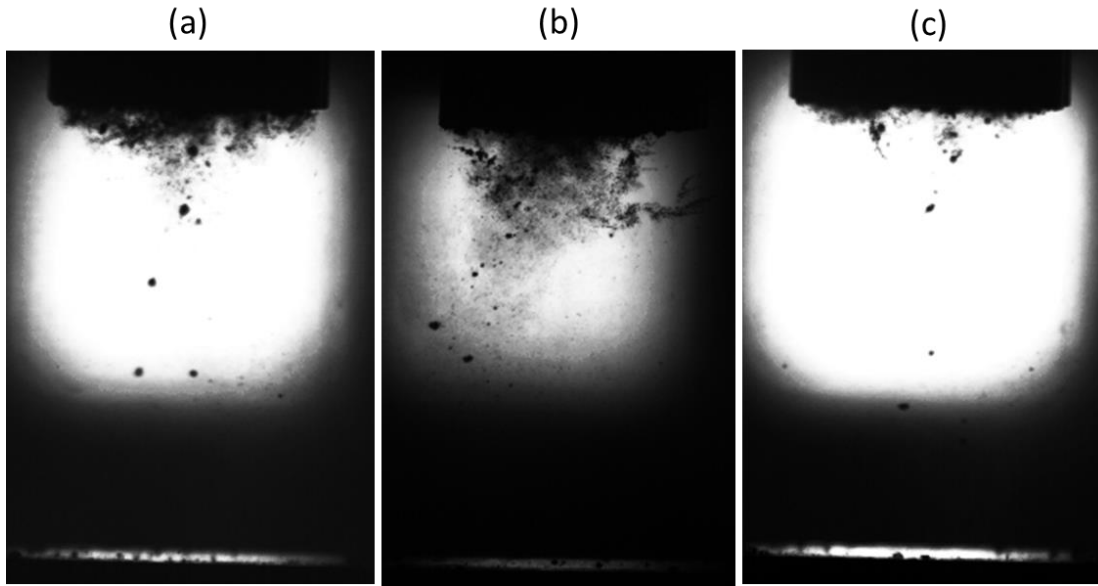
Figure 2 Stroboscopic images of the acoustic bubbles by shadowgraphy with an ultrasonic cavitation apparatus working at the driving frequency of 19.72 kHz and with a gap distance of 30 mm during an experiment. 6 units of 100 W LED light sources were used to produce the light. The dark shadow on the top of the figures is the ultrasonic horn tip (diameter: 16 mm) and the acoustic bubbles growing underneath the horn tip. The bright bottom represents the top of copper alloy specimen.

pillar in the case of bounded dispersion distance between the acoustic source and the solid bottom to confine the acoustic stream growth. Žnidarčič et al. (2014) suggested the same conclusion from their experiment that the sub-harmonic oscillation frequency could be approximated by Eq. (2.2) substituting R_0 for the radius of a sphere or a hemi-sphere that has an equivalent volume with the bubble cluster volume.

Figure 2 illustrates an example of the acoustic bubble cluster evolution beneath the ultrasonic horn tip (top of the images) vibrating at 19.72 kHz with peak-to-peak amplitude of 76 µm. In the figure, (a) and (c) show the bubble cluster that grows along the axis of the ultrasonic horn (a) and on the periphery of the ultrasonic horn tip (c) in alternating manner. (b) shows a bursting of the cavity cluster at the terminal stage of the growth along the axis. At the bottom of the images (top face of the soft paint coated test specimen) there are small number of bubbles reaching the bottom along the recirculating acoustic stream, which are recognisable but not very clear due to low light intensity there. The figures were taken at the frame rate of 2000 fps with different strobe light frequencies of (a) 250 kHz, (b) 500 kHz and (c) 166.7 kHz (the strobe light on and off time durations were always even) to capture different phases of the oscillation.

It is understood that the following process occurs with acoustic cavitation phenomenon. The acoustic bubbles produced by ultrasonic cavitation apparatus would have mostly a uniform size and it is equal to the resonant bubble radius corresponding to the acoustic driving frequency. The bubbles pulsate in phase with the driving pressure. Once the power intensity increases beyond a certain threshold, which is not clearly identified yet, the acoustic bubbles on the horn tip surface start to cover the whole surface and always attached to the surface forming a cluster. Once the outlying bubbles start to collapse, the collapse energy is transferred inward as suggested by Hansson and Morch (1980) or Wang and Brennen (1994). By this energy transfer the erosive power become far much enhanced compared with the collapse of individual bubbles and become dominant source of the erosion by acoustic cavitation. Once the acoustic power intensity becomes higher than a certain threshold, the acoustic bubble cloud becomes large and cannot shrink/expand according to the acoustic excitation. It is known to oscillate at a number of acoustic cycles. Therefore, it is called sub-harmonic oscillation. The sub-harmonic oscillation frequency will be the same as the inverse of the acoustic pressure wave propagation time from the outermost layer of a bubble cluster to the centre of the cluster.

To the author, it appears that the threshold power for the sub-harmonic oscillation phenomenon could be understood as the acoustic power intensity to create the acoustic bubble population enough to retard the propagation speed of the disturbance significantly, which is assumed to be the main driver of the sub-harmonic oscillation, compared with the individual bubble pulsation speed. The propagation speed of the acoustic pressure waves through a bubbly liquid medium heavily depends on the amount of bubbles (the number density of bubbles and their size distribution); barotropic cavitation models can depict the reduced sound speed in a bubbly medium. With the bigger volume fraction of bubble phase in a liquid medium, the slower the propagation speed of the disturbance becomes in the models. These barotropic cavitation models appear valid to explain the current phenomenon. As the sonotrode power intensity increases, the bubble population/volume increase to cover the whole surface of the ultrasonic horn tip and eventually start to form a slowly oscillating large bubble cluster as illustrated in Figure 2. Then, due to the increased bubble population/volume, the distance between the bubbles become close enough to interact with each other. At the same time, the disturbance propagation speed becomes significantly retarded compared with the pulsation speed of the individual bubbles. Hence, the pulsation frequency of the bubbles as a cluster becomes lower than the driving frequency. This appears to explain roughly the main driving mechanism of the sub-harmonic oscillation phenomenon associated with acoustic cavitation.

2.3   Theories of cavitation erosion mechanism

Traditionally the cavitation erosion mechanism has been studied in terms of the flow aggressiveness. It is now understood as a complex phenomenon involving the structural response characteristics of a material as well as the flow aggressiveness itself. Unfortunately, due to the complexity and huge computing cost, such a massive study is not yet practical to be applied to the industrial projects like assessment of the marine propeller cavitation erosion or even rudder cavitation erosion. The most typical form of practical approaches is that to utilise CFD simulation to estimate the pressure impact loading characteristics where the cavitation would occur.

With regard to the mechanism of creating the immense magnitude of pressure impulses, several mechanisms are known responsible, e.g. impulsive pressure waves from a spherical bubble collapse or the impinging liquid jet from the non-spherical collapse of a bubble due to a near-wall boundary. Such phenomena are all supported by much experimental evidence. The problem was that their effective ranges could not reach more than a distance of similar order as the micro bubble diameter (in the order of $10^{-3} \sim 10^{-6}$ m). In the 1980's and 90's many researchers tried to view the mechanism from a more macroscopic viewpoint. For example, it is very commonly observed that cavitation erosion accompanies cloud cavitation (cluster of many micro bubbles that appear as a cloud of bubbles). Therefore, a theory emerged to explain the cavitation erosion mechanism as a result of the chain reaction of bubbles. The static pressure fluctuations cause the bubbles at the outer boundary of the cavity cluster to start to collapse. Their collapse create higher pressure field for the inner bubbles. The inner bubbles collapse more violently. These further enhance the pressure field for the bubbles that are further inside again. In this manner, the potential energy of the outer bubbles is transferred inward and enhance the collapse intensity. When the cloud is near a wall boundary, by the same mechanism of the non-spherical bubble collapse, the collapse energy is concentrated to the wall boundary.

From the perspective of the structure or material, the mass loss by cavitation erosion is understood as a kind of fatigue failure process. It is believed that there are certain thresholds for both the magnitude of impact loadings and energy level to create a permanent deformation or loss of material. The thresholds will vary depending on the physical properties of individual material, e.g. yield strength, response characteristic to a sudden dynamic loadings, etc. A part of the potential energy of the cavity bubbles is transferred to the solid boundary in the form of acoustic pressure impacts. A part of the mechanical kinetic energy is accumulated near the boundary surface of the solid in the form of strain. Once the energy exceeds a certain threshold, that is believed relevant to the fatigue failure mechanism, erosion would start to occur. This

energy cascade theory is now widely accepted as an important main mechanism of the cavitation erosion.

If the acoustic emission signal level represents the pressure impact loading on a material, it could be used as a pressure sensor and one may be able to determine the risk of cavitation erosion at either full scale or model scale by comparing the signal with the known threshold at the corresponding scale. In the following sub-sections, the relevant theories are reviewed. The relevant works of literature are listed in Table 2 based on the theories of cavitation erosion.

Table 2 Cavitation erosion models and relevant literature.

Erosion mechanism	Short description of the mechanism	Relevant literature
Bubble implosion	Erosion caused by high amplitude of pressure waves from the bubble implosion.	Rayleigh (1917), Schneider (1949), Gilmore (1952), Ivany and Hammitt (1965), Plesset and Prosperetti (1977), Tomita and Shima (1977), Fujikawa and Akamatsu (1980)
Impinging micro-jet	An impinging micro water jet by proximity of a gas bubble to a solid wall causes erosion damage.	Naudé and Ellis (1961), Benjamin and Ellis (1966), Chahine (1982), Zhang et al. (2015), Beig et al. (2016)
Cloud cavitation	Bubble implosion at the outside of the cavity cloud triggers pressure waves directing towards the centre of the cluster of bubbles and create high amplitude pressure waves that exert damaging impact force to the solid surface.	Reisman and Brennen (1997), (1998), Kumar and Brennen (1991), (1993), (2015), Wang and Brennen (1994), (1999), Hsiao et al. (2016), Ma et al. (2015a), Raju et al. (2011)
Shock wave energy cascading	Accumulation of the energy of shock waves either by bubble implosions or impinging micro-jets whose magnitude are at or	Hammitt (1962), Karimi and Leo (1987), Franc et al. (1994), Pereira et al. (1998),

above a certain material-specific threshold energy eventually causes fatigue damage of a solid boundary.	Fortes-Patella et al. (2013), Roy et al. (2015)

2.3.1 Bubble implosion

This theoretical model was first put forward by Rayleigh (1917). Reyleigh equation as Eq. (2.1) in section 2.2.3 for the bubble motion provides the principal basis to understand the bubble dynamics. Therefore, it is worth to following how it was derived. The derivation follows Mehrem (2013).

A gas bubble in an unbounded fluid domain is considered with the following assumptions:

(1) Both the fluids (air and water) are assumed to be incompressible and inviscid.

(2) The pressure perturbation is small compared with the mean pressure of the field.

(3) The vapour pressure inside the bubble is constant everywhere inside
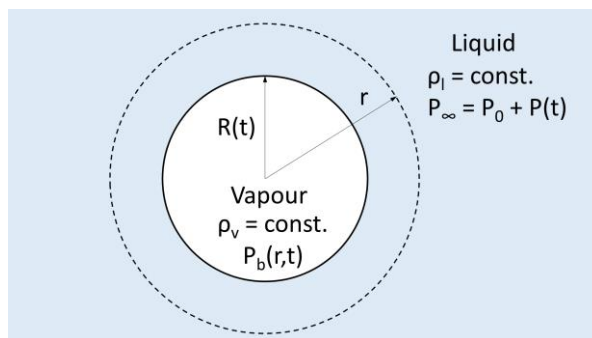
Figure 3 A fluid domain for the bubble dynamics model by the Rayleigh equation.

the bubble.

(4) The bubble remains spherically symmetric.

(5) There is no slip at the interface of the bubble and liquid.

(6) The surface tension of the bubble is negligible.

To describe the bubble motion, start from mass conservation. Firstly, define the bubble radius at a time point t as a function *R(t)*. The net mass flux through the bubble/liquid interface at a

bubble radius *R(t)* must be equal to the net flux through any imaginary surface of the concentric sphere with a radius of r in the liquid as Eq. (2.3) (See Figure 3).

$$4\pi r^2 \rho_L \frac{dr}{dt} = 4\pi R^2 \rho_V \frac{dR}{dt} \tag{2.3}$$

Hence, the net liquid velocity *dr/dt* at a location *r* can be related to the bubble interface growth *dR/dt* as Eq. (2.4).

$$\frac{dr}{dt} = \left(\frac{R}{r}\right)^2 \frac{dR}{dt} \tag{2.4}$$

Now, consider the momentum equation for the liquid in the spherical cooridinates. Since the viscosity and the surface tension are neglected, the momentum equation is written as Eq. (2.5).

$$\frac{\partial \boldsymbol{U}}{\partial t} + \boldsymbol{U} \cdot \frac{\partial \boldsymbol{U}}{\partial r} = -\frac{\nabla p}{\rho_L} \tag{2.5}$$

Substituting the flow velocity $\boldsymbol{U}$ with Eq. (2.4) into the momentum equation, Eq. (2.5), Eq. (2.6) is obtained where the overdot represents time derivate.

$$\left[\left(\frac{R}{r}\right)^2 \ddot{R} + \left(\frac{2R}{r^2} - \frac{2R^4}{r^5}\right)\dot{R}^2\right] dr = -\frac{1}{\rho_L} dp \tag{2.6}$$

Finally, integrating both sides from the bubble interface R to ∞, the Rayleigh equation is obtained as Eq. (2.1).

To solve the equation, a relation between the pressure inside the bubble and bubble radius is required. This may be modelled as an ideal gas in adiabatic process where κ is specific heat ratio, p_g pressure contribution from a non-resolvable gas inside a vapour bubble, p_{b0} initial pressure inside the bubble.

$$p_b = p_G - p_{b0}\left(\frac{R_0}{R}\right)^{3\kappa} \tag{2.7}$$

This model had been further developed to consider the viscosity, surface tension and the compressibility effects (Gilmore, 1952, Keller and Miksis, 1980, Plesset and Prosperetti, 1977).

These kinds of models assume a spherically symmetric vapour or vapour/gas mixture bubble within an incompressible or weakly compressible liquid. Collapse or rapid decrease in the size

of vapour cavities in a liquid can give rise to enormous magnitude of hydrodynamic pressures. However, the problems with these models are that (1) the high pressure pulses can be effective only within a short range as the same order of bubble size, and (2) a bubble does not keep its spherically symmetric shape when it approaches to a solid boundary within a distance as close to its radius. Theoretical investigation on the pressure waves (Ivany and Hammitt, 1965, Schneider, 1949) suggested the pressure wave amplitude by the implosion would be sufficiently large enough for causing erosion only if the impact occurred only within a distance as the same order of the initial bubble radius.

2.3.2 Impinging liquid jet

Naudé and Ellis (1961) demonstrated that a liquid jet forming at the final stage of bubble collapse in a liquid could damage an Aluminium specimen using a spark method. The spark method was heating a liquid to form a bubble by a momentary electric spark. Benjamin and Ellis (1966) critically reviewed the issues of the bubble implosion model in relation to its spherically symmetric bubble assumption and tried to explain the formation of a micro-jet of
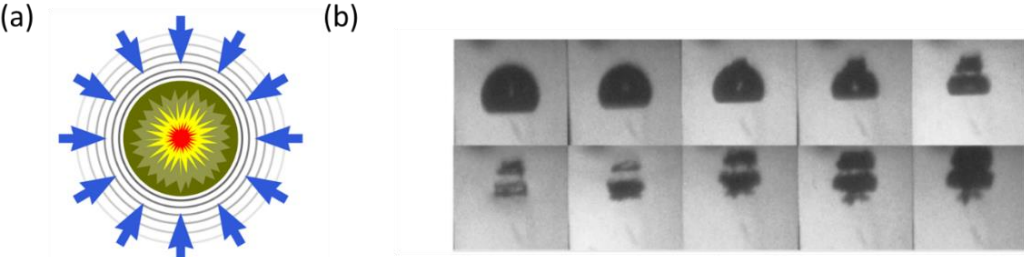
Figure 4 Illustrations of the two cavitation pressure wave emission mechanisms: implosion model (a), impinging liquid jet at the last moment of a bubble collapse near a solid boundary (the top edge of the figures) in sequence from the top left to the bottom right at 1 µs interval (after Brujan et al. (2002)) (b).

liquid under the influence of near solid boundary and its damaging mechanism in view of some aforementioned experimental results with spherically non-symmetric bubbles. Figure 4 (b) shows a sequence of a non-spherical bubble collapse as it approached a solid boundary (top of the figures) at 1 µs interval.

They considered a bubble in an inviscid liquid under pressure gradient and with a solid boundary on a side. Due to the pressure gradient, the bubble will get the momentum to translate, and if it is close enough, then the bubble will tend to move towards the solid boundary by the action of the surface tension, even if the pressure gradient is directed parallel to the boundary. This is because the flow passing through the space in between the bubble and the boundary becomes faster than the flow passing above the bubble. As the bubble is

accelerated towards the wall boundary and it approaches the wall close enough, the bubble face towards the wall starts to be retarded due to the wall while the rear is still being accelerated. Hence, the bubble is deformed into a torus or similar form as shown in Figure 4 (b). As this deformation occurs over an extremely short time scale, such deformation creates a liquid jet that penetrates the narrow spot of the bubble at this final stage to cause mechanical damage on the wall. The ability to cause damage was thought to largely depend on the translation velocity of the bubble.

This model explains why not all the violent looking cavity collapses lead to severe erosion damage and the fact that the bubbles of high erosive potential must be situated in close proximity of a solid surface.

2.3.3 Cloud cavitation

The interest starts from the fact that violent noise and material damage accompany the collapse of cloud cavitation. Thus, the cloud cavitation appears to be highly relevant to cavitation erosion damage. Hansson et al. (1982) were the people who suggested the idea. d'Agostino and Brennen (1983, 1989), Wang and Brennen (1994, 1999) sought the relevance theoretically, and Reisman and Brennen (1997), Reisman et al. (1998) tried to demonstrate such relevance by experimentation.

Wang and Brennen (1994, 1999) considered a spherical cloud of spherical bubbles of a uniform size and homogeneously distributed in an infinitely spaced incompressible liquid to investigate the erosive potential of a cloud cavitation theoretically. They formalised a ratio of the shockwave propagation time through the cloud and the oscillation period of individual bubbles as an indicator of the resulting violence of the cloud collapse. According to their investigation, there were two time scales involved in the bubble cloud dynamics; one for the global time scale T_C which represented the time for the acoustic pressure disturbance propagation through the cloud, and the other time scale T_B for the natural oscillation period of the individual bubbles. From the linear theory of d'Agostino and Brennen (1989), the propagation time T_C for a bubble cluster having the radius of A_0 in a liquid of density ρ_L was calculated as Eq. (2.8). T_B was the individual bubble collapse time that is the inverse of Minnaert frequency in Eq. (2.2).

$$T_B \approx 2\pi \left(\frac{\rho_L R_0{}^2}{3\kappa p} \right)^{1/2} , \quad T_C = \frac{A_0}{(\kappa p / \alpha_0 (1 - \alpha_0) \rho_L)^{1/2}} \tag{2.8}$$

They concluded that if the pressure disturbance were passing through the bubbles at similar or slower speed than the growth/collapse speed of the individual bubbles, the growth/collapse of bubbles would occur from outside inwards as a chain reaction and the resulting pressure impact loading should become much enhanced than the original driving pressure perturbation.

Recently, Hsiao et al. (2016) performed a numerical simulation based on a multi-scale Eulerian-Lagrangian model allowing large bubble oscillation and high amplitude of pressure perturbation to take account of highly non-linear individual bubble growth/collapse behaviour. Their bubble simulation results indicated so called 'shielding' effect of the outer-lying bubbles and geometric focusing towards the solid boundary with development of much higher pressure impact in the order of 100 times than the driving pressure perturbation in the case of the driving frequency matched the cloud resonance frequency. Figure 5 illustrates one of the results with a solid wall boundary at the bottom of the figures. In the early stage, the bubbles grow (t = 26
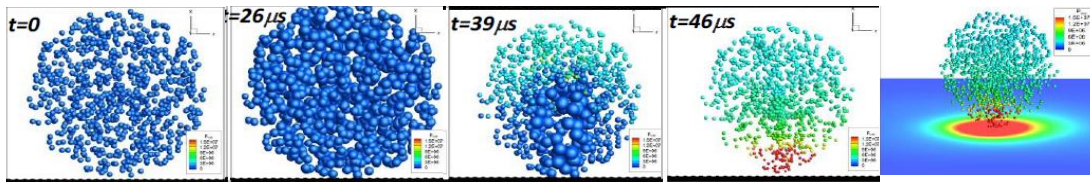
Figure 5 Time sequence images of bubble cloud emitting pressure waves (after Hsiao et al. (2016)). From the left, the bubbles grow and start to shrink. The collapse starts from the outer shell of the bubble cloud. At the presence of near-wall boundary, the shock waves propagate towards the wall boundary (t = 39, 46 µs). Finally, in the right end figure, the accumulated energy is transferred to the wall with far enhanced magnitude of pressure.

µs) and start collapsing from the outside (t = 39 µs). Further collapses are triggered inwards or towards the solid boundary with enhancement of the pressure (t = 46 µs). In the final stage, much higher pressure than the perturbing pressure is exerted on the solid surface (the right-end figure).

The assumptions in this theory are very similar as the sub-harmonic oscillation of acoustic cavitation and the conclusions about the cloud resonance frequency should also be relevant to acoustic cavitation phenomenon. Their conclusions about the resonance frequency of the bubble cluster are as follow;

(1) The resonance frequency of the bubble cloud was far lower than the prediction by the linear theory based on d'Agostino and Brennen (1989); the linear theory appears valid only for small perturbation pressure amplitude, e.g. 10 % of ambient pressure.

(2) The resonance frequency decreased almost linearly as the excitation pressure increased.

2.3.4   Shock wave energy cascading

Since hydraulic turbo-machinery cannot avoid aggressive cavitation environment, there has been a steady interest in the life span of such devices in a harsh working environment. This model is rooted by such a practical necessity. Therefore, it mainly concerns prediction of material loss rate or incubation period until the material loss starts to occur rather than the hydrodynamic causes of cavitation erosion. Likewise all the other cavitation erosion models, this model also assumes the pressure impact loadings are the primary cause of the erosion but it approaches in terms of accumulation of the impact energy of the shock waves similar to the fatigue failure process.

Hammitt (1962) observed cavitation damage on a number of specimens in a cavitating venturi tunnel filled with water and mercury respectively. A varying erosion rate and early formation of large pits were identified. The important results of this series of experiment were that large non-symmetric pits tended to form at the early stage. Their size and depth did not change after formation. From this fact, he thought this agreed well with the fatigue hypothesis by Boetcher (1936) and suggested an explanation that defective crystalline structures in the material 'peel off' as a result of work-hardening of the underlying layers by continuous shock wave impacts. This sort of activity was thought to occur very rapidly until no more such weak spots in the exposed region were left. After this, in the interim stage, the work-hardened surface could endure far longer, hence the erosion rate retarded for a while. Another suggested evidence to
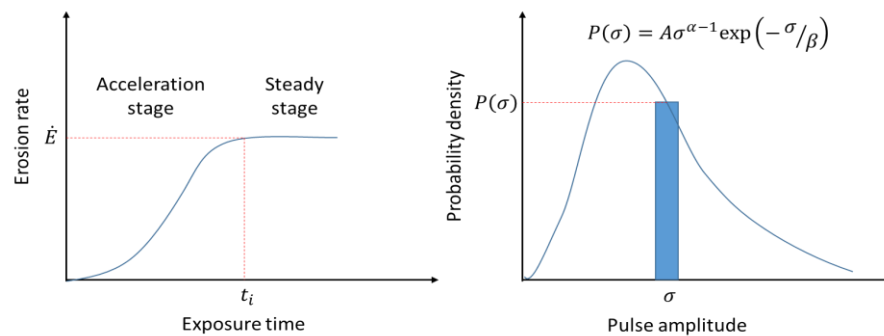
Figure 6 Typical pattern of erosion curves and PDF for pressure pulse amplitude distribution (Karimi and Leo, 1984). They found that the cavitation erosion process occurs in two stages (the right figure), and thought the cavitation erosion process as similar with the fatigue failure process. The amount of energy above a certain threshold pressure level was thought to be relevant to explain the cavitation erosion mechanism.
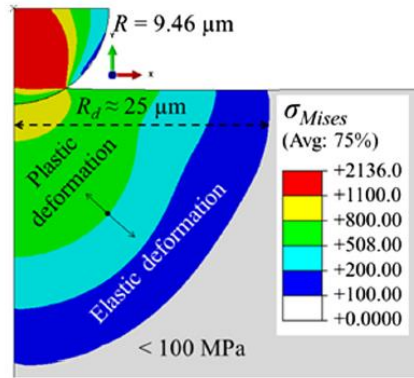
Figure 7 A nanoindentation simulation result illustrating the damage penetration (Roy et al., 2015).

support such an idea was the fact that sharp ridge structures of the large pits were mostly found at the downstream side. Based on the experimental results up to then, he assumed that cavitation erosion damage would only occur by shock waves of which energy exceeded a certain energy threshold depending on the material.

In the same line of thought, Karimi and Leo (1987) proposed a mathematical model to describe the cavitation erosion rate of alloys. The key idea was to build a statistical model of the spatial and temporal distribution of the shock waves of which the mean level was determined by flow condition. They decomposed the erosion rate as multiplication of the functions for the single damage size distribution, the damage penetration factor (relative size of region affected by stress wave over damage size) and the spatial temporal distribution of the impacts. The probability density functions (PDF) for the pressure impacts amplitude and single damage size were obtained from the experimental data such as illustrated in Figure 6. The damage penetration factor was estimated by a formula for strain attenuation at a relative distance over the work-hardening layer depth R_d as illustrated in Figure 7 (Francis, 1976, Karimi and Leo, 1987, Sundararajan and Shewmon, 1983). Figure 7 illustrates an example of impact and the damage penetration which occurs in a wider range than the impact radius.

Pereira et al. (1998) tried to formalise the cavitation erosion process in terms of an energy cascade. According to their theory, the potential energy contained in a bubble is transferred to a solid material at a certain ratio that depends on the material. They defined the ratio as 'collapse efficiency', which was reported in the order of $10^{-5} \sim 10^{-4}$ from their experiment with a symmetric NACA foil at different incidence angles. To further relate the energy involved in the material erosion, they introduced the concepts of 'erosive power' and 'erosive efficiency'. 'Erosive power' concept means the total amount of energy contributing to the damage process and 'erosive efficiency' is the ratio between erosive power and the total power of a bubble.

Momma and Lichtarowicz (1995a) and Okada et al. (1995) studied the relation between the pressure impact loads by bubbles collapse and the erosion damage. Both of them measured the cavitation impact pressure using a piezoelectric sensors and related it with the size and volume of erosion pits in time. Okada et al. (1995) suggested a linear relation between the pressure wave impact energy and the area of erosion pits.

2.4 Review of relevant works

Theories of cavitation erosion mechanism have been summarized in the previous section. In this section, some notable relevant works of the experimental/numerical studies are reviewed in terms of the mechanical effects of acoustic cavitation and the numerical simulation of acoustic cavitation ultimately allowing the risk assessment of the erosion by acoustic cavitation.

2.4.1 Works on acoustic cavitation

Study of cavitation began undoubtedly with Rayleigh (1917). Study of acoustic cavitation appears to have begun in the middle of 20th century where it began to be used as a tool to study cavitation erosion in a much accelerated manner in the laboratories. The peculiarity of acoustic cavitation compared with the other types of cavitation seems to have received attention of researchers then. Esche (1952) was the first person to report the existence of sub-harmonic frequency noise from the bubbly liquids in a sound field. There followed a number of experimental reports confirming his observation. But, there was no explanation of the physical mechanism of the phenomenon. In the 1960s, four possible mechanisms were suggested; (1) collapse of transient bubbles, (2) oscillation of the bubble surface, (3) parametric amplification of pre-existing component and (4) nonlinear oscillation of bubbles. While there was no good experimental support for any of them yet, hypotheses (2) and (4) received wider support from the researchers.

Ellis (1955) carried out an experiment with an ultrasonic cavitation apparatus to demonstrate the mechanical impact loadings due to bubble collapse was the main contributor of erosion and the magnitude was estimated at least of the order of 345 MPa (50000 PSI).

Neppiras (1969) measured the acoustic emission from gas bubbles of a uniform size injected into the water and glycerol-water mixtures under the sound field with a wide range of frequencies and intensities up to the transient cavitation threshold (pressure beyond which the bubble starts to rapidly grow and collapse). He suggested two possible mechanisms to generate sub-harmonic oscillation; (1) forced oscillations of bubbles of which resonance frequencies

are sub-multiples of the driving frequency or (2) presence of a preferred large bubbles that counts for the sub-harmonic frequency while there exist various size of bubbles generating wide band background noises.

Hansson and Morch (1980) suggested an idea to provide an explanation of the sub-harmonic frequency in terms of collective response of the acoustic bubble cluster either in a hemispherical shape or a cylindrical column shape. This idea was adopted also by Wang and Brennen (1994, 1999) that modelled the destructive potential of cloud cavitation. Experimental results by Žnidarčič et al. (2014) also appears to support this idea.

Leighton (1994) provided a good introduction to a wide range of research works and theories to understand acoustic cavitation phenomenon and actively working in the field (Birkin et al., 2005, Birkin et al., 2011, Jamaluddin et al., 2011, Leighton, 2015, Leighton et al., 2003, Leighton et al., 2008, Leighton et al., 2004, Leighton et al., 2012, Turangan et al., 2008, Vian et al., 2010). Vian et al. (2010) investigated a spatial correlation between the multi-bubbles sonoluminescence, the acoustic pressure and the erosion. They reported that erosion rate of acoustic cavitation showed different trend from the multi-bubble sonoluminescence or acoustic pressure in a high frequency ultrasonic field above 50 kHz, while a strong spatial coherence among the three phenomena was observed in the lower frequency range. They assumed insufficient bubble nuclei, that are suitable for the inertial cavitation at high frequency range, could be one of the main reasons for such deviating trend of erosion rate from the other phenomena in a high frequency range. Birkin et al. (2011) measured the correlation of the large pressure emissions with the collapses of acoustic bubble cluster and surface erosion occurrences that temporally coincided always with one another. To measure the surface erosion in real time, they used a passive metal electrode. Passive metals are metals that form an oxide film (passivating layer) to protect themselves from further oxidation. They measured the electric current required to re-grow the passivating layer that had been mechanically removed from the surface of the electrode.

Truong (2009) observed acoustic cavitation with a 47 kHz high intensity focused ultrasound (HIFU) device aiming for medical use of acoustic cavitation as a micro knife-less surgical tool. He measured the destructive potential of acoustic cavitation ranging 30 ~ 60 MPa. Also identified three main types of cavitation as (1) attached cavitation on the ultrasonic horn tip, (2) peripheral vortex cavitation round the tip and (3) cavity accompanied by the jet-like acoustic streaming below the horn tip. He reported the first type was the strongest source of the destructive potential.

Dular et al. (2012) tried to simulate acoustic cavitation generated by a 3 mm ultrasonic horn working at 20 kHz. They simulated the problem using a 2-D URANS simulation of a two-

phase flow with a mass transport cavitation model (Zwart et al., 2004) which failed to predict a correct sub-harmonic frequency of acoustic cavitation. The deviation was thought as a result of cavitation model that could not account for the increase of non-resolved gas contents in time or inability of the simplified bubble dynamics implementation into the source/sink terms to count for the longer life span of the real life bubbles. Žnidarčič et al. (2014), Žnidarčič et al. (2015) further examined the influencing physical parameters in the Rayleigh-Plesset (Plesset and Chapman, 1971, Rayleigh, 1917) equation as Eq. (2.9) by experiment. Here T_b denotes the temperature inside a bubble, σ_c surface tension, μ dynamic viscosity of the liquid respectively.

$$R\ddot{R} + \frac{3}{2}(\dot{R})^2 = -\frac{p_\infty - p_b(T_b)}{\rho_L} + \frac{p_G}{\rho_L}\left(\frac{R_0}{R}\right)^{3\kappa} - \frac{2\sigma_c}{\rho_L R} + \frac{4\mu}{\rho_L R}\dot{R} \qquad (2.9)$$

They concluded the temperature, viscosity and the surface tension of a liquid were not influential parameters for the sub-harmonic oscillation frequency and the nonlinear bubble acceleration term ($R\ddot{R}$) of the Rayleigh-Plesset (R-P) equation must be added to account for the longer life span of real life bubbles as observed from acoustic cavitation phenomenon. They validated the non-inertial term corrected mass transport model could account well for the sub-harmonic frequency.

Mottyll et al. (2014), Mottyll and Skoda (2015) carried out URANS simulation of acoustic cavitation. They used a density-based compressible multiphase flow code solving the Euler equations for the mass and momentum conservation with an isentropic barotropic cavitation model to correlate the pressure density relation. They reported a successful simulation results with the model in terms of sub-harmonic oscillation frequency, the cavity volume and the pressure peaks. Interesting fact was that they employed a full 360 degree 3-D model to avoid exaggerated concentration of the pressure impact events with a quarter (90 degree) model, which will be also discussed later in chapters 5 ~ 6. They determined the time step size to satisfy the acoustic CFL (Courant-Friedrichs-Lewy) condition (Courant et al., 1967) by setting the CFL number $\sigma \approx 1.2$, which is defined as Eq. (2.10) where Δt is the time step size, $\boldsymbol{U}$ the fluid velocity, c the speed of sound in the medium, V the cell volume, S_f the mass flux through the cell boundary surface respectively. The importance of the CFL condition in terms of the numerical solution stability will be briefly discussed in section 4.3.5.

$$CFL\ number\ (\sigma) = \frac{\Delta t \cdot (\boldsymbol{U} + c)}{(V/S_f)} \qquad (2.10)$$

 Bensow (2011) raised a question about the ability of RANS simulation to capture the physics of the secondary cavitation that is critical to cavitation induced erosion or noise. Secondary cavitation is detached from the primary cavitation by a re-entrant jet and develops in the wake

of strong shear layer by the primary cavitation evolution. To correctly capture such physics, he suggested the necessity of moving towards Large Eddy Simulation (LES) approach with high resolution in time and space and inclusion of the compressibility.

2.4.2   Cavitation erosion prediction models

Thanks to the greatly enhanced computational capacity since the 1990s, there were attempts to numerically simulate the cavitating flows and quantify the risk of erosion from the simulation. Kato et al. (1996) were one of these pioneers. They proposed a numerical framework for cavitation erosion prediction on hydrofoils without model testing. Their framework was in three steps; first, perform a RANS simulation to calculate a sheet cavity length for a hydrofoil under a given working condition. Based on the calculated sheet cavity length, the amount of air flow rate to keep the sheet cavity length could be determined from experimental data, which was assumed to be the generation rate of the cloud cavitation under the calculated working condition for the foil. Finally, assuming that the cloud cavitation was the source of erosion, they utilised a statistical model for the density and size distribution of bubbles in the cloud to determine the intensity of cavitation attack.
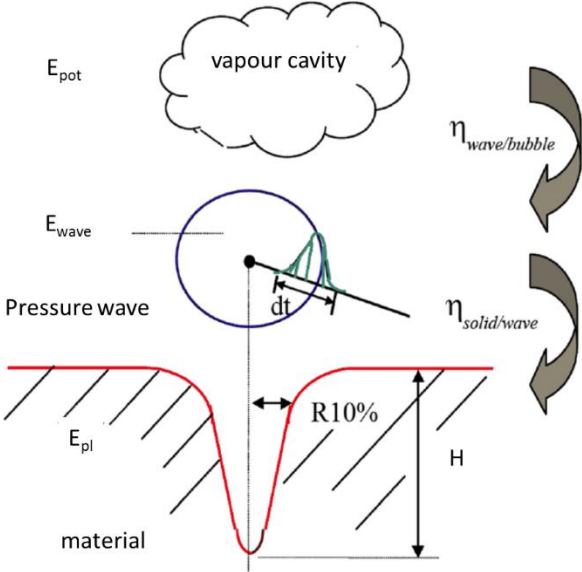
Figure 8 A schematic sketch of physical scenario of the energy balance (Fortes-Patella et al., 2013a). They suggested that a fraction of potential energy Epot is transferred to a material in a form of plastic deformation energy (Epl) via kinetic energy (Ewave) of a bubble with a certain efficiencies ηwave/bubble and ηsolid/wave leaving a pit of which size is represented by its depth (H) and a radius (R10%) at a depth of 10 % of H.

Fortes-Patella and Reboud (1998) put forward a cavitation erosion prediction model based on the physical scenario of the cavitation erosion process. They considered the energy balance through the process of bubble collapse, shock wave propagation and permanent deformation of solid material. The physical scenario is illustrated in Figure 8.

A portion of energy is converted into acoustic pressure wave energy (E_{wave}) from the potential energy (E_{pot}) contained in the collapsing bubbles. The acoustic pressure wave energy is transmitted into the solid material in the form of internal stress energy and kinetic energy, once the shock waves impact the material. The kinetic energy dissipates immediately. However, a part of the internal stress energy is accumulated to form plastic deformation of a depth H on the solid surface. The plastic deformation energy (E_{pl}) was thought to be proportional to the permanently deformed volume of material, which meant the material resistance to the cavitation erosion would be proportional to its ultimate yield strength. They represented the pit volume by two geometric parameters of the pit depth (H) and the pit radius ($R_{10\%}$) at 10 % of the pit depth. As noted by Fortes-Patella et al. (2001), the collapse efficiency could be underestimated for such cases as the initial bubble size being in the order of 0.1 mm due to neglecting the thermal conduction effect at the bubble interface. The structural model was valid only for the incubation stage because the model assumed the mass was conserved. Roy et al. (2015) performed a fluid-structure interaction simulation and highlighted the importance of dynamic properties like strain rate sensitivity in the erosion resistance of a material.

Whereas the above studies are useful in explaining the physical process of the cavitation erosion mechanism, it is difficult to utilize them directly for the routine assessment of cavitation erosion risk. In the same desire of a practical numerical assessment tool, Nohmi et al. (2008) suggested a possibility of defining rather simple numerical cavitation aggressiveness index. They performed two stages of CFD analyses; (1) a cavitating flow simulation around a hydrofoil without concerning the bubble dynamics and (2) analysis of several tracer bubbles travelling in the cavitating flow based on R-P equation (Eq. (2.9) with negligence of the temperature change inside the bubble). Based on the analysis, they considered the changes in the cavity volume and/or the surrounding pressure outside the cavity over time to be the most relevant physical quantities to represent the cavitation erosiveness. They suggested a general form of aggressiveness index as Eq. (2.11) where α denotes the vapour volume fraction, *p* pressure, p_{sat} saturated vapour pressure, *t* the time, *N1* and *N3* order of derivatives, *N2* and *N4* order of the terms. It took a similar form as the 'erosive potential' by Fortes-Patella et al. (2004) and the order of derivatives and influencing weights were to be experimentally determined. Finally, they recommended *N1~N4* to be 0 or 1.

$$(Agressiveness\ Index) = \left(\frac{\partial^{N1}\alpha}{\partial t^{N1}}\right)^{N2} \left(\frac{\partial^{N3}(p - p_{sat})}{\partial t^{N3}}\right)^{N4} \quad\quad (2.11)$$

Hasuike et al. (2009a) discussed good applicability of such indices calculated from a URANS calculation to predict the cavitation erosion risk of marine propellers working behind a ship wake field. They suggested four candidates of promising erosion aggressiveness indices; (1) the maximum change rate of pressure over time, (2) maximum surrounding pressure, (3) maximum change rate of cavity volume and (4) a combination of indices (2) and (3), which means the rate of work done by the fluctuating cavity volume. Those suggested erosion indices are simple and efficient to calculate from relatively cheap URANS simulations. Unfortunately, such indices are difficult to be directly translated and compared with the model experiment or any full scale measurements. Furthermore, any quantitative criteria for such indices are not suggested. Thus, their usefulness is limited only to a relative evaluation of the erosion risk during the design stage. Ponkratov (2015) calculated the same kind of indices for the case of a full scale propeller behind a ship using detached eddy simulation (DES) for better resolution to estimate the erosive potential. The simulation results qualitatively agreed well with the eroded area in the full scale counterpart.

Dular and Coutier-Delgosha (2009), Dular et al. (2006) proposed a phenomenological scenario-based erosion model combined with numerical simulation of cavitation. The erosion model was based on the impinging jet theory to account for the impact pressure on a solid boundary near the bubbles. They described the relation between the impinging jet velocity and pressure with density following Plesset and Chapman (1971). They calculated the velocity and pressure on a 2-D wedge surface by URANS using a compressible multiphase solver with a near-wall eddy viscosity corrected two-equation turbulence model. The results were validated by comparing the predicted velocity against PIV measurements. Peters et al. (2015) suggested a further improved erosion model. The model defined a coefficient representing concentration of effective cavitation impacts pressure exceeding material yield strength to estimate erosiveness. They solved URANS with a mass transport cavitation model (Sauer and Schnerr, 2001) by volume of fluid (VOF) method. Validation work had been performed with a NACA0009 foil and later with a ship propeller in model and full scales (Peters et al., 2018).

Li (2012) proposed a cavitation erosion index based on the time derivative of local pressure and tried to set a threshold value by comparing experiments with a NACA0015 hydrofoil and URANS simulations using a commercial CFD software FLUENT.

Mottyll and Skoda (2016) developed an erosion index based on cumulative probability distribution of the pressure impact loads above a threshold. They first validated the sub-harmonic oscillation frequency and volume of acoustic cavities using a density-based compressible inviscid multiphase flow solver with an isentropic barotropic cavitation model (Iben, 2002). To reduce the grid dependency of the pressure solution, they corrected pressure impact loading contributions on the nearby cells based on the pressure decay with the distance to the cells from the calculated pressures near a target surface. Finally, the erosion index was validated against their erosion test data qualitatively agreeing well each other. The threshold pressure value was suggested to choose a pressure value to give the probability of 1 % for the maximum pressure occurrences.

2.5   Summary

In this chapter, an overview of the cavitation, the mechanism of its destructive potential and models to predict the risk of such damaging potential was provided.

In section 2.1 a brief explanation of the cavitation phenomenon was provided. Some of the history of the research and the research field were also introduced. Cavitation is the term to describe a bubble formation without supply of the thermal energy but by inertial, viscous effects and/or surface tension. Lord Rayleigh provided a theoretical framework for this phenomenon and explained how this phenomenon could be so destructive as to cause severe material loss subjected to the phenomenon.

Section 2.2 provided the background information more specific to acoustic cavitation. Acoustic cavitation is caused by acoustical means such as ultrasonically vibrating transducers. It is accompanied by its own peculiar phenomenon such as sonoluminescence, sonochemical reactions, acoustic streaming and sub-harmonic oscillation of acoustic cavitation as well as the common erosive potential similar to any other types of cavitation.

Section 2.3 provided an overview of theories to explain the destructive mechanism of cavitation erosion. Bubble implosion theory is constructed on Rayleigh equation of the bubble dynamics. Another theory was water hammering effect from the micro-jet of the liquid. The major contribution of this theory was highlighting the role of a solid wall boundary near the bubble. With the existence of the wall, the spherical bubble is attracted to the wall and deformed to a non-spherical toroidal form. In the final stage, the weakest spot of the bubble (the centre of the toroidal form) is penetrated by the liquid jet and has a destructive potential in proportion with the momentum of the bubble translated towards the wall. Later collective chain reaction of the bubbles were proposed rather than act of any individual bubbles based

on the observation of the erosion accompanied by cloud cavitation in almost all the cases. Finally energy cascade theory was introduced. The erosion process is thought as a process very similar with fatigue failure caused by repetitive impacts of acoustic pressure waves either bubble implosion, impinging jet or collective chain reactions.

In section 2.4 some notable relevant works on cavitation simulation and the numerical prediction of the erosion risk have been reviewed. While the hydrodynamic cavitation problems can be well modelled by mass transport models, it was not able to predict the features of acoustic cavitation. The most recent and directly related works were carried out by Znidarcic et al. (2015) and Mottyll and Skoda (2016). They were able to simulate acoustic cavitation phenomenon with reasonable accuracy of the important features of the phenomenon either by source/sink terms-corrected mass transport model or by a custom in-house compressible multiphase flow solver with a barotropic cavitation model. The compressible solver required very small time step size due to the acoustic CFL condition for stable solutions. Bensow raised an essential question on the ability of RANS in capturing the physics relevant to cavitation erosion and noise radiation and suggested a move towards LES and inclusion of compressibility for reliable prediction of cavitation erosion and noise. A number of notable cavitation erosion prediction models were reviewed. Nohmi et al. proposed an erosion prediction model based on the time derivatives of pressure and the volume fraction. A number of validation works were reported for similar form of indices. In relation with an erosiveness index for acoustic cavitation, Mottyll and Skoda developed a function based on a cumulative probability distribution function of the impact pressures.

In the next chapter, acoustic emission is introduced as a promising tool to identify the risk of cavitation erosion. Experimental works are described to investigate the correlation between the acoustic emission signal level and the simulated erosion via a stencil ink to establish a threshold for paint erosion tests in cavitation tunnels. Then, a transfer function for impact force and acoustic emission signal response will be sought. This transfer function can be useful to construct virtual acoustic emission signals from the pressure impact loads calculated by numerical model that will be discussed in chapters 4 ~ 7. Unfortunately, it was not an easy task to construct a stable numerical model with a reasonable accuracy for acoustic cavitation phenomenon that involves high magnitudes of shock waves that occur in a very short time scale as 5×10^{-5} s in a physically bounded small domain. Hence, the focus of discussion in the chapters will be restricted in addressing the stability issue of the compressible multiphase flow solver. Implementation of the transfer function in the code and its verification work are left for future work.

Chapter 3   Acoustic Emission as a Cavitation Erosion Detection Tool

3.1   Introduction

Although our understanding of the complex cavitation erosion mechanism has been enhanced during the last decade, it is still a tricky process to assess the risk of marine propeller cavitation erosion at the early design stage either via computational fluid dynamics (CFD) study or experiment due to its complex geometrical form not to mention the complex nature of the phenomenon. To assess the risk, currently feasible methods are (1) soft paint method, (2) high speed video image analysis and (3) acoustic impact method. The last method appears promising although it needs further development (ITTC, 2005). In this work, it is aimed to explore the possibility of using the AE signals as a pressure sensor to enable the technique.

As already briefly defined in chapter 1 (p.3), AE is elastic stress waves spontaneously generated by abrupt localised changes of strain within a body. According to Eitzen and Wadley (1984b), dislocation motion and crack growth are the mechanisms by which these strain changes occur during growth of defects in a material; even minute crack propagation or plastic deformation result in elastic stress waves which can cause surface motion of a body. The surface motion due to an AE source contains information about both the location and characteristics of the source.

The first reporting of the acoustic emission phenomenon was by Portevin and Le Chatelier (1923); according to Cottrell (1953) and Rogers (2001), they found a small creaking sound accompanying abrupt stress changes in aluminium alloys experiencing large deformation. It was known as 'cry of tin' in English translation. Since its first engineering application in 1964, the technique gained popularity with a sort of illusion like a cure-all. It saw its highest popularity in the late 1970s but without full scientific understanding of AE.

In 1980s activities to make AE a firm scientific basis were sponsored by several organisations like the U. S. National Bureau of Standards and the Electric Power Research Institute. Eitzen and Wadley (1984a) summarised the physical characteristics of the AE events as an emission of elastic stress waves from abrupt release of potential energy from micro-fracture, sharp friction between crack surfaces, etc. and formulation of a mathematical framework for quantitative description of AE signal using a Green's function approach. The theoretical model was compared with experimentation data showing good agreement. According to their approach, the AE signal can be quantitatively predicted by knowing the AE source

characteristics and the transfer function which describes how the signal propagates through a material assuming linearity and time invariance of the source signal.

The technique had been mostly applied to detection and monitoring of the leakage or fatigue crack propagation in the engineering structures like pressure vessels, pipes, bridges or cranes and so forth until 1980s. Now the technique is finding its way to extend its new fields of application, e.g. detection and monitoring cavitation events in hydraulic machinery or condition monitoring of automobile engines mainly due to its cost-effectiveness. Recently the feasibility of its use for the detection of cavitation events on the ship propellers and rudders has been considered (Boorsma and Fitzsimmons, 2009).

3.2   Possibility as a sensor for cavitation events monitoring

Rus et al. (2007) compared AE, underwater noise and vibration signals versus cavitation events on Kaplan turbine blades and showed that the AE signal followed well the cavitation events as well as the other two methods. Meanwhile they chose the underwater noise signal acquired by hydrophones for their analysis due to its higher sensitivity than the others, considering the noisy real world underwater environment, AE or vibration signals may be more appropriate to track the ship propeller cavitation events.

Boorsma and Fitzsimmons (2009) reported the cavitation events on ship propellers or rudders also generate a detectable level of AE signal and thus the AE technique could be cost-effectively applied to detecting and monitoring erosive caviation events on the ship propellers and rudders in service (see Figure 9). There have been other works (Armakolas et al., 2015, Rus et al., 2007) as well to support such feasibility.
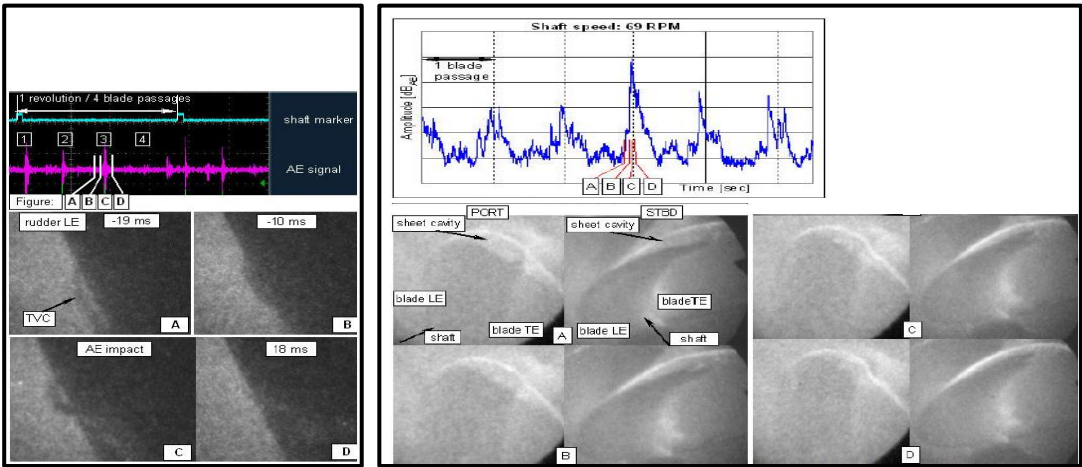
Figure 9 Measured acoustic emission and cavitation events (left: propeller tip vortex bursting on the rudder, right: propeller tip vortex bursting) (after Boorsma and Fitzsimmons, 2009)

3.3 Modelling of the acoustic emission

The objective of AE signal analysis is to identify the character and significance of an event of interest by proper choice of signal processing technique. Following the literature (Eitzen and Wadley, 1984b, Ono et al., 2008, Scruby, 1987), the AE signal can be modelled by convolving the transfer functions for the following;

(1) AE source characterisation

(2) Wave propagation through a medium

(3) The sensor response characterisation

In the following sub-sections, the modelling of AE signal will be discussed following the above scenario.

3.3.1 Impact loadings from the collapse of acoustic cavities

The cause of generating the elastic stress waves within a material is termed as the AE source. The AE source in this problem is the impact loading from the collapse of the acoustic bubbles either individually or collectively.

The acoustic bubbles are the micro gas bubbles formed (mostly) from desolved gas inside a liquid medium by the pressure change induced by any acoustical means that is in contact with the medium. The common way to do it is using an ultrasonically vibrating membrane or horn tip.

It is known that, once the power intensity of the acoustic source increases above a certain threshold level oscillating at an ultrasonic frequency range (the exact driving mechanisms are not clearly understood yet), the acoustic bubbles oscillate not only at the acoustic driving frequency but also at a lower frequency in a ratio of 1/n (n: a positive integer) of the driving frequency, which is termed as sub-harmonic oscillation frequency. Such sub-harmonic oscillation phenomenon was recognised long time ago and there were some efforts of theoretical treatment of it (Eller and Flynn, 1969, Hansson and Morch, 1980, Noltingk and Neppiras, 1950). But, reasonably accurate prediction of acoustic cavitation phenomenon was not possible until recently. Žnidarčič et al. (2015) and Mottyll and Skoda (2016) reported the possibility of predicting the behaviour acoustic cavitation and its pressure peaks by either (1) hydrodynamic cavitation models (Sauer and Schnerr, 2001, Zwart et al., 2004) modified to consider the non-linear bubble acceleration term ($R\ddot{R}$) of the R-P equation (Eq. 2.9) into the

vapour production/destruction terms, or (2) barotropic cavitation model (Wallis, 1969). The pressure impact loadings can be found from an appropriate CFD simulation.

The AE signal resulting from the cavitation impact loading is expected to consist of compression and shear waves directly caused by instantaneous compression of the metal surface and almost spontaneously following pulses that correspond to the subsequent micro-fracture events (Rogers, 2003). The AE response to a single impact loading may be estimated from the steel ball drop test results.

3.3.2 Wave propagation through solid bodies

The AE signal is a micro scale seismic waves. The stress waves are known to propagate through a solid medium in the four different modes; (1) longitudinal (compression) waves, (2) transverse (shear) waves, (3) Rayleigh (surface) waves and (4) Lamb waves (surface waves on a thin plate).

The longitudinal waves and the shear waves are generated simultaneously. The longitudinal waves propagate in the same direction as the medium is being compressed/expanded and a pair of shear waves propagate at 45 degrees to the longitudinal waves. According to Rogers (2001), in the near field, e.g. less than 20 times the thickness of any given material, the two propagation modes are the predominant propagation mechanism. Rayleigh (surface) waves propagate along the surface of a medium with the same mechanism as the free surface waves propagate in deep water. Lamb waves are similar as the surface waves but occur in the relatively thin (not more than the wave length) plate type media. In the current problem, Lamb waves are neglected due to the geometry of the test specimen. Since all of the above types of waves propagate at different speeds through a medium, they can be identified by measuring their arrival time. The propagation speed of each mode of the waves can be estimated by formulas given by Rogers (2001, p. 66), equations (3.1) ~ (3.3), where E, Υ, ρ denote the Young's modulus, the Poisson ratio and the density of the medium respectively.

$$Compression\ wave\ velocity = \sqrt{\frac{E}{\rho}\frac{1-\Upsilon}{(1+\Upsilon)(1-2\Upsilon)}} \tag{3.1}$$

$$Shear\ wave\ velocity = \sqrt{\frac{E}{\rho}\frac{1}{2(1-\Upsilon)}} \tag{3.2}$$

$$\frac{Surface\ wave\ velocity}{Shear\ wave\ velocity} = \frac{(0.87+1.12\Upsilon)}{1+\Upsilon} \tag{3.3}$$

Using these formulae and the properties of copper ($E = 117 \times 10^9 Pa, \rho = 8960 \frac{kg}{m^3}, \Upsilon = 0.33$), the wave velocities of respective modes are estimated to be 4399 m/s (compression), 3122 m/s (shear) and 2910 m/s (surface). For the copper samples (25 x 25 x 15 mm^3) used in this experiment, the estimated order of the arrival time difference between the signals of different modes is 1x 10^{-7} seconds. Hence, the sampling rate needs to be at least 10 MHz.

To account for the source strength reduction by the attenuation, a simple empirical relationship as Eq. (3.4) can be employed, where x is the distance between the source and the sensor, and x_{ref} ($x > x_{ref}$) is a reference distance where the source strength A(x_{ref}) is known (Rogers, 2001);

$$\frac{A(x)}{A(x_{ref})} = \left(\frac{x}{x_{ref}}\right)^{-a} \cdot exp\left(-b\left(\frac{x}{x_{ref}}\right)\right) \tag{3.4}$$

Here $\left(\frac{x}{x_{ref}}\right)^{-a}$ term accounts for the geometric spreading of the wave front in the near field and the other exponential part for the losses within the medium. The coefficients a and b of the exponents can be determined experimentally. The actual field measurements and the above empirical formula plotted and shown together in the Figure 10. Thus, by measuring the AE signal amplitude at two different distances from an AE source, we may be able to correct AE signal intensity or strength for any given distance.
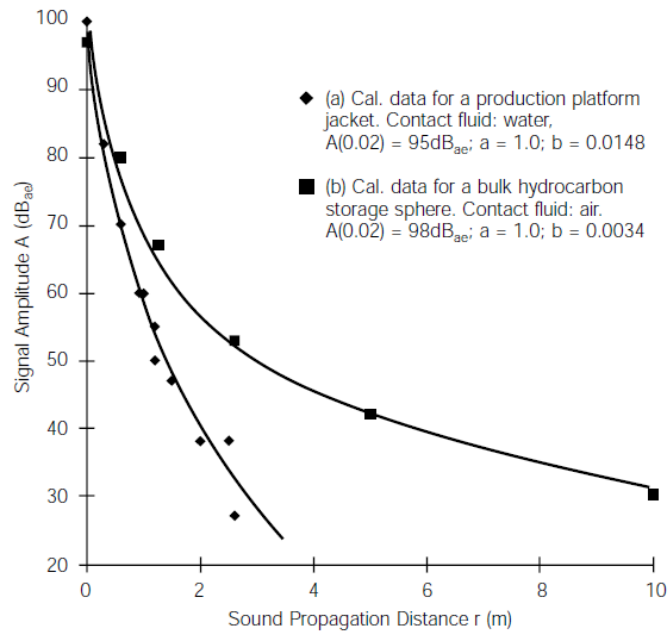
Figure 10 Hsu-Nielsen source attenuation curve for a subsea steel node joint measured using a 100-200 kHz resonant AE sensor (a), and a hydrocarbon bulk storage sphere (b) (Rogers, 2001).

3.3.3 Characterisation of an AE sensor

Piezo-electric AE sensors detect and measure elastic stress waves from AE source events by converting mechanical displacement to electrical voltage output. Characterisation of an AE sensor is simply acquiring the characteristics of frequency response and sensitivity information of a sensor. Ideal sensors should generate an output proportional with an input strength. Sensitivity is the slope of this output/input and typically represented in dB. Flat frequency response of an AE sensor is also an important characteristic. The typical frequency bandwidth of AE lies in between 100 ~ 300 kHz. 150 kHz resonant type piezo-electric sensors are designed to have a flat frequency response characteristics in the 100 ~ 300 kHz range as much as possible.

The sensitivity of AE sensors can be checked by either the PLB test or steel ball drop tests. In this study, it was carried out by steel ball drop tests. The frequency response characteristic of a sensor can be obtained from sensor manufacturer's data sheet. Unfortunately, the frequency response characteristic of the AE sensor used in this study was not available from either LR or the manufacturer, McWade.

3.4 Experimental setup

3.4.1 AE signal measurement system

The AE sensor (McWade, NS3303) used in this work was manufactured to produce consistent output voltages to industrial standard scale of unit dB_{AE} that is defined with reference to 1 μV. It is a piezoelectric resonant type sensor having a flat response for the frequency band of 100 ~ 200 kHz. The sensor signal is amplified by a pre-amplifier (McWade, PA3301). According to the manufacturer's data sheet, each manufactured unit was tested and has the accuracy of +/- 1dB_{AE} for the flat response band (McWade Monitoring Systems, 2016). Unfortunately, the accuracy information for the other frequency band was not available. The sensor after the pre-amplifier produces effective output voltage ranging from -10 to 10 V, and the output voltage can be converted to signal power level by Eq. (3.5) based on LR internal information.

$$(AE\ signal\ power)\ = 20 \cdot log_{10} \frac{V_s}{1 \times 10^{-6}} - 40\ dB_{AE} \tag{3.5}$$

The source of the constant -40 dB_{AE} in Eq. (3.5) was not clearly explained in the internal note. According to the manufacturer's datasheet mentioned above, the noise floor of their AE sensors is in between 0.5 and 1 mV. Hence, the actual reference voltage of the AE sensors
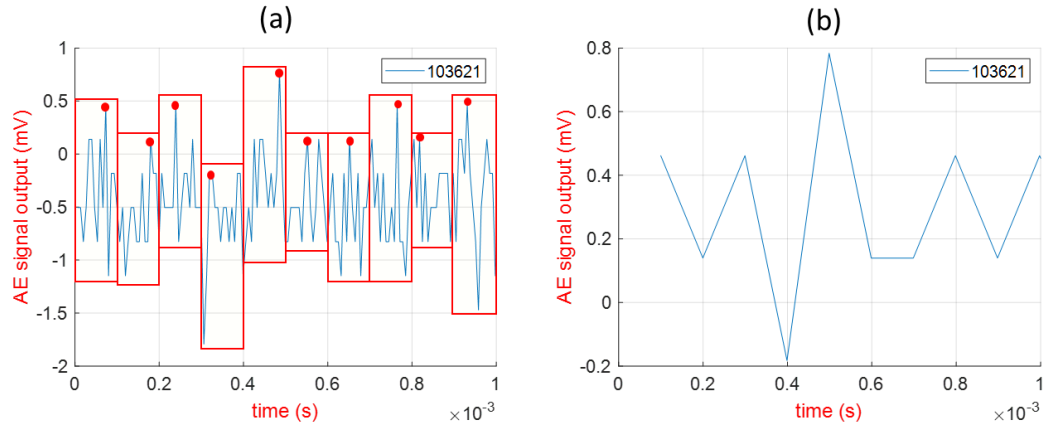
Figure 11 An illustration of the AE signals after 10 kHz peak-hold filtering: the original AE signal samples with the filter windows marked by the red boxes (a), and the filtered AE signal through the peak-hold filter (b). Only the highest peaks (red dots in (a)) are retained through the filter.

could be 1×10^{-4} V, which is one order lower than the noise floor level. This appears to be the reason why the manufacturer had provided such a formula as Eq. (3.5) to LR. According to the conversion formula and the manufacturer's datasheet, the sensor can detect AE events of the range in between 20 and 100 dB$_{AE}$.

Two different DAQ (Data AcQuisition) systems were employed to sample the signals. One was a conventional linear analogue-digital signal converter (National Instruments, NI 6251). It had the output voltage range of +/- 10 V that is the same as the sensor with pre-amplifier. This DAQ system was used to sample the AE signals from acoustic cavitation impact loadings and the background noise measurement. The other one was a similar converter (National Instruments, NI USB-9251) with a custom logarithmic amplifier with a built-in 10 kHz peak-hold circuit manufactured by McWade according to LR specification. The effective output voltage range of the logarithmic DAQ system was 1.35 ~ 4 V. The peak-hold records only the highest peak of the AE signals during every 0.1 ms interval as illustrated in Figure 11.

Since the latter is the same one as used to record full scale cavitation impact events on a number of ships by Lloyd's Register, the latter was intended to be used for the whole task to align with and provide any useful knowledge from this work for the actual field jobs. However, its low sampling rate was not enough to capture the characteristics of acoustic cavitation events by the sonotrode. So the latter was used only for recording and analysing the AE signals from the steel ball drop tests that are described in the next section. A block diagram of the AE measurement system is shown in Figure 12. The conversion from the log-amp signal to the signal power level is carried out by Eq. (3.6).
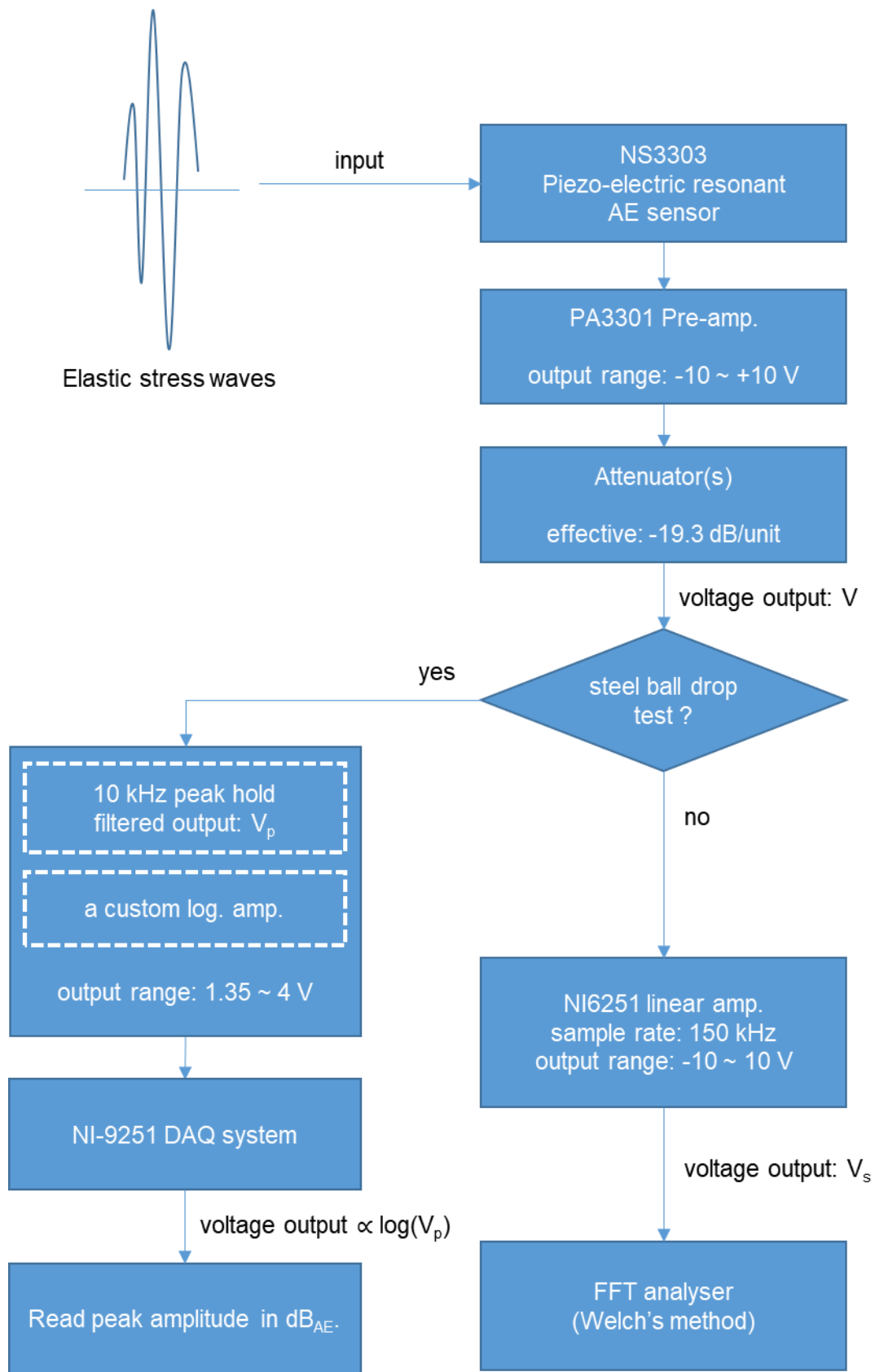
Figure 12 A block diagram of the AE signal measurement system used for the experiment.

$$(AE\ signal\ level) = 35V_p - 40\ dB_{AE}\ \ (1.36 \leq V_{out} \leq 4) \tag{3.6}$$

The deduction of 40 dB$_{AE}$ comes from the AE sensor as stated for Eq. (3.5). According to the sensor manufacturer's instruction, the AE output voltage value was taken as zero to peak for both the DAQ systems. The FFT of the absolute voltage output was taken based on the Welch's method. The Fourier transformed signal amplitudes were normalised by the window size of 131072 (2^{17}) data samples and the coherence gain (0.540) of the window function (the Hamming window was used). The coherence gain can be calculated by integrating the area under any given window function over the windowed temporal space. Finally, the conversion to signal power of the normalised signal amplitudes was carried out according to Eqs. (3.5) or (3.6) depending on the utilized DAQ system.

3.4.2 AE signal cut-off level for the background noise

To eliminate the background noise of the measurement system, the background noise of the system was measured twice by the linear DAQ system with exactly the same experimental setup, but without active sonotrode. The measured raw data of the AE background noise samples are shown in Figure 13 (a).

Zero to peak amplitudes were taken for the signal amplitudes according to the AE sensor manufacturer's guide (McWade Monitoring Systems, 2016). It is common practice to set a certain cut-off threshold for the AE signal analysis (The Japanese society for non-destructive inspection, 2008) so that uninterested noise can be removed.

The absolute values of the sensor output voltage from the background noise were equal or below about 8.555 mV. Both the signals indicated the minimum output of -8.555 mV, while
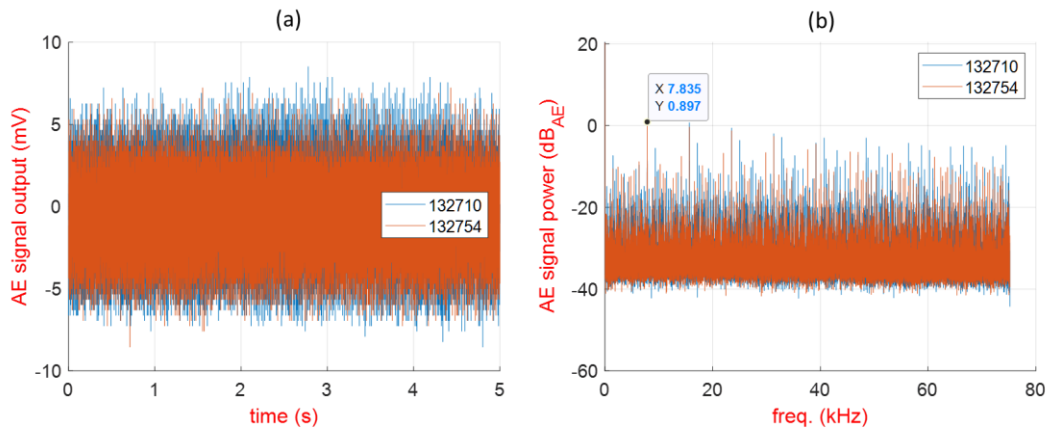
Figure 13 The AE system noise measurement results: raw data sampled at 150 kHz by the linear DAQ system (a), and FFT results of the signals with a cut-off threshold of 10 mV based on Welch's method (b).

41

indicated different levels of maximum positive output of 8.5 and 7.2 mV respectively. The statistical information of the measured samples are shown on Table 3 and Figure 14. The means and the standard deviations of the noise peaks were taken only for the peaks above or equal with 4 mV. Based on these results, the signal cut-off threshold for the AE signal analysis was set to 10 mV (= 40 dB$_{AE}$).
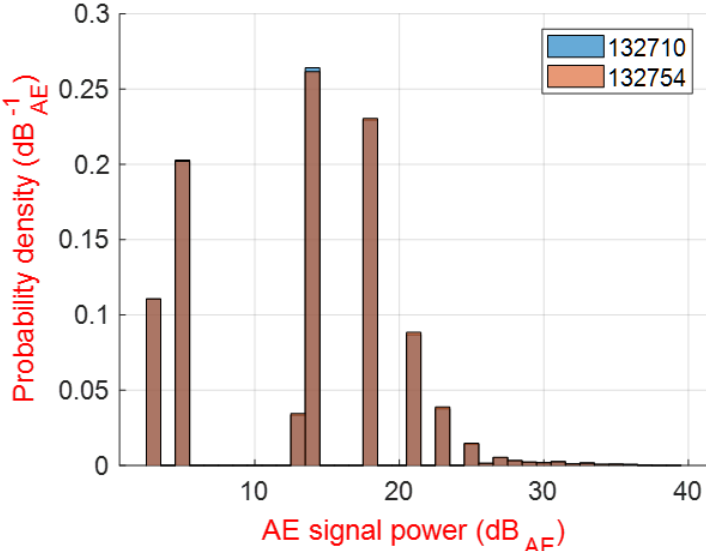
Figure 14 Probability density plots of the measured AE background noise.

Table 3 Statistical data of the measured AE background noise.

Run ID	Mean peak [mV]	Standard deviation [mV]	Maximum peak [mV]
132710	5.6	0.7	8.6 (+8.5[(*)])
132754	5.4	0.7	8.6 (+7.2[(*)])

(*) The figures in the parentheses indicate positive maximum noise peaks measured.

To identify the frequency characteristics of the linear AE measurement system, Fast Fourier Transform (FFT) was carried out based on Welch's method (Welch, 1967). Figure 13 (b) exhibited higher noise peaks around the frequencies of about 7.83 kHz and its harmonic frequencies. The minimum resolution of 1.92 mV that is the same as the absolute accuracy of the DAQ system (National Instruments, NI 6251) in the factory calibration condition (21 °C). The conversion to the AE signal level was calculated according to the conversion formula of Eq. (3.5). From Figure 13, All the signal output voltage data points below the threshold was replaced with the threshold.

3.4.3 Correlating AE signal level with impact loadings

To check the sensor integrity in the field, PLB test is commonly used. The method is generating an AE impulse to check the signal output voltage by breaking a Hsu-Nielsen source such as a 0.5 mm 2H mechanical pencil lead or a glass capillary on a test specimen where the AE signal propagates through. Such AE sources are known to produce a single impulse pattern with a known signal level. This method is easy and convenient to carry out to check the integrity of an AE sensor in the field.

Sometimes ball impacts are preferred source to study a correlation between the signal output voltage and a relevant physical quantity. To carry out the ball drop tests, a number of solid balls with different mass are dropped from a certain height on to a test specimen while the AE signal is recorded. This method is easy to quantify and control the exerted force in a repeatable way. A series of steel ball drop tests were carried out to correlate AE signal level with force impulse loading with a test setup shown in Figure 15.
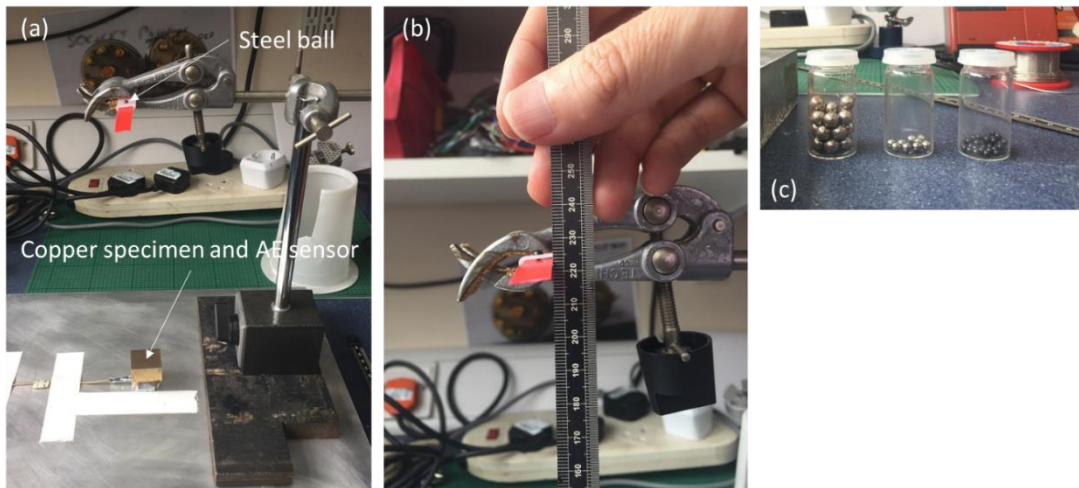
Figure 15 Setup of the steel ball drop tests (a), drop height measurement (b), steel balls used in the tests (c).

Table 4 and Table 5 show the actual test programme and the measured peak voltage and the signal power in dB_{AE}. Firstly, the attenuators (specified attenuation: -20 dB each) were checked with a small plastic ball (0.008 g) dropped at the height of 213 mm above the copper alloy specimen. The copper alloy specimen and the AE sensor were attached to the top face of a steel plate and their distance (D^* in Table 4) was kept the same all through the tests. The signals were recorded using the 10 kHz peak-hold log amp. The measured signal levels decreased by approximately 19.3 dB with each addition of the attenuators (Figure 16).

Checking the integrity of the AE sensor and the attenuators, three different mass of steel balls were dropped on top of the same specimen as per the programme in Table 5. The AE signals were recorded on the bottom face of the specimen by the 10 kHz peak-hold log amp.

The first two series runs from Run ID's 105421 to 112553 in Table 5 indicated clipping of the signal exceeding the measureable voltage range. Therefore, up to three -20 dB signal attenuators were serially connected and measured the signal peaks in the following runs. Each steel ball was dropped 10 times to take the average of the signal levels. The measurement result from the test run 130117 was removed from the analysis since it was a distinctive outlier compared with the other test points for the series. One of the measured AE signal with three attenuators is shown in Figure 17. If the steel ball rebounded several times on the specimen after the first hit, several more peaks followed accordingly with the amplitudes decaying slowly.
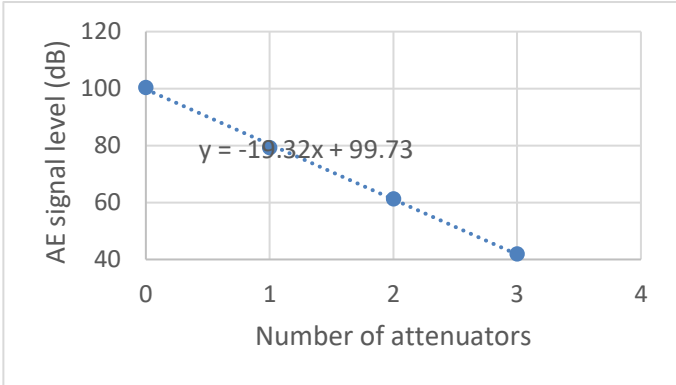
Figure 16 Signal measurement results with the AE sensor and attenuators (-20 dB).
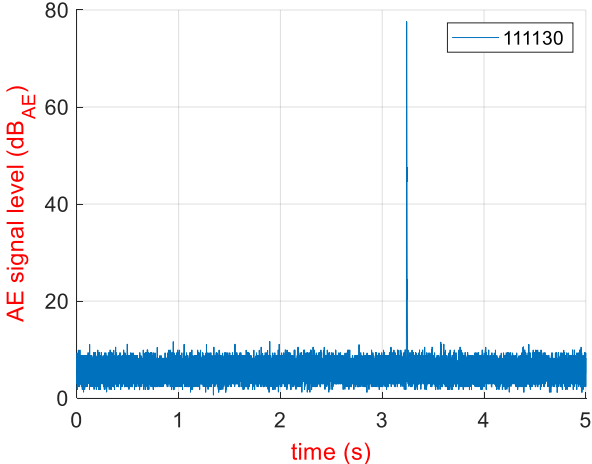
Figure 17 An example of the acoustic emission signal measured from the steel ball drop tests (Run ID 111130 in Table 4) with three attenuators (-19.3 dB each).

Table 4 Test programme for the attenuators check and the measured AE singal peaks.

Run ID	Ball weight (g)	Drop height (mm)	D^* (mm)	Attenuators	Peak (log V)	Mean (log V)	dB$_{AE}$
124211	0.008	213	250	0	4.014	4.010	100.4
124233					4.047		
124349					3.998		
124420					3.982		
124641	0.008	213	250	1	3.409	3.409	79.3
124704					3.394		
124721					3.458		
124742					3.378		
124842	0.008	213	250	2	2.915	2.894	61.3
124903					2.898		
124919					2.864		
124940					2.898		
125050	0.008	213	250	3	2.303	2.344	42.0
125107					2.319		
125145					2.367		
125204					2.387		

Table 5 Steel ball drop test programme and the measured AE signal output voltage peaks.

Run ID	Ball weight (g)	Drop height (mm)	Attenuators	Peak (log V)	Mean (log V)	dB$_{AE}$
105421	0.054	224	0	4.080	4.084	**102.9**
105457				4.097		
105522				4.080		
105548				4.080		
105639				4.079		
105709				4.096		
105749				4.063		
105825				4.080		
105851				4.096		
112145	0.054	224	1	4.047	4.058	**102.0**
112227				4.097		
112342				4.031		
112402				4.032		
112418				4.079		
112435				4.080		
112452				4.048		
112516				4.048		
112536				4.064		
112553				4.080		
122104	0.054	224	2	3.899	3.797	**92.9**
122131				3.752		

122151				3.768		
122211				3.784		
122225				3.800		
122241				3.752		
122249				3.818		
122319				3.818		
122333				3.784		
122350				3.785		
111130	0.054	224	3	3.360	3.245	**73.6**
111208				3.213		
111254				3.229		
111314				3.246		
111332				3.230		
111350				3.179		
111408				3.311		
111426				3.213		
111442				3.229		
111459				3.245		
130036	0.440	224	3	3.244	3.282	**74.9**
130100				3.327		
130117[(*)]				2.039[(*)]		
130129				3.245		
130146				3.294		
130226				3.327		
130248				3.327		
130311				3.277		
130353				3.212		
130512	1.400	224	3	3.310	3.326	**76.4**
130541				3.344		
130628				3.289		
130651				3.376		
130708				3.327		
130723				3.344		
130742				3.359		
130801				3.309		
130820				3.278		
130837				3.244		

(*) The marked test run was excluded from the analysis due to large discrepancy from the other measured data.

3.4.4 Formulation of a transfer function of AE signal level

Although the real AE phenomenon is quite a complex one, involving the elastic/anelastic deformation of the medium, geometry of the medium and the structural properties of the medium, the purpose of the transfer function in this study is developing rather a simple relation

with the impact loadings to use the AE signal level as a kind of pressure sensor. In this early stage of the technique development, it is assumed that there exists a correlation between the AE sensor output voltage and the pressure impact loading, and that this can be expressed by a simple linear relation. The linear relation between the AE signal level and the impact loading appears to be supported experimentally (Lee et al., 2006, McLaskey and Glaser, 2010, Ukpai et al., 2013). Now the simplified relation may be expressed as Eq. (3.7),

$$F = C_{AE} \cdot V_s \tag{3.7}$$

where F is the impact force, V_s the AE sensor output voltage (linear) and C_{AE} an experimental coefficient. It can be regarded as an analogy of Hook's law.
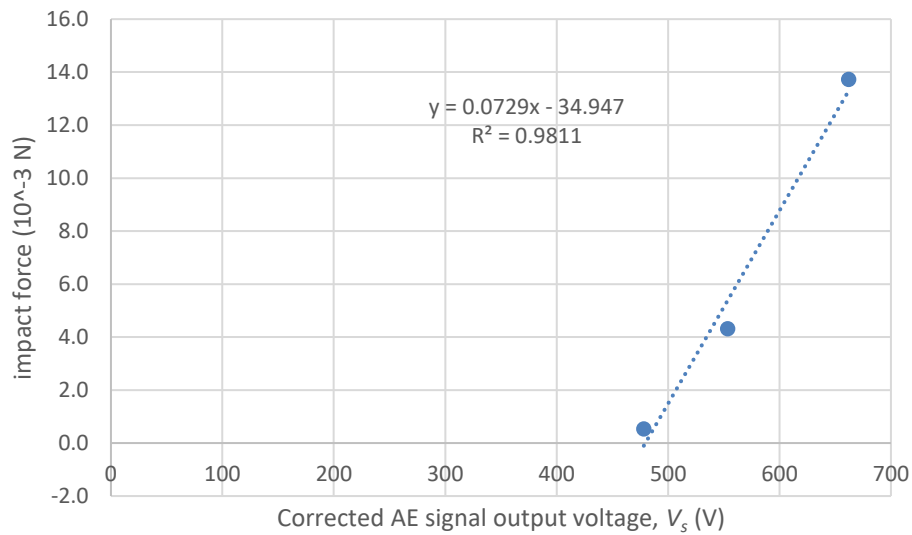
Figure 18 Steel ball drop test results with three different mass of small ball bearings. The signal voltage was measured by the logarithmic DAQ system and converted to the voltage output from the linear DAQ system from Eqs. (3.5) and (3.6). The non-zero intercept of the impact force axis could have been caused by drift of zero of the logarithmic DAQ system.

Table 6 Averaged steel ball drop test results.

Ball weight	Impact Force	Log Amp	Signal Level	Corrected Level
(g)	(x 10^{-3} N)	(V)	(dB$_{AE}$)	(dB$_{AE}$)
0.054	0.5	3.245	73.6	133.6
0.440	4.3	3.282	74.9	134.9
1.400	13.7	3.326	76.4	136.4

The experimental coefficient can be determined from the steel ball drop test results. To find the coefficient, the measured voltage from the log amp was converted to the corresponding voltage output from the sensor by equating the conversion formulae Eqs. (3.5) and (3.6). Before equating the formulae, the effect of the attenuators were compensated by adding 60 dB_{AE} to the calculated signal level from the log amp output voltage. From the plot of the corrected signal output voltage versus the impact force in Figure 18, it was found to be 7.29 x 10^{-5} N/V in this experiment case. With regard to the intercept (-34.947 x 10^{-3} N) of the regression line, theoretically it must be zero. The source causing this non-zero intercept was not analysed in the study. Possible reason could be from a large uncertainty with the calibration of the logarithmic amplifier. The linearity (in logarhimic scale) of logarithmic amplifiers are not guaranteed in the low voltage region. Furthermore, it was not certain whether the calibration of the logarithmic DAQ system had been accurately checked on periodical basis. As a combined result of the two reasons, the zero of the DAQ system might have drifted largely as indicated on the plot in Figure 18. This was noticed later and re-measurement of the force-AE signal voltage relation using the linear DAQ system had not been carried out within this project when this thesis was written unfortunately.

3.5 AE measurement with the paint tests by the sonotrode

3.5.1 Test setup

The soft paint test is one of the model test methods to assess any possible cavitation erosion occurrence on marine propellers. A paint coating is applied on a model propeller according to a certain prescribed application instructions. Then the cavitation test is performed with the model for a certain time duration, e.g. 20 minutes. If any pit or removal of the paint coating is found after the tests, it is judged the propeller has a risk of cavitation erosion damage. The purpose of this test was to establish an AE threshold for the cavitation erosion occurrence at model scale.

ASTM G-32 type ultrasonic cavitation apparatus or ASTM G-134 type cavitating jet apparatus are commonly used to study cavitation erosion in the lab environment. Examples of such apparatus are shown in Figure 19.

The sonotrode is one of the ASTM G-32 type apparatus that is compact and able to generate relatively regulated cavity bubbles to produce cavitation erosion in a much accelerated manner compared with the erosion process by hydrodynamic cavitation. Therefore, it has an advantage in studying the cavitation erosion threshold in the lab. An example of eroded steel plate (W x H = 24 x 24 mm^2) under the sonotrode is illustrated in Figure 20. The eroded surface shows
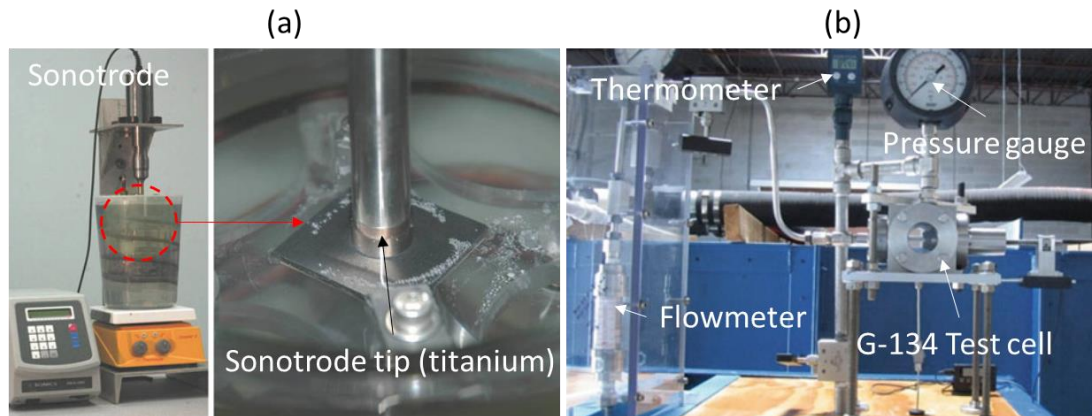
Figure 19 Examples of ultrasonic cavitation apparatus (a) and Cavitating jet apparatus (b) at DynaFlow Inc. (after Chahine et al. (2014))
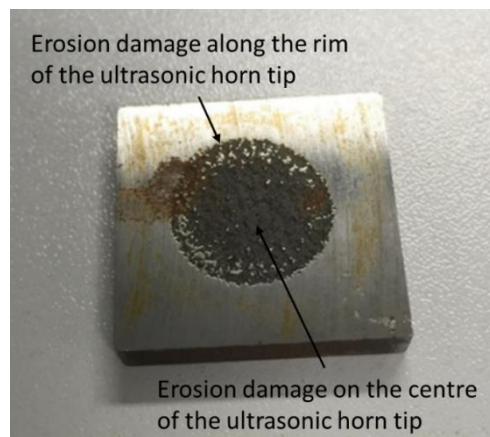
Figure 20 A test specimen eroded by an ASTM G-32 type cavitation device. The severest erosion damage occurred in the central region below the ultrasonic horn tip, while the secondary erosion damage occurred on the rim of the horn tip.

two distinct damage regions; one along the rim of the ultrasonic horn tip and the other in the centre where the deepest pits are found.

A stencil-ink-coated copper alloy specimen was placed under the ultrasonic horn tip with gap distances of 40, 30, 20, 15, 10, 5 and 0.5 mm. To minimize any uncertainty from the varying quality of paint coat, ten copper specimen were put into the same stencil ink and dried in the same environmental condition for each test batch. For similarity in the cavitation erosion tests in cavitation tunnel, the specimen was put in the water for about 15 minutes before the tests. The ultrasonic horn tip was partly submerged in the tap water by 10 mm. The AE sensor was attached to the bottom of the specimen by a silicon adhesive to ensure firm contact with the specimen. The specimen was fixed on a plastic base from two sides by two small pieces of

plastic jig tightened by screws. The actual test setup and technical specifications of the test equipment are shown in Figure 21 and Table 7 (at the end of this section).

An appropriate sonotrode test duration needs to be determined. Because the frequency of acoustic cavitation impact events will be different from the erosive cavitation events in the hydrodynamic cavitation tunnel, a proper duration similar or equivalent to 20 minutes test time in the cavitation tunnel must be estimated. The first guess was made based for acoustic cavitation oscillation frequency and the propeller blade frequency. The number of cavitation impact events for both the tests should be the same. Hence, Eq. (3.8) should hold.

$$f_{AC} \cdot t_{AC} = f_{HC} \cdot t_{HC} \tag{3.8}$$

The subscripts AC and HC denote acoustic cavitation and hydrodynamic cavitation respectively. Taking account only the large cavity collapse events, f_{AC} and f_{HC} may be chosen as the acoustic cavity oscillation frequency (2000 ~ 5000 Hz) and the model propeller rotation speed multiplied by the number of blades (80 ~ 125 Hz) respectively. Substituting these values into (3.8), the range of t_{AC} is 19 ~ 50 seconds. The test duration was determined to be 20 seconds minimum and extended up to 10 minutes. The test specimens were taken out to find any paint damage in 20 seconds and 1, 2, 5, 10 minutes (all accumulated time duration) after the start of each test run.

Table 7 Technical specifications of the experimental instruments.

Sonotrode	
Manufactuer, model	Hielscher, UIP1000hd
Power output range	500 ~ 1000 W
Driving frequency	20 kHz ± 500 Hz (non-adjustable)
Amplitude (peak-to-peak)	43 (50 %) ~ 96 (100 %)
Diameter of the ultrasonic horn	15.9 mm
Acoustic emission sensor	
Type	Ceramic-faced Piezoelectric resonant type
Resonance frequency	150 kHz
The test specimen	Copper alloy, 25 x 25 x 15 mm^3
Bath	
Material and shape	Transparent acrylic rectangular box
Dimensions (L x W x H, mm)	$305 \times 400 \times 115$
Liquid in the container	About 12 litres of tap water at ambient temperature
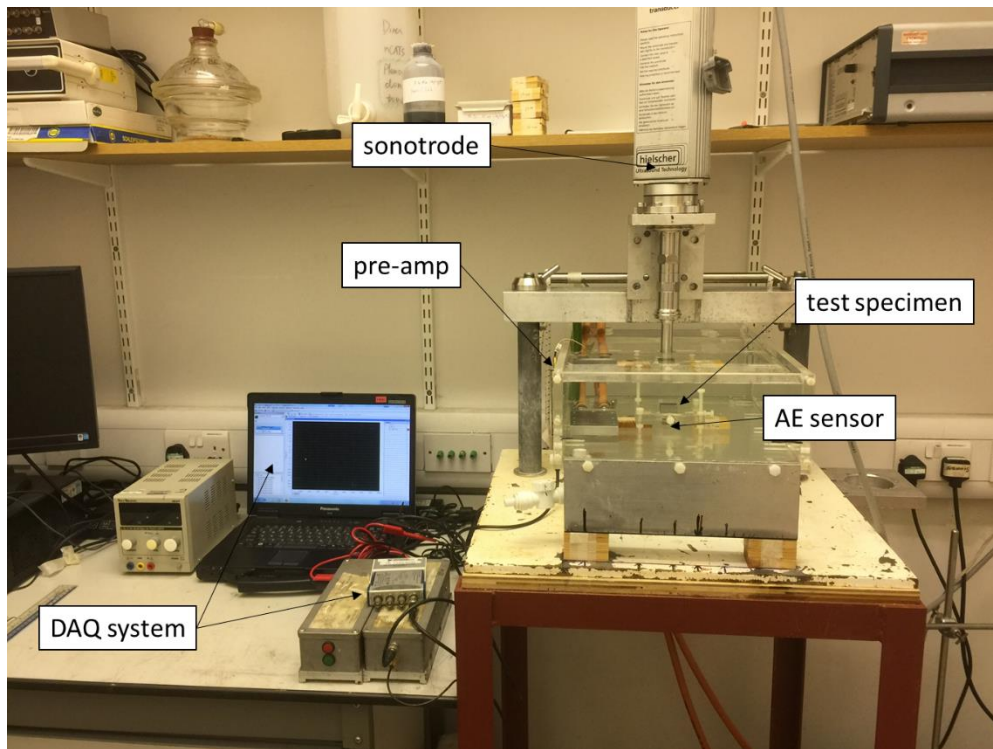
Figure 21 Instrumentation of the experimental setup that used in this research. The tap water was filled to 110 mm from the bottom of a transparent acrylic rectangular bath. An ultrasonic horn tip of a 1 kW sonotrode (Hielscher, UIP1000hd) was submerged in the tap water by 10 mm. A copper alloy test specimen was placed below the horn tip with a certain gap, and fixed in the recess of a 15 mm thick acrylic bed plate with two fixing bolts from the vertical and lateral sides. An AE sensor (McWade, NS3303) was glued to the bed plate ensuring firm contact to the bottom of the specimen through a hole with the same diameter of the sensor body. The sensor was connected to a DAQ system through either a pre-amp (McWade, PA3301) alone or the pre-amp with -20 dB attenuators as necessary.

Repeating the above stated test procedure, the threshold condition was determined by adjusting the sonotrode vibration amplitude and the gap distance until the coated paint started to get damage. All the tests had been repeated at least for three times with the test samples from the same batch to confirm the consistency of the results.

3.5.2   Analysis of the AE signals

From the literature (Dular et al., 2012, Eller and Flynn, 1969, Hansson and Morch, 1980, Mottyll and Skoda, 2016, Noltingk and Neppiras, 1950, Prosperetti, 1974, Truong, 2009, Žnidarčič et al., 2014), acoustic cavitation is known to exhibit the peculiar sub-harmonic oscillation phenomenon of the large acoustic cavity cluster as well as the oscillation of the micro acoustic bubbles as per the acoustic driving pressure perturbation. To capture such
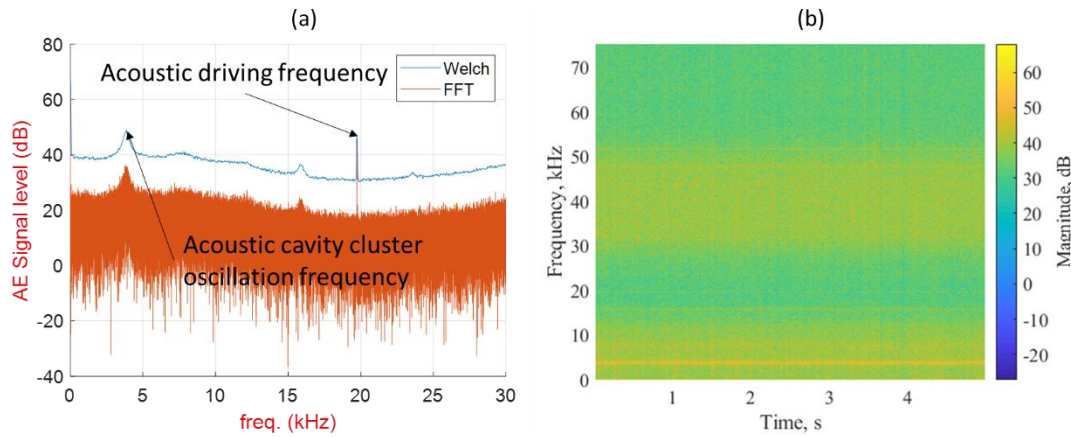
Figure 22 An illustration of acoustic cavitation analysis results by FFT and Welch's method (a), and Short Time Fourier Transform (STFT) (b).

characteristics, the signals were analysed in the frequency domain based on Welch's method (Welch, 1967).

The sub-harmonic oscillation frequency was expected to be somewhere in the frequency range of 1 ~ 10 kHz with the acoustic driving frequency of 20 kHz. Following Nyquist theorem (Nyquist, 1928), the sampling frequency must be equal or higher than 40 kHz. 150 kHz sampling rate was used for all the sampling of the AE signal in relation with acoustic cavitation. The sampling duration was set to 5 seconds (750,000 samples). Matlab (versions 2017b and 2018a) was used to analyse the signals.

To determine an appropriate analysis method to analyse the characteristics of the acoustic pressure impact loads from acoustic cavitation, one of the AE signals from the experiments that are described in section 3.5.3 were analysed by the conventional FFT (Frigo and Johnson, 1998), Welch's method and the Short-Time Fourier Transform (STFT) (Benesty et al., 2008, Boashash, 2003, Zhivomirov, 2013). The results are plotted in Figure 22.

The conventional FFT is a method to reveal the characteristics of the signal in the frequency domain instead of losing the information of the signal in time space. This is not suitable for the analysis of signals varying in time and frequency domains altogether. STFT or wavelet method (Haar, 1910) are the complements to fill such a gap. The difference between STFT and wavelet method is the scalability of the window. With STFT the window size is pre-determined and fixed through analysis, whereas, the window size in the wavelet method is scalable depending on the signal. More detailed explanation on the wavelet method is beyond this thesis. To retain both information of any given signals in the time and frequency domains, STFT divides a long time signal, which may vary in time and frequency, e.g. vocal sounds,

into small pieces to have short time span and carry out FFT for each chunk of the signals so that enables to capture the variation of the signals in time as well as the frequency character of each piece of signal. Hence, it is important to determine an appropriate size of the window for the chunks and how fast the window would slide along the whole data series. Welch's method divides a long time series data into the smaller data segments with or without an overlap between the segments and perform FFT for each segment. Finally, it takes the average of the power spectra of the segments to reduce the noise variance. Welch's method has advantages over the FFT in terms of memory space and improved signal-noise ratio by the averaging at the cost of lower frequency resolution (wider peaks). In Figure 22 (b), the STFT results indicate that acoustic cavitation phenomenon is almost steady. Hence, acoustic cavitation phenomenon can be analysed by either the FFT or the Welch's method. Welch's method was chosen for better signal-noise ratio.

Hamming window with different sizes from 1024 samples up to 131072 samples were tested with the overlap of 1/8, 1/4 or 1/2 of the window size. The dominant frequency components as those from the acoustic bubble cluster oscillation and the vibration of the ultrasonic horn tip were invariant with the changes. The finally determined window size and sliding width were 131072 samples per window and 1/4 of the window size. Power spectral density plots and the histograms were compared for various test condition to find the AE threshold that would be equivalent to the erosion criteria of the soft paint erosion test at the model scale.

3.5.3   Test programme

The test programme consisted of two parts. One was to study the relation of the AE signals with the test geometry and power condition. The other was to investigate the threshold of the AE signals equivalent to the conventional paint test method for the model scale cavitation erosion tests.

As for the first part of the work, it was necessary to know how the geometric confinement and the acoustic excitation power intensity could influence acoustic cavitation intensity. To the author's knowledge, it appears that very little work relevant to this question. The latest work was by Žnidarčič et al. (2014). To investigate influential parameters for acoustic cavitation phenomenon, they carried out a series of experiment varying the physical parameters that appear in the bubble dynamics equation, e.g. the viscosity, surface tension and temperature of the liquid medium, the air saturation level in the medium. They suggested that the non-linear inertial term should be taken into account to properly depict acoustic cavitation behaviour, or any inertial cavitation phenomenon in a rapidly changing pressure field. Unfortunately, their experiment was performed with a relatively large gap distance that could be regarded as an

unbounded bottom (5 ~ 10 times the horn tip diameter). They stated that too narrow gap changed the visual pattern of acoustic cavitation. Since their interest was mostly on the fully grown conical structure of the acoustic cavity cluster behaviour (they called it an 'acoustic super-cavity'), the changed behaviour by the geometric confinement was not covered in detail.

Another interesting work to fill the gap was carried out by Mottyll et al. (2014). A series of experiments were performed with very narrow gap distances such as 0.5, 2.5 and 4.5 mm and they found the acoustic cavity formation to be confined either on the surfaces of the ultrasonic horn or the test specimen and the sub-harmonic oscillation frequency became as low as 1/13 of the acoustic driving frequency.

From both the works, two different modes of the acoustic bubble cluster oscillation was anticipated. Still any concise information on the impact loading by the oscillation/collapse of acoustic cavitation was not available. The test matrix was constructed to cover the power range of 50 ~ 100 % and the gap distance of 0.5 ~ 40 mm (0.03 ~ 2.5 times the horn tip diameter). This part of the work may reduce such a gap in the field of acoustic cavitation study.

The second part tests were the main part of this experimental work. Using the knowledge of the first work, a matrix of the sonotrode test conditions was designed to cover the power range of 75 ~ 100 % and 20 ~ 10 mm gap distances to find a threshold of the AE equivalent to the conventional model scale cavitation erosion tests.

Finally, the AE background noise characteristic was analysed with two data sets measured with the same test configuration for the other tests except that the sonotrode was inactive.

3.5.4   Test results

The AE signals were analysed in the time and frequency domains to confirm they show the same characteristics of the acoustic pressure waves as previously reported by others (Mottyll and Skoda, 2016, Žnidarčič et al., 2014). The assumption of the AE signal as a pressure sensor appears reasonable. Figure 23 shows the AE signal in the time and frequency domains, which shows similar characteristics of the acoustic pressure signals published by Žnidarčič et al. (2015) or Mottyll and Skoda (2016). Other experimental work by Rus et al. (2007) also supports this assumption.

A different observation on the sub-harmonic oscillation frequency was that the acoustic bubble cluster oscillation frequency appeared as a narrow band with a centre frequency that is supposed to correspond to the sub-harmonic oscillation frequency (3.85 kHz $\approx$ (1/5) x f_d , f_d: acoustic driving frequency of 19.74 kHz). Indeed, the FFT result of Mottyll and Skoda (2016) as shown in Figure 23 (c) appears to show similar characteristics as the author's result although
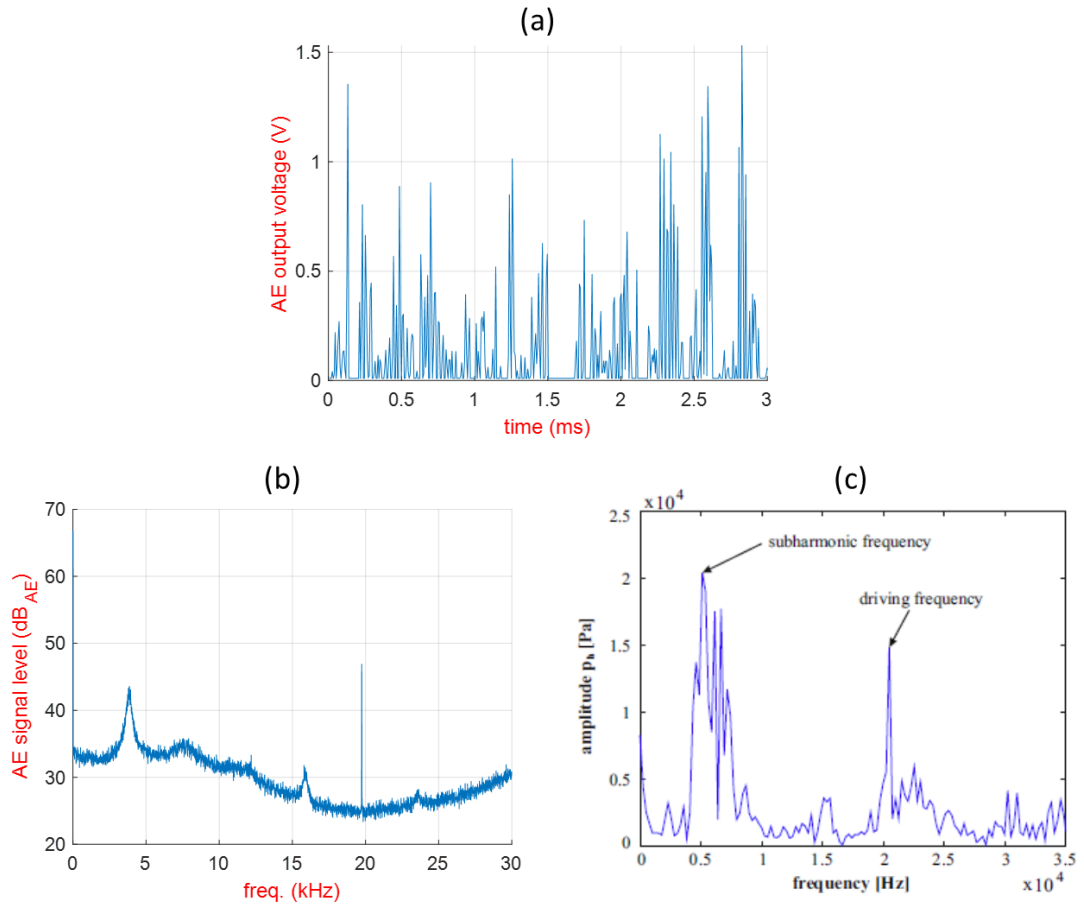
Figure 23 An illustration of the time history of AE signals for 3 ms (a), the averaged singal power spectral distribution of the signal with sampling time of 5 s (b), and acoustic pressure signal measured by a hydrophone (Mottyll and Skoda, 2016) (c). The signal of (a) and (b) was measured under 75 % sonotrode power output with the gap distance of 15 mm and with three attenuators (-19.3 dB each).

they picked up only the highest peak. The extracted oscillation frequencies from the test runs under the same test condition were slightly drifting within the order of +/-200 Hz. The frequency resolution was about 9 Hz. The smaller peaks in Figure 23 (b) correspond to the harmonics of the sub-harmonic frequency.

This narrow scatter of the bubble cluster oscillation frequencies seems to imply that the oscillation of the acoustic bubble cluster is not mechanically periodic most probably due to the fuzzy motions of the ultrasonic horn tip or due to the complicated interactions of the acoustic pressure waves with the ones reflected at the boundaries.

Using the Welch's method, the centre frequency of the acoustic bubble cluster oscillation and the AE signal level were analysed to investigate possible influences from the gap distance and power output condition. Figure 24 and Figure 25 show the influence of gap distance on the

centre frequencies and the AE signal power level. The test power output of the sonotrode was fixed at 75 % (vibration amplitude ~ 60 µm, peak-to-peak) with driving frequency (f_d) of 19.74 kHz during the gap distance variation. The trend of the centre frequency change with the gap distance is shown in Figure 24. The centre frequency tended to be almost invariant ($\sim (1/5)\, f_d$) while the gap distance was larger or equal to 10 mm. However, once the gap distance became narrower, the frequency tended to decrease; approximately 3.2 kHz ($\approx 1/6\, f_d$) at 5 mm and 1.8 kHz ($\approx 1/11\, f_d$) at 0.5 mm. These centre frequencies appear to correspond to the sub-harmonic oscillation frequencies and will be called sub-harmonic (oscillation) frequencies of the acoustic bubble cluster from here.

Acoustic cavitation impact loadings also demonstrated some dependence on the gap distance. Figure 25 shows the trend of AE levels corresponding to the 0-th harmonics of the Fourier transform coefficients and the two main components of the sub-harmonic frequency and the acoustic driving frequency with the gap distance change. The AE signal amplitude of the sub-harmonic frequency was comparable with that of the acoustic driving frequency component. All the three components tended to increase as the gap distance became narrower until 5 mm.
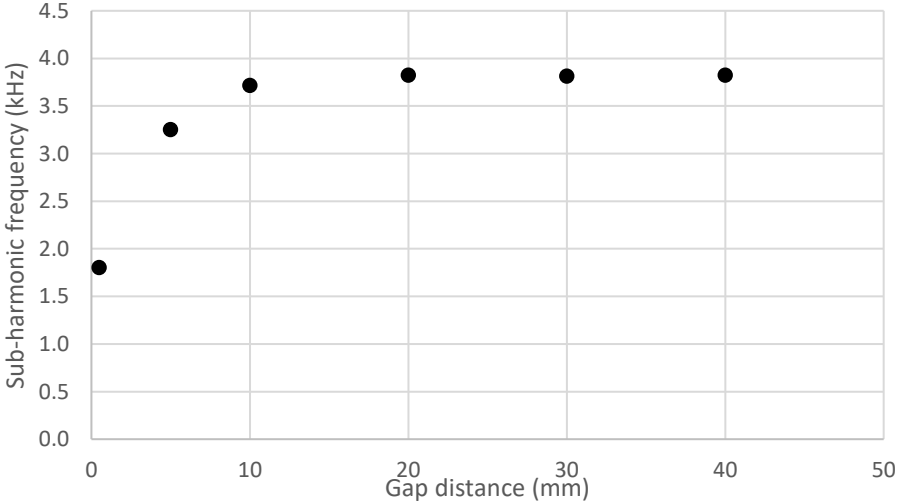
Figure 24 Trend of the sub-harmonic oscillation frequency of the aocustic cavitation with gap distance variation (acoustic driving amplitude and frequency: 60 µm at 19.74 kHz). Until the gap reduces to 10 mm, the oscillation frequency of the acoustic bubble cluster remained the same as approximately 1/5 of the acoustic driving frequency. As the gap reduced further, the oscillation frequency also reduced to 1/6 and eventually to 1/10 of the acoustic driving frequency.
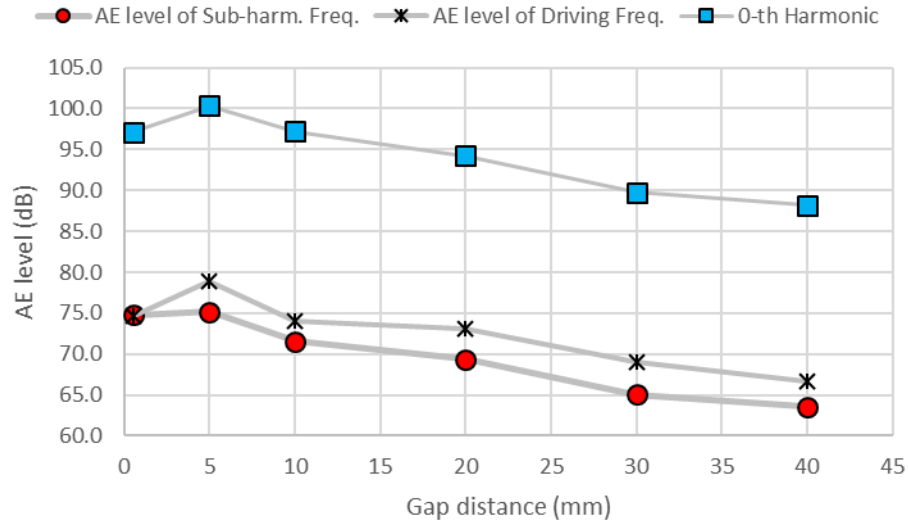
Figure 25 Trend of AE signal levels from the two main frequency components and the 0-th harmonic coefficients of their FFT results with varying gap distance. The trend of the 0-th harmonic coeffieient change appears to be similar with the trend of average or a certain harmonic means of the sub-harmonic components and the acoustic driving frequency componetns.

A possible reason of the reduction of the signal power with the gap distance below 5 mm appears to be related to the formation of the vortices on the rim of the ultrasonic horn tip. The experiment of Mottyll and Skoda (2016) indicated two distinctive areas of erosive attack; the primary damage occurred on the central region of the specimen, whereas the horn tip was primarily eroded on its periphery (Figure 27 (a)). To explain this, they suggested mechanisms to cause the impulses at the acoustic driving frequency and the sub-harmonic frequency as follows based on their experiment and CFD simulation results.

(1) Impulses at the sub-harmonic frequency: the acoustic bubble cluster developing in the central region of the ultrasonic horn tip.

(2) Impulses at the driving frequency: the acoustic cavity developing on the periphery of the ultrasonic horn tip, that is driven by the vortices on the rim of the horn tip.

They suggested the ring vortex round the ultrasonic horn tip as indicated in Figure 27 (b) was relevant with the primary erosion damage on the horn tip and it would be responsible for the impulses at the acoustic driving frequency. This appears to fit well to the current analysis results. If the gap becomes so narrow that would hinder the recirculation of the downward jet stream in the periphery of the horn tip, the strength of the ring vortex will be moderated by it. The erosive range of the mechanism (2) must be rather short considering the patterns of the
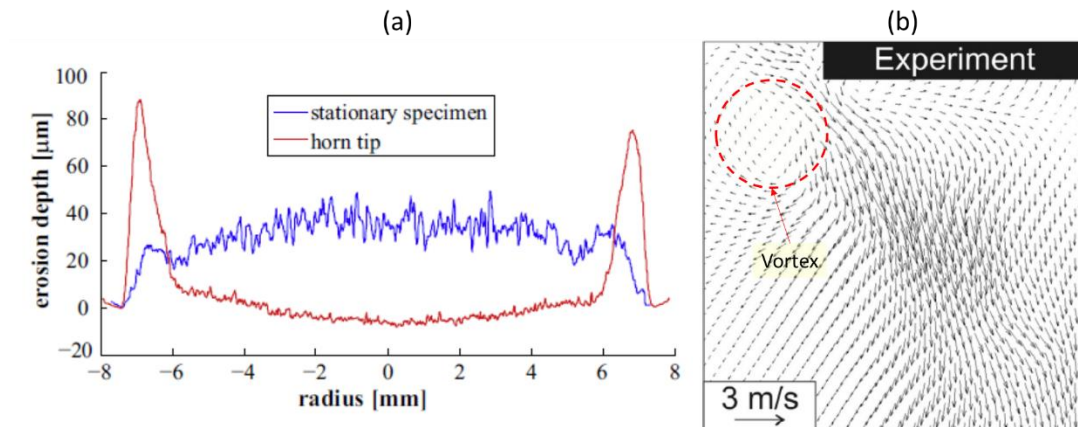
Figure 27 Erosion depth measurement results on an ultrasonic horn tip and the specimen beneath the horn tip (Mottyll and Skoda, 2016) (a), and a flow field near an ultrasonic horn tip (Žnidarčič et al., 2015) (b).
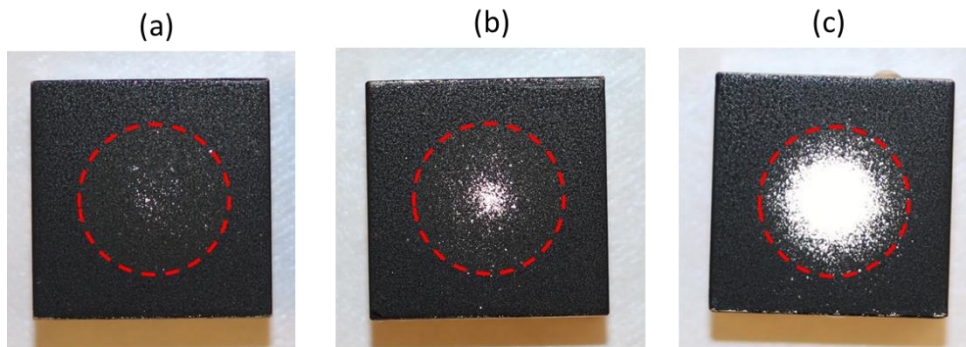
Figure 26 Damaged soft paint coat of the test specimens after exposure (20 s) to acoustic cavitation impacts (Peak-to-peak amplitude: 60μm @ 19.74 kHz): gap distance = 15 mm with exposure time 5 min. (a), gap distance = 10 mm (b), gap distance = 5 mm (c). The red dashed lines indicate the projected area of the ultrasonic horn tip (specimen width and height: 25 mm, the horn tip diametre 16 mm).

soft paint damage in Figure 26. Figure 26 shows the extent of the damage on the soft paint coat of the test specimens that underwent acoustic cavitation impacts for 20 s (except the photo (a), which was taken after 5 min exposure.) with different gap distances of 15, 10 and 5 mm. If the gap narrowed further to 0.5 mm, the paint coat within the projected area of the horn tip was completely removed in less than 1 ~ 2 s. After then, the damaged area did not grow any further. The fact that the erosion depth on the periphery of the ultrasonic horn tip in Figure 27 (a) was at least twice deeper than the other surfaces, whereas the damaged area of the soft paint was far enlarged only after the gap distance got narrowed by 5 mm or below suggests that the erosive range of the erosion mechanism by the ring vortex round the horn tip must be short

With regard to the meaning of the 0-th harmonic, if a sinusoidal wave signal with random noise were analysed by the FFT, the 0-th harmonic would represent the mean amplitude of the random noise. Figure 28 illustrates such an example. In the example, a sinusoidal wave was defined to have an amplitude of 1.5 oscillating at 100 Hz. White noise was added to the signal by generating random numbers in between 0 and 1. The signal with noise is represented in the time domain (a) and in the frequency domain (b). As stated above, the 0-th harmonic corresponds to the mean amplitude of the white noise in the signal and the frequency component at the oscillation frequency (100 Hz) indicates the amplitude of the signal.

However, the physical meaning of the 0-th harmonic of the AE signal may not be so obvious due to its impulsive nature and worth to thinking of it whether it can be physically interpreted. To investigate any possible physical meaning of the 0-th harmonic from the FFT, the PDF of the AE event strengths were plotted in respect to the gap distance (Figure 29, Table 8).

The PDF's of the AE signal power for the test cases of gap distance = 40, 20, 10, 5, 0.5 mm were plotted first with the bin size of 1 dB above the noise cut-off level of 40 dB_{AE} (Figure 29 (a)). The probability density of each bin was calculated based on the total number of the AE signals above the noise cut-off threshold. Their characteristics of the distribution are summarized in Table 8. Then the cumulative probability $P(A; x \geq A\ dB_{AE})$ of the AE events higher or equal with a certain signal power level A was calculated as shown in Figure 29 (b). Finally, the maximum AE signal power, mean signal power and the power level corresponding to $P(A; x \geq A\ dB_{AE}) = 0.05$, which was set arbitrarily for comparison purpose, were compared with the 0-th harmonics (Figure 30). All the AE signal power described in this section were corrected for the level deduction by the attenuators (-19.3 dB each).
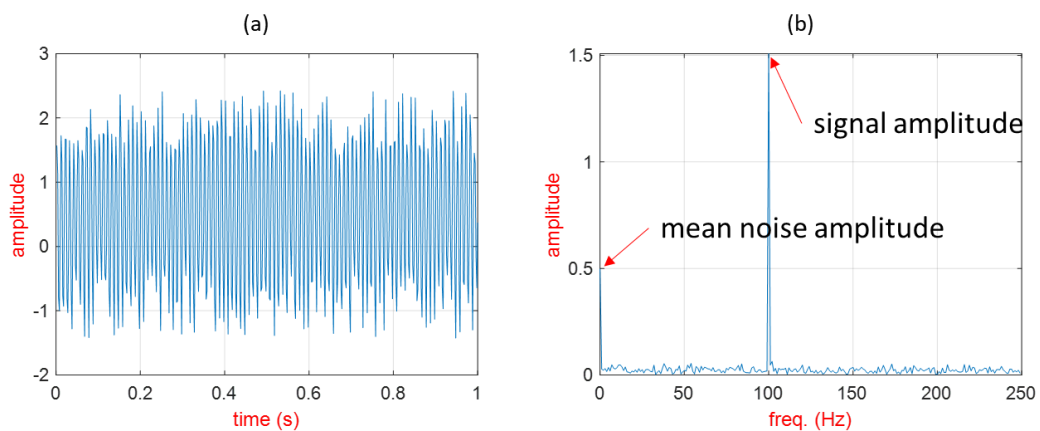
Figure 28 An illustration of sinusoidal waves (amplitude = 1.5) with white noise (amplitude range $\in [0, 1]$) in time domain (a) and their FFT analysis result (b).

From Figure 30, the trend of all the indices compared appeared similar each other except for the point of the maximum signal power with the gap of 0.5 mm. Hence, it looks reasonable to assume the 0-th harmonic coefficient as a weighted mean between the mean signal power and either the upper 5 % signal power or the maximum signal power.

Table 8 Moments of the PDF's for the test cases with the gap distances of 40, 20, 10, 5, 0.5 mm.

Gap distance	Mean signal power	Max signal power	Variance	Skewness	Kurtosis
[mm]	[dB$_{AE}$]	[dB$_{AE}$]	[dB$_{AE}^2$]	[-]	[-]
40	83.5	114	113.2	-1.01	4.79
20	88.8	120	113.4	-1.04	5.06
10	91.5	123	110.7	-1.09	5.25
5	94.8	126	113.8	-1.08	5.24
0.5	90.8	128	136.5	-0.78	4.35
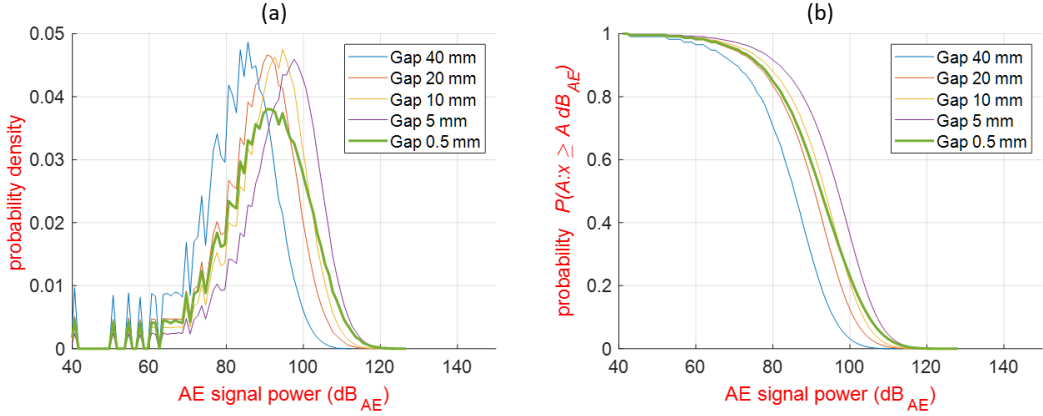
Figure 29 Comparison of AE signals for the gap distances of 40, 20, 10, 5 and 0.5 mm: probability density of the signals (a), cumulative probability of AE events greater or equal to a certain AE signal power level A dB$_{AE}$ (b).

The test results with power variation are plotted in Figure 33. AE signals were measured with sampling frequency of 150.376 kHz for three different gap distances of 0.5, 15 and 20 mm varying the power from 50 % to 100 %. To avoid the AE signal clipping, two (for 15, 20 mm gap distances) or three (for 0.5 mm gap distance) -19.3 dB attenuators were attached to reduce the signal amplitudes within the sensor range (40 ~ 100 dB_{AE}). All the figures in the plots were corrected for these reductions by the attenuators. In Figure 33 (a), the sub-harmonic oscillation frequency tended to decrease as the applied sonotrode power or the amplitude of the acoustic excitation increased (the excitation amplitude increases in proportion with the power increase). This tendency remained valid for all the tested gap distances. The 0-th harmonic of the signal showed a similar trend to that of the gap variation tests (Figure 33 (b)). The AE level of the sub-harmonic frequency component tended to increase as the power increases (Figure 33 (c)). The slope of increase was about 0.5 dB per 10 % power increase or driving amplitude increase of 10 µm (peak-to-peak). Meanwhile, the AE signal level of the acoustic driving frequency component was kept at 84 dB until 70 % power and started to decrease almost logarithmically for the gap distances of 15 and 20 mm. With the gap of 0.5 mm, it tended to increase (Figure 33 (d)). Figure 33 (d) may be explained as a result of shifting of the dominant impact source from the cavitation on the rim to that occurring on the central region of the horn tip.

Finally, paint tests with the sonotrode could reproduce a similar damage pattern development with the hydrodynamic cavitation erosion. If the cavitation intensity was weak, the damage pattern grew from the centre towards the rim of the sonotrode tip as the exposure time increased. However, if the intensity was too high, the damage pattern was formed instantly
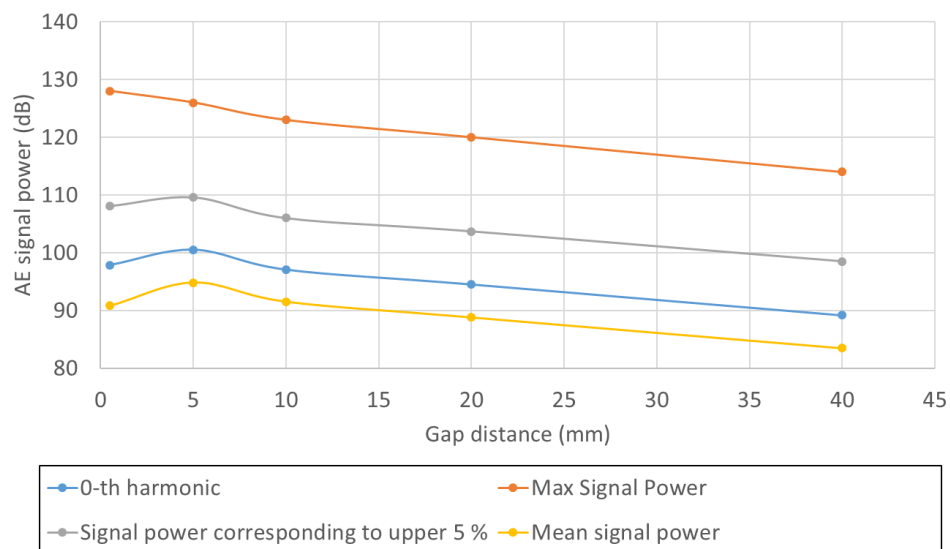
*Figure 30 Plots of the 0-th harmonic amplitudes, the maximum signal powers and the signal power thresholds corresponding to upper 5 % with regard to the gap distances. Extracted from the same data sets in **Error! Reference source not found.**.*

and similarly sized as the horn tip diameter. The patterns of damage never grew larger than the horn tip diameter in any case. In the cases of too weak cavitation, the pattern was never formed even in a 10 minute exposure. These patterns of damage development were regarded to agree well with the cavitation erosion of solid metals. However, it must be borne in mind that the paint coating damage heavily depends on the quality of the coating. For example, (1) if the test specimen surface was too smooth, or (2) contaminated by oily matters, or (3) the paint was too thin, or (4) the paint coating became too hard after long exposure to a hot and dry ambient condition before the test, the consistency of the results could not be expected.

Through repetition of the same test condition with different batches of painted copper alloy samples, the condition of approximately 60 µm (peak-to-peak) excitation amplitude with the gap distance of 15 mm was confirmed to be the threshold condition for the model scale cavitation erosion to occur. Figure 31 illustrates an example of the confirmation tests. Six sets of AE signal data were recorded to analyse the signal for the test condition. They were analysed by Welch's method and are plotted in Figure 32. The corresponding AE signal power levels from the FFT analysis based on the Welch's method were approximately 96 dB_{AE} for the 0-th harmonic, 71 dB_{AE} for the sub-harmonic oscillation component and 80 dB_{AE} for the driving frequency component after compensation of the signal attenuator (-19.3 dB). With regard to the determination of the magnitude of the AE signals using the Welch's method, it does not appear so straight forward at the moment.

From the measured signal strength distribution that indicated 118 ~ 119 dB_{AE} for the maximum range of the signals (Figure 32), the AE threshold for the soft paint erosion criteria was estimated to be approximately 119 dB_{AE}.

(a) 20 s   (b) 60 s   (c) 120 s   (d) 300 s
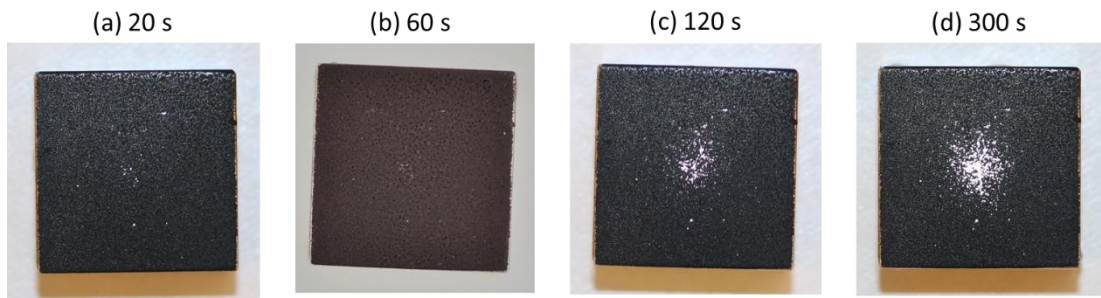
Figure 31 The development of the soft paint damage on a test sample under the test condition of the peak-to-peak amplitude 60 μm with the gap of 15 mm (the sample dimensions: 25 × 25 mm2, ultrasonic horn tip diameter: 16 mm).
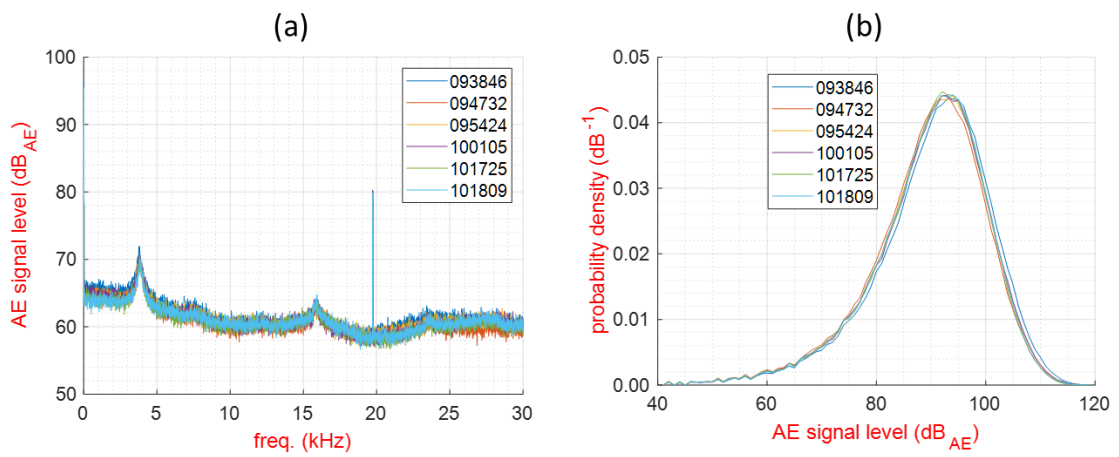
Figure 32 AE signal power spectra based on the Welch's method (a) and the PDF's of the signal power (b) under the soft paint erosion threshold condition (Peak-to-peak amplitude of ultrasonic horn tip vibration = 60 μm @19.74 kHz with the gap of 15 mm).
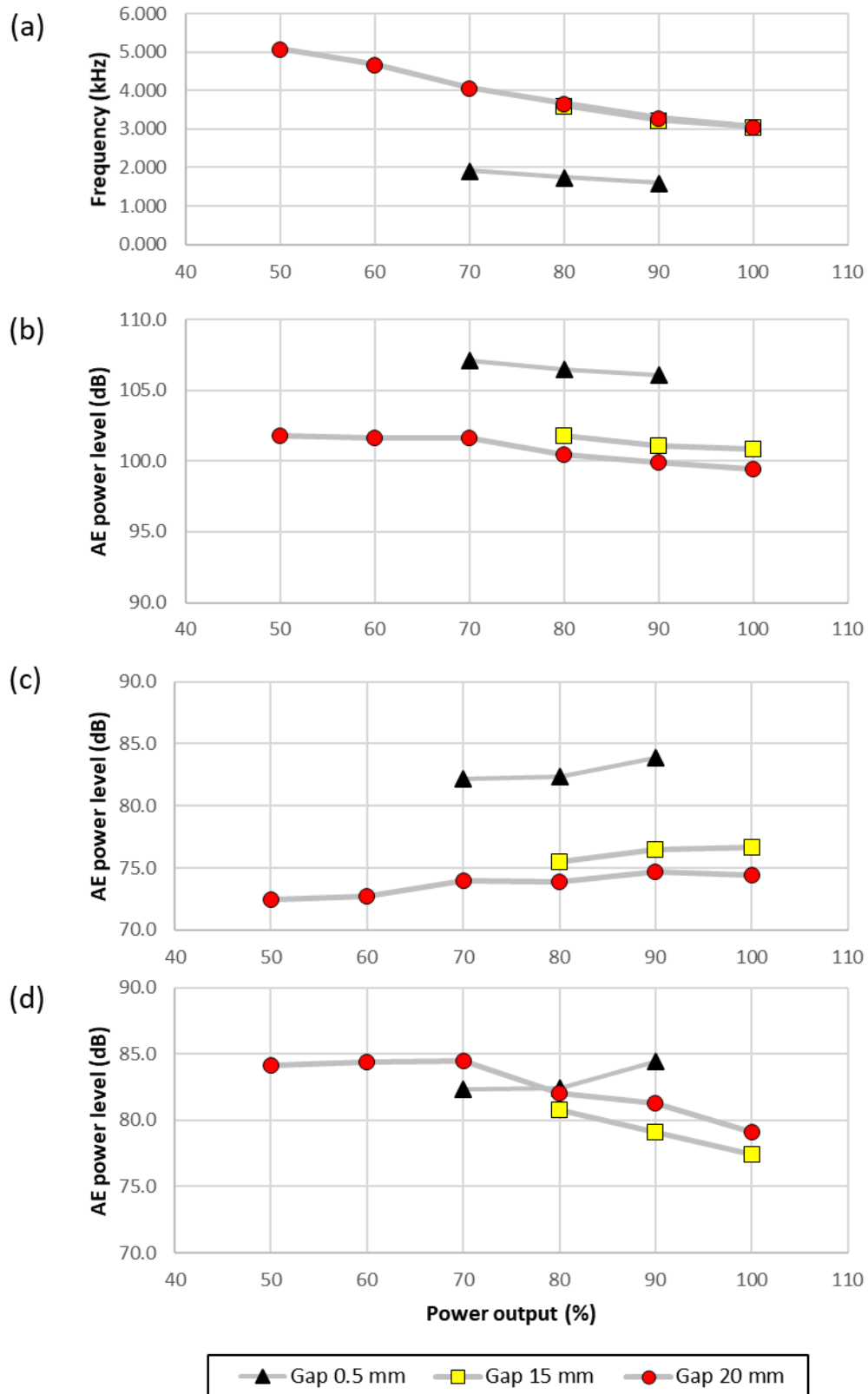
Figure 33 Power variation test results with the gap distance cases of 15 and 20 mm. 0.5 mm: sub-harmonic frequency (a), magnitudes of 0-th harmonics (b), AE level of the sub-harmonic frequency (c), AE level of the driving frequencyies (d).

64

3.6   Summary

This chapter discussed AE technique in the context of developing a quantitative measure to assess the risk of cavitation erosion. In spite of huge expansion of our understanding of cavitation erosion mechanism and computational capability in hand, still the job is challenging because, for now, we have only qualitatively valid means, which does not always meet the industry demand for higher accuracy.

A brief introduction of the acoustic emission (AE) was given in section 3.1. The AE is a micro-scale seismic waves typically in ultrasound range. It is generated from the sudden release of strain energy accumulated inside the medium under stress. It was reported that AE signals were generated from the cavitation attack and the signals could be probed inside a ship's engine room.

In section 3.2, the potential of AE as a quantitative measure to assess risk of cavitation erosion was explained. Although there were not many studies, a number of papers support that the AE signal amplitude showed meaningful relevance with the cavitation behaviour. Also one of the studies reported the AE signal actually showed the same behavioural character as that of the acoustic pressure waves or vibration measured by accelerometers on the shell encapsulating the cavitating flow. So there is a good possibility that the AE signal can be used as a pressure sensor to assess the risk of cavitation erosion.

Section 3.3 covered modelling of the AE signals. The AE signals can be found by convolving quantities for (1) AE source characteristics, (2) propagation in a medium and (3) an AE sensor characteristics. AE source characteristics can be found from an appropriate CFD simulation. The wave propagation has to be simplified only to consider the attenuation of the signal due to limited capability of DAQ system available. The sensor characteristics can be obtained from a frequency analysis of the measured background noise signals.

Section 3.4 and 3.5 described the actual experiment with an ASTM G-32 type cavitation apparatus (sonotrode). In section 3.4, AE sensor characteristic was described to convert the electric voltage signals to AE level (dB_{AE}). To correlate the signal output voltage with the impact force on a copper alloy specimen that is the same as the model propeller material, a series of steel ball drop tests had been carried out. The measured signal was consistent against given impact forces. Based on the linearity of AE response to the impact force, the correlation coefficient was found to be 7.29 x 10^{-5} N/V for the AE sensor that was used in the study.

Section 3.5 briefly introduced frequency analysis methods and discussed the problem with the frequency analysis approach to reveal the AE signal power contributing to the cavitation

erosion using the Welch's method. STFT analysis method is useful in analysing signals varying in time and frequency. STFT results of AE signals revealed that the frequency characteristics of the AE signal were almost invariant in time. Hence, the Welch's method was useful to analyse the frequency characteristics of acoustic cavitation phenomenon. To determine an appropriate test condition with the sonotrode to find a soft paint erosion threshold, the gap distance and the vibration amplitude of the ultrasonic horn tip were varied. Investigation on the influence on the sub-harmonic oscillation frequency and the resulting signal power distribution appeared to agree with other previous works qualitatively, except that the oscillation frequency of acoustic cavitation looked more like a narrow banded one with a centre frequency which closely coincides with the sub-harmonic frequencies in between 1/5 ~ 1/11 of the acoustic driving frequency. During the course, an experimental data for the trend of sub-harmonic frequency with the change of acoustic stream dispersion distance was produced to fill the gap in the existing works. Finally, soft paint tests were carried out using the sonotrode to estimate a rough equivalent AE threshold for the conventional cavitation erosion tests at the model scale. The frequency analysis approach was not straight forward as data analysis in time domain probably due to the impulsive nature of the AE signals. The estimated threshold for the AE signal power level from the analysis in time domain was about 119 dB_{AE} by reading the maximum signal power observed. This may be further refined by statistical treatment of the maximum loading, e.g. in the form of mean value of the impact loadings above a certain threshold, for example, upper 5 %. The appropriate threshold needs to be further refined in the future.

Chapter 4   Fundamentals of the Numerical Modelling of Acoustic Cavitation

4.1   Introduction

To estimate an AE threshold that is equivalent with the conventional soft paint erosion tests, an ultrasonic cavitation apparatus was used to mimic the cavitation impact loadings.

Since acoustic cavitation has several different characteristics compared with the hydrodynamic cavitation, e.g. uniformity in bubble size distribution, forming a stationary cloud cavitation, acoustic streaming, it is necessary to understand how they contribute to the impact loadings that cause soft paint coat damage on a test specimen. Numerical simulation can give an insight for this, which is not always easy to understand only through experiment.

In order to numerically simulate the acoustic pressure impacts from acoustic cavitation and to investigate energy transfer from the pressure impacts to acoustic emission, an appropriate numerical model is necessary. This chapter outlines the numerical methods and some relevant background information to understand them.

4.2   The OpenFOAM suite

There are several widely-used commercial CFD software packages that enable users to simulate compressible multiphase flows, e.g. FLUENT (https://www.ansys.com/en-gb/products/fluids/ansys-fluent), CFX (https://www.ansys.com/en-gb/products/fluids/ansys-cfx) or STAR-CCM+ (https://mdx.plm.automation.siemens.com/star-ccm-plus). In this research, an open source computational fluid dynamics (CFD) software suite (v. 3.0.1, https://openfoam.org/) was used to simulate acoustic cavitation through this work. Thanks to its open source policy, the software suite has been continuously improved in terms of correctness of the numerical methods, availability of variety of models to study a wide range of complex physics. Furthermore, it provides quite in-depth versatility in applying various numerical methods to approach physical or chemical problems, which is difficult to achieve with commercial software suites. There are disadvantages also with OpenFOAM such as steep learning curve and possible confusion of the model without an appropriate level of knowledge of numerical techniques. However, even these disadvantages provide a good opportunity for users to learn and understand how a certain numerical model was formulated under what kind of assumptions and philosophy. Therefore, it makes it easier for users to help improve the limitation of numerical models in a shorter time.

4.3　Governing equations and the finite volume method

4.3.1　Fluid viscosity and stress

The fluid is defined as matter that will be moved in the direction of an acting shear stress however small it is (White, 2011). It is obvious the stress causes the fluid to set in motion. What is the stress then? The stress is a force acting on any cross-section of a solid body and has the same unit as the pressure. Indeed the pressure is a specific component of the stress acting in the normal direction of the body surface. Newton conjectured the stress and the fluid motion could be related using a coefficient μ_V as Eq. (4.1) from the analogy of the relation between force and acceleration of solid particles.

$$\boldsymbol{\sigma_{ij}} = \mu_v \frac{dU_i}{dx_j} = \mu_v \nabla \boldsymbol{U} \quad (i, j = 1, 2, 3) \tag{4.1}$$

The coefficient μ_V is defined as the viscosity coefficient that represents the resistance or friction coefficient of fluid against motion. Not all fluids follow the assumed relation and a fluid that has a constant viscosity is termed as a Newtonian fluid. This property can vary significantly with temperature change, otherwise stays almost constant in many fluids. So fluids such as the air or water can be treated as Newtonian fluids in isothermal conditions or in a physics model in which the temperature is not accounted for.

In 3-D Cartesian space, a stress acting on the unit volume of fluid can be expressed as a 3 x 3 matrix that has three components (j = 1, 2, 3) in each principal direction i = 1, 2, 3. Mathematically to express such a matrix in a compact manner, tensor is defined as an expansion of the vector which can be treated as 1 x 3 matrix. A scalar is zeroth rank tensor and a vector is a rank one tensor in tensor space. So stress can be represented as a second rank tensor or simply a tensor.

The stress tensor is customarily expressed as the decomposed form of symmetric part and asymmetric part. The symmetric part can be written as a diagonal matrix whose components are the average of the normal stresses of the original tensor. The original stress tensor after subtraction of the symmetric part becomes the asymmetric part. The physical meaning of this decomposition is that the stress is now conceptually decomposed of the mean normal stress, which is the pressure indeed, and the shear stresses. The symmetric part has only the normal stress components that can only either expand or contract the volume, thus it is responsible for the deformation of the fluid and called as hydrostatic stress. Whereas, the asymmetric part has only the shear stress components, thus it cannot change the volume but exert torsion on the

68

volume. Therefore, it is responsible for the distortion or rotation of the fluid volume and called as deviatoric stress. It is noteworthy that the deviatoric stress tensor becomes symmetric in most cases (Sonin, 2001). Since the viscous stress is deviatoric stress, it can be mathematically expressed as Eq. (4.2) where I is identity tensor and S strain rate tensor.

$$T = 2\mu_v \left(S - \frac{1}{3}(\nabla \cdot U)I \right), \qquad S \equiv \frac{1}{2}(\nabla U + (\nabla U)^T) \tag{4.2}$$

4.3.2 Governing equations for the fluid motion

The fluid flow must satisfy the three basic laws of mechanics at all time and a thermodynamic state relation and associated boundary conditions (White, 2011). The basic laws are conservation of mass, momentum and the energy. According to Žnidarčič et al. (2014), the temperature did not have a significant influence to the physics of acoustic cavitation in terms of sub-harmonic frequency of the cavitation and the pressure peaks. Hence, the energy equation is not considered here. For the unit fluid volume, the mass conservation can be expressed as Eq. (4.3).

$$\frac{\partial \rho}{\partial t} + \nabla \cdot (\rho U) = 0 \tag{4.3}$$

The second Newton law about the linear momentum of the fluid is expressed as Eq. (4.4), where T is the viscous stress tensor written as Eq. (4.2). The fluid will stay at its original state unless arises the pressure difference in the fluid or shear force is exerted to the fluid.

$$\frac{\partial (\rho U)}{\partial t} + \nabla \cdot (\rho UU) = -\nabla p + T \tag{4.4}$$

Since the density of a compressible fluids can vary in space and time, the derivatives of density will not vanish in general. There are only two equations while there are three unknowns as ρ, U and p. To close the system of equations, a barotropic equation of state is introduced as Eq. (4.5) where c denotes speed of sound in a medium.

$$\frac{dp}{d\rho} = c^2 \tag{4.5}$$

There is no analytical solution that satisfies Eqs. (4.3) ~ (4.5) in general. Therefore, the equations need to be solved numerically. Finite difference method (FDM), finite volume method (FVM) or finite element method (FEM) are available to achieve this. A concise

explanation on each method can be found in Ferziger and Peric (2002). A short explanation of the methods are provided based on this.

FDM was the first-developed numerical method. All the derivatives are approximated by appropriate finite difference methods that are in principle approximating all derivatives by Taylor expansion. The method is simple and effective, however, the conservation is not guaranteed in itself and it is difficult to apply for a complex geometry.

FVM uses a conservative and integral form of the governing equations. The calculation domain is discretised into continuous smaller control volumes (cells) and the re-written governing equations are applied to each cell. This method can be used with any type of grid. Hence with this method the conservation is ensured and is applicable to any complex geometries. Furthermore, it is also simple to programme. The disadvantage compared with FDM is the difficulty of applying methods of higher order than the second order for 3-D domain. This is because FVM needs three levels of approximation as interpolation, differentiation and integration.

Similarly to FVM, FEM divides the domain into small elements typically in tetrahedral form and solves the approximated governing equations. The difference from FVM is that the governing equations are multiplied with a weighting function to ensure the continuity across the element boundaries. OpenFOAM suite is written based on the FVM method. Hence, the FVM method is used all through this work.

4.3.3   The finite volume method (FVM)

To apply the finite volume method, the differential form of governing equations are re-written in the conservation form or integral form over each cell volume *V*. For any physical quantity φ, the differential form of continuity equation can be re-written as Eq. (4.6a).

$$\frac{\partial \varphi}{\partial t} + \nabla \cdot (\varphi \boldsymbol{U}) = 0 \Longrightarrow \int_V \frac{\partial \varphi}{\partial t} dV + \int_V \nabla \cdot (\varphi \boldsymbol{U}) dV = 0 \qquad (4.6a)$$

Specifically the second term on the left hand side of the conservative form can be simplified using Gauss theorem, or more generally Stokes theorem, as the surface integral of the combined quantity $\varphi \boldsymbol{U}$ over the bounding surface *S* of the control volume *V*. Thus, Eqs. (4.2) ~ (4.3) can be re-written as the form of Eq. (4.6b).

70

$$\int_V \frac{\partial \varphi}{\partial t} dV + \int_S (\varphi \boldsymbol{U}) \cdot \boldsymbol{n} dS = 0 \qquad (4.6b)$$

where $\boldsymbol{n}$ is the surface normal vector of the boundary S. The physical meaning of this is clear. The first term of Eq. (4.6b) represents the change of the physical quantity φ in time within the fluid volume. The second term is the flux of φ through the boundary of the volume. Therefore, if any physical quantity is conserved, the change of the quantity in time within a fluid volume must be equal to the net flux of the quantity through the bounding surface. If the quantity is generated or destroyed by any external mechanism, e.g. turbulent kinetic energy, they are called source or sink terms and included on the right hand side of the equation (Lidtke, 2017).

4.3.4   Numerical schemes

The governing equations are all in essence the continuity equation as Eq. (4.6b). To solve these differential equations by numerical methods, the analytical differential equations can be approximated by difference equations using the Taylor expansion as Eq. (4.7).

$$\varphi(t - \Delta t) = \varphi(t) - \frac{\Delta t}{1!} \frac{\partial \varphi}{\partial t}\bigg|_t + \frac{\Delta t^2}{2} \frac{\partial^2 \varphi}{\partial x^2}\bigg|_t + \mathcal{O}(\Delta t^3) \qquad (4.7)$$

In this section, such numerical differencing schemes are discussed to solve the continuity equations. The continuity equation requires solving the volume integral of time derivative and the surface integrals with respect to a physical quantity. The physical quantities are typically stored in the cell centres for two or three time steps depending on the applied temporal discretisation scheme.

OpenFOAM provides a couple of temporal discretisation schemes such as Euler, backward and Crank-Nicolson (Crank and Nicolson, 2008). The time derivatives were discretised by either Euler or backward schemes in this study. Euler scheme approximates the time derivatives by backward Euler method as Eq. (4.8a) where the notations follow the schematic in Figure 34.

$$\frac{\partial \varphi}{\partial t}\bigg|_i^n = \frac{\varphi_i^n - \varphi_i^{n-1}}{\Delta t} + \frac{\Delta t}{2} \frac{\partial^2 \varphi}{\partial x^2}\bigg|_i^n - \frac{\Delta t^2}{6} \frac{\partial^3 \varphi}{\partial x^3}\bigg|_i^n + \mathcal{O}(\Delta t^3) \qquad (4.8a)$$

To investigate the accuracy of this scheme, Eq. (4.8a) is re-arranged as Eq.(4.8b) neglecting the second and higher order terms. Not necessarily the time step size Δt uniform through the calculation domain in general, Δt is assumed to be uniform here for simplicity of discussion.

$$\varphi_i^n = \varphi_i^{n-1} + \frac{\Delta t}{1!} \left.\frac{\partial \varphi}{\partial t}\right|_i^n + \mathcal{O}(\Delta t^2) \tag{4.8b}$$

Re-arranging Eq. (4.8b) about the residual error term and dividing both sides with Δt, an equation for the residual error between the analytical time derivative and the approximation by the difference equation is obtained as Eq. (4.8c).

$$\frac{\varphi_i^n - \varphi_i^{n-1}}{\Delta t} - \left.\frac{\partial \varphi}{\partial t}\right|_i^n = \frac{1}{\Delta t} \mathcal{O}(\Delta t^2) = \mathcal{O}(\Delta t) \tag{4.8c}$$

Thus, if the time step size is reasonably small, the Euler scheme is first order accurate. Since the discretization error of this kind of schemes increases in proportion with the time step size, the time step size must be small to obtain accurate solutions. Hence, the first order schemes are inefficient compared with the second or higher order schemes. The scheme can be extended to a second order version in the same manner, which is called 'backward' in OpenFOAM terms. The 'backward' scheme can be derived from Eq. (4.8a). Using the Euler scheme, the second time derivative can be written as Eq. (4.9a). Substituting Eq. (4.9a) into Eq. (4.8a) and re-arranging the equation with respect to $\partial\varphi/\partial t$, a new difference equation for the time derivative is obtained as Eq. (4.9b). The third derivative in Eq. (4.8a) was neglected. Finally, the leading truncation error term becomes proportional to Δt^2. Hence, backward scheme is a second order accurate formulation of the Euler scheme.
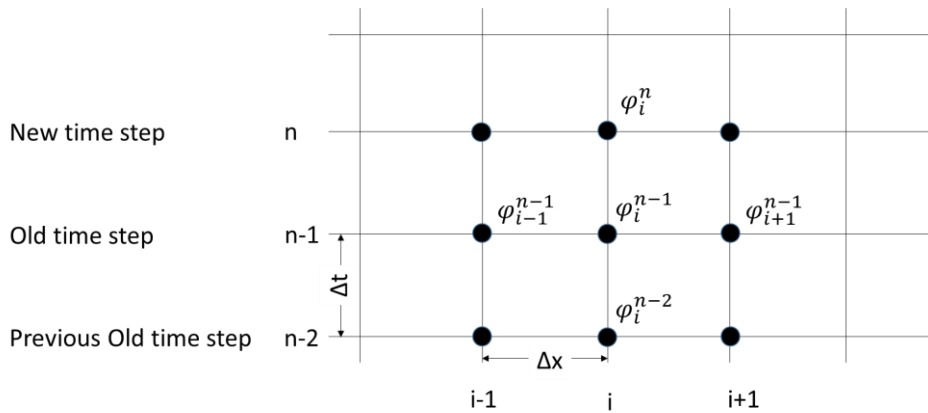
Figure 34 A schematic diagram of a 1-D problem discretized in space (x) and time (t) with a physical quantity φ_i^n at a calculation node (x_i, t_n).

$$\left.\frac{\partial^2 \varphi}{\partial t^2}\right|_i^n = \frac{1}{\Delta t}\left(\left.\frac{\partial \varphi}{\partial t}\right|_i^n - \left.\frac{\partial \varphi}{\partial t}\right|_i^{n-1}\right) = \frac{1}{\Delta t^2}\left(\varphi_i^n - 2\varphi_i^{n-1} + \varphi_i^{n-2}\right) \tag{4.9a}$$

$$\left.\frac{\partial \varphi}{\partial t}\right|_i^n = \frac{1}{2\Delta t}\left[3\varphi_i^n - 4\varphi_i^{n-1} + \varphi_i^{n-2}\right] + \mathcal{O}(\Delta t^2) \tag{4.9b}$$

Convection terms need to be approximated by appropriate differencing schemes as well. An important character of the convection terms is that they are physically directional. Hence, to make the convection differencing schemes also directional, upwinding schemes are used for the interpolation of the variables. Upwinding schemes adaptively determine the upwind or upstream cell based on the flow direction and apply backward differencing schemes to calculate any physical quantity.

All the convection terms in OpenFOAM are calculated using the Stokes theorem Eq. (4.6b). Hence, convection schemes need to calculate gradient of convecting quantities through the cell faces. Interpolation of the cell face values is carried out using a central differencing scheme by default. Take Taylor series expansion of the quantity $\varphi(x_i, t^n)$ about the cell faces $i \pm \frac{1}{2}$ for a node i as Eq. (4.10a) and Eq. (4.10b).

$$\varphi_{i+1/2}^n = \varphi_i^n + \frac{\Delta x}{2}\left.\frac{\partial \varphi}{\partial x}\right|_i^n + \frac{\Delta x^2}{4 \times 2!}\left.\frac{\partial^2 \varphi}{\partial x^2}\right|_i^n + \mathcal{O}(\Delta x^3) \tag{4.10a}$$

$$\varphi_{i-1/2}^n = \varphi_i^n - \frac{1}{2}\frac{\Delta x}{1!}\left.\frac{\partial \varphi}{\partial x}\right|_i^n + \frac{1}{4}\frac{\Delta x^2}{2!}\left.\frac{\partial^2 \varphi}{\partial x^2}\right|_i^n + \mathcal{O}(\Delta x^3) \tag{4.10b}$$

Subtracting (4.10b) from (4.10a) and dividing by Δx on both sides, a formula for $\partial \varphi / \partial x$ is obtained as Eq. (4.10c) of which the approximation error is of the second order.

$$\left.\frac{\partial \varphi}{\partial x}\right|_i^n = \frac{\varphi_{i+1/2}^n - \varphi_{i-1/2}^n}{2\Delta x} + \frac{1}{\Delta t}\mathcal{O}(\Delta t^3) \tag{4.10c}$$

While high order differencing schemes are preferred for more accurate solutions compared with the first order schemes, a problem with them is that they tend to produce unphysical oscillatory solution behaviour at the points where the real solution changes sharply, e.g. the points where a discontinuity or a shock occurs. This kind of errors often cause the numerical stability issues. Meanwhile, the first order schemes tend to become diffusive (physical but with much decreased accuracy). To ensure boundedness of the convection terms keeping high accuracy of solution, TVD (Total Variation Diminishing) schemes are often used such as

73

Godunov (1959) or van Leer (Van Leer, 1977b), which will be discussed in the following paragraphs.

TVD schemes are also called as MUSCL (Monotonic Upwind Scheme for Conservation Laws) scheme (van Leer, 1979). It is the key idea in those schemes that the monotonicity of gradient of the quantity is a necessary condition to prevent the numerical oscillation near the singular points. Van Leer scheme (Harten et al., 1983, Van Leer, 1977a) is such a TVD scheme. This can be understood as a second order version of Godunov's first order Lagrangian scheme (Godunov, 1959). Both schemes can be easily understood from the illustration in Figure 35 that shows how Godunov first order scheme treats the problems.

In Figure 35, the red solid line represents a physical quantity φ convected in space x, and the black solid line is the averages of the quantity determined in each cell space $x = i\text{-}1$, i and $i\text{+}1$. In Figure 35 (a), the averaged quantity at each cell is determined based on the physical quantity and the cell face flux is determined by upwinding scheme, meaning the face flux at $x = i\text{-}1/2$ will be determined as $\varphi_{i\text{-}1}$ if the convection is assumed to occur from left to right in the figure. In the next time step $\Delta t = (\sigma/a)\Delta x$, the physical quantity φ is convected by the distance of $\sigma\Delta x$ (Figure 35 (b)), where a and σ denote the convection velocity and the CFL number respectively. Based on the shifted quantity (blue dotted boxes), the new average quantity in each cell space is determined and the face flux is again determined by upwinding scheme. This is how Godunov first order scheme works and this is the first order scheme. Van Leer scheme enhances the method to approximate the face fluxes by using a linear function to approximate them and is second order accurate at least.

The scheme is realised in OpenFOAM as follows. To determine the direction of the flow, a scalar Λ_i is calculated as Eq. (4.11a) where the vector $\boldsymbol{d}$ represents a distance vector from a cell centre to its neighbour cell centre. Then the limiter function is calculated as Eq. (4.11b). Finally, the face flux $\varphi_{i\text{+}1/2}$ is calculated as Eq. (4.11c).
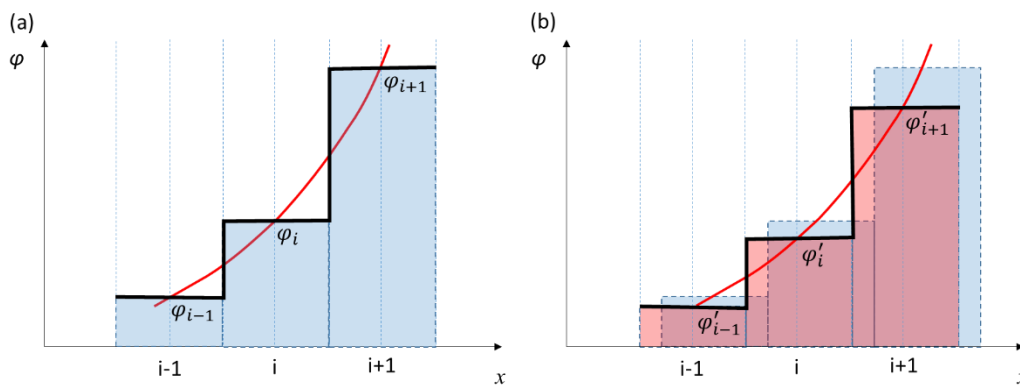
Figure 35 An illustration of Godunov 1st order upstream centred scheme (after van Leer, 1977).

$$\Lambda = 2 \cdot \frac{(\nabla \varphi)_c \cdot \boldsymbol{d}}{(\nabla \varphi)_f \cdot \boldsymbol{d}} - 1 = \frac{\varphi_i - \varphi_{i-1}}{\varphi_{1+1} - \varphi_i} \tag{4.11a}$$

$$\Gamma(\Lambda) \equiv \frac{\Lambda + |\Lambda|}{1 + |\Lambda|} \tag{4.11b}$$

$$\varphi_{i+1/2} = \varphi_i + \frac{1}{2}\Gamma(\Lambda)(\varphi_{i+1} - \varphi_i) \tag{4.11c}$$

The mass convection term in this study was modelled using either an upwind central differencing or the van Leer scheme. The upwind Central differencing scheme, which is termed Gauss linear convection scheme in OpenFOAM, tended to make the solution unstable and eventually diverged due to unboundedness that caused unphysical density and pressure development. For the solution stability and physicality, a high order convection scheme ensuring the boundedness is very important. The coefficient matrix is sparse matrix of which components are mostly zero except round the diagonal and one or two adjacent components depending on the adopted interpolation scheme.

4.3.5   The CFL condition

The condition arose from the discussion of Courant et al. (1967) on the stability of numerical solutions for a certain type of partial differential equations, e.g. wave equations. Numerical methods enable to solve complicated analytical partial differential equations for however complicated geometrical domains. Unfortunately, they introduce numerical diffusion in addition to the original physical governing equations depending on the numerical discretization methods. For example, a simple one dimensional wave equation as $\partial U / \partial t + c \cdot \partial U / \partial x = 0$ (*U*: flow velocity, *c*: wave propagation speed) can be discretised by a first order upwinding scheme as Eq. (4.12).

$$\frac{U_i^n - U_i^{n-1}}{\Delta t} + c \cdot \frac{1}{\Delta x}\left(U_{i+1}^{n-1} - U_i^{n-1}\right) = 0 \tag{4.12}$$

Each term of Eq. (4.12) can be substituted with Eq. (4.13a) and Eq. (4.13b).

$$\frac{U_i^n - U_i^{n-1}}{\Delta t} = -\frac{\partial U}{\partial t}\bigg|_i^n + \frac{\Delta t}{2}\frac{\partial^2 U}{\partial t^2}\bigg|_i^n + \mathcal{O}(\Delta t^2) \tag{4.13a}$$

$$\frac{c}{\Delta x}\left(U_{i+1}^{n-1} - U_i^{n-1}\right) = -c \cdot \frac{\partial U}{\partial x}\bigg|_i^{n-1} + \frac{c \cdot \Delta x}{2}\frac{\partial^2 U}{\partial x^2}\bigg|_i^{n-1} + \mathcal{O}(\Delta x^2) \tag{4.13b}$$

Since $U_t + c \cdot U_x = 0$ with a simplified notation of derivative $U_x \equiv \partial U / \partial x$ for any variable x, U_{tt} = $c^2 \cdot U_{xx}$. Therefore, the second time derivative in Eq. (4.13a) can be substituted by the Laplacian of U. Hence, the difference equation can be expressed in differential form as Eq. (4.14).

$$\frac{U_i^n - U_i^{n-1}}{\Delta t} + c \cdot \frac{1}{\Delta x}\left(U_{i+1}^{n-1} - U_i^{n-1}\right) = -\left.\frac{\partial U}{\partial x}\right|_i^n - c \cdot \left.\frac{\partial U}{\partial x}\right|_i^n$$
$$+ \frac{c \cdot \Delta x}{2}\left(1 - \frac{c \cdot \Delta t}{\Delta x}\right)\left.\frac{\partial^2 U}{\partial x^2}\right|_i^n + \mathcal{O}(\Delta t^2, \Delta x^2) \tag{4.14}$$

For an exact solution u of the difference equation Eq. (4.14), the left hand side must become zero. Hence, the difference equation solves a new partial differential equation that has a Laplacian term in addition to the original wave equation as Eq. (4.15).

$$\frac{\partial u}{\partial t} + c \cdot \frac{\partial u}{\partial x} = \frac{c \cdot \Delta t}{2}\left(1 - \frac{c \cdot \Delta t}{\Delta x}\right)\frac{\partial^2 u}{\partial x^2} + \mathcal{O}(\Delta t^2, \Delta x^2) \tag{4.15}$$

Since this additional Laplacian term has the same mathematical form with diffusion terms and it is introduced by numerical differencing schemes, this is called numerical diffusion. The non-dimensional coefficient $c \cdot \Delta t / \Delta x$ is called CFL number σ and it should be chosen to be close to one for the solution to be accurate. This is called CFL condition.

4.3.6   Deforming mesh scheme

To mimic the vibratory motion of the ultrasonic horn, either a deforming mesh scheme or static mesh scheme was used. The first method was directly mimicking the motion of the piston by deforming a group of cells. This requires re-meshing of the grid every time step. The deforming mesh scheme used in the study is illustrated in Figure 36.

A cell group (red coloured cells in Figure 36 (a)) is defined by the toposet utility in OpenFOAM to move with a moving boundary. The new positions of the cell nodes are calculated and re-meshed at each time step according to the prescribed motion equation for the moving boundary patches. While the grouped cells retain their original shape and size during the deformation, the first cells sharing the faces with the moving cell group are deformed depending on their relative locations about the motion as shown in Figure 36 (b). All the other cells remain unchanged. The final velocity field U_{flow} with the deforming mesh scheme is calculated by subtracting the grid velocity U_{grid} from its calculated velocity U to satisfy space conservation law (Demirzic and Peric, 1988).
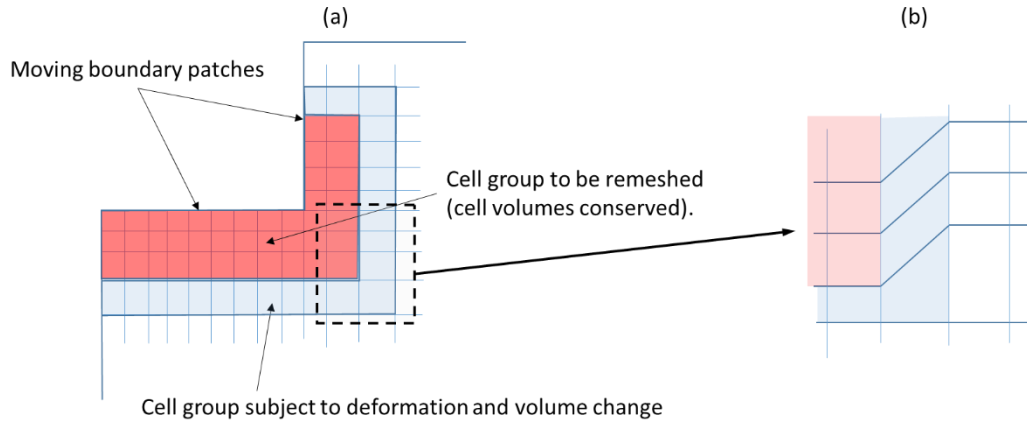
Figure 36 An illustration of the deforming mesh scheme. A moving boundary cells can be defined by an OpenFOAM utility 'toposet' (a). The cells defined in the process move at the same moving wall velocity of the moving boundary patches. Then their first neighbour cells are deformed accoding to the moving boundaries (b).

Hence, direct simulation of the motion by deforming mesh is not computationally cheap. A cheaper way is to impose sinusoidally oscillating velocity boundary condition at the boundary patches that move. In general, both are not expected to give differences in their simulation results. However, in some cases, e.g. flows in a narrow gap with a sinusoidally oscillating gap wall towards the opposite wall may be differently predicted from each other, if the oscillation amplitude is significantly large compared with the gap distance (Kim et al., 2016). For a realistic simulation, the motion of the ultrasonic horn tip was mimicked by this deforming mesh scheme in this study.

4.3.7   Solving equations

Once the discretised governing equations are linearised using appropriate numerical schemes, they can be written as a linear system of equations **Ax** = **b.** Here **A, x** and **b** represent coefficients depending on the fluid parameters or mesh discretisation, unknown physical properties to be solved and the boundary conditions respectively.

Various matrix solvers are provided in OpenFOAM, of which detailed descriptions can be found in Gerald and Wheatley (1985) or Saad (2003). Choice of them will affect the efficiency of solving the problems but does not have influence on the solution itself. Hence, there can be different preferences based on personal experience with the solvers for specific problems. Since it is beyond the purpose of this section to discuss or repeat full descriptions of them, only the matrix solving methods are named here that were used to solve the equations. The pressure was solved by Geometric Algebraic Multi-Grid solver (GAMG) preconditioned by

the Gauss-Seidel method. The density and the velocity field were solved by pre-conditioned bi-conjugate gradient (PBiCG) method with the diagonal incomplete LU (DILU) pre-conditioner. The turbulence model related properties were solved by smooth solver with Gauss-Seidel smoothing method.

4.3.8   Pressure-velocity coupling

In general the pressure and velocity are coupled to each other in solving the Navier-Stokes (NS) equations. Therefore, iterative methods are employed to solve this coupling. In OpenFOAM this is solved implicitly either by Pressure Implicit Splitting of Operators (PISO) (Issa, 1986) or PISO algorithm merged with SIMPLE (semi-implicit method for pressure linked equations, Patankar and Spalding (1972)) which is dubbed as PIMPLE in OpenFOAM (Holzmann, 2016). Initially PIMPLE had been utilised, but for better efficiency, PISO algorithm was preferred in this study from the work part of chapter 6.

4.4   Numerical schemes to model the transient flow problems

Cavitating flow problems have to deal with turbulent unsteady flows. Despite the recent huge performance leap in computing capacity, direct numerical simulation (DNS) can be applied only to low Reynolds number flows at small scales. Conventionally, the Reynolds averaged Navier-Stokes (RANS) approach has been favoured for its cheap computing cost with a 'reasonable' resolution. These days, as the problems for the engineers become more complex and the computing capability in hand increases, the large eddy simulation (LES) schemes are also getting attention from engineers. To take the advantage of LES in the flow resolution and to reduce the total computing cost, hybrid schemes (Detached Eddy Simulation) of RANS and LES are also being developed. DES switches the algorithm to LES where a flow region starts to separate. RANS and LES schemes are discussed in this section.

4.5   Reynolds Averaged Navier-Stokes (RANS) Equations

Not all but for many fluid dynamics engineering problems, only the mean motion of the fluid is interesting. Solving the fluctuating part will require finer spatial and temporal resolution with more calculation of matrix and memory space, but may not be so influential or informative for such engineering solutions. In such a case, it would be desirable to create a model only to resolve the significant mean motion part without making too much effort for the insignificant fluctuating part. RANS approach was the result of such a desire. The basic concept of RANS approach is to decompose any transient quantity ϕ into the time averaged

mean part $\bar{\varphi}$ and the remaining perturbation part φ'. This is called Reynolds decomposition, Eq. (4.16).

$$\varphi = \bar{\varphi} + \varphi' \qquad (4.16)$$

Important features of this decomposition are that (1) $\partial\bar{\varphi}/\partial t = 0$ and (2) $\overline{\varphi'} = 0$, where overbar means time average. Substituting Eq. (4.16) into Eqs. (4.3) and (4.4), the equations can be re-written as Eqs. (4.17a) and (4.17b).

$$\nabla \cdot (\bar{\rho}\overline{U}) = 0 \qquad (4.17a)$$

$$\frac{\partial(\bar{\rho}\overline{U})}{\partial t} + \nabla \cdot \bar{\rho}(\overline{U}\overline{U}) = -\nabla p + \mu_v T - \nabla \cdot \bar{\rho}(U'U') \qquad (4.17b)$$

The time derivatives of the product terms of the mean part and the fluctuating part become zero and the density fluctuation in time is neglected to derive the above equations. The last term of Eq. (4.17b) is Reynolds stress that cannot be directly resolved. This is modelled by a turbulence model, which will be discussed in section 4.8.

4.6   Large Eddy Simulation (LES) scheme

4.6.1   Overview

Large eddy simulation (LES) can compute the flow motion with a higher fidelity than RANS calculations since it resolves all the large eddies significant to a transient flow problem while modelling insignificant smaller eddies. The key ideas of LES scheme are that (1) only a few number of large scales are significant for many engineering problems and (2) the self similarity assumption of the smaller scales that are not significant to the resulting solutions.

For the first assumption, an appropriate mesh grid size ($\approx$ spatial filter size) needs to be determined to be approximately similar length scale as the smallest significant eddy size to a given problem. The separation of the (eddy length) scales is achieved by filtering the velocity field (Leonard, 1974).

Self similarity means that below a certain length scale the turbulence is assumed to become isotropic and similar to one another between the different length scales. Based on the assumption, the insignificant scales of eddies are modelled by a turbulence model.

While reasonable accuracy of URANS approach had been reported by Žnidarčič et al. (2015), Mottyll and Skoda (2015) and Rahimi et al. (2016) in resolving the acoustic cavity volume

and pressure peaks or the velocity of the acoustic stream, the works by the author as presented in chapters 6 and 7 relied on the LES approach. According to the author's experiment as discussed in chapter 3, this LES approach might not have been necessary to simulate acoustic cavitation, but during the study of the numerical modelling of acoustic cavitation, LES was expected to provide a higher fidelity of physics.

In the author's experiment, the acoustic pressure impact signals could be identified by either the conventional Fast Fourier Transform (FFT) or Welch's method. The author interpreted this analysis process as an implication of a statistical periodicity of the sub-harmonic oscillation phenomenon. Therefore, URANS could be reasonably applied to capture such statistical characteristics in the averaged sense. However, while the study was undertaken, LES was expected to simulate acoustic cavitation with a higher fidelity than the URANS approach as believed in general.

4.6.2 Spatial filtering of Navier-Stokes equations

To construct a spatial low pass filter, the space is mapped to a space based on wave number k = $2\pi/(2\Delta)$ where Δ is the filter width. The filter width is equal to or greater than the grid spacing of a calculation domain. The maximum resolvable wave number is attained with the minimum grid spacing size and 2Δ corresponds to the smallest resolvable turbulence eddies. All the higher harmonics beyond this wave number are not directly resolved and require a turbulence model to close the problem. The filtering operation is carried out by convolving any dummy quantity $\varphi(x,t)$ with a box filter kernel $G(x)$ in Fourier space as Eq. (4.18).

$$\bar{\varphi}(x,t) = \int_{-\infty}^{\infty} G(s)\varphi(x-s,t)ds$$

$$G(x) \equiv \begin{cases} \dfrac{1}{\Delta}, & |x| \le \dfrac{\Delta}{2} \\ 0, & |x| > \dfrac{\Delta}{2} \end{cases}$$

(4.18)

In OpenFOAM the filtering is operated implicitly by the box filter. The filter width is often calculated as $\Delta = \sqrt[3]{\Delta_x \cdot \Delta_y \cdot \Delta_z}$; Δ_x, Δ_y and Δ_z are the grid length in subscripted spatial directions.

To complete the LES filtering operation, there is another obstacle to be resolved for compressible flows. Unlike Reynolds averaging, the filtered product of two variables is not always the same as the product of each filtered variable. Thus, in construction of filtered

governing equations for compressible flow problems, Favre density weighted averaging (Favre, 1983) is commonly applied as Eq. (4.19).

$$\overline{\rho\varphi} = \bar{\rho}\tilde{\varphi} \qquad (4.19)$$

where φ represents for any physical quantity and overbar denotes the LES filtering operation and the tilde represents Favre filtering.

Finally, the LES filtred Navier-Stokes equations are written as Eqs. (4.20a) and (4.20b). In this study, to close the equations, the density and pressure are linked together via a barotropic equation of state as Eq. (4.20c).

$$\frac{\partial\bar{\rho}}{\partial t} + \nabla \cdot (\bar{\rho}\tilde{\boldsymbol{U}}) = 0 \qquad (4.20a)$$

$$\frac{\partial(\bar{\rho}\tilde{\boldsymbol{U}})}{\partial t} + \nabla \cdot (\bar{\rho}\tilde{\boldsymbol{U}}\tilde{\boldsymbol{U}}) = -\nabla\bar{p} + \nabla \cdot (\mu_{eff}\nabla\overline{\boldsymbol{U}}) - \nabla \cdot [\bar{\rho}(\widetilde{\boldsymbol{U}\boldsymbol{U}} - \tilde{\boldsymbol{U}}\tilde{\boldsymbol{U}})] \qquad (4.20b)$$

$$\mu_{eff} = \mu_v + \mu_t$$

$$\frac{d\rho}{dp} = \frac{1}{c^2} = \Psi \quad \Leftrightarrow \quad \rho = \Psi \cdot p + C \qquad (4.20c)$$

The last term on the right hand side of Eq. (4.20b) cannot be directly solved due to the difficulty of treating $\widetilde{\boldsymbol{U}\boldsymbol{U}}$. This unresolvable part is called sub-grid scale (SGS) Reynolds stress and is modelled by an appropriate turbulence model likewise RANS simulation. The SGS Reynolds stress may include an additional error from the numerical diffusion of the grid, which is difficult to separate from other numerical errors, especially with many LES models in which the spatial filtering is achieved in implicit way as described here; the filtering is automatically achieved in the process of volume averaging of FVM method. This is called Implicit LES (ILES) and all the LES schemes in OpenFOAM are ILES. Indeed, most of the studies of LES are about this turbulence modelling matter. Ferziger and Peric (2002) provides a concise summary of the development of such turbulence models. A digest of it is provided in section 4.8.

4.6.3　　　Boundary treatment

A critical issue in LES simulation with the acoustic pressure waves in a very confined domain is to avoid pressure waves reflected back from the walls into the calculation domain. To avoid this, one of the following treatment may be performed; (1) using a large domain with cell

stretching to damp out the pressure waves in the direct proximity of the calculation domain, (2) applying a non-reflecting boundary condition on the wall boundaries or (3) applying a convective boundary condition on the outlet boundary.

There is no non-reflecting boundary condition provided in OpenFOAM (v.3.0.1) in a rigorous sense. However, a simplified version of such a boundary condition is provided under the OpenFOAM terms of 'waveTransmissive' boundary condition. Indeed, this is a linear wave equation for a wave propagating at a speed of $\sqrt{\kappa/\Psi} + U_f$, where κ is specific heat ratio, Ψ compressibility of fluid ($d\rho/dp$) and U_f the face normal flow velocity flux at the boundary. Physically it means the quantity is convected at a speed of sound in the liquid medium and the fluid velocity, which becomes zero in case of backflow. Therefore, this condition could be applied for pressure boundary condition at the walls to suppress the reflecting pressure waves. Convective boundary condition is similar as the 'waveTransmissive' boundary condition except it considers only the face normal flux of the quantity on which the boundary condition imposed. In the middle of studies to settle the numerical model, those boundary conditions were tried to manage the excessive pressure wave reflection at the wall and outlet boundaries. Finally, these boundary conditions were replaced with a common no slip wall boundary and a fixed mean pressure boundary at the outlet since it was found the excessive pressure reflection had been caused mainly by the density getting unphysical due to the unboundedness of the mass convection scheme.

4.7   The Turbulence modelling

4.7.1   Law of the wall

For a fully developed turbulent channel flow, by introducing several assumptions of (1) a constatant total shear stress which is equal to the wall shear stress, (2) neglecting convection of the shear stress and (3) negligible shear stress by viscosity compared with turbulent viscosity, the Reynolds stress term can be approximated as Eq. (4.21).

$$-\overline{u_i' u_j'} \approx \frac{\tau_w}{\rho} \tag{4.21}$$

where τ_w is the wall shear stress and ρ density of fluid and define a velocity scale called 'friction velocity' (u_τ) so that the wall shear stress τ_w could be expressed in a similar form of kinetic energy per unit mass. That is;

$$\tau_w \equiv \rho u_\tau{}^2 \tag{4.22}$$

Now writing the Reynolds stress term in terms of the mixing length scale,

$$-\overline{u_i'u_j'} = \left(\kappa y \cdot \frac{du}{dy}\right)^2 = u_\tau{}^2 \tag{4.23}$$

$$\Longrightarrow \quad \frac{u}{u_\tau} = \frac{1}{\kappa}ln(y) + C \; [C: empirical\ constant] \tag{4.24}$$

$$u^+ = \frac{1}{\kappa}ln(y^+) + C^+ \tag{4.25}$$

This logarithmic relation between the flow velocity and the wall distance for a fully developed turbulent flow is called the law of the wall. From this relation, two non-dimensionalised scales of u^+ ($\equiv u/u_\tau$) and y^+ ($\equiv y/\eta_K = yu_\tau/v$) are derived which have the following relationship each other.

Experimentally, since the viscosity becomes comparable with the inertia within a very small distance from the wall such as in the viscous sub-layer, the validity of this law is said to hold for roughly in the range of $30 < y^+ < 130$, which is called logarithmic region.

4.7.2   Standard *k-ε* turbulence model

The turbulence modelling is a big branch of CFD research and beyond the scope of this thesis work. Only brief conceptual explanations and the final forms of several selected turbulence models that are useful to describe the work done in this study will be presented here as implemented in OpenFOAM suite.

To close the governing equations for the physical problems in which the turbulence is involved, almost all the engineering problems, Reynolds stress, or SGS Reynolds stress, must be modelled by an appropriate turbulence model. The most commonly used turbulence models are eddy viscosity models (Bredberg, 2001). The models are constructed on the ground of the Boussinesq hypothesis (Boussinesq, 1877) and Prandtl's mixing length model (Prandtl, 1925).

The two-equation models prescribe the turbulent kinetic energy (*k*) and the second quantity related to the dissipation (*ε*) of the kinetic energy via eddy visocity. The most well known two-equation models are *k-ε* models by Launder and Spalding (1972), (1974) and *k-ω* model by Wilcox and Rubesin (1980). *k-ω* SST model was developed later by Menter (1993) as a hybrid of the two models. All the two-equation eddy viscosity models are different from each other in how the dissipation of the turbulent kinetic energy dissipation is modelled. Therefore, all of

them have a transformation of the dissipation (ε) and the standard k-ε model forms the basis of those two-equation models.

The turbulent kinetic energy is expressed as the magnitude of normal stress components of the Reynolds stress term. The shear stress is assumed to increase as the normal stress increases. Therefore, it appears reasonable to relate the turbulent kinetic energy to determine eddy viscosity.

$$k = \frac{1}{2}\overline{u_i'u_i'} \qquad (4.26)$$

So the first equation to prescribe the turbulence becomes the transport equation of the turbulent kinetic energy k as Eq. (4.27) (Launder and Spalding, 1972, 1974).

$$\frac{Dk}{Dt} = \frac{1}{\rho}\frac{\partial}{\partial x_k}\left[\frac{\mu_t}{\sigma_k}\frac{\partial k}{\partial x_k}\right] + \frac{\mu_t}{\rho}\left(\frac{\partial U_i}{\partial x_k} + \frac{\partial U_k}{\partial x_i}\right)\frac{\partial U_i}{\partial x_k} - \varepsilon \qquad (4.27a)$$

The dissipation (ε) is chosen for the second quantity to prescribe the turbulence. The relation of k and ε with the eddy viscosity is the result of dimensional analysis as per Prandtl's mixing length scale. The relation is expressed as Eq. (4.27b):

$$\nu_t \sim \frac{k^2}{\varepsilon} \quad \Longrightarrow \quad \nu_t = C_\mu \frac{k^2}{\varepsilon} \qquad (4.27b)$$

The dissipation (ε) transport equation is written as Eq. (4.27c).

$$\frac{D\varepsilon}{Dt} = \frac{1}{\rho}\frac{\partial}{\partial x_k}\left[\frac{\mu_t}{\sigma_\varepsilon}\frac{\partial \varepsilon}{\partial x_k}\right] + C_1 \frac{\mu_t}{\rho}\frac{\varepsilon}{k}\left(\frac{\partial U_i}{\partial x_k} + \frac{\partial U_k}{\partial x_i}\right)\frac{\partial U_i}{\partial x_k} - C_2 \frac{\varepsilon^2}{k} \qquad (4.27c)$$

where the coefficients are determined as in Table 9. The limitation of the model is that the predicted eddy viscosity was similar with the experiment only for the fully developed turbulent flows. Therefore, this turbulence model has its weakness in predicting the near-wall flows such as the adverse wake flows. To compensate this problem, a damping function is introduced to the original model.

Table 9 Coefficients of k-ε model as used in OpenFOAM.

C_μ	C_1	C_2	σ_k	σ_ε
0.09	1.44	1.92	1.00	1.30

4.7.3 Standard *k-ω* and *k-ω* SST turbulence model

Standard k-ω model was developed by Wilcox and Rubesin (1980). The model considers the turbulence kinetic energy (k) and the 'turbulence frequency' or 'specific turbulent dissipation rate' (ω) to prescribe the turbulence model. The new quantity ω is defined as Eq. (4.28).

$$\varepsilon = \beta^* k \omega \tag{4.28}$$

where β^* is a coefficient to account for the eddy viscosity. It was the same as C_μ of the *k-ε* models and the same value of 0.09 was suggested originally. Later, the coefficient was modified as Eq. (4.29) in the *k-ω* SST model for different flow regimes.

$$\beta^* = \begin{cases} 0.09, & for\ high\ R_n\ flows \\ 0.09\dfrac{5/18 + (R_t/8)^4}{1 + (R_t/8)^4}, & for\ low\ R_n\ flows \end{cases} \tag{4.29}$$

where R_t is the relative turbulent viscosity over the kinematic viscosity of a fluid.

The model could describe better the fluid behaviour in the near-wall (logarithmic) region than the *k-ε* models. But, due to strong dependency of the original model on ω value of the free stream, the flow prediction in the free stream suffered. To overcome such a limitation, Menter (1993) brought up two modified models; so called the 'baseline' model and the SST (Shear Stress Transport) model. The baseline model combined the standard *k-ε* model into the form of *k-ω* model via the relation between ε and ω. Hence, in the near-wall region it employed the *k-ω* model and near the edge of the boundary layer it switched to the *k-ε* model. The SST model introduced the effect of the principal turbulent shear-stress transport based on the Bradshaw assumption (Huang and Bradshaw, 1995), which contributed a success of Johnson and King (1985) turbulence model, on top of the baseline model. The Bradshaw assumption is that the shear stress in a boundary layer is proportional to the turbulent kinetic energy *k*.

Bradshaw's assumption:
$$\tau = \rho a_1 k \tag{4.30}$$

For conventional two-equation turbulence models, the shear stress τ can be written as Eq. (4.31).

$$\tau = \mu_t \Omega = \rho \sqrt{\left[\frac{(Production)}{(Dissipation)}\right]_k} a_1 k, \qquad \Omega \equiv \frac{\partial U_i}{\partial x_j} \tag{4.31}$$

In the case of a strong adverse wake flow region, because the ratio of production/dissipation terms for the turbulent kinetic energy *k* would become much larger than unity in such a region, this situation must be avoided to prevent the eddy viscosity from being overestimated for such flows. Therefore, the constitutional relation of the eddy viscosity with *k* and *ω* was modified in SST model as Eq. (4.32) to ensure this. Figure 37 shows such modification made by SST model. This modification is reported largely improves the accuracy of the turbulence model in overall (Woelke, 2007).

$$\nu_t = \frac{a_1 k}{max(a_1 \omega, \Omega)} \ (a_1 = 0.31) \tag{4.32}$$
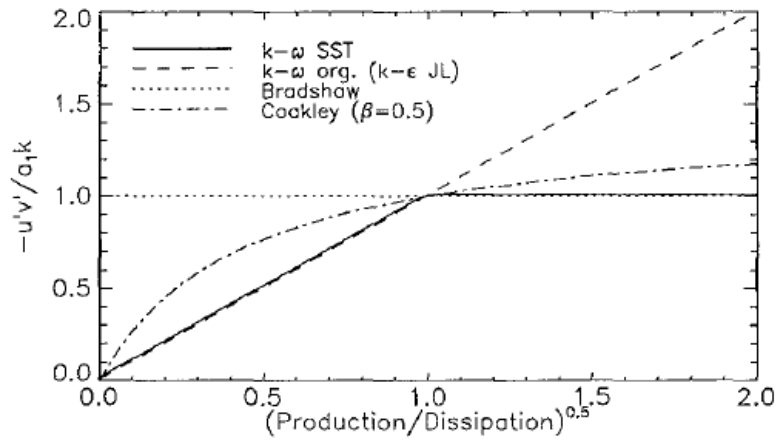
Figure 37 Relation between Reynolds stress divided by turbulent kinetic energy vs production over destruction of the kinetic energy (Woelke, 2007).

In OpenFOAM a variety of wall functions are provided. In this study, the 'kqR' wall function was given for the turbulent kinetic energy at the walls. Zero gradient condition was given for the other boundaries. The eddy viscosity at the walls was prescribed by 'nutUSpalding' wall function that automatically calculates the eddy viscosity for high and low Reynolds number (R_n) regions. The wall functions in OpenFOAM suite are tabulated in Table 10.

.

Table 10 Available wall functions in OpenFOAM (v.3.0.1)

Type of wall functions	Sub-category	Description
ε wall functions	epsilon wall function	High R_n mode only.
	epsilonLowRe wall function	High and low R_n modes are switched by y^+.
k wall functions	kqR wall function	High R_n mode only. $\nabla k = 0$.
	kLowRe wall function	High and low R_n modes are switched by y^+.
ν_t wall functions	nutLowRe wall function	Low R_n mode only. $\nu_t = 0$.
	nutk wall function	High and low R_n modes are switched by y^+. The first cell centre should be in the logarithmic region. y^+ is determined based on k.
	nutU wall function	Works the same as nutk wall function but determines y^+ based on U.
	nutUSpalding wall function	$$\nu_t = \frac{u_\tau^2}{\partial u/\partial n} - \nu$$ y^+-u^+ is approximated to follow law of the wall.
ω wall function	-	k-ω SST model (Menter, 1993)
$\overline{v^2}$ wall function	-	$\overline{v^2} - f$ turbulence model (Durbin, 1995).
f wall function	-	

4.7.4 Smagorinsky-Lilly model

Smagorinsky (1963) brought the first idea of the LES turbulence model (Smagorinsky model) from the analogy of eddy viscosity model of RANS approach. By dimensional analysis, a formula for the turbulent eddy viscosity is obtained as Eq. (4.33).

$$\mu_t = C_s^2 \rho \Delta^2 |\bar{S}| \qquad (4.33)$$

C_s (Smagorinsky coefficient) was initially proposed as a constant model parameter (≈ 0.16), but later learned it would vary depending on the flows. The coefficient value tended to be too high for the near-wall region where the isotropic assumption did not hold so well. To address this limitation, the model parameter is often modified by van Driest damping function (Ferziger and Peric, 2002).

An alternative SGS model was developed. The scale-similarity model (Bardina et al., 1980) assumes the smallest resolved scale and the largest unresolved scale would be similar each other. The yielded model obtains the turbulent stress tensor by re-filtering of $\widetilde{UU} - \widetilde{U}\widetilde{U}$. This model was quite successful in correlating with the actual SGS Reynolds stress, however, it did not dissipate almost any turbulent kinetic energy. Therefore, hybrid models of the above stated turbulence models were sought (Ferziger and Peric, 2002).

4.7.5 Dynamic models

Germano et al. (1991) developed the 'dynamic model' procedure expanding the concept of similarity assumption. The idea was that an identical SGS model with the same model parameter would hold for both LES done with fine and coarser filters. Any SGS model could be adopted for this model. Due to this fact, it is often understood as rather a dynamic modelling procedure. The SGS model parameter can be calculated as the ratio of two quantities from both LES done with different length scales. A detailed procedural overview can be found in Chai and Mahesh (2010). This dynamic procedure with Smagorinsky model significantly eased the most critical difficulty of LES with the model parameter change in the near-wall region automatically. The side effect was that the model parameter through the procedure was a rapidly varying function in space and time taking large values of both signs. Despite the suggestion of physical interpretation of the negative eddy viscosity as energy feed from small scale to larger scale (called "backscatter"), the long presiding negative eddy viscosity resulted in numerical instability. Cures for this are either by clipping of the negative eddy viscosity or by spatial and/or temporal averaging of the negative eddy viscosity.

4.7.6   *k*-equation model

The other well-known LES turbulence model is the *k*-equation turbulence model (Yoshizawa, 1982, Yoshizawa and Horiuti, 1985). The model also assumes the distinct separation of scales and adopts statistical representation of turbulence based on direct interaction approximation (DIA) of multiple scales of turbulence (Kraichnan, 1964). The model could describe the turbulence kinetic energy more accurately than Smagorinsky model and proved Smagorinsky model or RANS $k - \varepsilon$ model derived as its special cases. A useful outcome of the analysis was that the eddy viscosity ν_t and the dissipation rate ε could be expressed in terms of turbulent kinetic energy k. Therefore, to close the problem, one needs to solve the energy equation for the turbulent kinetic energy k only; the temporal change of the turbulent kinetic energy must be balanced with the production and diffusion (advection of the smaller scales by larger scale) of it plus dissipation of it. Hence, this model is called as *k*-equation model.

$$\frac{Dk}{Dt} = \nu_t \frac{\partial \widetilde{U}_i}{\partial x_j} \left(\frac{\partial \widetilde{U}_i}{\partial x_j} + \frac{\partial \widetilde{U}_j}{\partial x_i} \right) - \varepsilon \qquad (4.34a)$$

$$\nu_t = 0.0066 \Delta k^{\frac{1}{2}}$$
$$\varepsilon = 1.9 k^{3/2} / \Delta \qquad (4.34b)$$

In addition to the above mentioned LES models, there are several models available in the OpenFOAM (v.3.0.1) package such as Deardorff's differential stress model (Deardorff, 1973), Wall-adapting Local Eddy (WALE) viscosity model based on the squared flow velocity gradient (Franck and Ducros, 1999) or Spalart-Allmaras DES variants based on its RANS version (Spalart and Jou, 1997). Available LES turbulence models in OpenFOAM (v.3.0.1) are tabulated in Table 11.

Table 11 LES turbulence models in OpenFOAM (v.3.0.1)

Keyword	Description
Smagorinsky	Smagorinsky-Lilly model (Lilly, 1992)
kEqn	k-equation eddy-viscosity model (Yoshizawa, 1982)
dynamicKEqn	dynamic k-equation eddy-viscosity model (Chai and Mahesh, 2010)
DeardorffDiffStress	Deardorff differential SGS stress model (Deardorff, 1973)
SpalartAllmarasDDES SpalartAllmarasDES SpalartAllmarasIDDES	Spalart-Allmaras one equation mixing-length model (Spalart et al., 2006)
WALE	Wall-adapting local eddy viscosity model (Franck and Ducros, 1999)
dynamicLagrangian	Dynamic eddy-viscosity model with Lagrangian averaging for incompressible flow (Meneveau et al., 1996)

4.8   Modelling multiphase flow problems

The cavitating flow or multiphase flow models can be largely categorized in three groups of (1) discrete bubble models in Lagrangian approach, (2) homogeneous equilibrium mixture models and (3) two-fluid models like Euler-Eulerian, Euler-Lagrangian approaches (Figure 38). Yakubov et al. (2015) provides a good summary on possible cavitating flow models.

The Lagrangian methods directly track individual bubbles in a flow and calculate response of the bubbles and resulting pressure pulses using bubble motion equations like R-P equation. Bubble-bubble or bubble-flow interactions are iterated with the updated pressure-velocity fields. Although such models can accurately describe a bubble motion and its resulting pressure pulses, it requires a huge computational cost, hence impractical to apply for practical scale of problems, e.g. solving cavitation problems for hydro-/turbo-machinery.

To overcome such a limitation, a homogeneous mixture model approach was developed. In this Eulerian approach, the cavitating flow is treated as a homogeneously dispersed mixture of two Eulerian phases based on the VOF (Volume of Fluid) scheme.
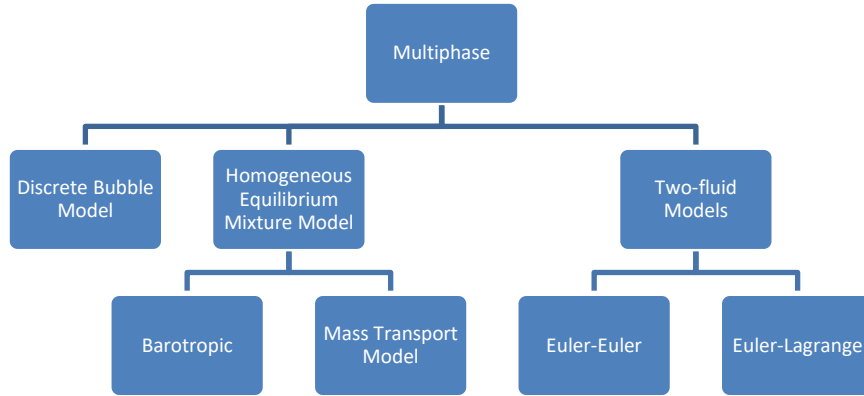
Figure 38 Category of multiphase flow solvers.

Assuming a constant bubble population density, the vapour volume fraction in a cell volume is conveyed to the bubble collapse pressure waves via a simplified R-P equation. This method gives highly cost-effective and accurate solutions to many practical engineering problems of large scale in which the influence of surface tension, viscosity effect or inertial force of bubble can be safely ignored.

Finally, the Eulerian-Lagrangian approach was developed to take advantages of both the approaches. In this approach, switching between the modes occur via a preset threshold vapour volume fraction. A larger volume of vapour structure is treated in Eulerian approach and once the VOF in a cell becomes smaller than the threshold, the vapour structure is tracked in Lagrangian way. Therefore, it is viable to obtain solutions that is more accurate than Eulerian methods for various scales of problems at cheaper computational cost than pure Lagrangian models. An example of this approach is shown in Figure 39. The simulations in the figure modelled only the half of the foil from its centre as marked by a red dash line in (a). Evidently, Homogeneous Equilibrium Mixture based model (b) could not show the small bubble clouds
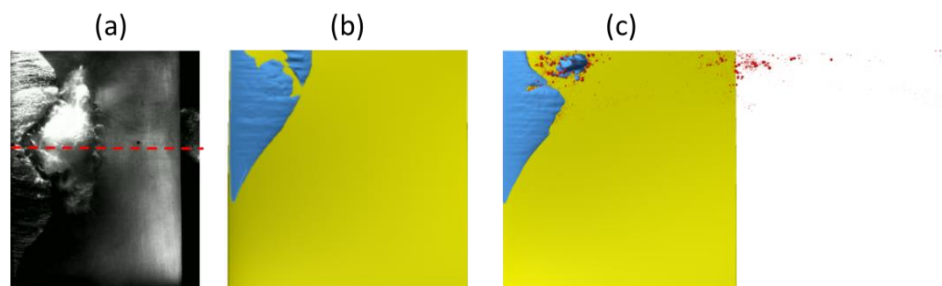
Figure 39 An illustration of cavitation simulation result with Delft Twist 11 foil from an Eulerian-Lagrangian model: experiment (a), Homogeneous Equilibirum Model with mass transport cavitation model (b), and Eulerian-Lagrangian model. The cyan coloured iso-surfaces represent the vapour volume by Eulerian model, and the red dots represent bubbles switched to the Lagrangean model (c) (after Lidtke et al. (2016)).

as predicted by the Eulerian-Lagrangian model (c). The cavity from Eulerian VOF model is shown as blue iso-surface ($\alpha = 0.5$) in both (b) and (c), and the Lagrangian cavity bubbles are shown as red spheres with appropriate instantaneous bubble radii representation.

4.8.1 Homogeneous equilibrium mixture models: mass transport models

The cavitating flow is treated as a homogeneous mixture of two different phases whose volume or mass fractions are transported to each other satisfying the continuity equation. Since the vapour volume fraction can grow and be outside the original cell where it was, the continuity equation for a cell volume does not always become zero but has source (evaporation rate) and sink (condensation) terms. Almost all of the cavitating flow models in this category employ this modified VOF scheme for their computational efficiency and robustness.

As this introduces a new unknown of the volume fraction, one additional relation is required to close the system of equations. Two types of methods are often used, i.e. vapour volume or mass transport model (simply 'mass transport model' herein after) or an isenthalpic model can be used to determine volume fractions of either phases. For the case of the mass transport model, the two fluids are assumed Newtonian and thus the mixture density is defined as a linear sum of each phase density in proportion with their volume fraction. Combining this relation into the continuity equation in non-conservative form provides a relation between the phase volume fractions and the phase velocity. The phase velocity is again combined with a linearised R-P equation to give bubble size in a vapour structure and pressure from it. With isentropic, isenthalpic or barotropic models, which adopt a certain gas state equation to relate vapour/gas phase density and pressure, the condensation and evaporation are assumed to occur only at the interface either instantly through the whole phase volume or partially depending on their assumptions. The vapour volume fraction is directly computed from the local pressure by the specific equation of state for the gas phase.

Mass transport models focus on prediction of large-scale behaviour of cavitation like sheet cavity or cavitating vortices. Therefore, the models are used for prediction of cavitation on the marine propellers, rudders and so on. The bubble dynamics equation is incorporated into the phase-change model or the two-phase volume of fraction model to provide the rates of evaporation and condensation by solving a simplified Rayleigh equation, say, the effects of surface tension, viscosity or inertial acceleration terms are typically ignored. These models are reported to be useful for modelling hydrodynamic cavitation problems (Asnaghi, 2013, Asnaghi et al., 2015, Žnidarčič et al., 2015).

Therefore, the models solve the following equations with only the difference in how to deal the vapour production and destruction rates in principle. The vapour production rates of several common cavitation models are tabulated in Table 12.

$$\text{Momentum equation:} \qquad R\ddot{R} + \frac{3}{2}\dot{R}^2 + \frac{p_\infty - p_{sat}}{\rho_L} = 0 \qquad\qquad (4.35)$$

$$\text{Mass transport equation:} \quad \frac{\partial}{\partial t}(\alpha\rho_V) + \nabla \cdot (\alpha\rho_V \boldsymbol{U}) = S_{prod.} - S_{dest.} = S_{net} \qquad (4.36)$$

Table 12 Vapour transport models of several cavitation models of common use.

Models	Source & sink terms
Zwart et al. (2004)	$S_{prod.} = C_{prod.}\dfrac{3\alpha_{nuc}\rho_V(1-\alpha)}{R}\sqrt{\dfrac{2}{3}\dfrac{\lvert(p_\infty - p_{sat})\rvert}{\rho_L}}$ $S_{dest.} = C_{dest.}\dfrac{3\alpha_{nuc}\rho_V\alpha}{R}\sqrt{\dfrac{2}{3}\dfrac{\lvert(p_\infty - p_{sat})\rvert}{\rho_L}}$
Singhal et al. (2002)	$S_{prod.} = C_{prod.}\dfrac{\sqrt{k}}{\sigma_c}\rho_V\rho_L\sqrt{\dfrac{2}{3}\dfrac{\lvert(p_\infty - p_{sat})\rvert}{\rho_L}}(1 - \gamma_V - \gamma_G)$ $S_{dest.} = C_{dest.}\dfrac{\sqrt{k}}{\sigma_c}\rho_V\rho_L\sqrt{\dfrac{2}{3}\dfrac{\lvert(p_\infty - p_{sat})\rvert}{\rho_L}}\gamma_V$
Sauer and Schnerr (2001)	$S_{net} = \dfrac{\rho_L\rho_V}{\rho}\dfrac{3\alpha(1-\alpha)}{R}\sqrt{\dfrac{2}{3}\dfrac{\lvert(p_\infty - p_{sat})\rvert}{\rho_L}}$

As an illustration of the models, an explanation on Schnerr-Sauer model (Sauer and Schnerr, 2001) is briefly given as follows. The following assumptions are made:

(1) Cavitation can be modelled as growth and collapse process of vapour bubbles.

(2) The nuclei, from which bubbles originate, pre-exist in the liquid and conserved.

(3) The slip between the bubbles and the liquid is negligible.

(4) Cavitation is dominated by heterogeneous nucleation; condensing flow is not modelled.

(5) The bubbles are always regarded as spherically symmetric.
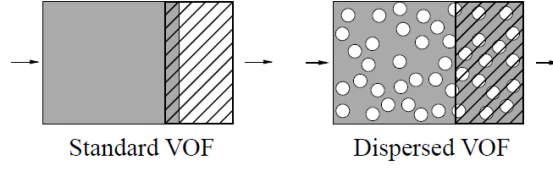
Figure 40 An illustration of the standard VOF (left) and the modified homogeneously dispersed VOF model (right) (after Schnerr and Sauer, 2001). The modified VOF model has the disperse phase homogeneously distributed within the control volume, whereas the standard VOF approach has two continuous phases separated by a distinct single interface based on the VOF ratio within the control volume.

Numerical modelling is based on the homogeneously dispersed VOF (Volume of Fraction) method. While the standard VOF method assumes two distinct phases in a control volume, this model assumes one phase is homogenously distributed in a discretized form in the control volume, otherwise the control volume is filled with the other phase (See Figure 40). Thus, it is commonly called as Homogeneous Equilibrium Mixture (HEM) model.

In the model, the volume fraction α of the vapour phase is defined as the ratio of vapour volume V_G over the cell volume V that contains the vapours, Eq. (4.37).

$$\alpha \equiv \frac{V_G}{V} = \frac{V_G}{V_G + V_L} \tag{4.37}$$

Let us consider the total number (N_b) of bubbles with radius R_b in the cell volume V and the bubble density (n_0) per unit volume of liquid. Then volume of the vapour phase (V_V) can be written as Eq. (4.38).

$$V_G = N_b \times \frac{4}{3}\pi R^3 = (n_0 V_L) \times \frac{4}{3}\pi R^3 \tag{4.38}$$

Substituting Eq. (4.38) into Eq. (4.37), the vapour volume fraction can be re-written as Eq. (4.39).

$$\alpha = \frac{(n_0 V_L) \times \frac{4}{3}\pi R^3}{(n_0 V_L) \times \frac{4}{3}\pi R^3 + V_L} = \frac{\frac{4}{3}\pi n_0 R^3}{1 + \frac{4}{3}\pi n_0 R^3} \tag{4.39}$$

The governing equations are the continuity equation Eq. (4.40) and the constitutive relation for the density and dynamic viscosity of the homogeneous mixture Eq. (4.41), where φ, φ_V and φ_L are dummy variables representing either the density or the dynamic viscosity of the mixture, the vapour and the liquid phases respectively.

$$\nabla \cdot u = -\frac{1}{\rho}\frac{d\rho}{dt} \tag{4.40}$$

$$\varphi = \alpha\varphi_V + (1-\alpha)\varphi_L \tag{4.41}$$

Differentiating Eq. (4.41) for the time t, one obtains the following Eq. (4.42).

$$\frac{d\rho}{dt} = \frac{d}{dt}[\alpha\rho_V + (1-\alpha)\rho_L] = (\rho_V - \rho_L)\frac{d\alpha}{dt} \tag{4.42}$$

Substituting Eq. (4.42) into Eq. (4.40), the continuity equation is re-written as Eq. (4.43) in terms of vapour volume fraction. The vapour volume fraction is found by Eq. (4.39).

$$\nabla \cdot u = -\frac{\rho_V - \rho_L}{\alpha\rho_V + (1-\alpha)\rho_L}\frac{d\alpha}{dt} \tag{4.43}$$

$$\frac{D\alpha}{Dt} = \frac{n_0}{1 + \frac{4}{3}\pi n_0 R^3}\frac{d}{dt}\left(\frac{4}{3}\pi R^3\right)$$

$$= \frac{n_0}{1 + \frac{4}{3}\pi n_0 R^3}(4\pi R^2)\dot{R} \tag{4.44}$$

Now if the net vapour production rate S_{net} is known, this will be the same as $\frac{D\alpha}{Dt}$. The bubble growth/collapse rate $\dot{R}$ can be approximated as Eq. (4.45) by solving the Rayleigh equation Eq. (4.35) neglecting the non-linear inertial acceleration term $R\ddot{R}$.

$$\dot{R} = \sqrt{\frac{2(p_\infty - p_{sat})}{3\rho}} \tag{4.45}$$

Since these types of models do not take account for the behaviour of individual bubbles, it is more cost-effective than directly solving for discrete bubbles at some cost of accuracy and physics of higher order e.g. bubble/bubble bubble/flow interactions. In spite of such a disadvantage, these types of cavitation models are widely used in practical engineering for study of cavitation behaviour on marine appendages or ship propellers.

4.8.2 Barotropic Cavitation Models

Barotropic cavitation models have a commonality with the mass transport models in that they employ homogeneous equilibrium mixture model based on the volume of fraction scheme. However, the phase change is driven by physical relations between the physical properties of

fluids via equations of state. Because these models assume the fluid density is a function of the pressure only and this is how the models determine the vapour volume fraction, they are called barotropic cavitation models. As the temperature is assumed not to change during the process of vapour growth/collapse, these models are also called isenthalpic or isentropic cavitation models.

Unlike the mass transport models, these models consider compressibility of fluids. Therefore, this sort of model has strength in describing acoustic pressure wave propagation through a medium and it requires much finer time resolution to get a stable solution; the acoustic CFL number cannot go too high, especially if the acoustic pressure wave propagation is important for the physical model of interest.

To derive the barotropic cavitation model, the pressure and velocity of each phase are assumed the same as those of the other phase. Depending on the assumptions, the thermal equilibrium can be assumed to occur instantaneously through the whole medium or only in part. Assuming the dispersed phase is very small and homogeneously distributed in a cell volume, the instantaneous thermal equilibrium assumption can be thought valid.

There are several models to describe the mixture density. The approaches taken by Delannoy (1990) or Koop (2008) employed a smooth continuous function to approximate the barotropic relation between the pressure and density and to provide a smooth transition of the mixture density between the two phases. The formulation is shown below in Eq. (4.46). Koop used the hyperbolic tangent function instead of the sine function. (Meijn, 2015).
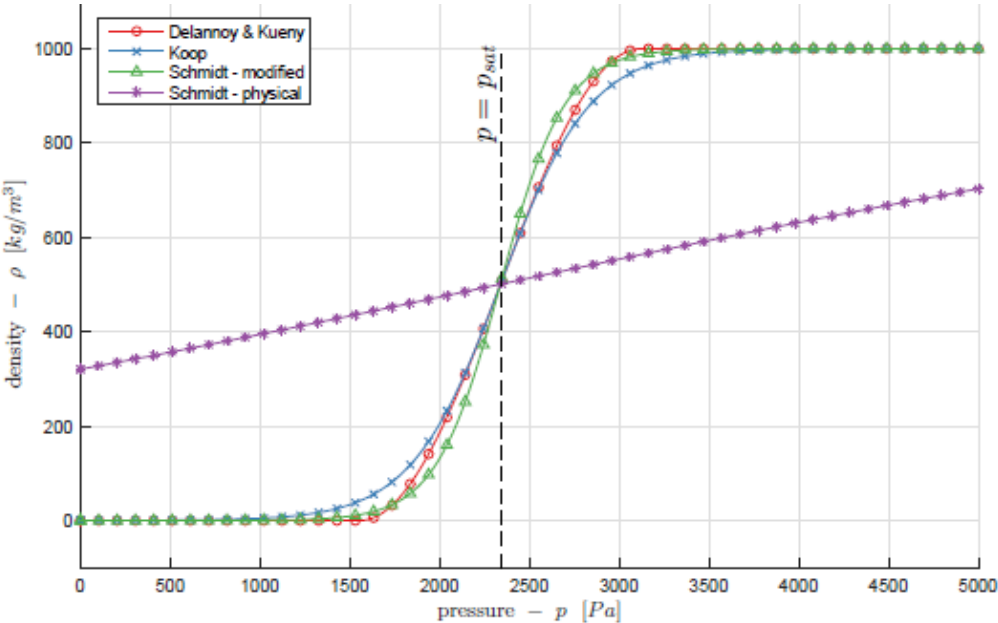
Figure 41 Pressure-density relation represented by various barotropic models. (Meijn, 2015, p. 20.)

96

$$\text{Delannoy (1990):} \quad \rho = \frac{\rho_L + \rho_V}{2} + \frac{\rho_L - \rho_V}{2} \sin\left(\frac{1}{c_{min}^2} \cdot \frac{p - p_{sat}}{(\rho_L - \rho_V)/2}\right) \tag{4.46}$$

As seen in Figure 41, the weak spot of such models by Delannoy & Kueny or by Koop was the physical relation between the pressure and the density is correct only near the vapour saturation pressure.

More physically linked barotropic cavitation model was suggested by Schmidt (1997). He adopted the Wallis model (Wallis, 1969) to model more physically meaningful barotropic relation instead of the arbitrary smooth functions. 'cavitatingFOAM' in OpenFOAM suite adopts his approach with provision of several different barotropic compressibility models such as linear, Wallis (1969) or Chung et al. (2001).

The cavitatingFOAM solver treats the liquid and the vapour as a homogeneous equilibrium mixture of the two compressible viscous fluid phases. The compressibility (ψ) of each phase is treated as a constant and related to the speed of sound (c) in the phase as Eq. (4.47).

$$\text{Compressibility:} \quad \Psi = \frac{d\rho}{dp} = \frac{1}{c^2} \tag{4.47}$$

The compressibility of the phase mixture is calculated differently depending on the individual barotropic compressibility models as named above. Their expressions are as Eqs. (4.48a) and (4.48b).

$$\textit{Linear model:} \quad \Psi = \alpha\Psi_V + (1 - \alpha)\Psi_L \tag{4.48a}$$

$$\textit{Wallis model:} \quad \frac{\Psi}{\rho} = \alpha\frac{\Psi_V}{\rho_V} + (1 - \alpha)\frac{\Psi_L}{\rho_L} \tag{4.48b}$$

In addition to the above models, OpenFOAM provides another barotropic compressibility model of Chung's model(Chung et al., 2001, 2004). This model considers the pressure difference at the interface of the two phases by the surface tension. Since the surface tension is ignored in this study based on the experimental results of Žnidarčič et al. (2014), Chung's model was not tested. The sound speed in the water/vapour mixture can become slower than those in the individual mediums and Wallis model can depict it better than the linear model (Brennen, 1995). Calculation results of the speed of sound in the water/vapour mixture by linear and the Wallis models is illustrated in Figure 42.

Since the mixture follows the barotropic relation, the mixture density can be expressed as Eq. (4.49) by integrating Eq. (4.44), where C is an integral constant.
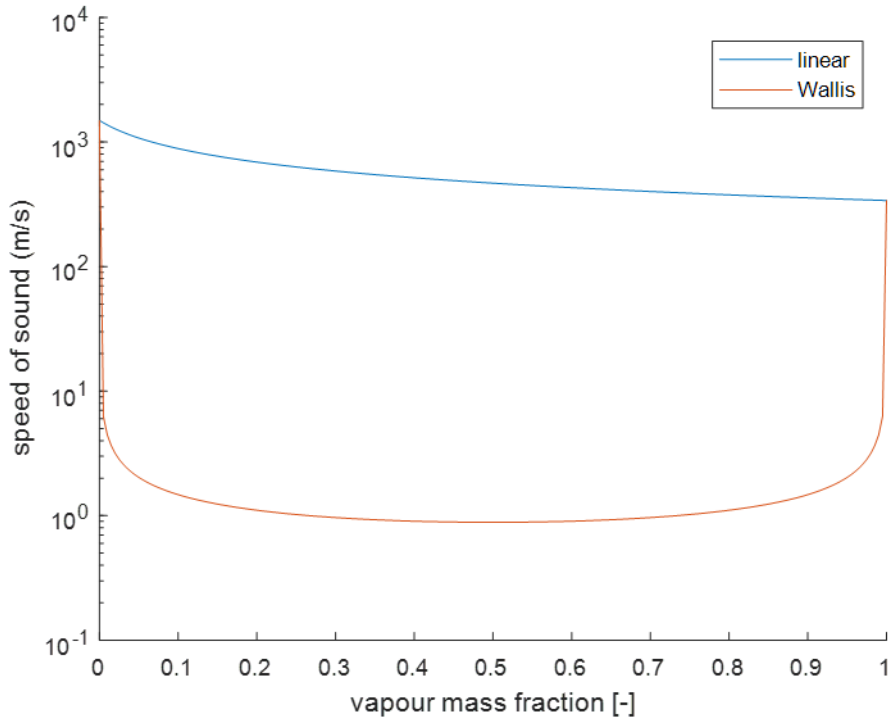
Figure 42 An illustration of the sound speeds in the water/vapour mixture with the vapour volume fraction based on the barotropic fluids assumption.

$$\rho = \Psi p + C \tag{4.49}$$

The constant C can be determined from the initial conditions specified at the vapour saturation pressure. The density of each phase at the vapour pressure is given as Eq. (4.50). Since the water density does not become zero at $p = 0$, a reference density of the liquid phase is defined as ρ_L^0.

Density of vapour: $\qquad\qquad \rho_{V,sat} = \Psi_V p_{sat}$

$$\tag{4.50}$$

Density of water: $\qquad\qquad \rho_{L,sat} = \rho_L^0 + \Psi_L p_{sat}$

Substituting Eq. (4.50) into the expression for the mixture density Eq. (4.41) and solving for the vapour saturation pressure, the constant C is found to be Eq. (4.51).

$$C = (1 - \alpha)\rho_L^0 + \{\alpha\Psi_V + (1 - \alpha)\Psi_L\}p_{sat} - \Psi p_{sat} \tag{4.51}$$

Thus, substituting Eq. (4.51) into Eq. (4.49), the final form of the mixture density expression is obtained as Eq. (4.52).

$$\rho = (1 - \alpha)\rho_L^0 + \{\alpha\Psi_V + (1 - \alpha)\Psi_L\}p_{sat} + \Psi(p - p_{sat}) \qquad (4.52)$$

This is the equation of state for the barotropic cavitation model and solved together with the governing equations (Navier-Stokes equations for the continuity and the momentum) either by PISO (Pressure Implicit Splitting Operators) (Issa, 1986) or PIMPLE algorithms, which is PISO algorithm merged with SIMPLE (Patankar and Spalding, 1972) algorithm. Since the barotropic cavitation model requires a very small time step size to cope with the speed of sound in the fluids, it is more expensive than the mass transport cavitation model. However, the barotropic cavitation model can capture better the physics of acoustic cavitation such as sub-harmonic oscillation of the acoustic bubble cluster, which is not possible for the mass transport cavitation models unless with the modification of their source term as suggested by Žnidarčič et al. (2015). But, such a modification makes the code very inefficient for the small time step calculations (Mottyll and Skoda, 2016). Therefore, in this study, the numerical model of acoustic cavitation was constructed based on this barotropic cavitation model.

4.8.3   Two-fluid models

These sorts of models apply Navier-Stokes equations to each fluid phase respectively. Application of Navier-Stokes equations to two-phase flow is justified by assumptions that (1) the dispersed phase elements are so small that they do not significantly affect the overall mixture density and (2) the momentum of them can be safely neglected (Sokolichin and Eigenberger, 1997). Interactions between the two phases are modelled by additional equations correlating with each other. These models do not need to assume the momentum equilibrium or the same velocity for each phase. Thus, phase slip velocities can be considered. The liquid phase is called the carrier phase and calculated in an Eulerian frame of reference. The vapour (gas) phase which is also called dispersed phase is tracked in either by an Eulerian frame of reference (Euler-Eulerian methods) or by a Lagrangian frame of reference (Euler-Lagrangian methods).

Euler–Lagrangian approach has several variations in application of Eulerian-/Lagrangian-modes, but in principle, calculates the continuous flow field properties by Eulerian frame and switches to Lagrangian frame to track disperse phase like individual bubbles. In Lagrangian mode, this method allows to consider various forces acting on the bubbly phase, bubble splitting, and bubble/bubble or bubble/wall interactions. Depending on the character of multiphase flow, the interaction between the two phases can be modelled in one or multiple way coupling as listed in Table 13. With higher volume fraction of the dispersed phase, higher

degree of coupling between the two phases becomes necessary to describe realistic physics involved (Loth et al., 2006).

As it does in the Euler-Euler approach, the fluid phases may be considered either as compressible or incompressible. An important benefit of a compressible flow approach lies in simulation of the pressure wave propagation due to the vapour collapse, which might be necessary for applications like the assessment of the erosiveness potential of a cavitating flow. Unfortunately, the compressible approach requires very small time steps to capture the shock wave propagation. This is more so in the cases with finer meshes, hence might be computationally expensive. As a trade-off, it is recommendable to study time step size or acoustic Courant number necessary to provide a reasonably accurate solution while keeping the computing cost low as possible. When compressible effects are not important, an incompressible approach seems to provide results similar to the compressible approach as regards to averaged cavitation and flow patterns or mean forces.

This approach allows solving the cavitating flow problems at multi-scales from individual bubble to large cavitation structures at relatively cheaper computing cost than fully Lagrangian approaches, and provides higher degree of physical accuracy than HEM or Euler-Eulerian approach. Therefore, it is becoming more popular in recent study of cavitating flows (Hsiao et al. (2017), Ma et al. (2015b), Raju et al. (2011), Lidtke et al. (2016), Abdel-Maksoud et al. (2010), Yakubov et al. (2013)).

Finally, multiphase flow solvers that are available in OpenFOAM are listed in Table 14. All of them are HEM based models. To the author's knowledge, there was only one two-fluid model available in OpenFOAM v3.0.1 under the name of 'reactingEulerFoam'.

Table 13 Methods to describe interactions between the phases in multiphase flows.

	Coupling methods	Considered interactions
Multiphase flow modelling	One-way coupling	Continuous phase affects motion of the disperse phase (particles).
	Two-way coupling	+ Reaction of the disperse phase to the continuum.
	Three-way coupling	+ Disturbance of continuum by one disperse phase affects the other disperse phase motion.
	Four-way coupling	+ Direction interactions between particles like collision.

4.9   Summary

In this chapter, some fundamental numerical methods and the relevant background knowledge were outlined necessary to settle an appropriate numerical model of acoustic cavitation phenomenon.

To obtain accurate solution as much as possible at a reasonable computing cost, second order numerical schemes will be used to discretise the temporal and spatial domains. The temporal discretisation will be achieved by 2nd order Euler scheme. The spatial discretisation will be carried out in principle second order upwind central differencing scheme throughout the numerical model studies discussed in chapters 5 ~ 6.

In chapter 5, a compressible multiphase flow solver is introduced to study the effect by the fluid compressibility, in conjunction with the difficulty with the shock waves propagation and reflection at the wall boundaries in a confined space.

Finally, in chapter 6, the importance of the boundedness in the mass convection term will be discussed in terms of realistic and stable solution with compressible flow solvers as well as satisfying the CFL condition. It will be shown that the decay of the acoustic stream and the acoustic pressure waves in the fluid domain could be reasonably simulated using a compressible multiphase flow solver based on the barotropic cavitation model by satisfying such requirements.

Table 14 Multiphase flow solvers available in OpenFOAM (v.3.0.1).

Category	Sub-categories	Available solvers
Incompressible	Isothermal	driftFluxFoam interFoam, interMixingFoam, interPhaseChangeFoam, multiphaseInterFoam, potentialFreeSurfaceFoam, twoLiquidMixingFoam
Compressible	Isothermal	cavitatingFoam
	Anisothermal	twoPhaseEulerFoam, multiphaseEulerFoam compressibleInterFoam, compressibleMultiphaseFoam

Chapter 5   **Numerical Simulation of Acoustic Cavitation**

5.1   Introduction

In the previous chapter, governing equations and numerical methods were discussed to model acoustic cavitation by a HEM multiphase flow solver. Žnidarčič et al. (2014) reported that the phase momentum transport cavitation models (Sauer and Schnerr, 2000, Singhal et al., 2002, Zwart et al., 2004) could not predict the oscillation frequency of acoustic cavity cluster volume and the pressure peaks without inclusion of the non-linear inertial acceleration term of the Rayleigh equation into the evaporation and condensation rate modelling. Mottyll and Skoda (2016) demonstrated applicability of a density based HEM multiphase flow solver with a barotropic cavitation model to predict the acoustic cavitation behaviour efficiently without introducing the iterations to solve the non-linear inertial acceleration term. Density based compressible flow solvers may suffer increased computational cost and inaccuracy problems in the low Mach number regime (Keshtiban et al., 2004). As the flow velocity involved in the current acoustic cavitation modelling is much lower than the speed of sound, a pressure based compressible multiphase flow solver 'cavitatingFOAM' was chosen for the modelling of the acoustic cavitation in this study.
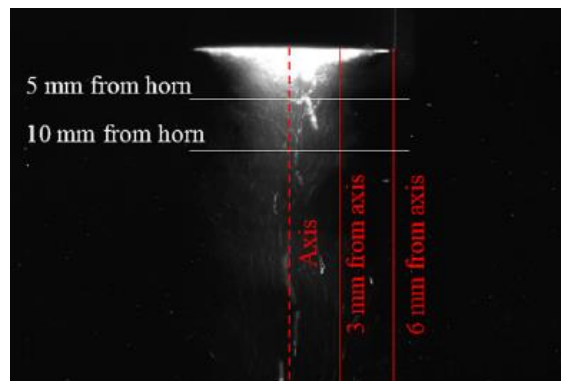
Figure 43 Locations of the velocity profile measurement (Rahimi et al., 2016).

Rahimi et al. (2016) investigated the velocity profile of the acoustic stream using the PIV (Particle Image Velocimetry) technique at the locations as shown in Figure 43. Since the velocity field is coupled with the pressure field, comparison of the velocity profile between the experiment and the numerical model might provide an insight on the cause of the high

pressure peaks. In this chapter, the velocity field of the acoustic streaming was explored in conjunction with the investigation of the pressure field.

Firstly, 'interPhaseChangeFOAM', a mass transport model based two-phase flow solver in which individual fluids are assumed incompressible, was used to compare with the experiment results. The solutions acquired at t = 0.128 s provided a reasonable looking flow pattern as compared in Figure 44. However, the solution from the solver exhibited at least 2.5 times higher jet flow velocity even compared with the maximum velocity from the experiment. Furthermore, the jet velocity was not reduced at all until it reached the bottom (Figure 45).
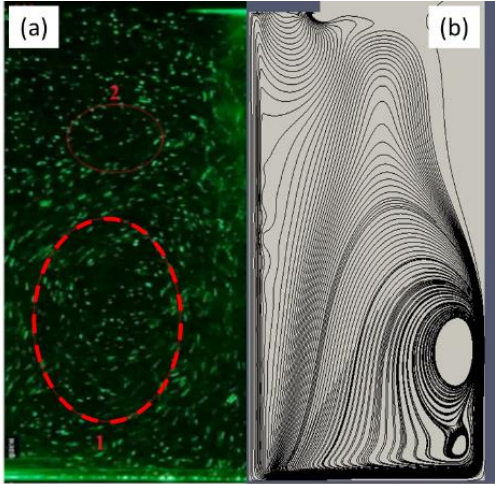
Figure 44 Comparison of the tracer particles movement in the experiment (a) and the streamline computed by interPhaseChangeFOAM solver at t = 0.128 s (b).
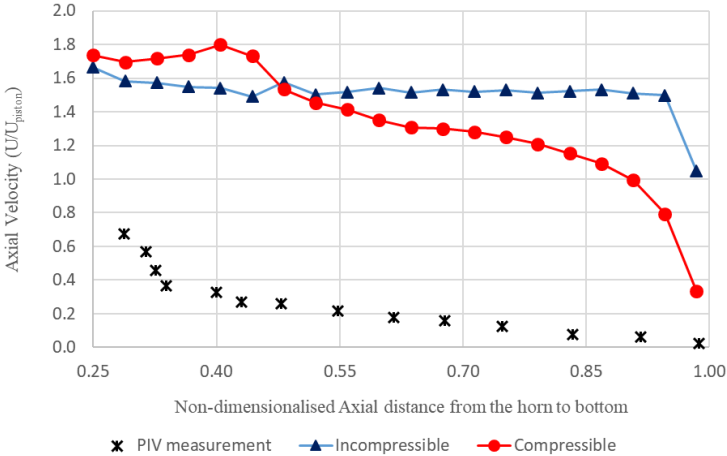
Figure 45 Comparison of the acoustic stream velocity profile along the ultrasonic horn axis. The incompressible two-phase flow solver 'interPhaseChangeFOAM' did not have very little decay of the flow velocity until it reached the bottom, whereas the compressible two-phase flow solver indicated gradual decay of the flow velocity.

This was thought as an inevitable consequence of incompressible fluids assumption for a small fluid domain with large pressure fluctuations. The vapour volume fraction was not high enough for the mixture density of the cells to become significantly different from that of the liquid alone. Hence, the pressure propagated instantly through the whole domain and it caused the fluid velocity field to become almost uniform. Therefore, it was necessary to study the influence of the compressibility on the flow velocity and eventually the impact pressure loadings on the bottom.

The exploration continued with a compressible two-phase flow solver 'cavitatingFOAM'. The challenge with the compressible flow solver was very high; it was never an easy task simply to run the solver without solution diverging. Most of this chapter describes the challenges with the solver and the efforts to stabilise the solution. The following had been tried here.

(1) Change of the numerical schemes.

(2) Change of the boundary conditions at the free surface ('outlet' boundary patch).

(3) Sub-harmonic oscillation frequency with linear barotropic cavitation model.

5.2   Case description

The principal parameters of the CFD simulations were set based on the experimental case of Rahimi et al. (2016) as shown in Table 15. The velocity profiles of the jet-like acoustic stream were compared with their measurement data at the depths of 0.005, 0.010 m below the ultrasonic horn and along the axis (Figure 43). For the reader's information, the liquid depth on the table had to be estimated because the information was not available in the paper. The estimation was made based on a figure (figure 4 of the paper). Also the physical quantities of water and vapour were taken to be the same quantities as used in the previous chapter, while the actual experiment reported the reference temperature of 300 °K. This should not cause any significant difference, at least, in terms of the pressure peaks and acoustic cavitation oscillation frequency according to the experiment reported by Žnidarčič et al. (2014). Therefore, the flow velocity field is not significantly affected by the difference of such physical quantities.

5.3   Numerical model

5.3.1   Governing equations and Numerical schemes

The NS equations were solved together with either linear or the Wallis barotropic equation of state by FVM method. RANS approach with a *k-ω* SST turbulence model was used. Further details can be found in chapter 4.

There is no analytic solution of the NS equations in general. Therefore, the equations are solved numerically. Temporal discretisation is achieved by a 'backward' scheme, which is second order Euler method. Spatial discretisation is achieved by constructing a mesh grid, which will be described in the section 5.3.3. All the field values are stored in the cell centres. Interpolation of variables was carried out by second order central differencing scheme. Divergence of field variables was calculated by Gauss theorem with linear upwinding scheme. The mass convection was calculated by central differencing scheme using Gauss theorem; it was later realised that this was the most dominant culprit of the solution divergence suffered in this study especially with Wallis barotropic compressibility model. The viscous diffusion term was calculated using Gauss theorem with second order central differencing. Gradients were calculated by a linear upwinding scheme. The face normal gradients were calculated by a limitng scheme to correct errors due to non-orthogonality of the cells. The time step size was set to be automatically controlled by OpenFOAM based on the maximum acoustic CFL number. The pressure and velocity coupling was solved initially by PIMPLE algorithm.

Table 15 Specifications of the CFD simulations based on the experiment by Rahimi et al. (2016).

Parameter	Value	Unit
Ultrasonic horn tip diameter	0.012	m
Acoustic driving frequency	20	kHz
Acoustic driving amplitude (peak-to-peak)	40×10^{-6}	m
Liquid bath dimensions (diameter x liquid depth)	0.040 x 0.042	m x m
Ultrasonic horn tip immersion	0.01	m
Liquid (water) density	998.2	kg/m^3
Dynamic viscosity of the liquid	1.002×10^{-3}	$kg/m{\cdot}s$
Liquid compressibility	4.582×10^{-7}	s^2/m^2
Vapour density	1.731×10^{-2}	kg/m^3
Dynamic viscosity of the vapour	9.727×10^{-6}	$kg/m{\cdot}s$
Vapour compressibility	7.410×10^{-6}	s^2/m^2
Minimum density value (ρ_{min})	0.001	kg/m^3
Turbulent kinetic energy (k)	1.186×10^{-2}	m^2/s^2
Turbulent eddy dissipation ratio (ω)	1.251×10^{3}	s^{-1}

5.3.2   Alteration of parameters of the numerical schemes

Compressible flow solvers often require very fine time resolution to correctly capture the propagation of the disturbance through a medium. If the propagation speed of the disturbance

in the propagation medium were important to the physics of any given problem, the acoustic CFL number should be chosen close to the value of 1. This often makes impractical the use of the compressible flow solvers in daily engineering problems because higher spatial resolution satisfying the acoustic CFL condition would mean the problem might not be solved within the typical time frames available. Thus, the acoustic CFL condition is often compromised by testing the solution against a real experiment data.

To reduce the computational cost for the study, a 2-D axi-symmetric wedge model (wedge angle: 2 degrees) was used at first. It was constructed using the total 11200 hexahedral cells and had the same mesh resolution as the 3-D mesh (Figure 46).

The first calculation up to 7×10^{-3} s was carried out with maximum acoustic CFL number of 1, which took about 68 hours with an Intel i7-4790k CPU. The next calculation up to 0.159 s was carried out with the acoustic CFL number of 50 to improve the calculation speed.

At the time of study, since the pressure tended to make the solution diverge, the relevant numerical schemes were suspected as well as the boundary condition at 'outlet' patch. The agglomeration level of the pressure equation matrix solver GAMG (Geometric-Algebraic Agglomeration Multi-Grid) was changed from two cells to ten cells. This had been misunderstood as improving the stability of the solution by solving the pressure on a coarser cell levels by agglomeration and refining the solution on the original cell level. Indeed, this might have helped to improve the pressure matrix solving speed but not the stability of the solution. The tolerance of the pressure solution during the iteration was relaxed from 10^{-8} to 10^{-6}, which was not clear how it affected the solution. Finally, the pressure-velocity couple solving algorithm was replaced with PISO algorithm to improve the computational efficiency. Contribution from each change was not studied. But, resultantly the calculation time was reduced to 40 hours to calculate the acoustic streaming up to 0.159 s. Most of this reduction is believed to come from increasing the acoustic CFL number from 1 to 50. It was not evident how the increased CFL number was deteriorating the pressure solution at the time of study. This will be further discussed in section 6.4.1.

5.3.3   Construction of mesh grid

A 2-D axi-symmetric model tends to underpredict the effect of spatial diffusion of the physical quantities due to limited spatial dimensions. Because of this, their results appeared too complex and confusing as a result of stronger interactions of the pressure waves with their reflections at the wall boundaries. A 3-D 360 degree model was used later to ease the problem at the cost of additional computing effort. Figure 46 shows (a) the overall mesh grid with (b) the detail of meshes for the ultrasonic horn tip region and (c) an alternative mesh construction

in the same region to see any difference in the predicted acoustic streaming velocity profile by the mesh resolution in the region. A total number of 1,632,000 cells were used to construct the model. The gap region between the piston and the bottom consumed 192,000 cells with the cell face area of 2.25 x 10^{-8} m^2 with the minimum cell height of 82 µm, which was difficult to reduce further due to the deforming mesh scheme that was used to mimic the motion of the ultrasonic horn tip. Difficult to calculate an exact y$^+$ value for compressible multiphase flows due to indeterminate nature of the viscosity and the density of the phase mixture, an estimate based on water phase indicated y$^+ \approx 28$. Mottyll and Skoda (2016) chose the cell size within the gap to be in between 25 ~ 100 µm depending on the refinement level of grids for a similar simulation work with RANS approach. Comparing the current grid with their work, the current minimum cell size may be judged as reasonable for a reasonable simulation. To avoid too much expansion/contraction of the cells near the moving boundary (the horn tip surface), the minimum cell size was kept large as possible compared with the vibration amplitude of the horn tip.
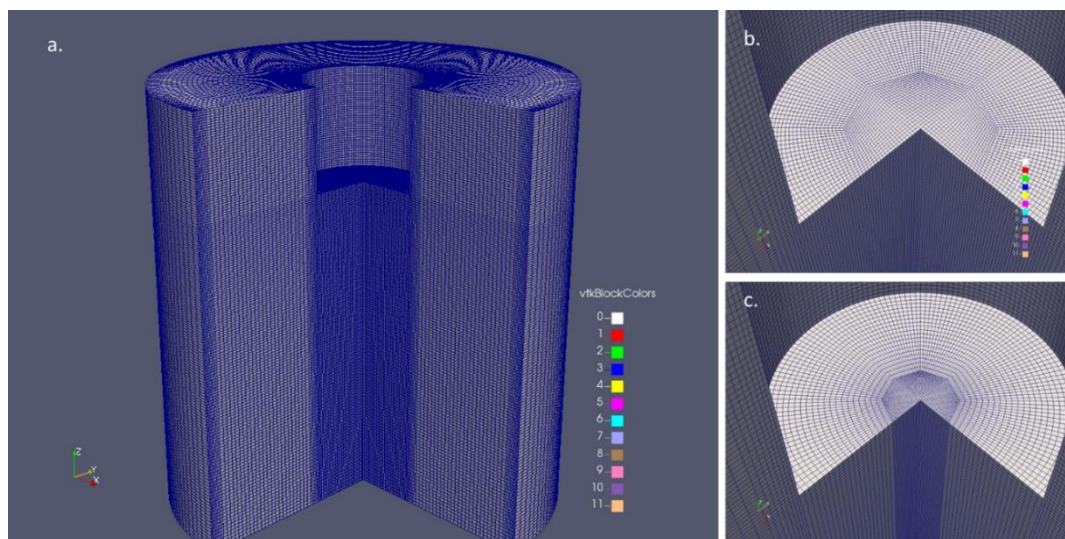
Figure 46 The full 360 degree model disected at 90 degrees to show the mesh construction.

5.3.4   Boundary conditions

The boundary patches defined for the model are shown in Figure 47. In principle, the same boundary conditions were applied as per the previous chapter (shown in Table 16).

Among the imposed boundary conditions, technically precise boundary condition of the velocity (U) field at 'bottom' and 'side wall' boundary patches could be 'no slip wall' ($U = 0$) condition. However, the difference or error due to this boundary condition should be small

anyway, considering the fact that the flow under investigation is mostly inertia-driven. Indeed, Mottyll and Skoda (2015) simply ignored the viscosity effect in their simulation of acoustic cavitation.

The 'pressureInletOutletVelocity' condition imposes zero gradient condition if the surface normal flux is greater than zero, otherwise, the condition calculates the flow velocity based on a specified flux value. The influx value was set to zero.

The 'inletOutlet' boundary condition is a generic outflow condition based on the sign of surface normal flux. If the flux is positive, a specified outflow flux value is assigned. Otherwise, an inlet value, which is also specified by the user, is imposed on the flux. Both values were set to zero. Therefore, it was assumed that there was no flux through the outlet boundary.

Because the solution continued to diverge in time at the outlet boundary, several different boundary conditions were studied as well as some changes in the numerical schemes to resolve such a solution instability problem. The alternative boundary conditions are listed in Table 17. A later study showed such an instability had been caused by the violation of the mass conservation due to unbounded convection scheme for the mass.

The boundary condition case C1 was based on an idea that the free surface should retain water in alignment with the constant pressure boundary condition there.

Case C2 was to investigate the effect of violation of the space conservation law (Demirzic and Peric, 1988). The total volume of the calculation domain fluctuates due to oscillatory displacement of 'piston' boundary patch and negligence of the slight water volume fluctuation at 'outlet' boundary. Although a part of that effect would be absorbed by the compressibility of the fluids, still the most of the effect could distort the pressure field calculation. Therefore, a forced oscillation of 'outlet' boundary was imposed to compensate the volume change at 'piston' boundary. This artificial oscillation of 'outlet' will be unrealistic. However, at least it might tell how much pressure peaks could be affected by the violation of the space conservation law.

Finally, case C3 was to investigate the influence of the pressure wave reflection at the outlet boundary. To remove the reflection, 'wave transmissive' boundary condition was imposed on the pressure field of 'outlet' boundary patch.

The 'wave transmissive' boundary condition is provided in OpenFOAM suite as a type of non-reflecting boundary condition. The surface normal flux of any given kinematic field variable (the field variable is denominated by density) is calculate to be convected at a velocity of

$|U_n| + \sqrt{\kappa/\psi}$, where κ is specific heat ratio, and ψ the compressibility of the fluid. This is a simple analogy with the linear wave equation. The field variable becomes a solution of the linear wave equation propagating outward at the above speed. Hence no reflection is achieved at the boundary.

The other small change in the case C3 was that the 'slip' boundary condition was corrected to the 'no slip' wall boundary condition.
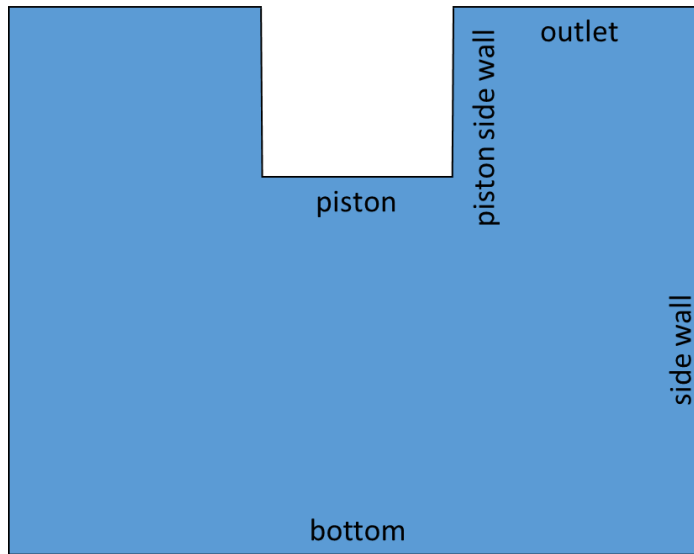
Figure 47 The boundary patches of the mesh grid.

Table 16 The base line of the boundary conditions.

variable	piston	bottom	side wall	outlet
p	zero gradient	←	←	p = 0
U	moving wall (no slip)	slip wall	←	pressureInletOutletVelocity
ρ	zero gradient	←	←	←
k	kqR wall function	←	←	inletOutlet
ω	omega wall function	←	←	inletOutlet
ν_t	nutUSpalding wall function	←	←	calculated
α	calculated.	←	←	←

Table 17 Alternative boundary conditions at outlet boundary patch.

Case ID.	C1 (2-D mesh)	C2 (2-D mesh)	C3 (2-D, 3-D mesh)
p	$p = 0$	$p = 0$	wave transmissive
U	pressureInletOutletVelocity	moving wall	zero gradient
ρ	$\rho = 998.2$	$\rho = 998.2$	zero gradient
α	$\alpha = 0$	$\alpha = 0$	calculated

5.4   Results

5.4.1   Solutions with 'cavitatingFOAM' solver: initial boundary condition

Figure 48 shows the evolution of the acoustic stream in time. The predicted streamlines appear to capture the flow pattern of the acoustic streaming such as a jet-like downward stream under the ultrasonic horn and the recirculation flow round the core flow. Although Figure 49 (a) was a calculation result of streamlines with the 'slip' wall boundary condition, the predicted flow pattern appears to show the similar flow pattern with the streamline at time t = 0.413 s in Figure 48.

However, looking at the results together with the axial velocity (Figure 49 (b)) and the pressure field (Figure 49 (c)), the strongest pressure occurred not on the piston but at outlet. This high pressure must have created a strong pressure gradient in the narrow region between the cells on outlet boundary and their neighbour cells due to the fixed pressure boundary condition on the outlet boundary. Since no flux was assumed through the outlet boundary, flow by the pressure gradient has to move along the outlet boundary creating a strong circulation flow. This pressure gradient is believed to be the prime mover of the whole flows. Figure 49 (b) shows an accelerated flow on the side wall due to lack of viscous stress by the 'slip' wall boundary condition combined with the re-circulating flow in its vicinity. The recirculation flow was accelerated in between the eye of recirculation and the side wall as if the flow had passed a venturi tube. The predicted velocity profile showed similar patterns of decay with the experimental measurement by Rahimi et al. (2016), but the magnitude of the flow velocity was ten times higher than the experiment (Figure 50). This was thought to be a result of violation of the space conservation law.

Figure 48 Formation of the acoustic stream in time that were calculated by cavitatingFOAM solver with the baseline boundary conditions..
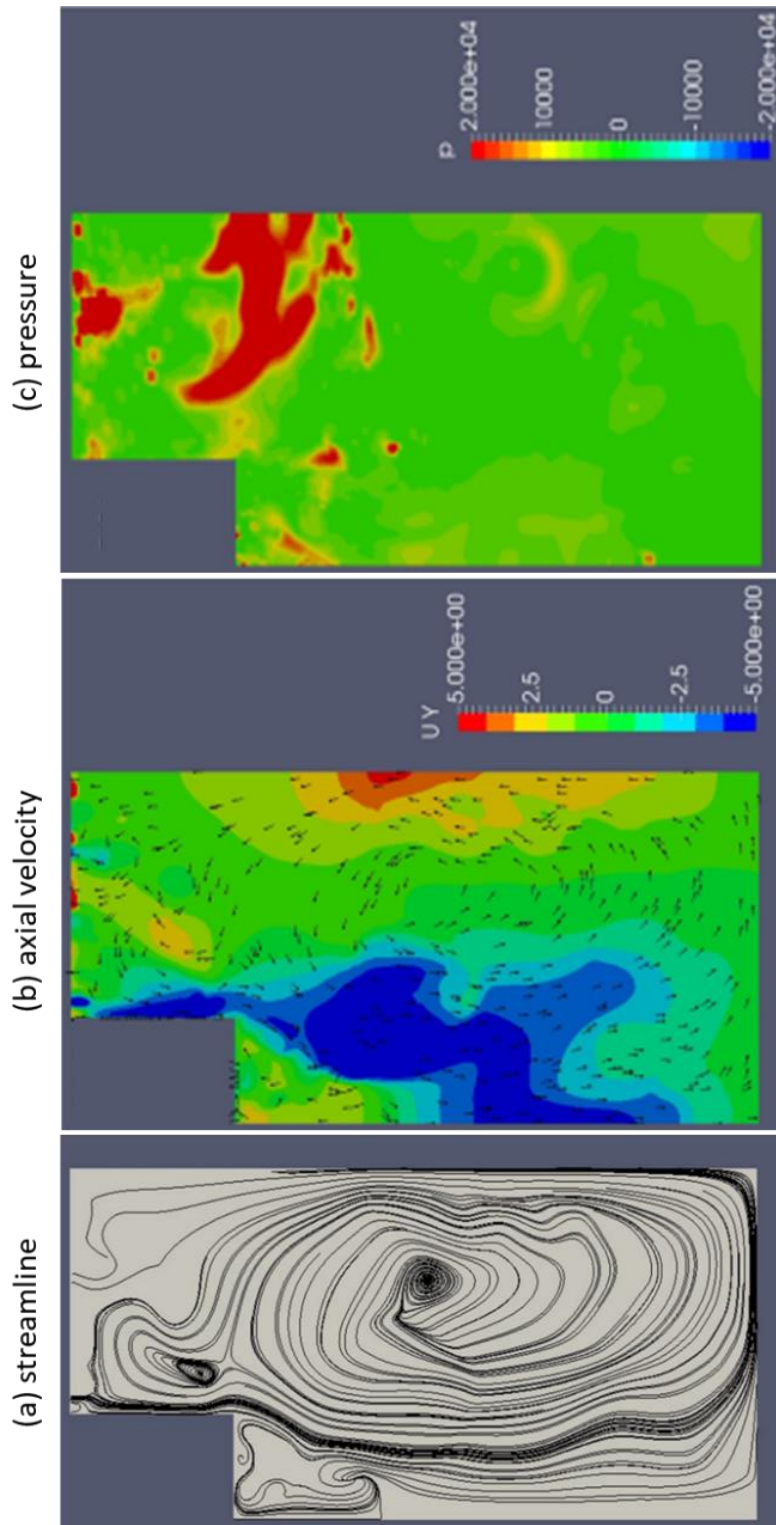
Figure 49 Streamlines (a), axial velocity of the acoustic stream (b), and pressure field (c) at time t = 0.413 s.
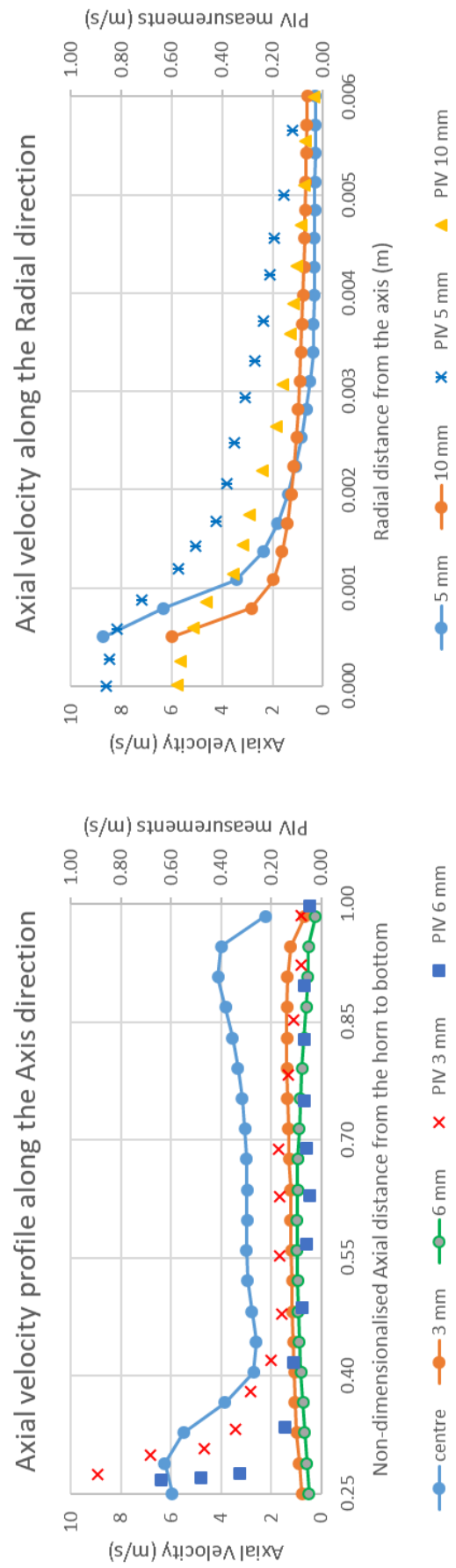
Figure 50 Comparison of acoustic stream velocity between the experiment (Rahimi et al., 2016) and the the simulation with the baseline boundary conditions.

5.4.2   Solution with the outlet forced to oscillate

The results with the forced oscillation of the outlet boundary are shown in Figure 51 and Figure 52. Due to the forced oscillation and the 'slip' wall boundary condition, the velocity field does not look correct, although the predicted flow pattern from the streamlines looks qualitatively correct. The main point of this study is that the velocity of the flow reduced when the total calculation domain volume is conserved. This appears to imply that the pressure boundary condition imposed on the outlet boundary should not be like a solid wall. Otherwise unrealistically high pressure gradient will be created near the outlet due to periodic contraction and expansion of the space by the motion of the ultrasonic horn. Therefore, a more relaxed pressure boundary condition than the symmetry or a fixed pressure conditions would be favourable to stabilise the solution with more reliable pressure field creation.
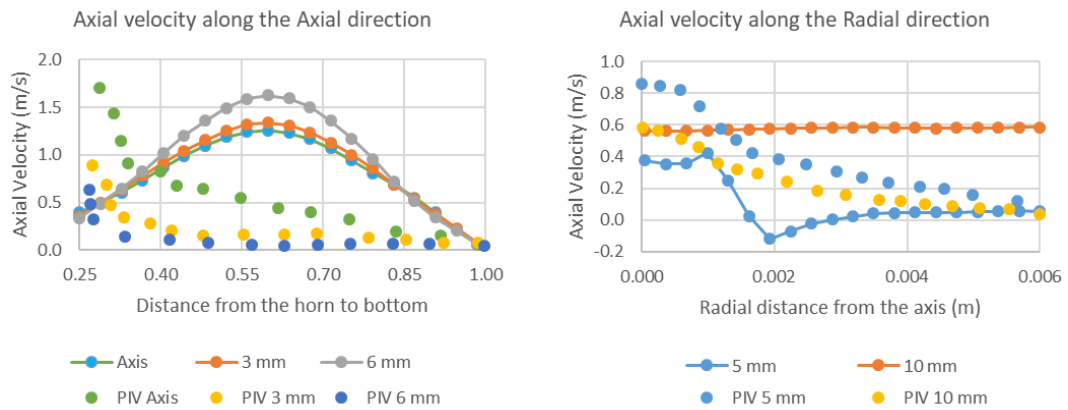
Figure 51 Flow velocity profiles with the forced oscillating outlets
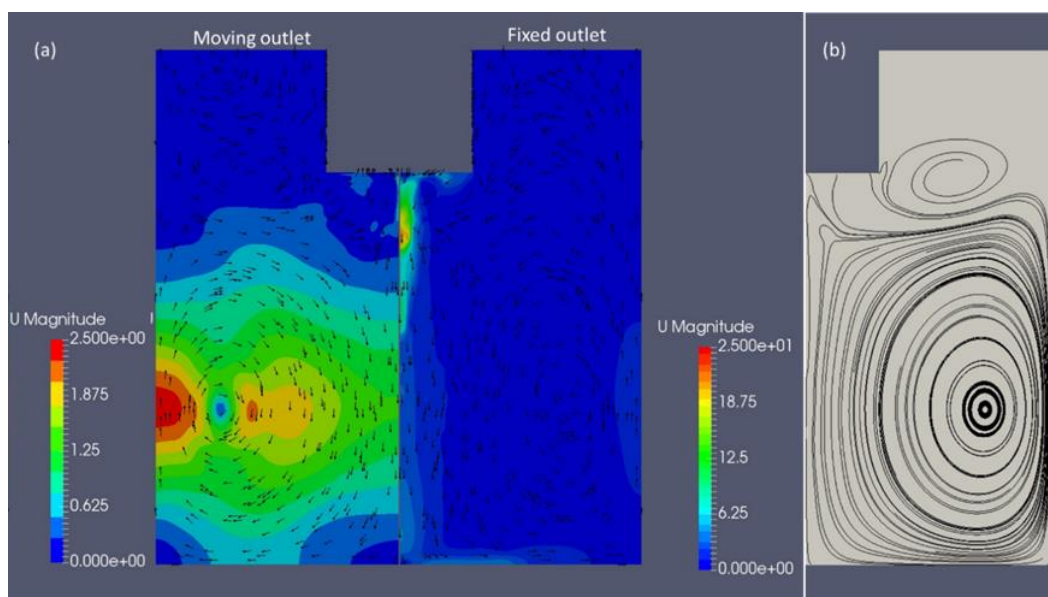
Figure 52 Flow velocity field and the streamlines with the oscillating outlet.

5.4.3 Solution with non-reflecting boundary

The acoustic stream velocity profiles with the non-reflecting boundary condition on the wall boundaries except for the piston wall boundaries were calculated with the 2-D and 3-D models. The profiles are shown in Figure 54. Comparing with the results shown in Figure 50, the velocity magnitudes were reduced by a half compared with the reflecting wall boundaries case. Also the results from the 3-D domain shows smaller magnitudes of the profile and faster decay of the velocity along the axis. These confirm again the predicted flow velocity could be largely overpredicted with the small fluid domain. Still, even (almost) without the pressure reflection from the outlet boundary, the flow velocities were largely overpredicted. It may be accounted for the violation of the space conservation law. In spite of this flaw, the visualised flow in Figure 53 appears promising. It was concluded that the 'no slip' wall boundary condition would be necessary to predict a physically reasonable flow structure.
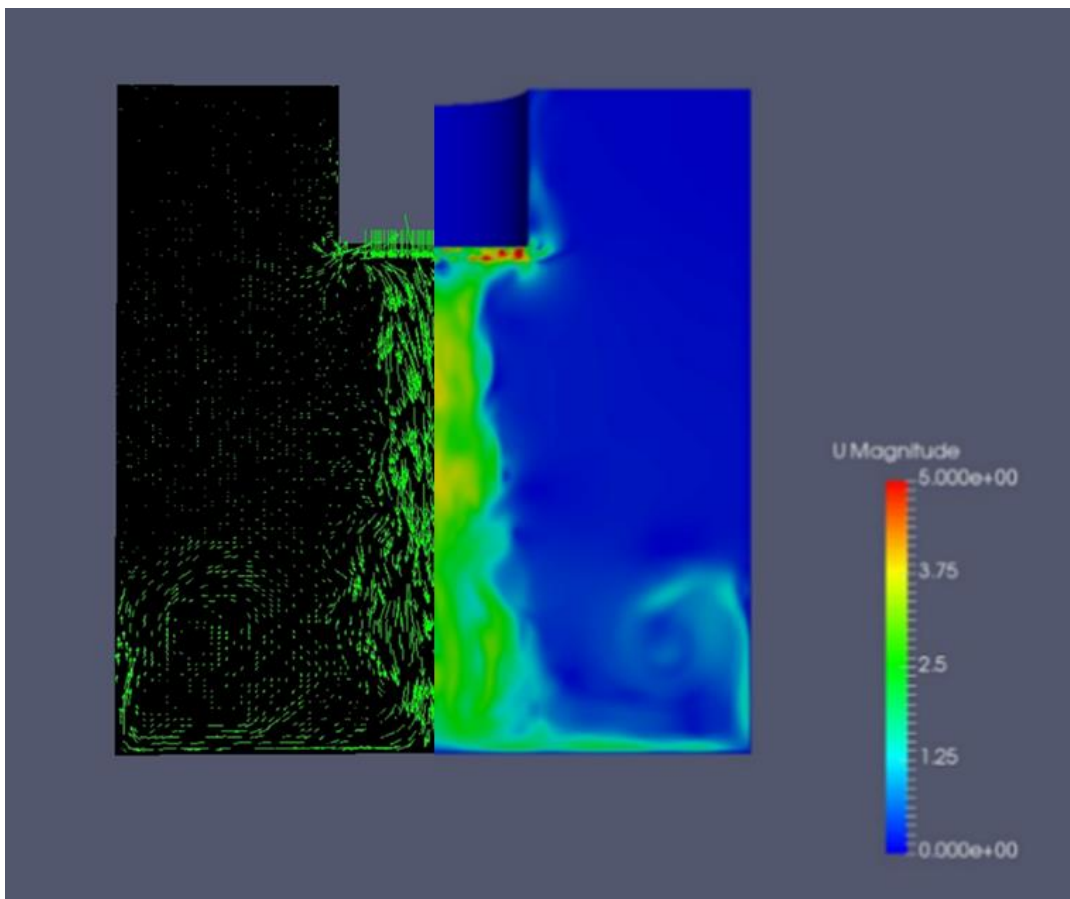
Figure 53 The acoustic stream prediction result.
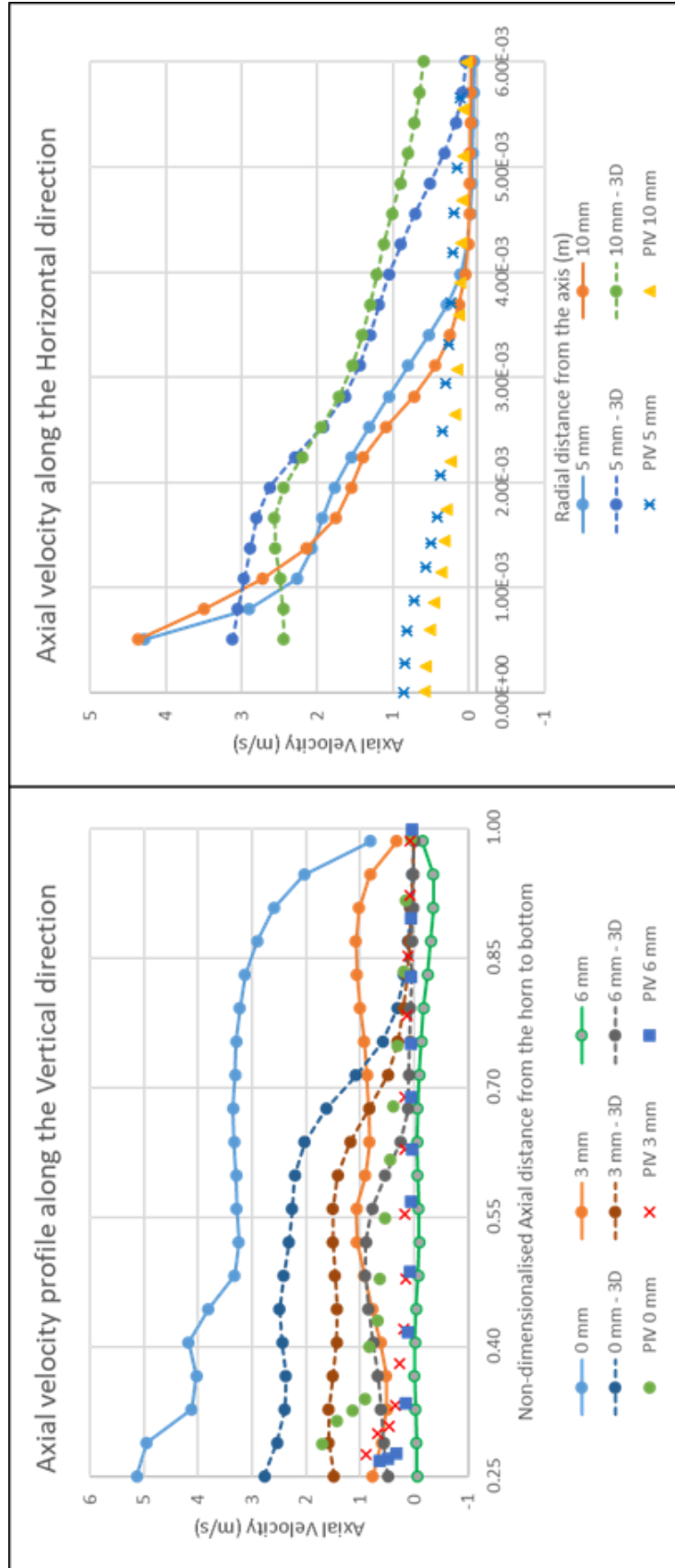
Figure 54 The velocity profiles in 2-D and 3-D models for case C3.

5.4.4   Sub-harmonic frequency with linear model

The pressure signal extracted from the case C3 results were analysed in the frequency domain. Although it was feasible that the actual experiment did not show the sub-harmonic oscillation of the acoustic cavity either since the vibration amplitude (peak-to-peak) was only 40 x 10^{-6} m, the frequency analysis indicated only a very weak one at half the driving frequency (Figure 55). It was necessary to confirm if this was from the limitation of the linear barotropic compressibility model.
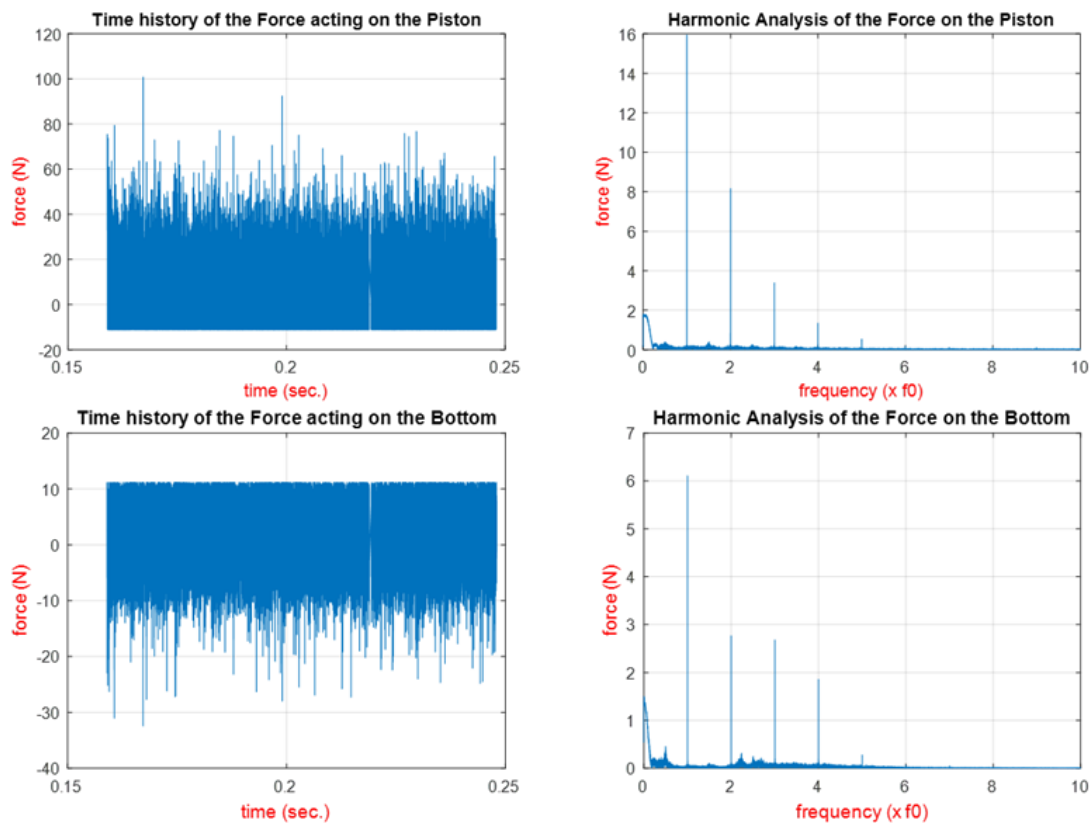
Figure 55 The pressure signals in time domain (left) and frequency domain (right).

5.5   Conclusion

With the compressible multiphase flow solver, it was possible to see a number of improvements in the quality of the simulation.

It was learned that the retarding jet-like flow in the acoustic stream could be better depicted with consideration of the compressibility.

The fixed pressure boundary condition to approximate the free surface with slip wall boundaries produced overly similar-looking flow pattern as the real acoustic stream. However,

the solution tended to diverge due to probably an artificial high pressure gradient near the approximated pressure boundary. To ease the potential problem, a more relaxed pressure boundary condition would be preferred. 'No slip' wall boundary condition is appropriate to simulate more realistic velocity field near the wall and the overall structure of the acoustic stream surrounding the core stream under the ultrasonic horn.

Due to the violation of space conservation law at the moving boundary, the pressure and velocity field in the fluid domain tended overpredicted. This is a kind of limitation of the current deforming mesh scheme.

While the current numerical model appears promising to predict the acoustic streaming and cavitation, it is not clear yet if the linear barotropic cavitation model can predict the sub-harmonic oscillation frequency reasonably. Furthermore, the current numerical model diverges with Wallis model. This appears to imply the current model has a potential flaw in predicting the density of the mixture. Since the current cavitation model relies on the barotropic relation, the density and the pressure are directly interlinked. Therefore, this could be an important issue of the model. This will be further investigated in the next chapter.

5.6   Summary

A study with a compressible multiphase flow solver 'cavitatingFOAM' had been carried out. This part of the work was more like a learning step of the computational fluid dynamics. Numerical schemes were reviewed and could improve the efficiency of the solution process, although there were still some misunderstanding in application of individual functions of OpenFOAM suite.

Through the numerical experimentation there were several important lessons learned as follow:

(1) With the inclusion of the compressibility, the velocity profile of the acoustic stream can be better depicted.

(2) Due to violation of space conservation law, the predicted acoustic stream velocity could be over-predicted. In the same line of thought, 2-D axi-symmetric models tend to produce over-prediction in the physical quantities that disperse through the space.

(3) A rigid approximation of the free surface as the pressure outlet such as a fixed pressure boundary or symmetry condition appears susceptible to potential divergence of the solution due to an unphysical steep pressure gradient near the boundary that might be caused by local pressure change near the free surface in real life. A more relaxed pressure outlet boundary condition would be preferable in terms of solution stability.

(4) The solution divergence of the current numerical model with Wallis barotropic compressibility model appears to imply a potential flaw in calculation of the mixture density that would appear as the denominator to calculate the compressibility of the mixture. This can be an important issue since the current cavitation model relies on the barotropic relation. The current model needs to be further improved in terms of this. This shall be further investigated in the next chapter.

(5) Finally, the capability of linear barotropic compressibility model to predict the sub-harmonic oscillation of the acoustic cavities were not clear through the study carried out here. It should be also confirmed in the next chapter.

Chapter 6   Refining the Numerical Model and Validation

6.1   Introduction

Through the studies discussed in the previous two chapters, there remain several questions to be answered.

(1) The capability of linear barotropic compressibility model to predict the sub-harmonic oscillation.

(2) The solution divergence with the Wallis barotropic compressibility model.

(3) A more relaxed pressure outlet boundary condition in terms of solution stability.

The first question will be an interesting one in terms of modelling acoustic cavitation. Previously Mottyll and Skoda (2015) successfully demonstrated that the Wallis barotropic compressibility model could be useful in studying acoustic cavitation and its erosiveness. If the linear compressibility model could do the same, the computational effort could be slightly reduced with better stability. To answer this, the linear model was tested against the reference experiment results of Žnidarčič et al. (2015) who measured the sub-harmonic oscillation frequency of acoustic cavitation and the pressure peaks with a hydrophone varying the vibration amplitude of an acoustic excitation source.

To enable the use of the Wallis barotropic compressibility model, the density solution had to be stabilised to avoid it becoming unphysical. This could be achieved either by controlling the minimum density value or by ensuring the boundedness of the mass convection term in the continuity equation according to the study in sections 6.4.2 and 6.4.3.

Before explaining the basic idea underlying in the first approach, the meaning and role of the minimum density value is described. The barotropic relation (Eq. (4.47)) means that the density of the phase mixture will be a linear function of the pressure with a positive proportional factor. Hence, if a large negative pressure appears in the calculation domain for some reason, the density can go negative, which is unphysical. Therefore, to prevent such an erroneous situation, a minimum density value should be set appropriately. There is no known general guide for this other than that the value should be a small positive value and it really depends on individual problems. With the linear barotropic compressibility model, the value was chosen as 0.001 kg/m^3, which was small enough compared with the vapour density at the

saturation pressure. Hence, the minimum density value was ensured not to influence the pressure prediction results. However, with the Wallis model, such a small value caused the simulation to diverge just in several acoustic cycles.

Back to the explanation, the basic idea of the first approach, though temporary and incomplete, was based on observation of the calculated pressure values in the simulations that often appeared to go far below the vapour pressure, so the mixture density become very small, leading to an unphysical value for the vapour volume fraction. Of course, such things do not happen, since the pre-set limiting conditions in the solver routine constrain the volume fraction in between zero and one. However, once such an event occurs in the domain, the solution becomes abnormal. For example, the pressure stays very low for a relatively long period or instantly rebounds generating an enormous magnitude. This sharp change of pressure would cause numerical instability because of a high pressure gradient that could not be followed ensuring the boundedness of the relevant physical quantities. With a raised minimum density value such as 300 or even 950 kg/m^3, such instability problem became noticeably rare, and the Wallis model ran for a long duration without diverging solution. However, since raising the minimum density value meant limiting the vapour volume fraction to be equal or above a certain value, which can be found by equating the left hand side of Eq. (4.41) with the minimum density value, the solution could be distorted by any minimum density value higher than the vapour density. Therefore, study had been carried out to see any trend in the solution by lowering the density limiter value again without causing the solution to diverge.

Finally, to improve the stability of the numerical simulation further, several pressure boundary conditions were compared. The influence of the applied turbulence models and the mesh quality on the solution were reviewed. Since the author's experimental results were obtained while these benchmark tests began already, the numerical model was verified against a series of experiments by Žnidarčič et al. (2014) instead of the author's experimental results.

6.2   Simulation case description

Benchmark tests were carried out with the experimental cases reported by Žnidarčič et al. (2014) as shown in Table 18 (A1 ~ A3). Case A4 was an extended case to confirm the consistency of the numerical simulation, which does not have a real experiment data. Based on the experiment of the power variation (the excitation amplitude of 70 µm falls into the tested sonotrode power range of 80 ~ 90 %) in chapter 3, the tendency of increasing sub-harmonic frequency was anticipated. The liquid bath dimensions were 0.050 x 0.050 x 0.050 m^3 with 100 % air saturated water filled up to the height of 0.040 m. The calculation domain was simplified to a 2-D axi-symmetric one to reduce the computational cost for the benchmark

tests. While there was no rigorous comparison, an LES approach was used for all the study here hoping to better depict the pressure impact events. A small discrepancy with the actual experiment was in the temperature condition. While the actual experiment benchmarked here were reported to have been carried out at the temperature of 296 °K, the physical properties of the water and vapour phases were taken for 293 °K. This should not affect the results of the oscillation frequency of the acoustic cavity cluster according to the reference experiment results.

Table 18 Specifications of the benchmark test cases.

Case ID.	Vibration amplitude (µm)	Driving frequency (kHz)	Tip diameter (mm)	Gap distance (mm)	Temperature (°K)
A1	100	20	3	30	293
A2	132	20	3	30	293
A3	164	20	3	30	293
A4	70	20	3	30	293

Table 19 Physical quantities used for the simulation

Parameter	Value	Unit
Liquid domain dimensions (half width x depth)	0.025 x 0.050	m^2
Ultrasonic horn tip immersion	0.010	m
Liquid (water) density	998.2	kg/m^3
Dynamic viscosity of the liquid	1.002×10^{-3}	kg/m·s
Liquid compressibility	4.582×10^{-7}	m^{-2}/s^{-2}
Vapour density	0.8031	kg/m^3
Dynamic viscosity of the vapour	9.727×10^{-6}	kg/m·s
Vapour compressibility	3.492×10^{-4}	m^{-2}/s^{-2}
Vapour pressure	-9.9×10^4	Pa
Turbulent kinetic energy (initial)	3.36×10^{-3}	m^2/s^2

6.3 Numerical modelling

6.3.1 Governing equations

The same governing equations as in chapter 5 are solved but using a large eddy simulation (LES) scheme (Smagorinsky, 1963). The spatial low pass filter width was calculated from the cubed root of each cell volume and then an additional treatment was carried out by either 'smooth' or 'maxDeltaxyz' filtering function. The 'smooth' function calculates the filter size Δ from the cube-root of a cell volume and suppresses the ratio of the filter sizes of the neighbour cells within the user-specified value. The default value of OpenFOAM is 1.15 and a slightly smaller value of 1.1 was applied. The SGS Reynolds stress were modelled by the *k*-equation model (Yoshizawa, 1986) as in section 4.7.6.

6.3.2 Construction of mesh grid

The same deforming mesh scheme as used in the previous chapters was used to mimic the ultrasonic horn tip vibration in the axial direction. The constructed mesh grid specifications are shown in Table 20.

OpenFOAM provides several important mesh quality indices with regard to non-orthogonality and skewness. A non-orthogonality index is defined as the angle θ between the lines $\overline{PQ}$ and $\overline{PC}$ in Figure 56. The skewness is defined as $\overline{QC}/\overline{PN}$ in the same figure. The mesh quality indices in the table indicate the values based on the state when the cells under deformation reach the maximal deformed state. A schematic drawing of the mesh grids and the actual meshes used in the study are shown in Figure 57. A virtual hydrophone probe was put on the point P1 as per the benchmark experiment. All the pressure signals were extracted at the location at every time step. Two time stepping methods were used in the study. Firstly, a fixed time step size of 1 x 10^{-8} s was used. Later, an automatic time stepping based on acoustic CFL
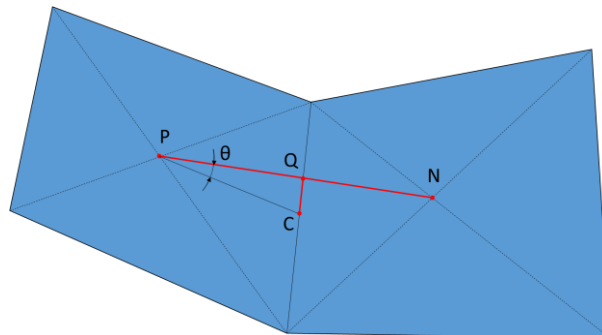
Figure 56 Definition of the mesh quality indicies in OpenFOAM.
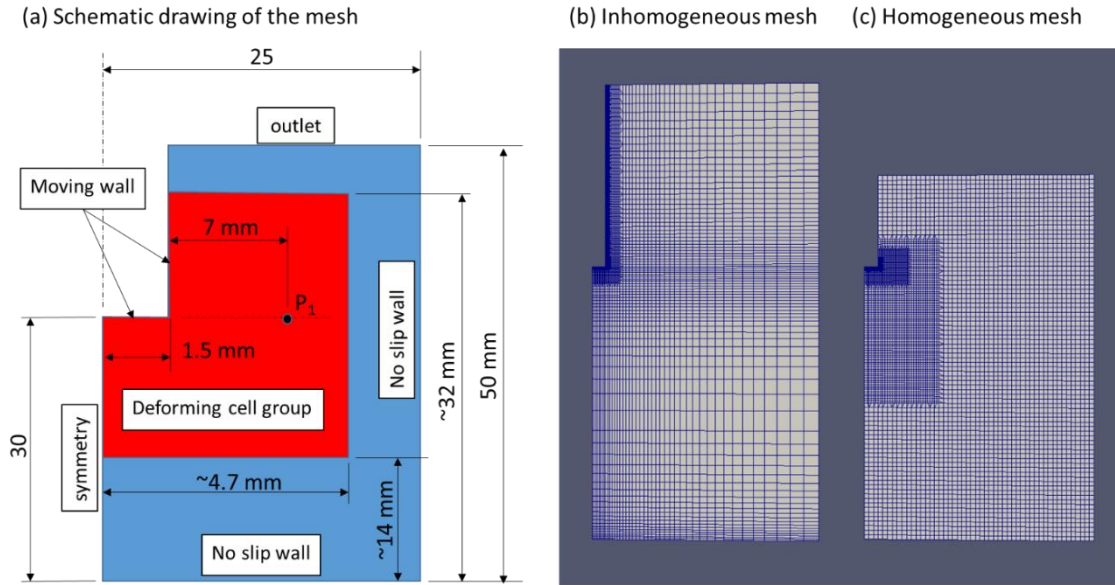
Figure 57 An illustration of the mesh grid used in the study.

number was used. With the automatic time stepping, the extracted data were re-sampled for the Fourier analysis at a uniform time interval of 1×10^{-8} s as per the fixed time step size. In the final stage of study, two alternative mesh grids as shown in Figure 57 (b) and (c) were used to investigate the influence of the mesh grids.

Table 20 Specifications of the constructed mesh grids

Parameter		Values		Unit
		inhomogeneous	homogeneous	
Total number of cells		6559	7827	-
Δx	Min.	47×10^{-6}	63×10^{-6}	[m]
	Max.	1.64×10^{-3}	0.50×10^{-3}	[m]
Δz	Min.	52×10^{-6}	63×10^{-6}	[m]
	Max.	2.18×10^{-3}	0.50×10^{-3}	[m]
Cells in the gap region under the horn tip (Hor. x Vert.)		32 x 42	24 x 101	-
Maximum non-orthogonality		53.96	27.78	[degrees]
Maximum skewness		0.352	0.361	-

6.3.3   Boundary conditions

The same boundary conditions were imposed in principle as per the study in the previous chapter. To the outlet boundary, a new pressure boundary condition as 'fixed mean value' was introduced. The base line boundary conditions are tabulated in Table 21. The piston side wall not covered by the deforming cell group was defined as a static no slip wall boundary. Different turbulent kinetic energy wall boundary conditions were compared. The base line wall function was 'kqR' wall function. This wall function, which imposes zero gradient condition, is a proper approximation of high Reynolds number turbulent flows (Liu, 2017). However, it was not clear if the flow near the moving piston could be described appropriately by that wall function. Therefore, a comparison test was necessary to choose more appropriate wall function. Since 'kLowRe' wall function can switch modes between the logarithmic region and the fully turbulent region based on the calculated y^+ value, it appeared appropriate for the purpose. The turbulent kinetic energy at the wall boundaries was given an initial value of 0.01 m^2/s^2 assuming 2 % of turbulence.

Table 21 The base line of the boundary conditions.

variable	piston	bottom	side wall	outlet
p	zero gradient	$\leftarrow$	$\leftarrow$	$p_{mean} = 0$
U	moving wall (no slip)	no slip wall	$\leftarrow$	inletOutlet
ρ	zero gradient	$\leftarrow$	$\leftarrow$	$\leftarrow$
k	kqR wall function	$\leftarrow$	$\leftarrow$	inletOutlet
ν_t	nutUSpalding wall function	$\leftarrow$	$\leftarrow$	calculated
α	calculated.	$\leftarrow$	$\leftarrow$	$\leftarrow$

6.3.4   Numerical schemes to solve the equations

The convection or advection process in nature is directional and bounded. The upwinding schemes are a typical choice to model such directionality of convection. Since the density calculation was suspected as the main culprit of the solution instability and abnormally high pressure peaks compared with the experiment, the relevant numerical schemes were revisited if they were chosen to correspond to the real physics. It was found that the central differencing scheme had been used for the mass convection, which represented an isotropical propagation, instead of an upwinding scheme. To ensure the boundedness as well as the directionality the

scheme was substituted for van Leer scheme (Harten et al., 1983, Van Leer, 1977a). Otherwise the same numerical schemes as in the previous chapter were applied.

Since there was no good information on the flow velocity of the problem, an automatic time stepping algorithm of OpenFOAM was used to keep the calculated acoustic CFL number (Courant et al., 1967) close to unity. The coupling of the velocity and the pressure was solved by PISO algorithm. The convergence criteria for the pressure and velocity iteration were set to 1×10^{-8} and 1×10^{-9} respectively.

Finally, the last detail aspect of the numerical model such as turbulent wall functions, the LES filter and the mesh grid itself had been investigated. Previously 'kqR' wall function had been used for the turbulent kinetic energy boundary condition for the wall boundaries. However, this boundary condition imposes a zero gradient condition, which is valid only for high Reynolds number flows. An alternative wall boundary condition of the 'kLowRe' wall function switches between the flows in the logarithmic region and the outer region based on the calculated friction velocity. Hence, this wall function was a better choice without good knowledge of the flow near the ultrasonic horn.

Another potential issue was the LES filter function. Since the filter determines the scales of the resolved eddies, it should be closely matched with the actual mesh grid. The LES filtering in OpenFOAM is achieved implicitly based on the cubed root of each cell volume. The filter size is determined by the cubed root of each cell volume. Then, depending on the filter functions, some additional treatment can be added. 'Smooth' filter function restricts the size difference between the filter sizes of the adjacent neighbour cells to ensure smooth transition across the calculation domain. However, if the default cell refinement utility is used, the actual cell sizes between the cells treated by the utility become half the size of its neighbours that are not refined. Therefore, the filter size will become smaller than the actual cell dimensions. Another choice can be determining the filter size based on the maximum dimension of a cell, namely 'maxDeltaxyz' function. The function can be applied without restriction on the mesh size ratio between the neighbouring cells. Hence it does not have the potential issue of the filter size as the smooth filter. The difference in the solution was investigated using the latter.

6.4 Results

6.4.1 Sub-harmonic oscillation and barotropic compressibility models

The barotropic cavitation model required a small time step size such as the order of 1×10^{-8} s at least. Either the linear or the Wallis model were not able to predict a correct sub-harmonic

oscillation behaviour with a high acoustic CFL number as 25. In Figure 60 and Figure 59, two sets of calculation results are compared. The first set (a) of the figures show the results with the automatic time stepping algorithm of OpenFOAM (v.3.0.1) to keep the acoustic CFL number not greater than 25. The other set (b) shows the results with a fixed time step size of 1×10^{-8} s ,which corresponds to CFL number of approximately 1.5. The Wallis model appeared to suffer from the high CFL number.

Another observation of the noise in the frequency domain with the calculation set (b) was that they showed more high frequency noise compared with the same plot for the calculation set (a). It is thought that the noise must have come from sudden pressure jumps that might have been caused by the fixed time step; with a fixed time step, the CFL number varies depending on the phase of the ultrasonic horn tip movement (Figure 58). Hence, it is possible that not all the pressure peaks were correctly captured due to increased CFL number during the compression phase. Then the missed pressure peaks might continue to grow, leading to over-predicted pressure peaks with either compressibility model. Such sudden large pressure peaks naturally require more high frequency components in Fourier space to follow them. Therefore, a part of the high frequency noise may be explained in terms of the CFL number variation.

Finally, it appears that both the barotropic compressibility models are capable of predicting the subharmonic oscillation behaviour of acoustic cavitation from the frequency analysis results in Figure 60 (b) and Figure 59 (b). It is crucial to satisfy the CFL condition ($\sigma \approx 1$) to obtain physically sound solutions using either the barotropic cavitation models.
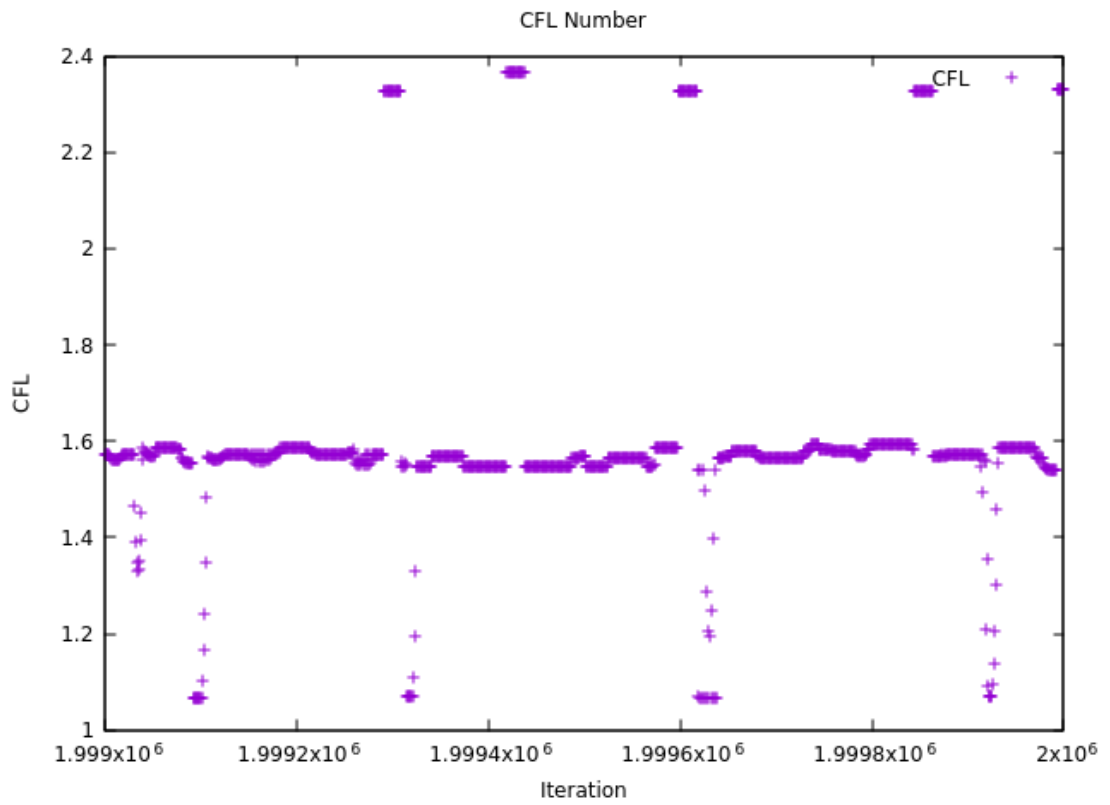
Figure 58 An illustration of the fluctuating CFL number during the simulation with a fixed time step for the test case shown in Figure 60 (b).
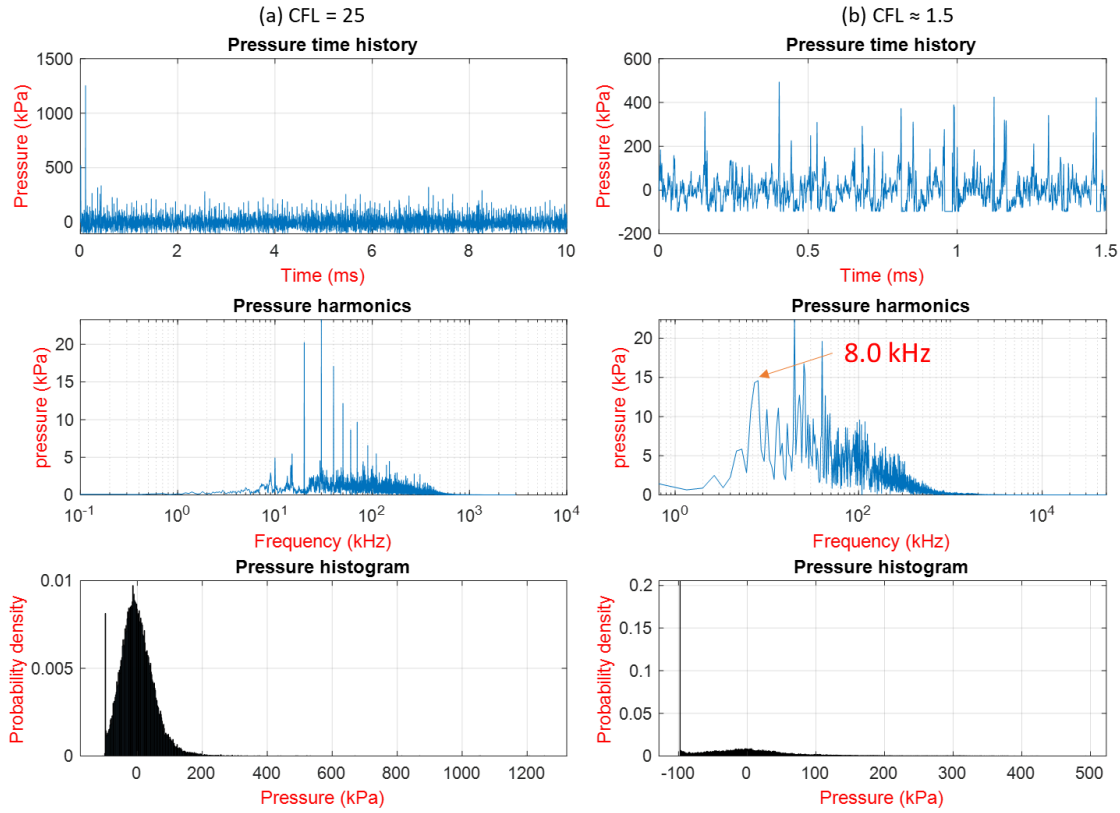
Figure 60 Predicted pressure signals with linear model and different CFL numbers.
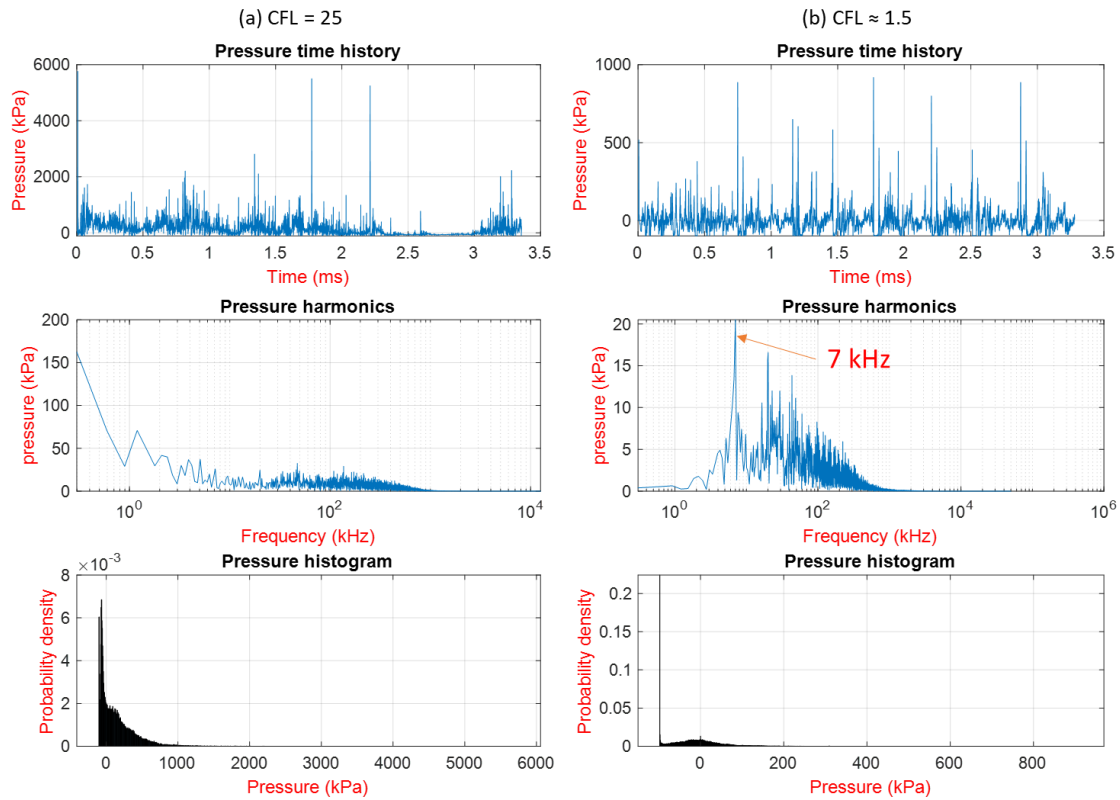
Figure 59 Predicted pressure signals with Wallis model and different CFL numbers.

6.4.2   Variation of the minimum density value

While this study was being conducted, the quality of the linear barotropic compressibility model to investigate the sub-harmonic oscillation behaviour of the acoustic cavity was not properly evaluated and overlooked. Therefore, the study only focused on the Wallis model. As stated earlier, the Wallis model tended to diverge with a low minimum density value such as 0.1 kg/m^3 or below.

Firstly, the source of the pressure peaks measured at the virtual hydrophone probe was investigated by comparing the cavity volume oscillation on the ultrasonic horn tip and the pressure peaks occurrences. The cavity volume was calculated by integrating the vapour volume in the cells below the height slightly above the ultrasonic horn tip location. The vapour volume in the individual cells was calculated by multiplying the vapour volume fraction of the cell and the cell volume. The threshold to determine the existence of the vaporous phase was set to one for the water phase. The results are shown in Figure 61. The cavity volume became minimal when the pressure peaks occurred in general. Therefore, the pressure peaks were considered as the result of the cavity oscillation.

Next, the trend of the solution was investigated by gradually lowering the minimum density value. Figure 62 shows the pressure peaks predicted with Wallis model varying the minimum density value with a fixed time step size of 1×10^{-8} s. The lower minimum density value seemed to yield a higher sub-harmonic oscillation frequency but not always. Indeed, with the higher minimum density value as 950 kg/m^3 yielded the sub-harmonic frequency as 9.47 kHz. The overview of the results did not appear to suggest any consistent physical relation with acoustic cavitation behaviour. This may be a combined result of too coarse temporal resolution and the unbounded convection scheme.
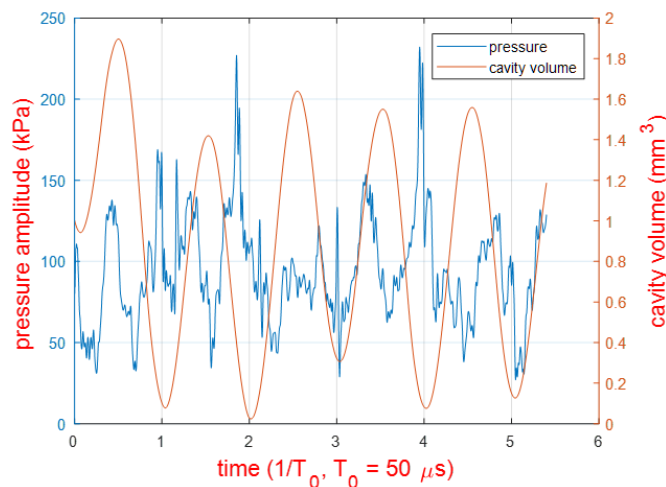
Figure 61 Pressure peaks and cavity volume oscillation.

131
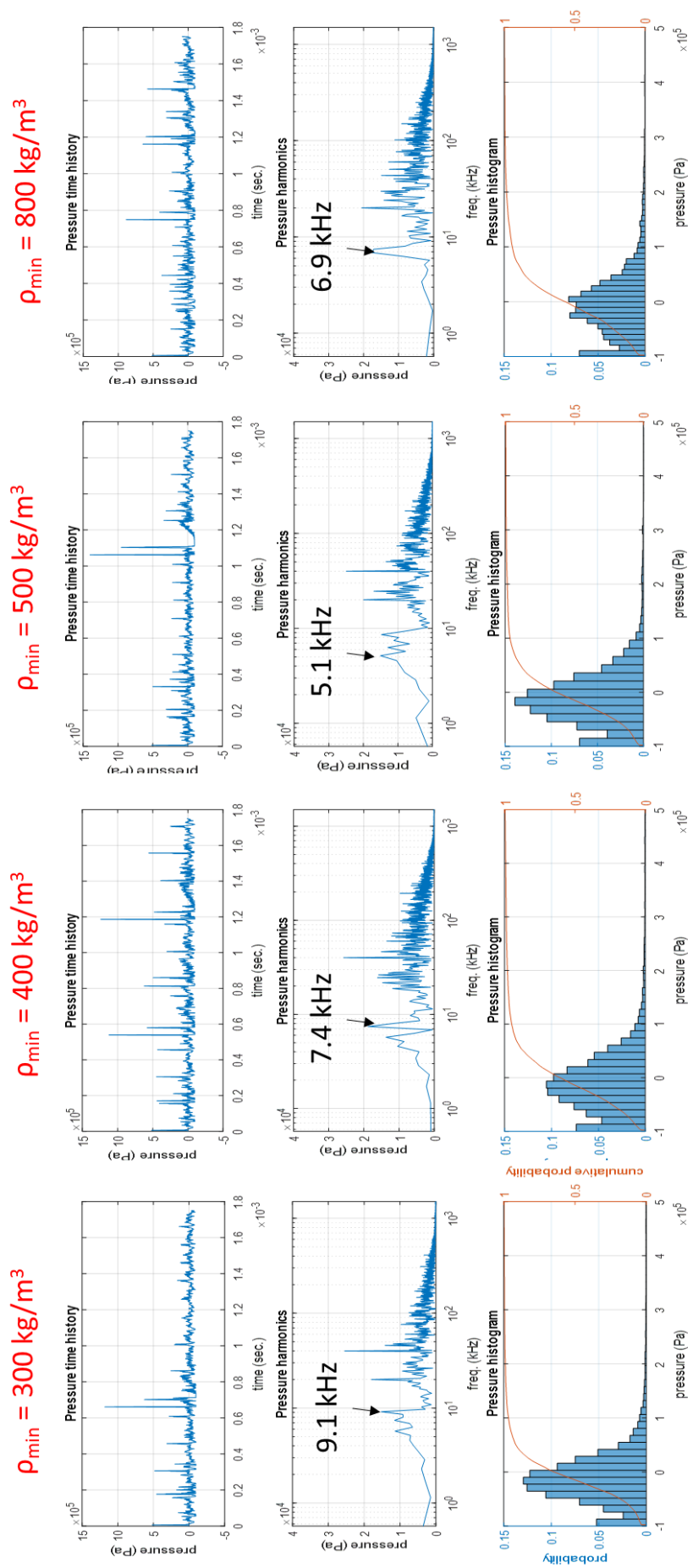
Figure 62 Predicted pressure signals with different minimum density values.

6.4.3   Effects of the bounded convection scheme

The most important and notable difference using the van Leer scheme was that the Wallis model could be run with low minimum density values. 0.017 kg/m^3 was used in the following. Two interesting results were observed with the introduction of the van Leer scheme. Firstly, it had a significant effect on the velocity field prediction (Figure 63). The figure shows a non-dimensionalised velocity field based on the maximum piston speed simulated by the above-stated numerical schemes and the minimum density values of the same order as the error in the mass continuity equation in Figure 64. Previously the jet velocity field seemed overly accelerated with very little decay. This was changed to be more realistic with much reduced magnitude of the jet velocity with fast decay as reported by Rahimi et al. (2016) or Žnidarčič et al. (2014). They reported the maximum jet velocity would reach approximately not more than 70 ~ 80 % of the maximum speed of the ultrasonic horn. The cloudy velocity field that appears in the middle of the gap near the end of the jet was thought to be contributed from numerical errors due to the non-orthogonality and the non-hexagonal mesh caused by the OpenFOAM built-in mesh refinement utility.
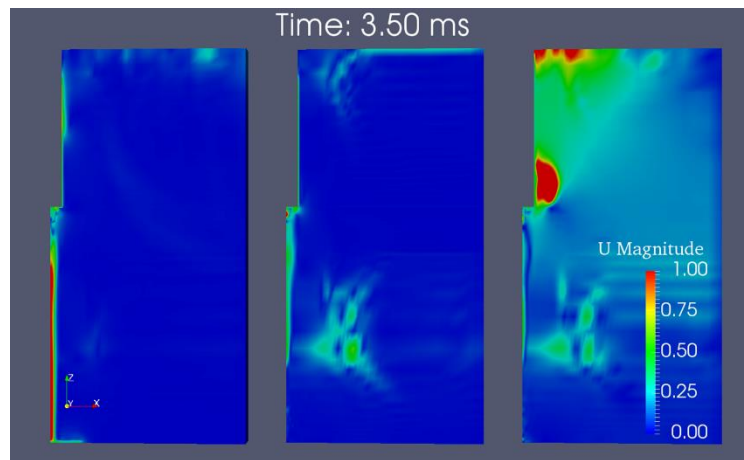
Figure 63 Non-dimesionalised fluid velocity field with different convection schemes.

Secondly, if the boundary meshes near the ultrasonic horn were too coarse and the minimum density value set low as 0.017 kg/m^3, the solution could indicate a large formation of vapour on the side of the ultrasonic horn and this lead to a significant mass loss in the system as shown in Figure 64. In the figure, (a), (b) and (c) show the vapour volume fraction at a time of t = 3.5 ms and the mass change in the domain with different convection schemes and minimum density values (ρ_{min}). The mesh grid used in this study was the inhomogeneous mesh without the refinement at the moving piston region as shown in Figure 57.

Meanwhile the solution with either scheme did not exhibit a significant mass loss with relatively high ρ_{min} value, a lower ρ_{min} value predicted a large volume of vapour on the side of the moving piston and the mass loss which is tightly linked with the vapour production. This was suspected as a result of coarse meshes in the boundary layer region that might have led to a too high a shear force in the region due to movement of the piston and no slip wall boundary condition. Improved results are shown with four times refined boundary layer meshes in Figure 65. With the refinement, the shear flow near the boundary was resolved well and the large vapour structure disappeared. As a result, the mass loss became less than 0.5 % of the total mass.

Mass loss in the numerical simulation occurs due to numerical diffusion in the solution of the continuity equation or numerical errors from non-orthogonal meshes or deforming mesh scheme violating the space conservation law. To reduce the numerical mass diffusion, meshes should be constructed to satisfy the geometric CFL number close to one. An inhomogeneous mesh grid or that violates the space conservation law will increase numerical errors. Unfortunately, with the meshes for the current problem, it is practically impossible to meet all of the requirements. It is the most important in this problem to satisfy the acoustic CFL condition to keep the accuracy of acoustic cavitation simulation. Then the geometric CFL number has to be very small, meaning the solution of the continuity equation will be highly diffusive. The homogeneity of the mesh grid should be respected at least in the important flow regions to reduce the numerical errors from the inhomogeneity. The current deforming mesh scheme needs further improvement in terms of the space conservation law and the good orthogonality of the mesh grid. Another type of mesh refinement scheme combined with the moving boundary had been tried such as mesh layer addition/removal based on the boundary movement or re-meshing a certain deforming region by solving Laplace equation for the motion. While the latter method appeared feasible and promising, negative volume cells often appeared that caused solution to diverge. It remains a limitation in the current numerical method.
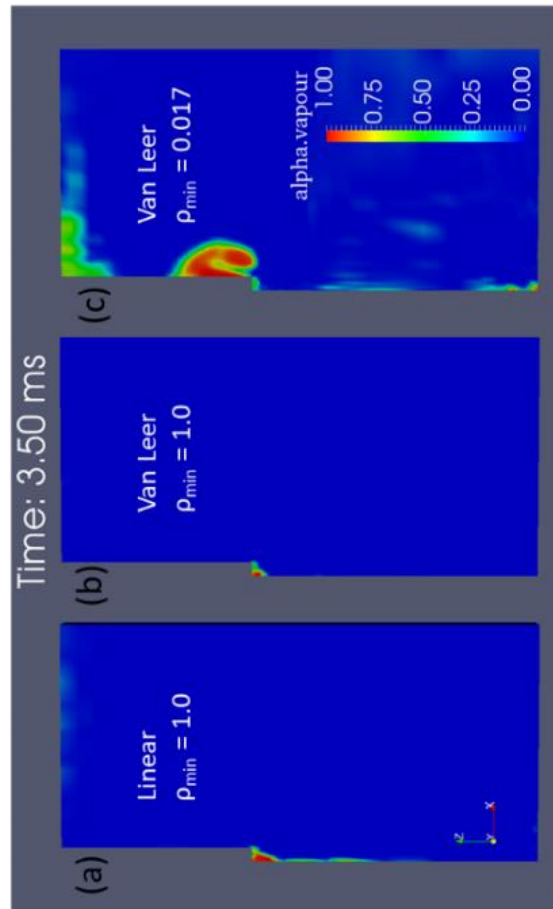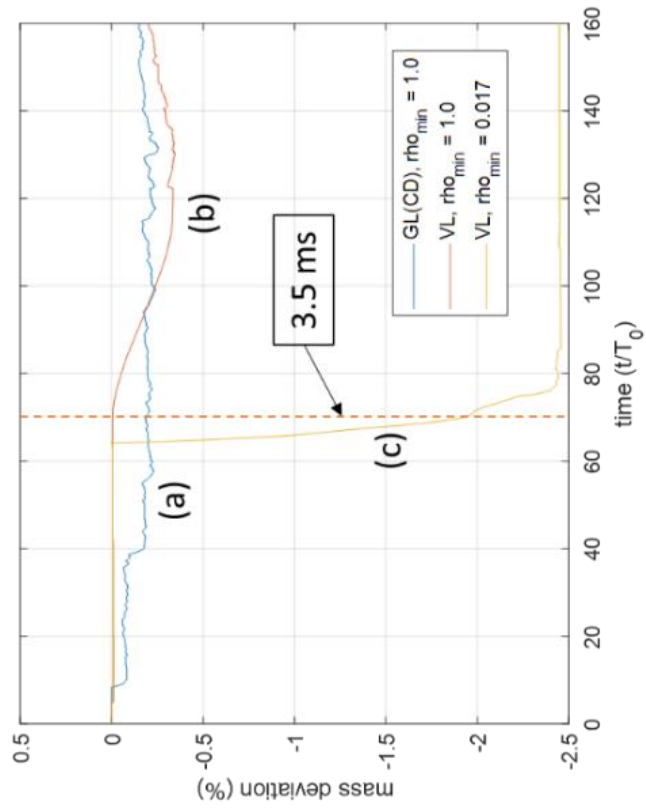
Figure 64 Predicted cavity volume with different numerical schemes.
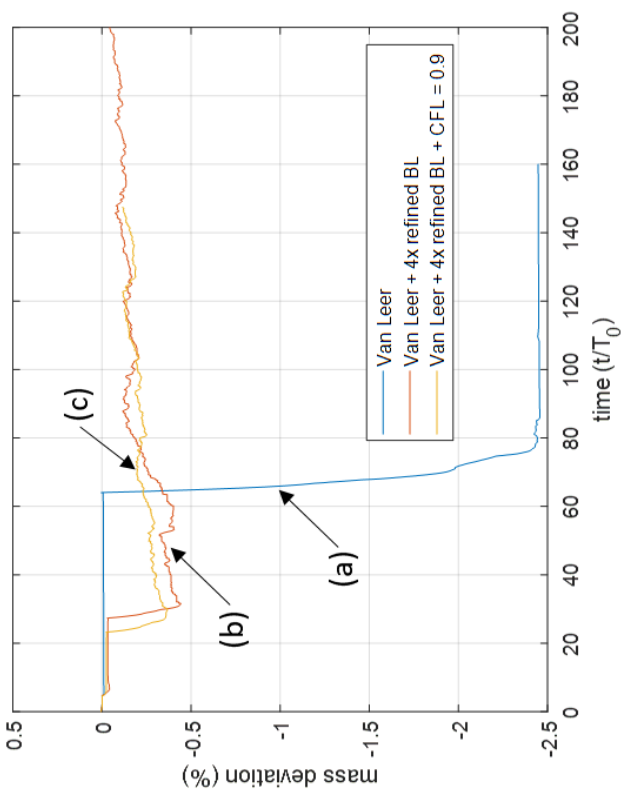
Figure 65 The solution improved with the refined boundary layer meshes.

6.4.4   Influence of the turbulent wall functions, LES filter functions and mesh grid

Figure 66 shows the first results for the benchmark test case A3 with the two turbulent wall functions and LES filter. The figure shows Reynolds number calculated from the flow (top) and the non-dimensionalised velocity field based on the maximum ultrasonic horn speed (bottom) with kqR wall function and smooth LES filter function (left) and the combination of '*k*LowRe' wall function and maxDeltaxyz LES filter function (right).

It shows a significant change in decay of the jet velocity again. Reynolds number resides in the range of 10000~50000, which is in the same order as reported by Žnidarčič et al. (2014). Because the left side results show the combined effect from wall function and LES filter, it was necessary to separate the effects.
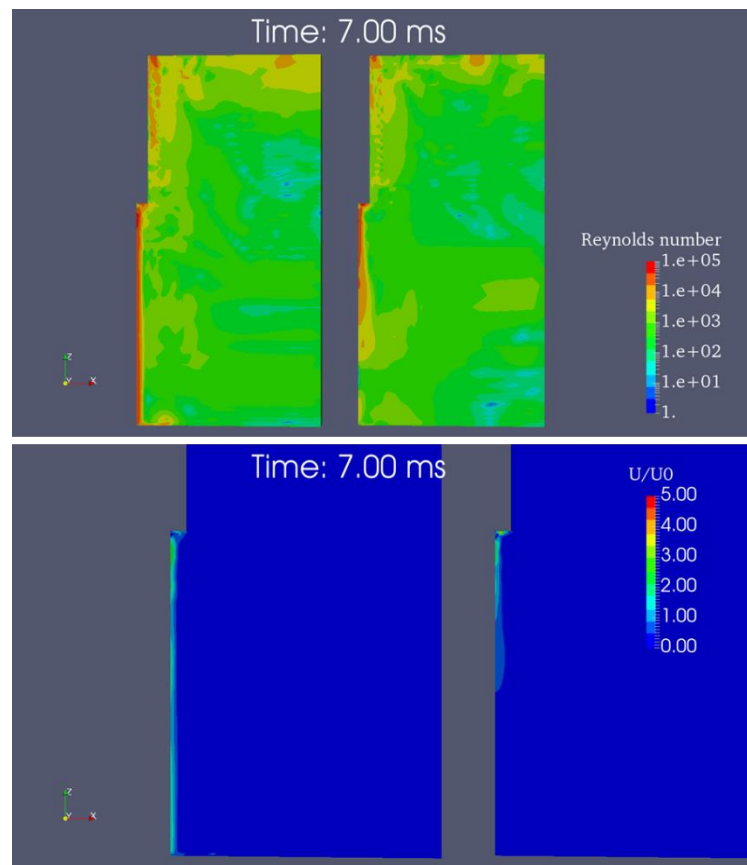
Figure 66 Reynolds number and the flow velocity field with different turbulent wall functions and the mesh grids.

Another comparison run had been carried out to identify the main contributor and the results are shown in Figure 67. The figures (a) and (b) show a different velocity profile with the same wall function but with different LES filters. The figure (b) is similar as the result with the original combination of the '*k*qR' wall function and 'smooth' filter function as shown in the

left side of Figure 66. This makes sense because the wall function is applied only on the piston. Therefore, it may have an influence on the generation of the turbulence on the piston surface, but the convection of it is independent from it. It should be more relevant with the mesh grid and the LES filter function as the current result suggests. The figures (a) and (c) suggest the initial turbulent kinetic energy level would not be so influential for the formation and decay of the acoustic streaming under the ultrasonic horn.

Finally, the influence of the mesh grid was compared in Figure 68. The figure shows the results with the same 'k Low Re' wall function and 'maxDeltaxyz' filter function applied to the different mesh grids. The figure (b) with the homogeneous meshes shows that the jet velocity magnitude tended to be further reduced to a level of $50 \sim 100$ % of the maximum piston speed. If the meshes in the gap region could be further refined the resulting velocity field may be able to reach the level observed in the real experiment. Unfortunately, with the current deforming mesh scheme, it cannot be fully satisfied without sacrificing the mesh quality where the deformation occurs.
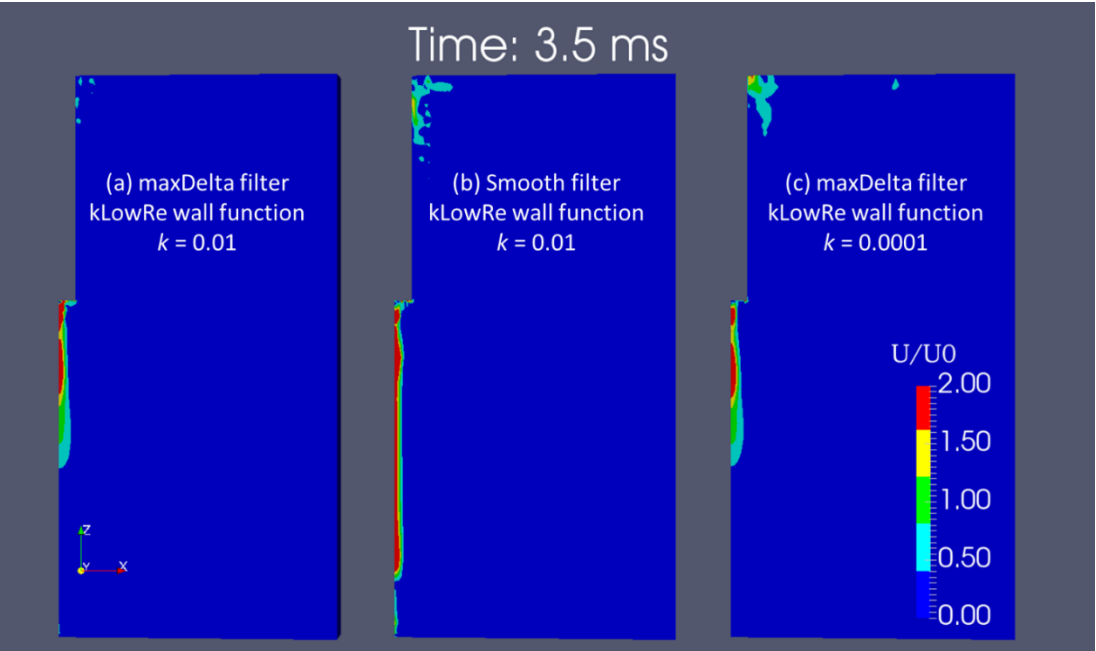
Figure 67 Comparison of different LES filter and the influence of initial turbulent kinetic energy.
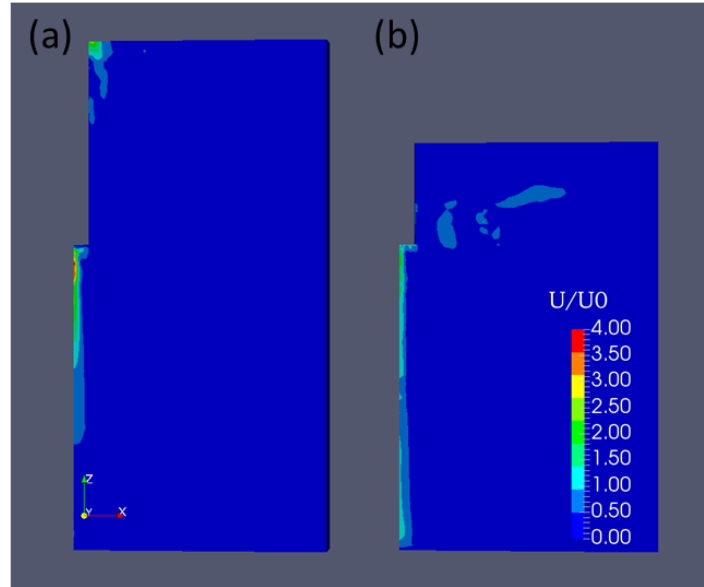
Figure 68 Acoustic stream velocity fields with different mesh grids: inhomogeneous meshes (a), homogeneous meshes (b).

6.4.5 Benchmark test results

With all the updates to the numerical model, the benchmark tests were carried out. The main results are summarised in Table 22 and Figure 71. In the table, the pressure peaks and the cavity volumes were calculated by averaging the local maxima marked in Figure 70 for the simulated time duration of 8 ms. The cavity volumes were calculated by integrating the vapour volume fractions in the spatial domain below the ultrasonic horn tip.

The Fourier analysis results based on Welch's method (Figure 69) shows a strong contribution from the acoustic driving frequency component and increasing contribution of the sub-harmonic oscillation of the acoustic cavity as the driving oscillation amplitude increases. This trend qualitatively agrees well with the experimental results discussed in chapter 3.

Trends of the sub-harmonic frequency, pressure peaks amplitude and the cavity volumes were plotted together with the experimental results in Figure 71. Although there are large differences between the prediction and the experiment, the prediction appears to follow the experimentally observed trends of the same physical quantities reasonably well. Since it took a long time for the investigation on the solution stability of the current compressible two-phase flow solver, investigation on the grid convergence and accuracy of the solutions had to be left for future work.

Table 22 Summary of the benchmark tests for Znidarcic et al. (2014) cases.

Case	A (μm)	Sub-harm. frequency (kHz)		Cavity Volume (mm3)		Pressure Peak (kPa)	
		Sim.	Exp.	Sim.	Exp.	Sim.	Exp.
A4	70	10.0	-	2.0	-	253	-
A1	100	8.406	6.510	2.4	4.5	300	310
A2	132	6.619	6.115	4.1	5.5	449	340
A3	164	6.190	5.058	5.2	8.9	521	410
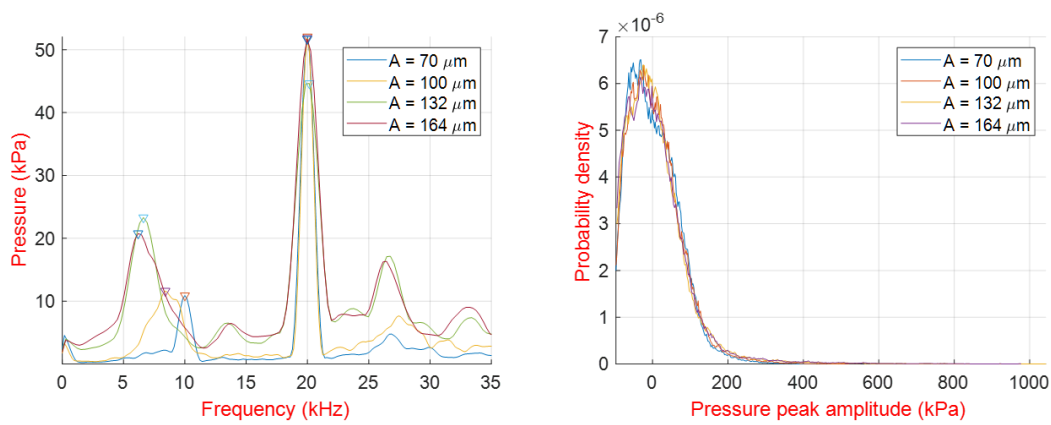
Figure 69 Sub-harmonic oscillation frequencies and PDF predicted from the simulations with different excitation amplitudes. The marked peaks on the left plot indicate the sub-harmonic and driving frequencies.
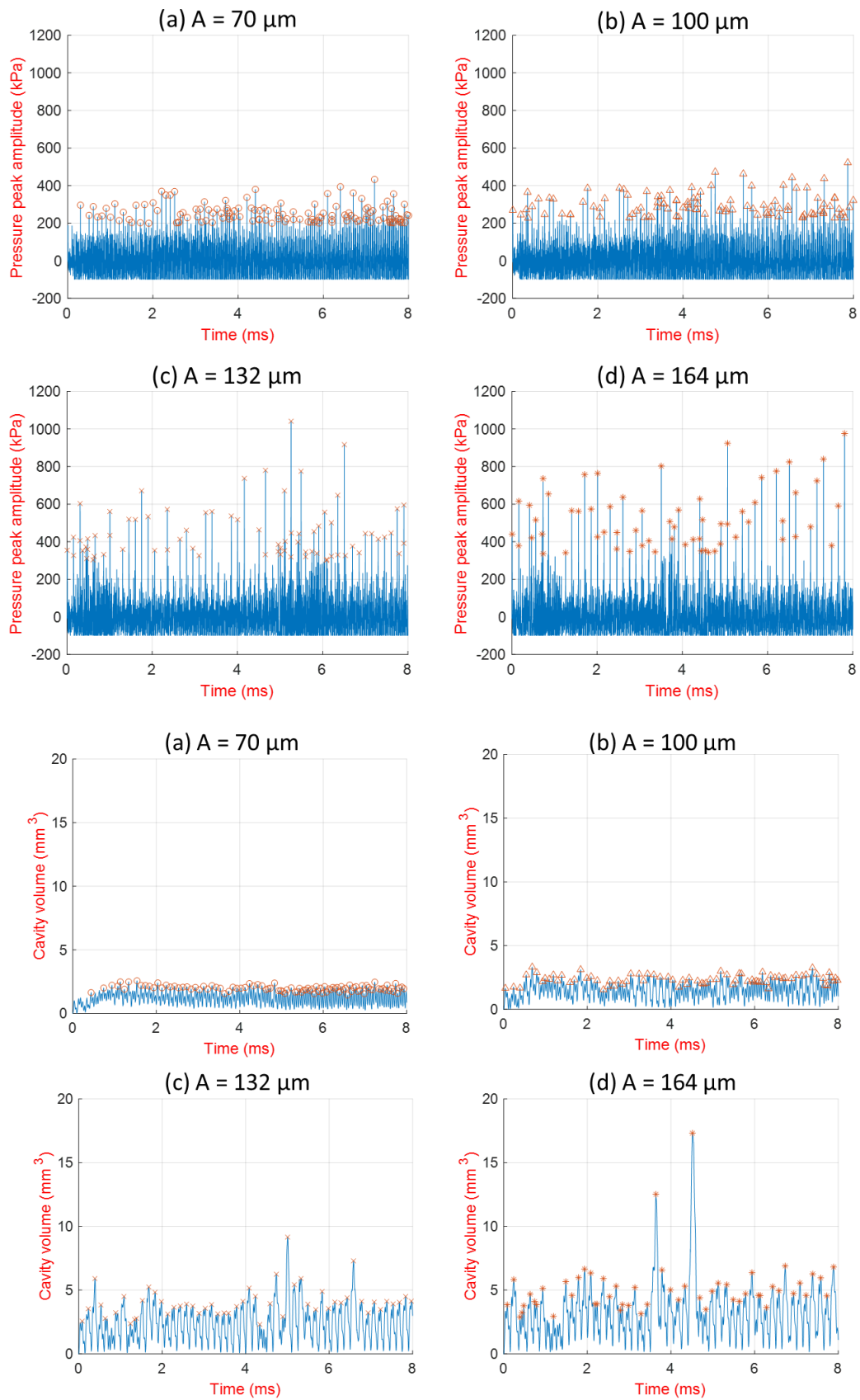
Figure 70 Pressure peaks (top) and Cavity volume predicted by integrating the vapour volume fractions (bottom) from the simulations. Local maxima that were used to calculate the mean peak pressure and volume of cavity on Table 22 are indicated by marks.
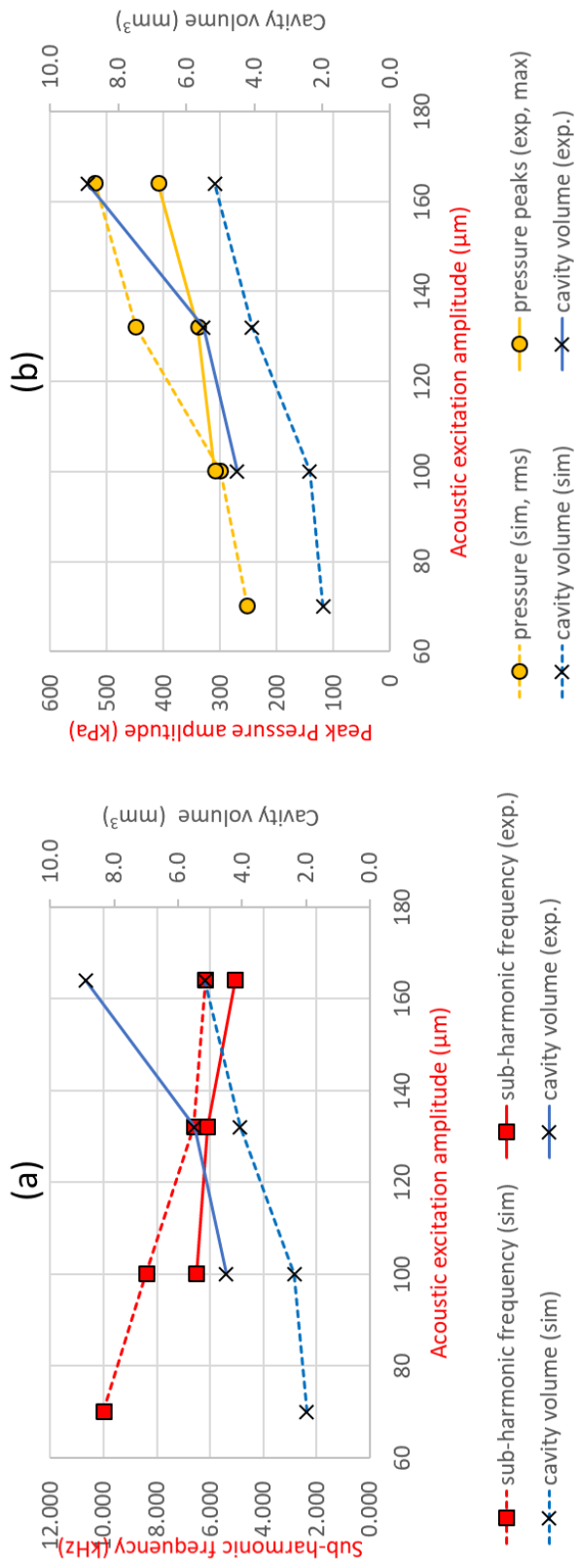
Figure 71 Comparison of the benchmark test results with acoustic excitation amplitude: trends of acoustic cavity volume and sub-harmonic frequency (a), and trends of acoustic cavity volume and peak pressure amplitude (b).

6.5   Limitations

6.5.1   Grid size

Because LES approach solves the turbulent eddies directly, appropriately designed mesh grid size is important to obtain reasonably accurate solutions. Typically, the grids are designed to satisfy y^+ to be close or smaller than unity.

The mesh grid used in this LES simulation was approximately 50 µm. Since any appropriate grid convergence study could not have been carried out at the time of writing this thesis, it is difficult to judge whether the current mesh size was appropriate for the LES simulation.

A comparison with a similar simulation work may give some indication of the appropriateness of the current mesh grid. Mottyll and Skoda (2015) designed their mesh grid size within the gap to br 25 ~ 100 µm subject to the mesh refinement level, and used the URANS approach. With the RANS approach, the mesh grids are designed to be in the y^+ range of 30 ~ 100 to use the wall functions. In this respect, with the current grid size it may be difficult to expect solutions with better resolution than those of the RANS simulation. Reducing the cell size further to make y^+ close to unity is difficult with the current deforming mesh scheme unfortunately, since the deforming cells may suffer from too high cell aspect ratio or even negative volume. This was left for future improvement of the numerical model.

6.5.2   LES with wall functions

LES simulation directly solves turbulent eddies larger than the designed spatial filter size. Therefore, if the y^+ value for the spatial filter size becomes smaller than unity, it becomes identical with solving the Direct Navier-Stokes (DNS) equations. Since, LES will resolve only a few large turbulent eddy scales significant to any given engineering problem, the smaller SGS Reynolds stresses have to be modelled by the wall functions. Therefore, the grid design of any LES simulation should be verified against the grid dependence check. This had to be left for future validation work.

6.6   Conclusions

Further to the findings in the previous chapter, the numerical model of acoustic cavitation has been studied based on the barotropic cavitation model. Through the study of the model, several important outcomes were identified.

(1) The acoustic CFL condition should be satisfied to correctly simulate acoustic cavitation using the barotropic cavitation model.

(2) In addition to Wallis model that had been successfully applied as reported by Mottyll and Skoda (2015), a good feasibility of the linear barotropic compressibility model was identified to simulate acoustic cavitation phenomenon. The linear model has the advantage over Wallis model in terms of computing cost and stability.

(3) It was crucial for a stable and physical simulation of acoustic cavitation to use a bounded numerical scheme such as van Leer scheme for the mass convection term in the continuity equation of the numerical model.

(4) The numerical model constructed through the study could produce reasonable agreement in terms of the acoustic cavity volume and pressure peaks although gave a bit higher pressure peaks than the experiment. This is believed to be caused by confined 2-D axi-symmetric model itself. A full 360 degree model would be able to improve the accuracy of the solution.

6.7   Summary

Through the previous chapters and this chapter, a numerical model to simulate acoustic cavitation phenomenon has been studied. The study covered investigation on the barotropic cavitation model, numerical schemes to discretise the mathematical model, turbulent wall functions, influence of the mesh grid on the solution, CFL condition to properly simulate acoustic cavitation phenomeon and so forth.

A good feasibility was identified using the linear barotropic compressibility model to simulate acoustic cavitation instead of relatively more time-consuming and unstable Wallis model.

The most important factor in utilising the barotropic cavitation model to predict acoustic cavitation phenomenon was identified to keep the acoustic CFL number close to 1. The sub-harmonic oscillation frequency may be easily identified without setting CFL number so low, however, the pressure peaks and the cavity volume would often go unphysically high. So for accurate pressure peak simulation, the CFL condition is very crucial for accurate solutions.

Chapter 7   **Conclusions and Future works**

7.1   **Conclusions**

As a preliminary step of developing a new cavitation erosion test method based on an acoustic emission technique, an experimental study on a threshold of acoustic emission signal level that is equivalent to the conventional soft paint tests had been carried out. Also a numerical model was studied to understand the physical mechanism of acoustic cavitation and to provide a platform for future works to further develop the new methodology of an acoustic impact method of the cavitation erosion tests.

An empirical transfer function of the acoustic emission signal level was formulated to correlate it with the physical impact loadings. To do it the drop tests had been carried out with the steel balls of different mass measuring acoustic emission signals. The acoustic emission signals showed rather consistent linear response to impact loadings. By use of this correlation, it should be possible to correlate individual AE sensor responses with the physical impact loadings.

The sub-harmonic oscillation frequency and the acoustic emission signal strength were investigated to determine an appropriate soft paint erosion test condition varying the acoustic stream dispersion distance by adjusting the gap distance between the sonotrode tip and the top face of the test specimen as a fundamental characteristic to determine an equivalent test time duration. In principle, the acoustic emission signal was expected to show the same characteristics as the cavitation-induced noise or vibration measurement signals. The sub-harmonic oscillation frequency was found rather invariant as approximately 1/5 of the driving frequency while the dispersion distance was large as 10 mm in the current test setup. The frequency decreased rapidly towards 1/10 of the driving frequency as the dispersion distance reduced below it. The acoustic emission signal strength from the sub-harmonic oscillation also showed a similar tendency as rather invariant while the dispersion distance was large as 10 mm and rapidly intensified once the distance reduced below the distance. Meanwhile, the mean level of the acoustic emission signal continued to increase as the dispersion distance reduced down to 5 mm, which seems to be reasonably counted as the contribution of the jet-like acoustic stream. As the dispersion distance gets narrower, the power intensity of the acoustic stream will become higher. However, once the dispersion distance become very narrow, formation of the recirculating acoustic stream inside the gap will be rather difficult. Hence, the intensity of the jet stream would become weaker. It appears that we have at least two paint damage mechanisms by acoustic cavitation. One will be by the direct cavitation

impact loadings and the other will be by the momentum of the jet-like acoustic stream. Apparently the latter does not appear in the frequency domain as a distinctive frequency component, but should contribute to the background noise level of the acoustic emission signal. Since this does not happen with the hydrodynamic cavitation, a caution and further distinction of its contribution compared with the direct impact loadings of the cavitation should be further investigated in the future.

The soft paint erosion tests had been carried out using the sonotrode to establish an AE threshold equivalent to the conventional soft paint tests. The equivalent test duration could be determined based on acoustic cavitation oscillation frequency and the model propeller blade frequency, which was based on a conventional 4-bladed propeller in the current study. The previous similar experimental or numerical studies used a short time series of the acoustic pressure signals or the conventional Fast Fourier Transformation (FFT) algorithm to analyse the sub-harmonic frequency of the pressure peaks induced by acoustic cavitation. It was found that the acoustic emission signals could be appropriately analysed by an Averaged Short Time Fourier Transformation (ASTFT) rather than by the conventional FFT algorithm. This was understood as an implication that the pressure peaks from acoustic cavitation occurred only in a loosely periodical manner.

Finally a numerical model to simulate acoustic cavitation have been settled based on the experimental cases of Žnidarčič et al. (2014). Important outcomes from the study are as follows:

(1) Direct simulation of the ultrasonic horn tip movement was recommendable in terms of capturing the acoustic streaming flow feature specifically when the acoustic streaming dispersion distance becomes narrow.

(2) Inclusion of the compressibility of fluids were necessary to appropriately depict the acoustic streaming.

(3) The barotropic cavitation model is confirmed useful in predicting the main features of acoustic cavitation phenomenon such as the sub-harmonic oscillation frequency and the behaviour of the acoustic bubble cluster. The sub-harmonic oscillation frequency was rather insensitive to the temporal resolution. It could be reliably captured even with a coarse temporal resolution of CFL number 25.

(4) A bounded high order convection scheme is highly recommended to guarantee the stability of the solution with the cavitatingFOAM, a compressible multiphase flow solver using a barotropic cavitation model, especially for Wallis model.

(5) Acoustic CFL number needed to be close to 1 for proper simulation of the acoustic pressure waves. This requirement mainly increases the computational cost as typically requires time step size below 5 x 10^{-9} s depending on the mesh grid sizes. The conventional problem in numerical simulation with shock waves in a small confined space appears not fully resolvable just by satisfying CFL condition. The author assumes this comes from the negligence of thermal dissipation of the potential energy of bubbles. Since the current numerical model neglects the thermal dissipation of the potential energy of the acoustic bubble, the whole energy seems to be converted into the acoustic pressure waves, which explains the most probable reason of higher acoustic pressure wave amplitudes compared with the experimental measurement data.

The following publication of the outcomes were produced during this research work.

Peer reviewed conference article:

(1) Kim, B. G., Wilson, P. A. & Turnock, S. R. (2018). "Exploration of a Possibility to Assess Erosive Cavitation by Acoustic Emission Technique". 14-16 May, 10th International Symposium on Cavitation. Baltimore, ML, USA.

Conference articles:

(2) Kim, B. G., Wilson, P. A. & Turnock, S. R. 2016. Numerical Simulation of an Ultrasonic Vibratory Cavitation Device. *In:* Wackers, J. (ed.) *19th Numerical Towing Tank Symposium.* St. Pierre d'Ole'ron.

(3) Kim, B. G., Wilson, P. A. & Turnock, S. R. (2017). *"Simulation of Acoustic Stream with a Sonotrode".* In: Lloyd, T. P. & Ploeg, A. V. D. (eds.) 20th Numerical Towing Tank Symposium. Wageningen, the Netherlands: MARIN.

7.2 Future works

This research had been carried out as an initial step towards development of a quantitative means to assess the risk of cavitation erosion on marine engineering structures subjected to the cavitation. Ultimately this research aims to develop an assessment tool to be useful in both early design stage and the full scale investigations. The focus of the research was mostly on a preliminary estimation of the acoustic emission threshold that is equivalent to the conventional soft paint erosion tests for the purpose to replace the qualitative assessment method with a quantitative means to remove uncertainties coming from the qualitative nature of the current method in the evaluation process. The current research work identified the following limitations and future works to do:

(1) The paint damage mechanism with acoustic cavitation apparatus appears to involve at least two different mechanisms: one is by the cavity-collapse-induced acoustic

pressures and the other is by the momentum of the jet-like acoustic streaming, which does not present in hydrodynamic cavitation phenomenon. At the moment, it seems the latter is reflected in the form of background noise in the Fourier space for acoustic cavitation. While the contribution of the jet momentum is reflected in the estimation of the acoustic emission threshold by taking the mean level of the signals, it is not clear yet how this difference will affect the threshold level of the acoustic emission in a large cavitation tunnel compared with the tentatively determined threshold level with a sonotrode. This will be necessary to be verified by comparing the figure measured in a large cavitation tunnel.

(2) The current numerical model as a means to study acoustic cavitation will need some further improvement in the mesh grid construction scheme to ensure smoother transition between the fine mesh part and the coarse part which was difficult to achieve only by the default mesh construction utility 'blockMesh' provided by OpenFOAM suite. This could be easily overcome by adopting a higher level of meshing utilities available in the open source/commercial market, unfortunately it has not been practiced in the current study due to limited time resource allowed for the study. The deforming mesh scheme adopted in the current study also has a clear limitation in refining the meshes in the interesting region. To overcome this inherent problem with the scheme, a higher level of re-meshing scheme to maintain the fine spatial resolution and mimic the boundary motion should be sought. A promising scheme in the OpenFOAM suite was a re-meshing scheme by resolving the interactions between the solid boundary motion and fluid reaction forces. This method had been once tried but seemed to suffer often from the creation of a negative volume mesh. Maybe this method is worth to revisiting with the currently settled model.

(3) In terms of the whole research aiming a development of a quantitative measures to assess the risk of cavitation erosion, the practical validation and application of the acoustic emission threshold from the large cavitation tunnel or real full scale ship measurement will be necessary.

References

Abdel-Maksoud, M., Hanel, D. & Lantermann, U. 2010. Modeling and Computation of Cavitation in Vortical Flow. *International Journal of Heat and Fluid Flow,* 31**,** 1065-1074.

Armakolas, I., Carlton, J., Vidakovic, M., Sun, T. & Grattan, K. T. V. 2015. The Acoustic Signatures of Cavitation Erosion on Grade Dh36 Steel. *Journal of Physics: Conference Series,* 656**,** 012109.

Ashokkumar, M. 2011. The Characterization of Acoustic Cavitation Bubbles - an Overview. *Ultrason Sonochem,* 18**,** 864-72.

Asnaghi, A. 2013. Interphaschangefoam Tutorial and Pans Turbulence Model. *In:* NILSSON, H. (ed.) *CFD with OpenSource software.* Goteborg, Sweden: Chalmers University of Technology.

Asnaghi, A., Feymark, A. & Bensow, R. E. Computational Analysis of Cavitating Marine Propeller Performance Using Openfoam. Fourth International Symposium on Marine Propulsors, June 2015 2015 Austin, TX, USA.

Bardina, J., Ferziger, J. & Reynolds, W. 1980. Improved Subgrid-Scale Models for Large-Eddy Simulation. *13th Fluid and Plasmadynamics Conference.* American Institute of Aeronautics and Astronautics.

Beig, S. A., Rodriguez, M. & Johnsen, E. 2016. Non-Spherical Bubble Collapse near Rigid and Compliant Surfaces. *31st Symposium on Naval Hydrodynamics.* Monterey, CA, U.S.A.

Benesty, J., Sondhi, M. M. & Huang, Y. 2008. *Springer Handbook of Speech Processing*, Springer-Verlag Berlin Heidelberg.

Benjamin, T. B. & Ellis, A. T. 1966. The Collapse of Cavitation Bubbles and the Pressures Thereby Produced against Solid Boundaries. *Philosophical Transactions of the Royal Society of London A: Mathematical, Physical and Engineering Sciences,* 260**,** 221-240.

Bensow, R. E. 2011. Capturing Secondary Cavitation – a Step Towards Numerical Assessment of Cavitation Nuisance. *Ship Technology Research,* 58**,** 70-81.

Biçer, B., Tanaka, A., Fukuda, T. & Sou, A. Numerical Simulation of Cavitation Phenomena in Diesel Injector Nozzles. 16th Annual Conf. ILASS-ASIA, 2013 Nagasaki, Japan. pp. 58-65.

Billet, M. L. & Weir, D. 1975. The Effect of Gas Diffusion on the Flow Coefficient for a Ventilated Cavity. *Journal of Fluids Engineering,* 97**,** 501-505.

Birkin, P. R., Offin, D. G. & Leighton, T. G. 2005. Experimental and Theoretical Characterisation of Sonochemical Cells. Part 2: Cell Disruptors (Ultrasonic Horns) and Cavity Cluster Collapse. *Physical Chemistry Chemical Physics,* 7**,** 530-537.

Birkin, P. R., Offin, D. G., Vian, C. J. B. & Leighton, T. G. 2011. Multiple Observations of Cavitation Cluster Dynamics Close to an Ultrasonic Horn Tip. *Journal of the Acoustical Society of America,* 130**,** 3379-3388.

Bjerknes, V. 1906. Recherche Sur Les Champs De Force Hydrodynamiques. *Acta Math.,* 30**,** 99-143.

Blake, F. J. 1949. Bjerknes Forces in Stationary Sound Fields. *The Journal of the Acoustical Society of America,* 21**,** 551-551.

Boashash, B. 2003. *Time Frequency Signal Analysis and Processing: A Comprehensive Reference.,* Oxford, Elsevier.

Boetcher, H. 1936. Failure of Metals Due to Cavitation under Experimental Conditions. *TRANS. ASME,* 58**,** 355-360.

Boorsma, A. 2009. Erosion Detection with Acoustic Emission: Application of Threshold. Lloyds Register.

Boorsma, A. & Fitzsimmons, P. Quantification of Cavitation Impacts with Acoustic Emissions Techniques. 7th International Symposium on Cavitation, 2009 Ann Arbor, Michigan, USA., 1-6.

Boussinesq, J. 1877. *Essai Sur La Théorie Des Eaux Courantes*, Imprimerie nationale.

Bredberg, J. 2001. On Two Equation Eddy-Viscosity Models. Goteborg, Sweden: Charlmers University of Technology.

Brennen, C. E. 1969. The Dynamic Balances of Dissolved Air and Heat in Natural Cavity Flows. *Journal of Fluid Mechanics,* 37**,** 115-127.

Brennen, C. E. 1995. *Cavitation and Bubble Dynamics*, Oxford University Press.

Brujan, E. A., Keen, G. S., Vogel, A. & Blake, J. R. 2002. The Final Stage of the Collapse of a Cavitation Bubble Close to a Rigid Boundary. *Physics of Fluids,* 14**,** 85.

Carlton, J. 2007. *Marine Propellers and Propulsion*, Elsevier.

Catarino, S. O., Miranda, J. M., Lanceros-Mendez, S. & Minas, G. 2014. Numerical Prediction of Acoustic Streaming in a Microcuvette. *The Canadian Journal of Chemical Engineering,* 92**,** 1988-1998.

Ceccio, S. L. & Brennen, C. E. 1991. Observations of the Dynamics and Acoustics of Travelling Bubble Cavitation. *Journal of Fluid Mechanics,* 233**,** 633-660.

Chahine, G. L. 1982. Experimental and Asymptotic Study of Nonspherical Bubble Collapse. *Applied Scientific Research,* 38**,** 187-197.

Chahine, G. L. 1984. Pressures Generated by a Bubble Cloud Collapse. *Chemical Engineering Communications,* 28**,** 355-367.

Chahine, G. L., Duraswami, R. & Rebut, M. 1992. Analytical and Numerical Study of Large Large Bubble/Bubble and Bubble/Flow Interaction. *19th ONR Symp. of Naval Hydrodynamics.* Seoul, South Korea.

Chahine, G. L., Franc, J.-P. & Karimi, A. 2014. Laboratory Testing Methods of Cavitation Erosion. *In:* KIM, K.-H., CHAHINE, G., FRANC, J.-P. & KARIMI, A. (eds.) *Advanced Experimental and Numerical Techniques for Cavitation Erosion Prediction.* Springer.

Chai, X. & Mahesh, K. 2010. Dynamic K-Equation Model for Les of Compressible Flows. *40th Fluid Dynamics Conference and Exhibit.* Chicago, Illinois, USA: AIAA.

Choi, P.-K. 2017. Sonoluminescence and Acoustic Cavitation. *Japanese Journal of Applied Physics,* 56**,** 07JA01.

Chung, M. S., Lee, S. J. & Chang, K. S. 2001. Effect of Interfacial Pressure Jump and Virtual Mass Terms on Sound Wave Propagation in the Two-Phase Flow. *Journal of Sound and Vibration,* 244**,** 717-728.

Chung, M. S., Park, S. B. & Lee, H. K. 2004. Sound Speed Criterion for Two-Phase Critical Flow. *Journal of Sound and Vibration,* 276**,** 13-26.

Cottrell, A. 1953. Lxxxvi. A Note on the Portevin-Le Chatelier Effect. *The London, Edinburgh, and Dublin Philosophical Magazine and Journal of Science,* 44**,** 829-832.

Courant, R., Friedrichs, K. & Lewy, H. 1967. On the Partial Difference Equations of Mathematical Physics. *IBM Journal of Research and Development,* 11**,** 215-234.

Crank, J. & Nicolson, P. 2008. A Practical Method for Numerical Evaluation of Solutions of Partial Differential Equations of the Heat-Conduction Type. *Mathematical Proceedings of the Cambridge Philosophical Society,* 43**,** 50-67.

Crum, L. A. Acoustic Cavitation. 1982 Ultrasonics Symposium, 27-29 Oct. 1982 1982. 1-11.

D'agostino, L. & Brennen, C. E. 1983. On the Acoustical Dynamics of Bubble Clouds. *Applied Mechanics, Bioengineering, and Fluids Engineering Conference.* Houston, Texas, USA: American Society of Mechanical Engineers, New York.

D'agostino, L. & Brennen, C. E. 1989. Linearized Dynamics of Spherical Bubble Clouds. *Journal of Fluid Mechanics,* 199**,** 155-176.

Deardorff, J. W. 1973. The Use of Subgrid Transport Equations in a Three-Dimensional Model of Atmospheric Turbulence. *Journal of Fluids Engineering,* 95**,** 429-438.

Delannoy, Y. Two Phase Flow Approach in Unsteady Cavitation Modelling. Proc. of Cavitation and Multiphase Flow Forum, 1990, 1990.

Demirzic, I. & Peric, M. 1988. Space Conservation Law in Finite Volume Calculations of Fluid Flow. *International Journal For Numerical Methods In Fluids,* 8**,** 1037 - 1050.

Dular, M. & Coutier-Delgosha, O. 2009. Numerical Modelling of Cavitation Erosion. *International Journal for Numerical Methods in Fluids,* 61**,** 1388-1410.

Dular, M., Mettin, R., Znidarcic, A. & Truong, V. A. 2012. Dynamics of Attached Cavitation at an Ultrasonic Horn Tip. *In:* OHL, C.-D., KLASEBOER, E., OHL, S. W., GONG, S. W. & KHOO, B. C. (eds.) *International Symposium on Cavitation.*

Dular, M. & Osterman, A. 2008. Pit Clustering in Cavitation Erosion. *Wear,* 265**,** 811-820.

Dular, M., Stoffel, B. & Širok, B. 2006. Development of a Cavitation Erosion Model. *Wear,* 261**,** 642-655.

Durbin, P. A. 1995. Separated Flow Computations with the K-Epsilon-V-Squared Model. *AIAA Journal,* 33**,** 659-664.

Eitzen, D. G. & Wadley, H. N. G. 1984a. Acoustic Emission: Establishing the Fundamentals. *Journal of Research of the National Bureau of Standards,* 89**,** 75-100.

Eitzen, D. G. & Wadley, H. N. G. 1984b. Acoustic Emission: Establishing the Fundamentals. *Journal of Research of the National Bureau of Standards,* 89**,** pp. 1-26.

Eller, A. & Flynn, H. 1969. Generation of Subharmonics of Order One-Half by Bubbles in a Sound Field. *The Journal of the Acoustical Society of America,* 46**,** 722-727.

Ellis, A. T. 1955. Production of Accelerated Cavitation Damage by an Acoustic Field in a Cylindrical Cavity. *The Journal of the Acoustical Society of America,* 27**,** 913-921.

Esche, R. 1952. Untersuchung Der Schwingungskavitation in Flüssigkeiten. *Acta Acustica united with Acustica,* 2**,** 208-218.

Favre, A. 1983. Turbulence: Space-Time Statistical Properties and Behavior in Supersonic Flows. *Physics of Fluids,* 26**,** 2851.

Ferziger, J. H. & Peric, M. 2002. Computational Methods for Fluid Dynamics. 3rd ed. ed.: Springer, Berlin, Heidelberg.

Fortes-Patella, R., Challier, G. & Reboud, J. 2001. Cavitation Erosion Mechanism: Numerical Simulations of the Interaction between Pressure Waves and Solid Boundaries. *International Symposium on Cavitaiton.* Pasadena, California, USA: California Institute of Technology.

Fortes-Patella, R., Choffat, T., Reboud, J. L. & Archer, A. 2013. Mass Loss Simulation in Cavitation Erosion: Fatigue Criterion Approach. *Wear,* 300**,** 205-215.

Fortes-Patella, R. & Reboud, J. L. 1998. A New Approach to Evaluate the Cavitation Erosion Power. *Journal of Fluids Engineering-Transactions of the Asme,* 120**,** 335-344.

Frampton, K. D., Martin, S. E. & Minor, K. 2003. The Scaling of Acoustic Streaming for Application in Micro-Fluidic Devices. *Applied Acoustics,* 64**,** 681-692.

Franc, J.-P., Michel, J.-M., Trong, H. N. G. & Karimi, A. From Pressure Pulses Measurements to Mass Loss Prediction: The Analysis of a Method. 2nd International Symposium on Cavitation, 1994.

Francis, H. A. 1976. Phenomenological Analysis of Plastic Spherical Indentation. *Journal of Engineering Materials and Technology,* 98**,** 272-281.

Franck, N. & Ducros, F. 1999. *Subgrid-Scale Stress Modelling Based on the Square of the Velocity Gradient Tensor*.

Frigo, M. & Johnson, S. G. Fftw: An Adaptive Software Architecture for the Fft. Proceedings of the 1998 IEEE International Conference on Acoustics, Speech and Signal Processing, ICASSP '98 (Cat. No.98CH36181), 15-15 May 1998 1998. 1381-1384 vol.3.

Fujikawa, S. & Akamatsu, T. 1980. Effects of the Non-Equilibrium Condensation of Vapour on the Pressure Wave Produced by the Collapse of a Bubble in a Liquid. *Journal of Fluid Mechanics,* 97**,** 481-512.

Ganesh, H., Wu, J. & Ceccio, S. L. Investigation of Cavity Shedding Dynamics on a Naca0015 Hydrofoil Using Time Resolved X-Ray Densitometry. 31th Symposium on Naval Hydrodynamics, 11-16 September 2016 2016 Monterey, CA, USA.

George, W. K. 2013. Lectures in Turbulence for the 21st Century. Chalmers University of Technology: turbulence-online.com.

Gerald, C. F. & Wheatley, P. O. 1985. *Applied Numerical Analysis,* Reading, Mass, Addison-Wesley Pub. Co.

Germano, M., Piomelli, U., Moin, P. & Cabot, W. H. 1991. A Dynamic Subgrid-Scale Eddy Viscosity Model. *Physics of Fluids A: Fluid Dynamics,* 3**,** 1760-1765.

Gilmore, F. R. 1952. The Growth or Collapse of a Spherical Bubble in a Viscous Compressible Liquid. Pasadena, CA, USA.: California Institute of Technology.

Godunov, S. K. 1959. A Difference Method for Numerical Calculation of Discontinuous Solutions of the Equations of Hydrodynamics. *Matematicheskii Sbornik,* 89**,** 271-306.

Haar, A. 1910. Zur Theorie Der Orthogonalen Funktionensysteme. *Mathematische Annalen,* 69**,** 331-371.

Hammitt, F. G. 1962. Observations on Cavitation Damage in a Flowing System. Final ed.: National Aeronautics and Space Administration Grant No. Ns 6-39-60.

Hansson, I., Kedrinskii, V. & Morch, K. A. 1982. On the Dynamics of Cavity Clusters. *Journal of Physics D: Applied Physics,* 15.

Hansson, I. & Morch, K. A. 1980. The Dynamics of Cavity Clusters in Ultrasonic (Vibratory) Cavitation Erosion. *Journal of Applied Physics,* 51**,** 4651-4658.

Harten, A., Lax, P. D. & Leer, B. V. 1983. On Upstream Differencing and Godunov-Type Schemes for Hyperbolic Conservation Laws. *SIAM review,* 25**,** 35-61.

Hasuike, N., Yamasaki, S. & Ando, J. 2009a. Numerical Study on Cavitation Erosion Risk of Marine Propellers Operating in Wake Flow. *Proceedings of the 7th International Symposium on Cavitation.*

Hasuike, N., Yamasaki, S. & Ando, J. 2009b. Numerical Study on Cavitation Erosion Risk of Marine Propellers Operating in Wake Flow. *Proceedings of the 7th International Symposium on Cavitation***,** 1-14.

Hasuike, N., Yamasaki, S. & Ando, J. 2011. Numerical and Experimental Investigation into Propulsion and Cavitation Performance of Marine Propeller Marine 2011. *Computational Methods in Marine Engineering Iv (Marine 2011)***,** 470-481.

Hattori, S., Hirose, T. & Sugiyama, K. 2010. Prediction Method for Cavitation Erosion Based on Measurement of Bubble Collapse Impact Loads. *Wear,* 269**,** 507-514.

Hattori, S. & Kishimoto, M. 2008. Prediction of Cavitation Erosion on Stainless Steel Components in Centrifugal Pumps. *Wear,* 265**,** 1870-1874.

Holzmann, T. 2016. *The Pimple Algorithm in Openfoam* [Online]. [Accessed].

Hsiao, C.-T., Ma, J. & Chahine, G. L. 2014. Multi-Scale Two-Phase Flow Modelling of Sheet and Cloud Cavitation. *30th Symposium on Naval Hydrodynamics.* Hobart, Tasmania, Australia.

Hsiao, C.-T., Ma, J. & Chahine, G. L. Numerical Study of Bubble Cloud Dynamics near a Rigid Wall. 31th Symposium on Naval Hydrodynmics, 11-16 September 2016 2016 Monterey, CA, USA.

Hsiao, C.-T., Ma, J. & Chahine, G. L. 2017. Multiscale Tow-Phase Flow Modeling of Sheet and Cloud Cavitation. *International Journal of Multiphase Flow*.

Huang, P. & Bradshaw, P. 1995. Law of the Wall for Turbulent Flows in Pressure Gradients. *AIAA journal,* 33**,** 624-632.

Iben, U. 2002. Modeling of Cavitation. *Systems Analysis Modelling Simulation,* 42**,** 1283-1307.

Issa, R. I. 1986. The Computation of Compressible and Incompressible Recirculating Flows by a Non-Iterative Implicit Scheme. *Journal of Computational Physics,* 62**,** pp. 66-82.

Ittc. The Specialist Committee on Cavitation Erosion on Propellers and Appendages on High Powered/High Speed Ships - Proceedings of the 24th International Towing Tank Conference. International Towing Tank Conference, 2005 Edinborough, U.K., 509-542.

Ivany, R. D. & Hammitt, F. G. 1965. Cavitation Bubble Collapse in Viscous, Compressible Liquids—Numerical Analysis. *Journal of Basic Engineering,* 87**,** 977-985.

Jamaluddin, A. R., Ball, G. J., Turangan, C. K. & Leighton, T. G. 2011. The Collapse of Single Bubbles and Approximation of the Far-Field Acoustic Emissions for Cavitation Induced by Shock Wave Lithotripsy. *Journal of Fluid Mechanics,* 677**,** 305-341.

Johnson, D. A. & King, L. 1985. A Mathematically Simple Turbulence Closure Model for Attached and Separated Turbulent Boundary Layers. *AIAA journal,* 23**,** 1684-1692.

Kamono, H., Kato, H., Yamaguchi, H. & Miyanaga, M. 1993. Simulation of Cavity Flow by Ventilated Cavitation on a Foil Section. *ASME-PUBLICATIONS-FED,* 153**,** 183-183.

Karimi, A. & Avellan, F. 1986. Comparison of Erosion Mechanisms in Different Types of Cavitation. *Wear,* 113**,** 305-322.

Karimi, A. & Leo, W. R. 1987. Phenomenological Model for Cavitation Erosion Rate Computation. *Materials Science and Engineering,* 95**,** 1-14.

Kato, H., Konno, A., Maeda, M. & Yamaguchi, H. 1996. Possibility of Quantitative Prediction of Cavitation Erosion without Model Test. *Journal of Fluids Engineering-Transactions of the Asme,* 118**,** 582-588.

Keller, J. B. & Miksis, M. 1980. Bubble Oscillations of Large Amplitude. *The Journal of the Acoustical Society of America,* 68**,** 628-633.

Keshtiban, I. J., Belblidia, F. & Webster, M. F. 2004. Compressible Flow Solvers for Low Mach Number Flows - a Review. Swansea: Institute of Non-Newtonian Fluid Mechanics, University of Wales.

Kim, B. G., Wilson, P. A. & Turnock, S. R. 2016. Numerical Simulation of an Ultrasonic Vibratory Cavitation Device. *In:* WACKERS, J. (ed.) *19th Numerical Towing Tank Symposium.* St. Pierre d'Ole'ron.

Kohama, Y., Hishinuma, N., Ohta, F. & Segawa, K. 1993. Interaction between Boundary-Layer-Transition and Cavitation Phenomena on a Yawed Cylinder. *Jsme International Journal Series B-Fluids and Thermal Engineering,* 36**,** 245-251.

Konno, A., Kato, H., Yamaguchi, H. & Maeda, M. 1995. Prediction of Cavitaton First Report: Impact Force Spectra Caused by Cavitation Bubble Collapse. *J Soc Naval Arch Japan,* v 177**,** 9 p.

Konno, A., Kato, H., Yamaguchi, H. & Maeda, M. Observation of Cavitation Bubble Collapse by High-Speed Video. Proceedings of The Fifth Asian Symposium on Vsiualization, 1999.

Konno, A., Kato, H., Yamaguchi, H. & Maeda, M. 2002. On the Collapsing Behavior of Cavitation Bubble Clusters. *JSME International Journal Series B,* 45**,** 631-637.

Koop, A. H. 2008. *Numerical Simulation of Unsteady Three-Dimensional Sheet Cavitation*, University of Twente.

Kornfeld, M. & Suvorov, L. 1944. On the Destructive Action of Cavitation. *Journal of Applied Physics,* 15**,** 495-506.

Kraichnan, R. H. 1964. Direct-Interaction Approximation for Shear and Thermally Driven Turbulence. *Physics of Fluids,* 7**,** 1048.

Kubota, A., Kato, H. & Yamaguchi, H. 1992. A New Modelling of Cavitating Flows: A Numerical Study of Unsteady Cavitation on a Hydrofoil Section. *Journal of Fluid Mechanics,* 240**,** 59.

Kumar, S. & Brennen, C. E. 1991. Nonlinear Effects in the Dynamics of Clouds of Bubbles. *The Journal of the Acoustical Society of America,* 89**,** pp. 707-714.

Kumar, S. & Brennen, C. E. 1993. A Study of Pressure Pulses Generated by Traveling Bubble Cavitation. *Journal of Fluid Mechanics,* 255**,** 541-564.

Launder, B. E. & Spalding, D. B. 1972. *Lectures in Mathematical Models of Turbulence,* London, New York, Academic Press.

Launder, B. E. & Spalding, D. B. 1974. The Numerical Computation of Turbulent Flows. *Computer Methods in Applied Mechanics and Engineering,* 3**,** 269-289.

Lauterborn, W. & Bolle, H. 1975. Experimental Investigations of Cavitation-Bubble Collapse in the Neighbourhood of a Solid Boundary. *Journal of Fluid Mechanics,* 72**,** 391-399.

Lee, M. K., Hong, S. M., Kim, G. H., Kim, K. H., Rhee, C. K. & Kim, W. W. 2006. Numerical Correlation of the Cavitation Bubble Collapse Load and Frequency with the Pitting Damage of Flame Quenched Cu–9al–4.5ni–4.5fe Alloy. *Materials Science and Engineering: A,* 425**,** 15-21.

Leighton, T. G. 1994. *The Acoustic Bubble,* London, UK, Academic Press Limited.

Leighton, T. G. 2015. The Acoustic Bubble: Oceanic Bubble Acoustics and Ultrasonic Cleaning. *5th Pacific Rim Underwater Acoustics Conference.* Vladivostock, Russia.

Leighton, T. G., Farhat, M., Field, J. & Avellan, F. 2003. Cavitation Luminescence from Flow over a Hydrofoil in a Cavitation Tunnel. *Journal of Fluid Mechanics,* 480**,** 43-60.

Leighton, T. G., Fedele, F., Coleman, A. J., Mccarthy, C., Ryves, S., Hurrell, A. M., De Stefano, A. & White, P. R. 2008. A Passive Acoustic Device for Real-Time Monitoring of the Efficacy of Shockwave Lithotripsy Treatment. *Ultrasound in medicine & biology,* 34**,** 1651-1665.

Leighton, T. G., Meers, S. & White, P. Propagation through Nonlinear Time-Dependent Bubble Clouds and the Estimation of Bubble Populations from Measured Acoustic Characteristics. Proceedings of the Royal Society of London A: Mathematical, Physical and Engineering Sciences, 2004. The Royal Society, 2521-2550.

Leighton, T. G., Turangan, C. K., Jamaluddin, A. R., Ball, G. J. & White, P. R. 2012. Prediction of Far-Field Acoustic Emissions from Cavitation Clouds During Shock Wave Lithotripsy for Development of a Clinical Device. *Proceedings of the Royal Society A: Mathematical, Physical and Engineering Sciences,* 469**,** 20120538-20120538.

Leighton, T. G., Walton, A. J. & Pickworth, M. J. W. 1990. Primary Bjerknes Forces. *Europian Journal of Physics,* 11**,** pp. 47-50.

Leonard, A. 1974. *Energy Cascade in Large Eddy Simulations of Turbulent Fluid Flow*.

Li, Z. R. 2012. *Assessment of Cavitation Erosion with a Multiphase Reynolds-Averaged Navier-Stokes Method.* PhD Dissertation, Technical University of Delft.

Lidtke, A. K. 2017. *Predicting Radiated Noise of Marine Propellers Using Acoustic Analogies and Hybrid Eulerian-Lagrangian Cavitation Models.* Doctor of Philosophy, University of Southampton.

Lidtke, A. K., Turnock, S. R. & Humphrey, V. F. Multi-Scale Modelling of Cavitation-Induced Pressure around the Delft Twist 11 Hydrofoil. 31th Symposium on Naval Hydrodynamics, 11-16 September 2016 2016 Monterey, CA, USA.

Lighthill, J. 1978. Acoustic Streaming. *Journal of sound and vibration,* 61**,** 391-418.

Lilly, D. K. 1992. A Proposed Modification of the Germano Subgrid-Scale Closure Method. *Physics of Fluids A: Fluid Dynamics,* 4**,** 633-635.

Liu, F. 2017. A Thorough Description of How Wall Functions Are Implemented in Openfoam. *In:* NILSSON, H. (ed.) *CFD with OpenSource Software, 2016.* Chalmers University of Technology, Goteborg.

Loth, E., Tryggvason, G., Tsuji, Y., Elghobashi, S., Crowe, C. T., Berlemont, A., Reeks, M., Simonin, O., Frank, T. & Onishi, Y. 2006. 13.1 Overview of Multiphase Modeling.

Louisnard, O. & González-García, J. 2011. Acoustic Cavitation. *Ultrasound Technologies for Food and Bioprocessing.* Springer.

Ma, J., Chahine, G. L. & Hsiao, C.-T. 2015a. Spherical Bubble Dynamics in a Bubbly Medium Using an Euler–Lagrange Model. *Chemical Engineering Science,* 128**,** 64-81.

Ma, J., Hsiao, C.-T. & Chahine, G. L. 2015b. Euler–Lagrange Simulations of Bubble Cloud Dynamics near a Wall. *Journal of Fluids Engineering,* 137**,** 041301.

Mclaskey, G. C. & Glaser, S. D. 2010. Hertzian Impact: Experimental Study of the Force Pulse and Resulting Stress Waves. *J Acoust Soc Am,* 128**,** 1087-96.

Mcwade Monitoring Systems 2016. Sensor and Preamplifier Calibration. McWade Monitoring Systems.

Mehrem, A. 2013. *Theoretical Study of Microbubble Dynamics under the Action of Ultrasound Fields.* Master en Ingeniería Acústica, Universidad Politecnica De Valencia.

Meijn, G.-J. 2015. *Physical Modeling of Cavitation Using an Enthalpy Based Model.* Master of Science Final thesis, Delft University of Technology.

Mekki-Berrada, F., Combriat, T., Thibault, P. & Marmottant, P. 2016. Interactions Enhance the Acoustic Streaming around Flattened Microfluidic Bubbles. *Journal of Fluid Mechanics,* 797**,** 851-873.

Meneveau, C., Lund, T. S. & Cabot, W. H. 1996. A Lagrangian Dynamic Subgrid-Scale Model of Turbulence. *Journal of Fluid Mechanics,* 319**,** 353-385.

Menter, F. R. Zonal Two Equation Kw Turbulence Models for Aerodynamic Flows. 23rd fluid dynamics, plasmadynamics, and lasers conference, 1993. 2906.

Mettin, R. 2005. Bubble Structures in Acoustic Cavitation. *Bubble and particle dynamics in acoustic field: Modern trends and applications***,** 1-36.

Minnaert, M. 1933. Xvi. On Musical Air-Bubbles and the Sounds of Running Water. *The London, Edinburgh, and Dublin Philosophical Magazine and Journal of Science,* 16**,** 235-248.

Momma, T. 1991. *Cavitation Loading and Erosion Produced by a Cavitating Jet.* University of Nottingham.

Momma, T. & Lichtarowicz, A. 1995a. A Study of Pressures and Erosion Produced by Collapsing Cavitation. *Wear,* 186**,** 425-436.

Momma, T. & Lichtarowicz, A. 1995b. A Study of Pressures and Erosion Produced by Collapsing Cavitation. *Wear,* 186**,** 425-436.

Mottyll, S., Müller, S., Niederhofer, P., Hussong, J., Huth, S. & Skoda, R. Analysis of the Cavitating Flow Induced by an Ultrasonic Horn–Numerical 3d Simulation for the Analysis of Vapour Structures and the Assessment of Erosion-Sensitive Areas. EPJ Web of Conferences, 2014. EDP Sciences, 02078.

Mottyll, S. & Skoda, R. 2015. Numerical 3d Flow Simulation of Attached Cavitation Structures at Ultrasonic Horn Tips and Statistical Evaluation of Flow Aggressiveness Via Load Collectives. *Journal of Physics: Conference Series,* 656**,** 012052.

Mottyll, S. & Skoda, R. 2016. Numerical 3d Flow Simulation of Ultrasonic Horns with Attached Cavitation Structures and Assessment of Flow Aggressiveness and Cavitation Erosion Sensitive Wall Zones. *Ultrasonics sonochemistry,* 31**,** 570-589.

Moudjed, B., Botton, V., Henry, D., Millet, S., Garandet, J.-P. & Ben-Hadid, H. 2014. Oscillating Acoustic Streaming Jet. *Applied Physics Letters,* 105**,** 184102.

Mozurkewich, G. 2002. Heat Transport by Acoustic Streaming within a Cylindrical Resonator. *Applied acoustics,* 63**,** 713-735.

Naudé, C. F. & Ellis, A. T. 1961. On the Mechanism of Cavitation Damage by Nonhemispherical Cavities Collapsing in Contact with a Solid Boundary. *Journal of Basic Engineering,* 83**,** 648-646.

Navarrete, M., Godínez, F. A., Castellanos, F., Mejía-Uriarte, E. V., Naude, J. L. & Méndez, F. 2015. Dynamics and Acoustic Energy Dissipation in Conical Bubble Collapse. *International Journal of Multiphase Flow,* 76**,** 86-100.

Neppiras, E. 1969. Subharmonic and Other Low-Frequency Emission from Bubbles in Sound-Irradiated Liquids. *The Journal of the Acoustical Society of America,* 46**,** 587-601.

Nilsson, H. 2015. Basics of C++ in Openfoam. *MSc/PhD course in CFD with OpenSource Software.* Goteborg, Sweden: Chalmers University of Technology.

Nohmi, M., Ikohagi, T. & Iga, Y. Numerical Prediction Method of Cavitation Erosion. ASME 2008 Fluids Engineering Division Summer Meeting collocated with the Heat Transfer, Energy Sustainability, and 3rd Energy Nanotechnology Conferences, 2008. American Society of Mechanical Engineers, 1139-1145.

Noltingk, B. E. & Neppiras, E. A. 1950. Cavitation Produced by Ultrasonics. *Proceedings of the Physical Society. Section B,* 63**,** 674.

Nowak, T., Cairós, C., Batyrshin, E. & Mettin, R. 2015. Acoustic Streaming and Bubble Translation at a Cavitating Ultrasonic Horn. *AIP Conference Proceedings,* 1685**,** 020002.

Nyborg, W. L. 1953. Acoustic Streaming Due to Attenuated Plane Waves. *The Journal of the Acoustical Society of America,* 25**,** 68-75.

Nyborg, W. L. 1958. Acoustic Streaming near a Boundary. *The Journal of the Acoustical Society of America,* 30**,** 329-339.

Nyquist, H. 1928. Certain Topics in Telegraph Transmission Theory. *Transactions of the American Institute of Electrical Engineers,* 47**,** 617-644.

Ohl, C. D., Kurz, T., Geisler, R., Lindau, O. & Lauterborn, W. 1999. Bubble Dynamics, Shock Waves and Sonoluminescence. *Philosophical Transactions of the Royal Society of London A: Mathematical, Physical and Engineering Sciences,* 357**,** 269-294.

Okada, T., Iwai, Y., Hattori, S. & Tanimura, N. 1995. Relation between Impact Load and the Damage Produced by Cavitation Bubble Collapse. *Wear,* 184**,** 231-239.

Okitsu, K. & Cavalieri, F. 2018. *Sonochemical Production of Nanomaterials: Ultrasound and Sonochemistry*, Springer, Cham.

Ono, K., Cho, H. & Matsuo, T. 2008. Transfer Functions of Acoustic Emission Sensors. *journal of Acoustic Emission*.

Osterman, A., Bachert, B., Sirok, B. & Dular, M. 2009. Time Dependant Measurements of Cavitation Damage. *Wear,* 266**,** 945-951.

Parsons, C. A. & Cook, S. S. 1919. Investigations into the Causes of Corrosion or Erosion of Propellers*. *Journal of the American Society for Naval Engineers,* 31**,** 536-541.

Patankar, S. V. & Spalding, D. B. 1972. A Calculation Procedure for Heat, Mass and Momentum Transfer in Three-Dimensional Parabolic Flows. *Int. J. Heat Mass Transfer,* 15**,** pp. 1787-1806.

Patella, R. F., Reboud, J.-L. & Briancon-Marjollet, L. A Phenomenological and Numerical Model for Scaling the Flow Agressiveness in Cavitation Erosion. Cavitation Erosion Workshop, 2004. xxx.

Pereira, F., Avellan, F. & Dupont, P. 1998. Prediction of Cavitation Erosion: An Energy Approach. *Journal of Fluids Engineering-Transactions of the Asme,* 120**,** 719-727.

Peters, A., Lantermann, U. & El Moctar, O. 2018. Numerical Prediction of Cavitation Erosion on a Ship Propeller in Model- and Full-Scale. *Wear,* 408-409**,** 1-12.

Peters, A., Sagar, H., Lantermann, U. & El Moctar, O. 2015. Numerical Modelling and Prediction of Cavitation Erosion. *Wear,* 338-339**,** 189-201.

Plesset, M. & Mitchell, T. 1956. On the Stability of the Spherical Shape of a Vapor Cavity in a Liquid. *Quarterly of Applied Mathematics,* 13**,** 419-430.

Plesset, M. S. & Chapman, R. B. 1971. Collapse of an Initially Spherical Vapour Cavity in the Neighbourhood of a Solid Boundary. *Journal of Fluid Mechanics,* 47**,** 283-290.

Plesset, M. S. & Prosperetti, A. 1977. Bubble Dynamics and Cavitation. *Annual Review of Fluid Mechanics,* 9**,** 145-85.

Pöhl, F., Mottyll, S., Skoda, R. & Huth, S. 2015. Evaluation of Cavitation-Induced Pressure Loads Applied to Material Surfaces by Finite-Element-Assisted Pit Analysis and Numerical Investigation of the Elasto-Plastic Deformation of Metallic Materials. *Wear,* 330-331**,** 618-628.

Ponkratov, D. 2015. Des Prediction of Cavitation Erosion and Its Validation for a Ship Scale Propeller. *9th International Symposium on Cavitation (Cav2015),* 656.

Portevin, A. & Le Chatelier, F. 1923. Sur Un Phénomène Observé Lors De L'essai De Traction D'alliages En Cours De Transformation. *Comptes Rendus de l'Académie des Sciences Paris,* 176**,** 507-510.

Pouffary, B. 2006. Numerical Modelling of Cavitation. DTIC Document.

Prandtl, L. 1925. Bericht Über Untersuchungen Zur Ausgebildeten Turbulenz. *Z. Angew. Math. Mech,* 5**,** 136-139.

Prosperetti, A. 1974. Nonlinear Oscillations of Gas Bubbles in Liquids: Steady-State Solutions. *The Journal of the Acoustical Society of America,* 56**,** 878-885.

Rahimi, M., Movahedirad, S. & Shahhosseini, S. 2016. Cfd Study of the Flow Pattern in an Ultrasonic Horn Reactor: Introducing a Realistic Vibrating Boundary Condition. *Ultrasonics sonochemistry,* 35**,** 359-374.

Raju, R., Singh, S., Hsiao, C.-T. & Chahine, G. 2011. Study of Pressure Wave Propagation in a Two-Phase Bubbly Mixture. *Jounal of Fluids Engineering,* 133**,** 12.

Rapposelli, E. & D'agostino, L. 2003. A Barotropic Cavitation Model with Thermodynamic Effects. *Fifth International Symposium on Cavitation.* Osaka, Japan.

Rayleigh, L. 1917. Viii. On the Pressure Developed in a Liquid During the Collapse of a Spherical Cavity. *The London, Edinburgh, and Dublin Philosophical Magazine and Journal of Science,* 34**,** 94-98.

Reisman, G. E. & Brennen, C. E. 1997. Shock Wave Measurements in Cloud Cavitation. *The 21st International Symposium on Shock Waves.* Great Keppel Island, Australia.

Reisman, G. E., Wang, Y.-C. & Brennen, C. E. 1998. Observations of Shock Waves in Cloud Cavitation. *Journal of Fluid Mechanics,* 355**,** pp. 255-283.

Rogers, L. M. 2001. Structural and Engineering Monitoring by Acoustic Emission Methods—Fundamentals and Applications. *Lloyd's Register Technical Investigation Department.*

Rogers, L. M. 2003. Bubble-Collapse Impact Correlation with Erosion Rate Using Acoustic Emission Transducers

a Theoretical Investigation to Determine Experimental Methodology and Equipment Requirement. Lloyd's Register.

Roy, S. C., Franc, J.-P. & Fivel, M. 2015. Cavitation Erosion: Using the Target Material as a Pressure Sensor. *Journal of Applied Physics,* 118**,** 164905.

Rus, T., Dular, M., ŠIrok, B., HočEvar, M. & Kern, I. 2007. An Investigation of the Relationship between Acoustic Emission, Vibration, Noise, and Cavitation Structures on a Kaplan Turbine. *Journal of Fluids Engineering,* 129**,** 1112.

Saad, Y. 2003. Iterative Methods for Sparse Linear Systems. 2nd Ed. ed.

Sauer, J. & Schnerr, G. Unsteady Cavitating Flow: A New Cavitation Model Based on a Modified Front Capturing Method and Bubble Dynamics. Proceedings of 2000 ASME fluid engineering summer conference, 2000. 11-15.

Sauer, J. & Schnerr, G. 2001. Development of a New Cavitation Model Based on Bubble Dynamics. *Zeitschrift für Angewandte Mathematik und Mechanik,* 81**,** 561-562.

Schenker, M. C., Pourquie, M. J., Eskin, D. G. & Boersma, B. J. 2013. Piv Quantification of the Flow Induced by an Ultrasonic Horn and Numerical Modeling of the Flow and Related Processing Times. *Ultrason Sonochem,* 20**,** 502-9.

Schmidt, D. P. 1997. *Cavitation in Diesel Fuel Injector Nozzles.* University of Wisconsin-Madison.

Schneider, A. J. R. 1949. *Some Compressibility Effects in Cavitation Bubble Dynamics.* PhD Final Thesis, California Institute of Technology.

Scruby, C. B. 1987. An Introduction to Acoustic Emission. *Journal of Physics E: Scientific Instruments,* 20**,** 946.

Setareh, M. 2016. Acoustic Streaming Modeling. *MsC/PhD course in CFD with OpenSource Software.* Goteborg, Sweden: Chalmers University of Technology.

Singhal, A. K., Athavale, M. M., Li, H. & Jiang, Y. 2002. Mathematical Basis and Validation of the Full Cavitation Model. *Jounal of Fluid Engineering*.

Smagorinsky, J. 1963. General Circulation Experiments with the Primitive Equations: I. The Basic Experiment. *Monthly weather review,* 91**,** 99-164.

Sokolichin, A. & Eigenberger, G. 1997. Dynamic Numerical Simulation of Gas-Liquid Two Phase Flows Euler-Euler Vs Euler-Langrange. *Chemical Engineering Science,* 52**,** 16.

Sonin, A. 2001. Equation of Motion for Viscous Fluids. Massachusetts Institute of Technology.

Soyama, H., Futakawa, M. & Homma, K. 2005. Estimation of Pitting Damage Induced by Cavitation Impacts. *Journal of Nuclear Materials,* 343**,** 116-122.

Soyama, H., Kumano, H. & Saka, M. 2001. A New Parameter to Predict Cavitation Erosion. *CAV2001: Fourth International Symposium on Cavitation.* California Institute of Technology, Pasadena, CA, USA.

Spalart, P. & Jou, W. 1997. Comments on the Feasibility of Les for Wings, and on a Hybrid Rans/Les Approach.

Spalart, P. R., Deck, S., Shur, M. L., Squires, K. D., Strelets, M. K. & Travin, A. 2006. A New Version of Detached-Eddy Simulation, Resistant to Ambiguous Grid Densities. *Theoretical and Computational Fluid Dynamics,* 20**,** 181.

Sundararajan, G. & Shewmon, P. G. 1983. A New Model for the Erosion of Metals at Normal Incidence. *Wear,* 84**,** 237-258.

The Japanese Society for Non-Destructive Inspection 2008. *Practical Acoustic Emission Testing,* Seoul, South Korea, Goomibook.com.

Tomita, Y. & Shima, A. 1977. On the Behavior of a Spherical Bubble and the Impulse Pressure in a Viscous Compressible Liquid. *Bulletin of JSME,* 20**,** 1453-1460.

Truong, V. A. 2009. A Study of Impulsive Pressure Distribution of Cavitation Generated by a High Frequency Vibrational Probe. *J. Sci. Technol.(Technical Universities Pub. Hanoi, Vietnam),* 73**,** 78-84.

Turangan, C. K., Jamaluddin, A. R., Ball, G. J. & Leighton, T. G. 2008. Free-Lagrange Simulations of the Expansion and Jetting Collapse of Air Bubbles in Water. *Journal of Fluid Mechanics,* 598.

Ukpai, J. I., Barker, R., Hu, X. & Neville, A. 2013. Exploring the Erosive Wear of X65 Carbon Steel by Acoustic Emission Method. *Wear,* 301**,** 370-382.

Van Leer, B. 1977a. Towards the Ultimate Conservative Difference Scheme Iii. Upstream-Centered Finite-Difference Schemes for Ideal Compressible Flow. *Journal of Computational Physics,* 23**,** 263-275.

Van Leer, B. 1977b. Towards the Ultimate Conservative Difference Scheme. Iv. A New Approach to Numerical Convection. *Journal of Computational Physics,* 23**,** 276-299.

Van Leer, B. 1979. Towards the Ultimate Conservative Difference Scheme. V. A Second-Order Sequel to Godunov's Method. *Journal of Computational Physics,* 32**,** 101-136.

Vian, C. J., Birkin, P. R. & Leighton, T. G. 2010. Cluster Collapse in a Cylindrical Cell: Correlating Multibubble Sonoluminescence, Acoustic Pressure, and Erosion. *The Journal of Physical Chemistry C,* 114**,** 16416-16425.

Wallis, G. B. 1969. One Dimensional Two-Phase Flow.

Wang, J., Petkovsek, M., Liu, H. L., Sirok, B. & Dular, M. 2015. Combined Numerical and Experimental Investigation of the Cavitation Erosion Process. *Journal of Fluids Engineering-Transactions of the Asme,* 137.

Wang, Y.-C. & Brennen, C. E. Shock Wave Development in the Collapse of a Cloud of Bubbles. ASME, 1994. American Society of Mechanical Engineers, 15-19.

Wang, Y.-C. & Brennen, C. E. 1999. Numerical Computation of Shock Waves in a Spherical Cloud of Cavitation Bubbles. *Journal of Fluids Engineering,* 121**,** 872-880.

Welch, P. D. 1967. The Use of Fast Fourier Transform for the Estimation of Power Spectra: A Method Based on Time Averaging over Short, Modified Periodograms. *IEEE Transactions on Audio and Electroacoustics.*

White, F. M. 2011. *Fluid Mechanics*, McGraw-Hill.

Wilcox, D. C. & Rubesin, M. W. 1980. Progress in Turbulence Modeling for Complex Flow Fields Including Effects of Compressibility. NASA.

Woelke, M. 2007. Eddy Viscosity Turbulence Models Employed by Computational Fluid Dynamic. *Prace Instytutu Lotnictwa*, 92-113.

Yakubov, S., Cankurt, B., Abdel-Maksoud, M. & Rung, T. 2013. Hybrid Mpi/Openmp Parallelization of an Euler–Lagrange Approach to Cavitation Modelling. *Computers & Fluids,* 80**,** 365-371.

Yakubov, S., Maquil, T. & Rung, T. 2015. Experience Using Pressure-Based Cfd Methods for Euler–Euler Simulations of Cavitating Flows. *Computers & Fluids,* 111**,** 91-104.

Yasui, K. 2002. Influence of Ultrasonic Frequency on Multibubble Sonoluminescence. *The Journal of the Acoustical Society of America,* 112**,** 1405.

Yoshihara, K., Kato, H., Yamaguchi, H. & Miyanaga, M. Experimental Study on the Internal Flow of a Sheet Cavity. Proceedings Cavitation and Multiphase Flow Forum, 1988. 94-98.

Yoshizawa, A. 1982. A Statistically-Derived Subgrid Model for the Large-Eddy Simulation of Turbulence. *The Physics of Fluids,* 25**,** 1532-1538.

Yoshizawa, A. 1986. Statistical Theory for Compressible Turbulent Shear Flows, with the Application to Subgrid Modeling. *The Physics of fluids,* 29**,** 2152-2164.

Yoshizawa, A. & Horiuti, K. 1985. A Statistically-Derived Subgrid-Scale Kinetic Energy Model for the Large-Eddy Simulation of Turbulent Flows. *Journal of the Physical Society of Japan,* 54**,** 2834-2839.

Zhang, A., Li, S. & Cui, J. 2015. Study on Splitting of a Toroidal Bubble near a Rigid Boundary. *Physics of Fluids (1994-present),* 27**,** 062102.

Zhivomirov, H. 2013. *Short-Time Fourier Transformation (Stft) with Matlab Implementation* [Online]. MathWorks. Available: https://www.mathworks.com/matlabcentral/fileexchange/45197-short-time-fourier-transformation-stft-with-matlab-implementation [Accessed 31.8.2018 2018].

Zhong, P. & Chuong, C. J. 1993. Propagation of Shock-Waves in Elastic Solids Caused by Cavitation Microjet Impact .1. Theoretical Formulation. *Journal of the Acoustical Society of America,* 94**,** 19-28.

Žnidarčič, A., Mettin, R., Cairós, C. & Dular, M. 2014. Attached Cavitation at a Small Diameter Ultrasonic Horn Tip. *Physics of Fluids,* 26**,** 023304.

Žnidarčič, A., Mettin, R. & Dular, M. 2015. Modeling Cavitation in a Rapidly Changing Pressure Field - Application to a Small Ultrasonic Horn. *Ultrason Sonochem,* 22**,** 482-92.

Zwart, P. J., Gerber, A. G. & Belamri, T. A Two-Phase Flow Model for Predicting Cavitation Dynamics. Fifth International Conference on Multiphase Flow, Yokohama, Japan, 2004.